1 2 9 0

UNIVERSIDADE Đ
COIMBRA

Alyne Cristina Lamy Mendes

INCORPORATION OF CARBON
NANOSTRUCTURES IN SILICA AEROGELS

December 2020

Department of Chemical Engineering

Faculty of Sciences and Technology

University of Coimbra

INCORPORATION OF CARBON NANOSTRUCTURES IN SILICA AEROGELS

Alyne Cristina Lamy Mendes

PhD Thesis in Chemical Engineering supervised by Professor Doctor Luísa Maria Rocha Durães and Professor Doctor Rui Ramos Ferreira e Silva and submitted to the Department of Chemical Engineering of the Faculty of Sciences and Technology of University of Coimbra.

December 2020

1 2 9 0

UNIVERSIDADE Đ
COIMBRA

Financial Support

Acknowledgments

I would like to express my gratitude to my supervisor, Prof. Dr. Luísa Durães, for her support during these years, for sharing her experience and knowledge with me. I also want to thank my supervisor of the University of Aveiro, Prof. Dr. Rui Silva, for his guidance and for making this work possible.

I would like to extend my appreciation to Dr. Violeta Girão, that throughout this period helped me to characterize the samples, and was always available for the necessary exchange of ideas so that the goal of this work could be achieved.

My thank you to all the team at Laboratory for Building Energy Materials and Components, Empa, in particular to Dr. Matthias Koebel and Dr. Wim Malfait, for their collaboration, helpful contributions, and for making me feel welcome in Dübendorf. Thank you to Dr. Amin Sadeghpour for performing the SAXS analysis and engaging in productive discussions about data interpretation. I also want to thank Dr. Goreti Sales' group, BIOMARK, especially Dr. Ana Moreira and Verónica Serrano, for so kindly giving me access to their equipment, and allowing the electrochemical tests to be carried out.

Special thanks to the friends that this PhD gave me, Rafael Torres, Joana Ramos, Isabel Gonçalves, Cláudio Almeida, Dora Pontinha, Mariana Fonseca, David Lopes and Vinicius Andrade, each one, in their own way, helped me to reach this goal. You are the best. A sincere thanks to Prof. Portugal, who always had a kind and encouraging word, these moments made a great difference. I also want to thank Olga Terreiros who was always so willing to help me.

I would also like to extend my deepest gratitude to Márcio Ferreira, for all the companionship, support and strength he has always given me. Without his incentive I wouldn't be able to achieve any of this.

Finally, I have no words to express my gratefulness to my parents, Wilson and Adriana, and my sister Amanda. Thank you for all your unconditional support and encouragement, without you I would not be here and none of this would had been possible.

Abstract

Silica aerogels are three-dimensional porous networks that present a unique combination of properties, with high surface area and porosity and simultaneously low density and thermal conductivity. However, due to their intrinsic brittleness, the processing of native silica aerogels is not feasible without significantly damaging them, which limits their use in several applications. One possibility to improve the mechanical properties of these materials has been the addition of carbon nanostructures to the silica matrix that, besides improving the resistance of aerogels, gives new characteristics to the final composites. Motivated by the promising properties of these materials, the objectives of this work were to develop composites of silica aerogels with different carbon nanostructures (carbon nanotubes (CNTs) - 1D, and graphene oxide (GO) - 2D), to study their influence on the characteristics of the final composite materials and evaluate the possibility of their application in several areas.

The sol-gel technology was used for the synthesis of these composites, with methyltrimethoxysilane (MTMS) and 3-aminopropyltrimethoxysilane (APTMS) as silica precursor and co-precursor, respectively. The CNTs were submitted to surface modification (acid treatments and silanization) in order to improve their interaction with the silica network. The solvent mixture used during the synthesis allowed the composites to dry at ambient pressure, without significant shrinkage and with properties similar to those of their counterparts dried under supercritical conditions. The developed materials were extensively characterized, which allowed a better understanding of the effect of these carbon nanostructures on the silica matrix.

The presence of carbon nanomaterials did not prevent the formation of the silica network and, while the GO caused some impact on the chemical structure, the CNTs did not cause significant changes. As for the physical properties, the addition of these materials modified mainly the specific surface areas and pore size, however, the greatest impact on these properties was caused by the addition of APTMS in the silica matrix. Regarding the microstructure, the addition of a co-precursor had again considerable impact, but the presence of CNTs also caused a significant change, in particular the

silanized CNTs, which allowed the growth of the silica matrix around them following a more elongated shape than normally obtained for silica aerogels. An improvement in the mechanical properties was observed, with the addition of amine groups and CNTs having a synergistic effect, leading to a significant increase in the Young's modulus (up to 14 MPa). Regarding the thermal properties, the addition of small amounts of carbon materials led to a reduction in thermal conductivity, when compared with the silica matrices developed here. The greatest decrease was obtained for the sample containing 1 wt% of silanized CNTs in the matrix with only MTMS as precursor. This improvement is even more evident for temperatures above 50 °C, in which the composite material presents values up to 30% lower than the silica aerogel. Electrochemical properties were also determined, with the addition of carbon nanostructures having a substantial impact, leading to an increase in specific capacitance and a reduction in resistance.

The aerogels developed in this work also showed properties that allow their application as adsorbents, being tested for the removal of organic compounds and drugs from aqueous solutions. The materials could be tailored for each contaminant, since each type of matrix and nanomaterial used allowed a different interaction with the pollutants. While materials containing only MTMS showed better removal rates for benzene, toluene and xylene, the addition of APTMS improved the removal of phenol and tested drugs, amoxicillin and naproxen. For most pollutants the addition of carbon nanostructures led to an increase in removal rates, which can be attributed to the modification that they caused in the microstructure of silica aerogels and to a greater affinity of the carbon materials with pollutants. It was possible to verify a chemical interaction between the silica composite aerogel with GO and naproxen, which led to removals up to 99%.

In conclusion, it was possible to extensively study the properties of carbon nanostructures-MTMS-based silica aerogel composites, which allowed an understanding of the interactions between the two phases. In general, carbon nanotubes had a greater impact on the properties of these silica aerogels than graphene oxide. Due to the possibility of obtaining composite materials with specific properties, these aerogels can be used in several areas, such as thermal insulation, energy storage and adsorption, as demonstrated here.

Resumo

Aerogéis de sílica são redes porosas tridimensionais que possuem uma combinação única de propriedades, com elevadas área de superfície e porosidade e simultaneamente baixas massa volúmica e condutividade térmica. No entanto, devido à sua fragilidade intrínseca, o processamento dos aerogéis de sílica nativos não é exequível sem os danificar significativamente, o que limita seu uso em diversas aplicações. Uma possibilidade para aprimorar as propriedades mecânicas desses materiais tem sido a adição de nanoestruturas de carbono à matriz de sílica, que além de melhorar a resistência dos aerogéis, confere novas características aos compósitos finais. Motivados pelas propriedades promissoras destes materiais, os objetivos deste trabalho consistiram em desenvolver compósitos de aerogéis de sílica com diferentes nanoestruturas de carbono (nanotubos de carbono (CNTs) - 1D, e óxido de grafeno (GO) - 2D), estudar a influência destes nas características finais dos materiais compósitos e avaliar a possibilidade da sua aplicação em diversas áreas.

A tecnologia sol-gel foi utilizada para a síntese desses compósitos, com metiltrimetóxisilano (MTMS) e 3-aminopropiltrimetóxisilano (APTMS) como precursor e co-precursor de sílica, respectivamente. Os CNTs foram submetidos a modificações de superfície (tratamentos com ácido e silanização) para melhorar sua interação com a rede de sílica. A mistura de solventes utilizada durante a síntese permitiu a secagem dos compósitos à pressão ambiente, sem encolhimento significativo e com propriedades similares às dos seus homólogos secos em condições supercríticas. Os materiais desenvolvidos foram caracterizados extensivamente, permitindo um maior entendimento do efeito destas nanoestruturas de carbono na matriz de sílica.

A presença dos nanomateriais de carbono não impediu a formação da rede de sílica e, enquanto o GO causou algum impacto na estrutura química, os CNTs não causaram alterações. Quanto às propriedades físicas, a adição desses materiais modificou principalmente as áreas de superfície e tamanho de poros, no entanto, o maior impacto nessas propriedades foi causado pela adição de APTMS na matriz de sílica. Em relação à microestrutura, a adição de um co-precursor teve novamente impactos consideráveis,

porém a presença de CNTs também causou uma alteração significativa, em particular os CNTs silanizados, que permitiram o crescimento da matriz de sílica em seu redor seguindo um formato mais alongado do que o normalmente obtido para aerogéis de sílica. Foi observada uma melhora nas propriedades mecânicas, com a adição de grupos amina e CNTs tendo um efeito sinérgico, levando a um aumento significativo do módulo de Young (até 14 MPa). Quantos às propriedades térmicas, a adição de pequenas quantidades de materiais de carbono levou à diminuição da condutividade térmica, se comparados com as matrizes de sílica aqui desenvolvidas. A maior redução foi obtida para a amostra contendo 1% em peso de CNTs silanizados na matriz com apenas MTMS como precursor. Essa melhoria fica ainda mais evidente para temperaturas acima dos 50 °C, nas quais o material compósito apresenta valores até 30% menores que o aerogel de sílica. As propriedades eletroquímicas também foram determinadas, tendo a adição das nanoestruturas de carbono um impacto substancial, levando a um aumento da capacitância específica e uma redução da resistência.

Os aerogéis aqui desenvolvidos apresentaram propriedades que permitem a sua aplicação como adsorventes, sendo testados para a remoção de compostos orgânicos e fármacos de soluções aquosas. Os materiais puderam ser preparados à medida para cada contaminante, já que cada tipo de matriz e de nanomaterial utilizado permitiu uma interação distinta com os poluentes. Enquanto os materiais contendo apenas MTMS apresentaram melhores taxas de remoção para benzeno, tolueno e xileno, a adição de APTMS aprimorou a remoção do fenol e dos fármacos testados, amoxicilina e naproxeno. Para a maioria dos poluentes, a adição das nanoestruturas de carbono levou a um aumento nas taxas de remoção, o que pode ser atribuído tanto à modificação causada na microestrutura dos aerogéis de sílica quanto a uma maior afinidade dos materiais de carbono com os poluentes. Foi verificada uma interação química entre o aerogel compósito de sílica com GO e o naproxeno, o que levou a remoções de até 99%.

Em conclusão, foi possível estudar extensivamente as propriedades dos materiais compósitos de aerogéis de sílica baseados em MTMS com nanoestruturas de carbono, o que permitiu um entendimento das interações entre as duas fases. No geral, os nanotubos de carbono tiveram maior impacto nas propriedades desses aerogéis de sílica do que o óxido de grafeno. Devido à possibilidade de obter materiais compósitos com propriedades específicas, esses aerogéis podem ser utilizados em diversas áreas, como isolamento térmico, armazenamento de energia e adsorção, conforme aqui demonstrado.

Acronyms

1D	One-Dimensional
2D	Two-Dimensional
3D	Three-Dimensional
AEGM	14,14-diethoxy-3,3-dimethoxy-2,7,15-trioxa-10-aza-3,14-disilaheptadecan-8-ol
AIC	Akaike's information criteria
AMX	Amoxicillin
APD	Ambient pressure drying
APTES	(3-Aminopropyl)triethoxysilane
APTMS	(3-aminopropyl)trimethoxysilane
ARGs	Antibiotic resistance genes
BET	Brunauer–Emmett–Teller
BG	Bilayer graphene
BJH	Barrett–Johner–Halendar
BO	Bridging oxygen
BTESB	1,4-bis(triethoxysilyl)-benzene
BTMSH	1,6-bis(trimethoxysilyl)hexane
CNFs	Carbon nanofibers
CNTs	Carbon nanotubes
CP	Cross-polarization
CPE	Constant phase element
CTAB	Hexadecyltrimethylammonium bromide
CV	Cyclic voltammetry
CVD	Chemical vapor deposition
DCCA	Drying control chemical additives
DE	Diatomaceous earth
DLS	Dynamic light scattering
DMF	Dimethylformamide

DOC	Sodium deoxycholate
EDL	Electrical double layer
EDX	Energy-dispersive X-ray spectroscopy
EIS	Electrochemical impedance spectroscopy
FG	Few-layer graphene
FTIR	Fourier transform infrared transmission spectroscopy
GA	Graphene aerogel
GCNFs	Graphitic carbon nanofibers
GN–DE	Graphene–diatomaceous earth
GO	Graphene oxide
GtO	Graphite oxide
HFCVD	Hot filament chemical vapor deposition
HMDSO	Hexamethyldisiloxane
HMDZ	Hexamethyldisilazane
HOPG	Highly oriented pyrolytic graphite
HRTEM	High resolution transmission electron microscopy
HTSCD	High temperature supercritical drying
IFT	Indirect Fourier transformation
IUPAC	International union of pure and applied chemistry
LIBs	Lithium ion batteries
LTSCD	Low temperature supercritical drying
MAS	Magic angle spinning
MF	Melamine-formaldehyde
MTES	Methyltriethoxysilane
MTMS	Methyltrimethoxysilane
MWCNTs	Multi-walled carbon nanotubes
NBO	Non-bridging oxygen
NMR	Nuclear magnetic resonance
NPX	Naproxen
OD	n-octadecanol
ORMOSIL	Organically modified silica
PAN	Polyacrylonitrile
PCM	Phase change material
PDDF	Pair-distance distribution function
PECVD	Plasma-enhanced chemical vapor deposition
PEG	Poly(ethylene glycol)

PF	Phenol-formaldehyde
PFO	Pseudo-first order
PhACs	Pharmaceutical active compounds
PI	Polyimide
PL	Photo-luminescence
PSO	Pseudo-second order
PVA	Poly(vinylalcohol)
PVDF	Poly(vinylidenefluoride)
R/C	Resorcinol/catalyst
RF	Resorcinol-formaldehyde
rGO	Reduced graphene oxide
SAXS	Small angle X-ray scattering
SCD	Supercritical fluid drying
SDS	Sodium dodecylsulfate
SEM	Scanning electron microscopy
SG	Single-layer graphene
SSNMR	Solid-state nuclear magnetic resonance
STEM	Scanning/transmission electron microscopy
SWCNTs	Single-walled carbon nanotubes
TCVD	Thermal chemical vapor deposition
TEM	Transmission electron microscopy
TEOS	Tetraethylorthosilicate
TGA	Thermogravimetry analysis
TMCS	Trimethylchlorosilane
TMOS	Tetramethylorthosilicate
TPS	Transient plane source
UV-Vis	Ultraviolet–visible
VD	Vacuum drying
VOCs	Volatile organic compounds
VTMS	Vinyltrimethoxysilane
XRD	X-Ray diffraction

Contents

List of Figures

List of Tables

xxvii

Chapter 1

Introduction

Aerogels are nanostructured materials usually synthesized by the sol-gel methodology, in which a three-dimensional network is formed by a gradual changing from the liquid precursors to a colloidal solution and finally to a gel, followed by the drying of that network [1]. Even though silica gels are the most studied ones, it is possible to obtain sol-gel derived materials from several other precursors, for example metal oxides, resorcinol-formaldehyde (RF), chalcogenides, polymers and carbon nanomaterials, as well as the development of composite materials, which have attracted significant interest due to the possibility of properties' tailoring [1, 2].

The term aerogel is usually associated with gels dried by approaches using supercritical fluids, however, with the prospects of these materials, significant improvements have been made in preventing shrinkage during drying, even if this step is not carried out in supercritical conditions, either by adding fibers, polymers or by changing the surface chemistry of the gels. Due to these great developments, a new definition for the term aerogel was necessary in order to have a more appropriate description, taking into account the preservation of the network and the materials' final properties, instead of only considering the applied drying methodology.

1.1 Aerogel's definition and related properties

The first definition of aerogels was introduced in 1931 by Kistler [3], to describe gels that undergo negligible or no shrinkage of the solid network during the replacement of the liquid phase by a gas. Different definitions were proposed through the years, such as the one suggested by the International Union of Pure and Applied Chemistry (IUPAC), with aerogels being described as gels consisting of a microporous solid in which the dispersed phase is a gas [4]. Many experts, however, consider this definition incorrect, as the majority of aerogels are composed by multiple types and sizes of pores, especially mesopores [5–9].

Among the different definitions present in the literature, Leventis *et al.* [10] defined aerogels as "an open non-fluid colloidal network or polymer network that is expanded throughout its whole volume by a gas, and is formed by the removal of all swelling agents from a gel without substantial volume reduction or network compaction", while Hüsing and Schubert [11] use the term aerogels for "materials in which the typical pore structure and network are largely maintained when the pore liquid of a gel is replaced by air". Some common points can be found in these descriptions, such as, aerogels are derived from gels and the mention of changes suffered by the gel structure during drying. None of these definitions, however, mention how these changes should be measured and evaluated. Thus, the aerogels are often viewed as materials dried only with supercritical approaches, as they allow minimal changes in the gel network during the drying [12].

A more quantitative description was recently presented by Ziegler *et al.* [13]: "an aerogel is a solid with meso- and macropores with diameters up to a few hundred nanometers and a porosity of more than 95% in which the dispersed phase is a gas". Despite its restrictiveness regarding the pore sizes and porosity range, the definition gives a way, even if indirectly, of measuring the extent of network shrinkage through porosity values.

A dominant approach to obtain aerogels includes three steps: synthesis of the gel by sol-gel chemistry, aging and drying of the gels. During the synthesis stage, hydrolysis and condensation reactions occur between the chosen precursors, leading to the formation of a nanostructured solid network called gel. The aging step allows the strengthening of the gel network through polycondensation reactions [14]. The drying of the gel is the final and most critical stage. The solvent removal can be accomplished through different methodologies [7, 8, 14, 15]:

- Supercritical drying: the liquid-gas equilibrium line is bypassed via high temperature (HTSCD) or low temperature supercritical drying (LTSCD);

- Freeze-drying: the solvent is frozen and then sublimated under vacuum, bypassing

the triple point;

- Evaporative drying: the solvent entrapped in the gel is evaporated using ambient pressure drying (APD) or vacuum drying (VD).

Different conditions for drying the gels lead to distinct classifications. The alcogel's structure typically suffers minimal impact with supercritical drying techniques resulting in aerogels; using freeze-drying, the structure suffers changes as the growth of solvent crystals (most commonly water) leads to the fragmentation of the samples, common characteristic of cryogels; for evaporative drying, irreversible shrinkage of the gel and a collapse of its pores are caused by the capillary tensions, resulting normally in xerogels [8, 11, 15].

The aerogels' properties are determined by their porous matrix, and, due to the impact of the drying conditions on the matrix, the same gel can generate dried materials that possess different final macroscopic and microscopic properties. In addition, aerogels obtained by precursors with distinct chemical nature will lead to different properties, even if dried by the same methodology. Some typical properties of aerogels obtained with different precursors are summarized in Table 1.1.

Table 1.1: Selected typical properties of some types of aerogels. (Reprinted with permission from ref. [36]. Copyright (2018) Elsevier).

Samples	Bulk density (g.cm^{-3})	Specific surface area (m^2.g^{-1})	Pore size (nm)	Porosity (%)
Silica Aerogels	0.003-0.35 [14]	600-1000 [14]	5-100 [8]	> 90 [8]
Zirconia Aerogels	-	55-112 [8, 16]	7-15 [8, 16]	-
Alumina Aerogels	0.05 - 0.2 [5]	∼290-700 [5]	20-36 [[5]]	∼ 90 [17]
Titania Aerogels	-	∼80 [8] - ∼600 [18]	15-58 [18]	-
Vanadium Oxide Aerogels	-	280 [19–21]	-	98.0 [19, 21]
Manganese Oxide Aerogels	-	250 [22]	32 [22]	-
Ceria Aerogels	-	225 [23] - 345 [24, 25]	14 [25] - 24 [23]	-
Resorcinol-Formaldehyde Aerogels	0.04-0.10 [26]	∼800 (base-catalyzed) [8] ∼300 (acid-catalyzed) [8]	10-20 [8]	-
Cellulose Aerogels	0.02-0.2 [6]	100-400 [6]	1-100 [6]	-
Polyamide Aerogels	0.06 [27] - 0.29[9]	215 [9] - 470 [27]	3-60 [9]	81-94 [9]
Polyimide Aerogels	∼ 0.21 [28]	429 [28]	19.2 [28]	85.6 [28]
Polyurea Aerogels	0.02-0.54 [29, 30]	4-321 [29, 30]	6.6-54 [29, 30]	53-99 [29, 30]
Polyurethane Aerogels	0.09-0.87 [31]	0.5 - 239 [31]	8.3-66.5 [31] 15-210$^{(a)}$ [32]	28-92 [31]
Carbon Aerogels $^{(b)}$	0.05-1.0 [33]	400 [34] - 1100 [35] up to ∼3000$^{(c)}$ [34]	0.5-50 [33]	80-98 [35]

^{a} Values obtained by Hg porosimetry. ^{b} Most carbon aerogels are obtained by the pyrolysis of organic aerogels (resorcinol-formaldehyde (RF), phenol-formaldehyde (PF), cellulose, polyurethane, among others), being the values presented in this table referent to the ones obtained from RF. ^{c} Values obtained after thermal activation of carbon aerogels.

For a long time, attaining minimal impact on the gels' structure and obtaining

monolithic samples were only possible with supercritical drying approaches. However, strategies have been developed throughout the years to get monolithic samples via simpler and easier approaches than supercritical drying. Some procedures were exploited to minimize shrinkage during ambient pressure drying: surface chemistry modification of the gels with apolar groups, solvent exchange with solvents with low surface tension, and the use of drying additives which reduce the surface tension [7, 14, 15]. Materials obtained via such procedures can be named as ambigels [19, 20, 22, 23]. Molecules that show a porogen effect (*e.g.* polymers, surfactants) in the gelation stage are used to create a more narrow pore size distribution of the network, helping during the drying process via evaporative drying. As larger pores empty faster than smaller pores, uneven stresses to the walls that separate these pores are created if the pore size distribution is wide, leading to the cracking of the structure [37].
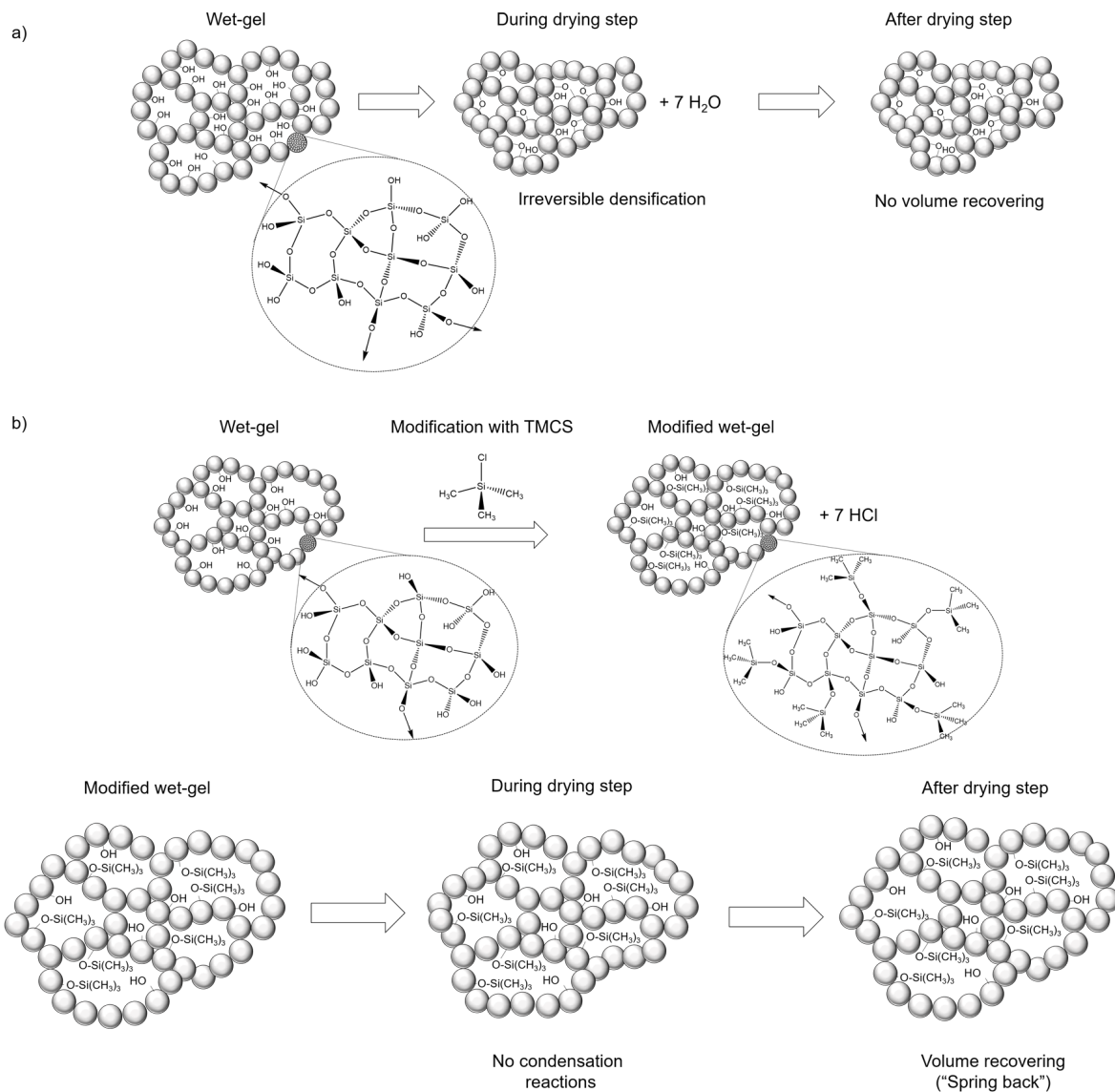
Figure 1.1: Schematic representation of a silica network during the drying step: a) without modification and b) modified with TMCS.

For the frequently studied case of silica aerogels, the surface chemistry modification of the gels can be achieved either via a co-precursor method (using an organosilane that features a non-hydrolysable apolar group like methyltrimethoxysilane - MTMS) or via a surface derivatization method with trimethylchlorosilane (TMCS), hexamethyldisilazane (HMDZ), hexamethyldisiloxane (HMDSO) or MTMS [38–42].

An example of the surface modification effect is given in Figure 1.1. Without the modification (Figure 1.1a), the silanol groups in the aerogel structure continue to react during the drying step forming siloxane bridges. The latter cause an irreversible network shrinkage. When surface modification is performed, for example with TMCS (Figure 1.1b), this modification not only avoids further condensation reactions, due to the suppression of reactive groups in the alcogel structure, but also lowers the surface tension [7, 15]. Even that some shrinkage occurs during the drying, the matrix is able to recover the original volume/shape, in an effect known as "Spring Back".

Solvent exchange can be performed using non-polar solvents like hexane and heptane [39, 41, 43–45]. Drying control chemical additives (DCCA) such as glycerol, dimethyl formamide, oxalic acid, and tetramethylammonium hydroxide can be used for reducing surface tensions in evaporative drying [8, 46, 47]. Furthermore, using fibers and/or polymer cross-linking in mechanical reinforcing of aerogels may also prevent network shrinkage during drying [15, 48–53].

Monolithic gels with high porosity and surface areas prepared via non-supercritical drying approaches are widely used nowadays. A compilation of some properties for materials presenting aerogel characteristics is presented in Tables 1.2, 1.3 and 1.4, for ambient pressure drying, vacuum drying and freeze-drying, respectively. The samples' designations are the ones used by the respective authors.

Table 1.2: Works in the literature where aerogel-like materials were obtained via ambient pressure drying. (Reprinted with permission from ref. [36]. Copyright (2018) Elsevier).

Samples [a]	Bulk density (g.cm^{-3})	Specific surface area (m^2.g^{-1})	Pore volume (cm^3.g^{-1})	Pore size (nm)	Porosity (%)	Shrinkage (%)	Ref.
Water glass-derived silica aerogel	0.14	670	3.36	11.0	92.0	$\sim$0 [b]	[39]
Water glass-derived silica aerogel	0.12	730	-	12.7	94.5	4.2 [b]	[41]
Water glass-derived silica aerogel	0.11	494	3.28	18.5	95.7	-	[42]
MTMS-derived xerogel	0.08	437	-	3.8	93.9	-	[54]
Bridged silsesquioxane aerogel	0.15	106	0.46	15.6	90.4	-	[55]
MTES-derived silica ambigel	0.41	471	0.83	7.0	-	-	[56]

Continued on next page

Table 1.2 : Works in the literature where aerogel-like materials were obtained via ambient pressure drying. (*Continued*)

Samples [a]	Bulk density (g.cm^{-3})	Specific surface area (m^2.g^{-1})	Pore volume (cm^3.g^{-1})	Pore size (nm)	Porosity (%)	Shrinkage (%)	Ref.
Silica fiber reinforced silica aerogel (7% fiber)	0.11	805	3.37	11.4	95.1	0.0 [b]	[57]
AEGM-modified silica xerogel[c]	0.40	439	1.97	17.9	-	26 [d]	[58]
AEGM-modified silica xerogel[e]	0.46	471	1.64	13.9	-	29 [d]	[58]
Cellulose fiber-silica composite aerogels (10% fiber)	0.11	680	-	-	-	15 [b]	[59]
Polyurethane/silica hybrid aerogels	0.21	845	2.83	13	86.0	12 [b]	[60]
Silica-titania aerogel (5% titania)	0.38	685	2.34	13.6	-	-	[40]
Titania xerogel	0.30	444	0.82	7.0	92.5	-	[61]
Alumina aerogel	0.17	428	-	2.2	-	-	[62]
Vanadium oxide ambigel	-	200	0.60	-	86.0	-	[19–21]
Ceria ambigels	-	200	0.21	7	-	-	[23]
MWCNTs-silica aerogel	0.20	-	4.58	~ 20	92.0	-	[63]
Graphene aerogel	0.008	26.3	0.07	9.6	-	-	[64]
Carbon aerogel[f]	0.18	857	0.53	-	-	8.7[g] 51.6[h]	[65]
Carbon aerogel[i]	-	2620	1.56	7	-	-	[66]

[a] AEGM - 14,14-diethoxy-3,3-dimethoxy-2,7,15-trioxa-10-aza-3,14-disilaheptadecan-8-ol; MWCNTs - multi-walled carbon nanotubes. [b] Volumetric shrinkage. [c] Pre-hydrolysed sample. [d] Linear shrinkage. [e] One-step sample. [f] From an organic aerogel synthesized with phenolic resin and hexamethylenetetramine. [g] Volumetric shrinkage during ambient pressure drying. [h] Volumetric shrinkage during carbonization process. [i] From an organic aerogel synthesized with resorcinol-formaldehyde.

Table 1.2 shows monolithic materials that were obtained via ambient pressure drying. To control the evaporation process of the solvent, minimizing the capillary tension, strategies as above-described ones were used. It is worth mentioning that some of these samples showed very high specific surface areas (higher than 600 m^2.g^{-1}) and low bulk densities (lower than 0.2 g.cm^{-3}). Moreover, they also exhibit high porosities and a reduced average pore size, mostly in the mesopores region. The alumina aerogel [62] seems to have a high percentage of micropores, as its average pore size is at the lower limit of the mesopores region. This value is, however, certainly biased for lower values due to the technique's limitations in the assessing the number of macropores, since it is clear the existence of large pores from scanning electron microscopy (SEM) images of these alumina aerogels. An exception in terms of surface area and pore volume is the graphene aerogel presented by Li *et al.* [64], with very low reported values for an aerogel. Nonetheless, these results are likely related to the absence of a pearl-necklace like morphology in their microstructures.

Although having quite different compositions, it is noticeable that the monoliths materials presented in Table 1.2 feature properties that are typical of aerogels when comparing the classes of the same materials from Tables 1.1 and 1.2. For example, the water glass-derived silica material obtained by Hwang *et al*. [39], dried at ambient pressure, has a bulk density of 0.14 g.cm^{-3}, a specific surface area of 670 m^2.g^{-1}, an average pore size of 11 nm and a porosity of 92%, and all these values are in agreement with the ones expected for silica aerogels (bulk density between 0.003 and 0.35 g.cm^{-3}, surface area in the range of 600-1000 m^2.g^{-1}, pore size from 5 to 100 nm, and porosities higher than 90% [8, 14]). Thus, the name aerogel seems more appropriate than xerogel for many cases illustrated in Table 1.2.

Table 1.3: Works in the literature where aerogel-like materials were obtained via vacuum drying. (Reprinted with permission from ref. [36]. Copyright (2018) Elsevier).

Samples [a]	Bulk density (g.cm^{-3})	Specific surface area (m^2.g^{-1})	Pore volume (cm^3.g^{-1})	Pore size (nm)	Porosity (%)	Shrinkage (%)	Ref.
Bridged silsesquioxane aerogel	0.09	363	0.31	7.4	96.7	no shrinkage	[67]
Resorcinol-Formaldehyde aerogel	0.24	217.2	-	11.8	-	-	[68]
Carbon aerogel[a]	0.03	1340	0.75	-	-	-	[69]
Graphene aerogel	0.79 x 10^{-2}	26.5	0.08	11.1	-	-	[64]
Manganese Oxide ambigel	-	210	1.6	29	-	-	[22]

[a] From an organic aerogel synthesized with phenol-formaldehyde.

Table 1.4: Works in the literature where aerogel-like materials were obtained via freeze-drying. (Reprinted with permission from ref. [36]. Copyright (2018) Elsevier).

Samples [a]	Bulk density (g.cm^{-3})	Specific surface area (m^2.g^{-1})	Pore volume (cm^3.g^{-1})	Pore size (nm)	Porosity (%)	Shrinkage (%)	Ref.
Silica cryogel	0.05	825	19.5	14.1	-	-	[70]
Poly(aryl ether ketone ketone)-silica composite aerogel	0.25	354	3.24	36.6	81.0	21 [a] 15[b] 6[c]	[71]
Poly(3-hydroxybutyrate) aerogel	0.04	72	-	9.8	97.0	-	[72]
Polyimide aerogels	0.19	310	2.32	29.9	86.0	23 [a] 14[b] 6[c]	[73]
Zirconia aerogel	-	397	-	0.6	-	-	[74]
SiO$_2$-graphene aerogel	-	396.9	0.672	6.77 - 8.24	-	-	[75]
3D graphene aerogels-mesoporous silica frameworks	-	1000.8	0.93	2.0	-	-	[76]
Si and N- incorporated graphene aerogels	-	312.6	1.55	19.8	-	-	[77]
Graphene aerogel	0.006	27.8	0.08	10.0	-	-	[64]

[a] Linear shrinkage during aging. [b] Linear shrinkage during solvent exchange. [c] Linear shrinkage during freeze-drying.

The monolithic samples reported in Table 1.3 were obtained via vacuum drying, where the solvent was evaporated in a vacuum oven as slowly as possible. The properties of these materials are very sensitive to their composition. Whereas the carbon aerogel features a very high surface area [69], typical of an aerogel, both the graphene aerogel synthesized by Li *et al*. [64] and the resorcinol-formaldehyde aerogel reported by Yang *et al*. [68] presented lower surface areas. Nevertheless, the latter features a typical surface area value for aerogels obtained with this system (*cf*. Table 1.1). The remaining materials show relative high surface areas, but lower than the usual values for silica or carbon aerogels (*cf*. Table 1.1). Aside from the resorcinol-formaldehyde aerogel [68], the materials exhibit low-density with a average pore size frames in the low range of the mesoporous region. These materials, once more, do not feature characteristics that are expected for xerogels. It is worth to mention that this drying approach is uncommon, with only a few published studies being available.

Works that resulted in the production of monoliths via freeze-drying are in Table 1.4. Materials with distinctive values of surface area were reported, with silica aerogel [70] and 3D graphene aerogels-mesoporous silica frameworks [76] having high surface areas, while the poly(3-hydroxybutyrate) aerogel [72] showed very low surface areas. Most materials feature surface area values between 300 and 400 $m^2.g^{-1}$ and have average pore sizes in the mesoporous region. With the exception of the poly(aryl ether ketone ketone)-silica aerogel composite, the materials in Table 1.4 show low bulk densities, with some being even lighter than aerogels. Several of these materials show properties that are similar to the ones of aerogels, and so the cryogel designation may be replaced by aerogel.

In the following paragraphs, few studies in which gels were dried with different techniques are reported, which makes the comparison more valid.

MTMS-derived gels prepared by Durães *et al*. [54] were dried with APD and HTSCD, with the xerogel and aerogel counterpart showing fairly similar properties. The xerogels presented higher values of densities (30-47% increase, depending on the temperatures used) and lower surface area (19% less). Nevertheless, porosity was almost the same, with deviations of less than 2%.

Markevicious *et al*. [59] studied the influence of LTSCD and APD in cellulose fiber-silica gel composites. As expected, higher shrinkages were verified in the APD dried aerogels, up to 5% in volumetric shrinkage if compared with their supercritically dried counterparts, and, consequently, these were slightly more dense (up to 6% more). However, the differences between these properties were not significant, confirming the possibility to obtain materials with similar properties using different drying methodologies (Figure 1.2).
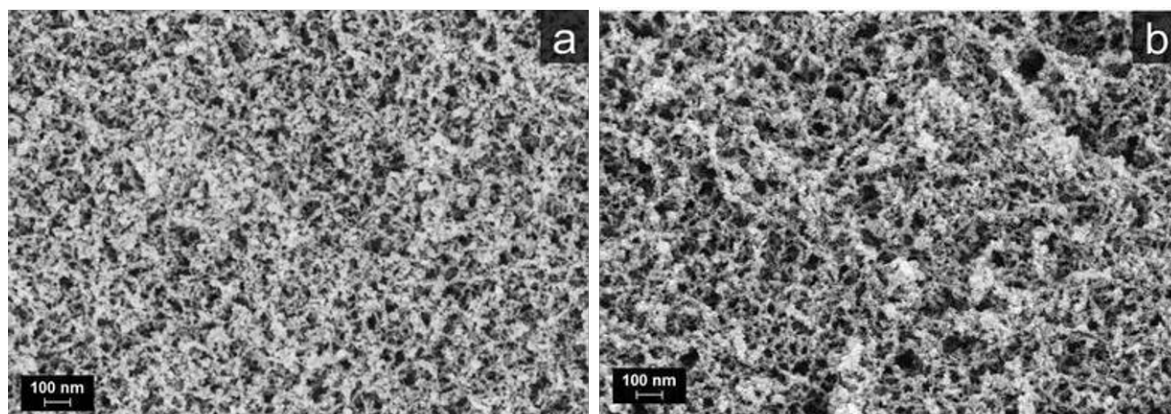
Figure 1.2: Microstructure of the silica phase in (a) supercritically dried and (b) ambient dried composite aerogels. Reprint from Ref. [59] with permission from Springer.

Graphene aerogels were prepared by Li *et al.* [64] by three different methodologies, namely APD, under vacuum and freeze-drying. Higher shrinkages were obtained by the samples dried by APD and vacuum, with these having similar bulk densities (Tables 1.2 and 1.3). The freeze-drying was the approach that least impacted the gels, with the materials showing the lowest bulk densities, allowing these to be considered aerogels. Nevertheless, when the gels were reinforced with acrylamide their shrinkage was restricted during the drying in ambient pressure and vacuum, so these samples can also be called aerogels.

Taking into account the porosity values established by Ziegler's definition, only few materials here presented would be considered aerogels, leaving out even most of the supercritically dried materials (Table 1.1), and this restriction is the weak point of this description. As here reported, materials with properties similar to the ones of aerogels can be obtained with drying approaches other than supercritical. Given these considerations and knowing that aerogels can be obtained of many compounds, Kistler's original definition proved to be the most adequate and acceptable, and prevents that aerogels are labelled as materials exclusively obtained via supercritical drying or have very narrowed intervals of some specific properties. This is also in line with the definitions proposed by Hüsing and Leventis.

An all-purpose comment on the deviation between aerogel and aerogel-like materials properties cannot be made, as this needs to be assessed for every type of aerogel, since the different chemical systems and/or synthesis conditions have a major impact in the obtained properties. However, this evaluation is not always needed as some properties can be straightforwardly labeled as being typical of an aerogel, xerogel or cryogel. Aerogels should be considered as porous materials that can be obtained from gels with multiple drying approaches, as long as the drying step does not have a significantly impact in the

gel structure. Monolithic samples and the matrix porosity (preferably above 90%) are good indicators of the gel's impact. Thus, we suggested [36] that aerogels are highly porous nanostructured solid materials derived from gels, in which the pores' filling phase is a gas and whose properties/structure are not significantly affected by the removal of swelling agents.

The properties mentioned before are structural properties like the ones reviewed in this paper. Yet, we should think that a material derived from a gel can be called an aerogel based on other properties, for example their performance on specific applications - refraction index, thermal conductivity, sound speed, adsorption capacity, *etc.*, not just structural characteristics. This new perspective on the aerogels' definition allows it to keep up with currently developed materials. The definitions of xerogels and cryogels still make sense and should be used for all the other cases where there are relevant deviations from the typical properties of aerogels.

1.2   Carbon nanostructures - silica aerogel composites

1.2.1   Silica Aerogels - typical properties and applications

Silica aerogels are generally amorphous materials, with an open and porous three-dimensional silica network, frequently prepared by a sol–gel process [78]. They have an unique combination of properties, showing porosities above 90%, high values of optical transmission ($\sim$93%) and specific surface area (typically from 250 to 800 $m^2.g^{-1}$), associated with low densities and thermal conductivities, that can be as low as 0.003 $g.cm^{-3}$ and $\sim$ 15 $mW.m^{-1}.K^{-1}$, respectively [79, 80]. These characteristics have allowed these aerogels to be used, for example, as adsorbents [81, 82], drug carriers [83, 84], for hyper-velocity particles capture and as thermal insulators in space [85], catalysts [86] and Cherenkov detectors [87].

However, some applications have been restricted due to the limitations in the aerogel's mechanical strength, which lead to the material's failure during processing [15, 88]. The possibility of incorporating different compounds into their network may overcome some of these limitations, and distinctive characteristics can be achieved when compared to the native silica aerogels [89]. For example, the incorporation of aramid fibers into tetraethylorthosilicate (TEOS) based-aerogels increases their flexural strength and reduces the thermal conductivity [48], and the addition of magnetite (Fe_3O_4) nanoparticles to silica aerogels imparts magnetic properties to the final composite [90].

Incorporation of carbon-based nanomaterials such as carbon nanotubes (CNTs) and graphene oxide (GO) with high electrical conductivity and mechanical strength [91] is

another alternative. In the following section, examples for each type of these additive phases is given to illustrate these modifications.

1.2.2 Synergistic effect of silica aerogels and carbon nanostructures combination

Some works were already developed with systems composed by CNTs or GO and silica aerogels, in which some silica precursors were employed for the synthesis of these composites, such as TEOS and water-glass, as well as distinct drying methodologies, from supercritical to APD [89].

Duque and co-authors [92] were able to access new photophysical properties by incorporating single-walled carbon nanotubes (SWCNTs) into silica sols, developing a photo-luminescent SWCNTs-aerogel matrix free of surfactants and solvent. The composites showed blue-shifted spectral features and a significant increase, at cryogenic temperatures, in photo-luminescence intensities. Optical properties were also studied by Chernov *et al.* [93] in silica aerogels embedded with multi-walled carbon nanotubes (MWCNTs), giving the possibility of controlling the composite optical transmission by modifying the amount of MWCNTs, which allows their application as optical elements for various photonic devices.

The adsorption capacities of CNTs-silica aerogel composites were also tested by different authors [63, 94, 95]. A composite system developed by Bargozin *et al.* [94], using water-glass as silica precursor and MWCNTs, showed higher adsorption capacities for kerosene and petroleum, when compared with those of activated carbon. However, the composites showed worse results in comparison with the silica aerogel. Huang *et al.* [63] verified a synergistic effect between the MWCNTs and silica aerogel in oil adsorption. Sun and co-authors [95] obtained a recyclable CNTs-silica aerogel with high absorptive ability for organic solvents or oils and that could be recycled more than 30 times.

Thermal properties were also assessed in CNTs-silica aerogel composites. For example, Mahesh and Joshi [96] tested the effect of silica aerogel granule size and mass ratio of COOH-functionalized MWCNTs on the thermal conductivity of the composites. It was observed that, generally, the increase in granule size results in an increment in thermal conductivity. The authors were able to obtain a material with 16 mW.m^{-1}.K^{-1}, for 0.042 wt% of carbon nanotubes incorporated into a gelatin–silica aerogel. Thus, it is possible to consider that if the carbon nanostructures do not form an interconnected network within the silica skeleton, they can act as opacifiers, decreasing the thermal conductivity of the final materials.

The addition of carbon nanotubes also allows the improvement of mechanical properties

of silica aerogels, as reported by Sun *et al*. [95] and Piñero *et al*. [97]. Both studies used TEOS as silica precursors and COOH-functionalized MWCNTs. In the work of Sun and co-authors [95], the aerogel composite was able to bear a load of 12.6 MPa, 90 times greater than the results obtained for the silica aerogel prepared in the same synthesis conditions. The hybrid aerogels prepared by Piñero *et al*. [97], with the optimum amount of CNTs between 0.5 and 1.0 wt%, were able to withstand compressive strengths up to 0.9 MPa and strain levels up to 75%, while the silica aerogel collapsed under a stress of 0.2 MPa and endured less than 50% strain.

Lei *et al*. [98] were also able to improve both thermal and mechanical properties by adding graphene oxide into the silica matrix. When 5 wt% of GO were added to the composite, a thermal conductivity of 7.5 $mW.m^{-1}.K^{-1}$ and a compressive strength of 0.394 MPa were obtained, leading to a reduction of around 16% and an increase of 65% of these properties, respectively, if compared with the silica aerogel. The authors ascribed this improvement in the mechanical behavior to the anchoring effect of GO nano-sheets in the silica network.

Graphene-silica aerogel composites can also be applied as adsorbents, as described by Loche *et al*. [99] and Kabiri *et al*. [100]. Loche and co-authors [99] used the composite materials as sorbents to remove oil pollutants from water. Even though a reduction in the surface area and pore volume was verified with the addition of graphene, improvements in the adsorption capacities were obtained. Even a small addition of graphene (0.1 wt%) in the material generates a relative increase of the absorption property of 20%, if compared to the unmodified silica aerogel. The target pollutant of Kabiri and co-authors [100] was mercury ions. Graphene–diatomaceous earth (GN–DE) aerogel displayed higher surface area ($368 \ m^2.g^{-1}$) and porosity than graphene aerogel. Besides, the composite material exhibited distinguished removal performance, achieving an adsorption capacity of Hg ions higher than $500 \ mg.g^{-1}$ (at $400 \ mg.L^{-1} \ Hg^{2+}$).

1.3   Objectives

Inspired by the promising properties observed in the referred systems, the main objectives of this research were to develop composite materials of silica and carbon nanostructures, namely carbon nanotubes and graphene oxide, and study the influence of these nanomaterials on the composites final properties, thus assessing the possibility of using these materials in areas requiring greater performances. The main silica precursor will be methyltrimethoxysilane (MTMS) due to the high porosity and flexibility of the obtained aerogels [80]. The chosen co-precursor is (3-aminopropyl)trimethoxysilane

(APTMS), for incorporation of amine groups in the silica matrix, allowing their interaction with the modified carbon nanostructures and for reduction of the gelation time of the system in order to avoid settling of the carbon nanostructures.

To assess the effect of the carbon materials addition in the silica matrix, this project aims to extensively characterize the obtained materials in terms of their morphology and structure, chemical composition, thermal and electrical conductivities, mechanical resistance, among others. Thermo-mechanical assessment will be applied to evaluate the potential use of the obtained aerogels as thermal insulators. The estimation of specific surface area, as well as the determination of porosities, pore volumes and hydrophobic character, will provide the key characteristics to evaluate the use of the composite aerogel as adsorbent.

1.4   Thesis outline

This thesis is organized as follows. In Chapter 2, a literature review is presented on the following topics: silica aerogels, their processing and functionalization; the synthesis and properties of carbon nanostructures, focusing in carbon nanotubes, carbon nanofibers, graphene and carbon aerogels; carbon nanostructures-silica aerogels composites and their applications. In Chapter 3, the experimental methodologies and characterizations performed in the carbon nanotubes-silica aerogels composites are reported. In Chapter 4, a comparison between the effects of adding carbon nanotubes and graphene oxide into MTMS-based silica aerogels is performed, with their influence in the properties being assessed by different characterization techniques. A possible environmental application of these composites materials is shown in Chapter 5, with carbon nanostructures-silica aerogels composites being used as adsorbents for relevant pollutants, benzene and its derivatives and drugs, in water. The conclusions and future perspectives of the work developed throughout the thesis are presented in Chapter 6.

1.5   List of publications of the author

2021

Lamy-Mendes, Alyne; Pontinha, Ana D. R.; Alves, Patrícia; Santos, Paulo; Durães, Luísa. *Progress in silica aerogel-containing materials for buildings' thermal insulation*. Construction and Building Materials, v.286, 122815, 2021.

2019

Lamy-Mendes, Alyne; Torres, Rafael B.; Vareda, João P.; Lopes, David; Ferreira, Marco; Valente, Vanessa; Girão, Ana V.; Valente, Artur J. M.; Durães, Luísa. *Amine modification of silica aerogels/xerogels for removal of relevant environmental pollutants*. Molecules, v.24, p.3701, 2019. (*Open Access*)

Lamy-Mendes, Alyne; Girão, Ana V.; Silva, Rui F.; Durães, Luísa. *Polysilsesquioxane-based silica aerogel monoliths with embedded CNTs*. Microporous and Mesoporous Materials, v.288, 109575, 2019.

Torres, Rafael B.; Vareda, João P.; **Lamy-Mendes, Alyne**; Durães, Luísa. *Effect of different silylation agents on the properties of ambient pressure dried and supercritically dried vinyl-modified silica aerogels*. Journal of Supercritical Fluids, v.147, p.81, 2019.

Ochoa, Marta; **Lamy-Mendes, Alyne**; Maia, Ana; Portugal, António; Durães, Luísa. *Influence of Structure-Directing Additives on the Properties of Poly(methylsilsesquioxane) Aerogel-Like Materials*. Gels, v.5, p.6, 2019. (*Open Access*)

2018

Lamy-Mendes, Alyne; Silva, Rui F.; Durães, Luísa. *Advances on carbon nanostructures-silica aerogel composites: a review*. Journal of Materials Chemistry A, v.6, p.1340 - 1369, 2018.

Vareda, João P.; **Lamy-Mendes, Alyne**; Durães, Luísa. *A reconsideration on the definition of the term aerogel based on current drying trends*. Microporous and Mesoporous Materials, v.258, p.211 - 216, 2018.

2017

Durães, Luísa; Maleki, Hajar; Vareda, João P.; **Lamy-Mendes, Alyne**; Portugal, António. *Exploring the Versatile Surface Chemistry of Silica Aerogels for Multipurpose Application*. MRS Advances, v.2, p.3511 - 3519, 2017.

Chapter 2

State of the art

This chapter comprises the work *Advances in carbon nanostructure–silica aerogel composites: a review* published in the Journal of Materials Chemistry A (2018), 6:1340-1369, by Alyne Lamy-Mendes, Rui F. Silva and Luísa Durães.

2.1 Introduction

The term aerogel was introduced by Kistler in 1931 [3] to define gels in which the liquid is replaced by a gas without the collapse of the polymer network. The first precursor used to obtain an aerogel was sodium silicate, resulting in the so-called water glass. Nowadays, among the high number of different obtainable aerogel types, silica aerogels represent the most widespread and studied class.

The synthesis of aerogels involves usually the following stages: (i) the formation of a gel by sol–gel chemistry, called the gelation stage; (ii) aging, for the reinforcement of the gel; and (iii) drying under supercritical conditions [14]. The silica aerogels obtained by this methodology exhibit exceptional properties such as high porosity and specific surface area, low bulk density and very low thermal conductivity [8].

The high surface area and the possibility of modifying the final characteristics of the material from the synthesis allow the use of aerogels in several areas, such as air cleaning and water purification [101], thermal insulation and electronic devices. The low thermal conductivity and very low density enable the silica aerogels to be applied as aerospace thermal insulators. For instance, these materials were already used for insulation of the batteries in the Mars Sojourner Rover [85] and are being considered to insulate extra-vehicular activity suits in future missions to Mars [102]. The silica aerogels can also be used as collectors of aerosol particles, to protect space mirrors or to design tank baffles [15].

A significant feature of these materials is the easy functionalization of their structure with different compounds. This versatility permits obtaining materials with different characteristics from those of pure silica aerogels. Thus, new materials may be developed with properties not yet found in the existing materials. There are studies in the literature that report the doping of silica aerogels, for example, with metal oxide-based compounds in the synthesis process to improve some characteristics or develop new properties. As examples, the insertion of TiO_2 as an opacifier helps to significantly reduce the thermal conductivity of SiO_2 aerogels at high temperatures [103], while the doping of the silica aerogel with iron salt ($Fe(NO_3)_3.9H_2O$) leads to the formation of iron oxide inside the material structure, which gives magnetic properties to the aerogel composite [104, 105].

Another interesting modification is the insertion of carbon-based nanomaterials into the silica matrix, for instance carbon nanotubes and graphene [106, 107]. These carbon nanostructures have well-known characteristics, such as high electrical conductivity and, especially, high mechanical strength [108, 109]. These properties, combined with the characteristics of the silica aerogels may lead to the development of extremely lightweight, porous materials with high mechanical strength and robustness. The possibility of adding these or other carbon nanostructures into the silica matrix also allows the tailoring of other interesting characteristics of the resulting composites. The high electrical conductivity and chemical stability of the carbon materials with the high surface area and porosity of the silica aerogels enable the application of these aerogel composites, for example, in electronic devices or as adsorbents [110, 111].

This review is devoted to the last kind of silica aerogel based composites. It is composed of three main parts: firstly, a brief description of the main stages of silica aerogel preparation and modification is given; secondly, a description of how carbon nanotubes, carbon nanofibers, graphene and carbon aerogels can be synthesized, and their main properties are presented; and finally, the insertion of these carbon nanostructures into silica aerogels and the applications of the resulting composites are surveyed. Thus, the goal of this work is to show the recent advances regarding the incorporation of carbon nanotubes, carbon nanofibers, graphene and carbon aerogels into silica aerogels, and the future applications of these newly developed materials.

2.2 Silica aerogel processing - the main stages

2.2.1 Synthesis

The formation of aerogels using the sol–gel technique involves three main stages: synthesis, aging and drying of the gel. The first stage consists of the synthesis of wet gels

from precursors by sol–gel chemistry: the nanostructured solid network of silica is formed as a result of hydrolysis and condensation reactions of the silica precursors, in which siloxane bridges (Si–O–Si) are formed.

Silicon alkoxides are currently the most used precursors for the preparation of silica aerogels [112–114]. The hydrolysis step involves the conversion of the alkoxide to a silanol. Once there are hydrolyzed species, the condensation reactions start to occur [115]. In this phase, two reactions can occur: (i) two silanols undergo condensation forming the siloxane linkage and one equivalent of water, (ii) a silanol and an alkoxide condense resulting in a siloxane bond and one equivalent of alcohol. During these events, primary particles are formed in the solution, with a binding capacity to form secondary particles (Figure 2.1), giving a dispersion of nanoparticles in solution called a "sol". The secondary particles can then form connections with each other (neck regions), creating a continuous and interconnected solid network that occupies the entire volume of the solution and is known as the "gel" [14, 15].
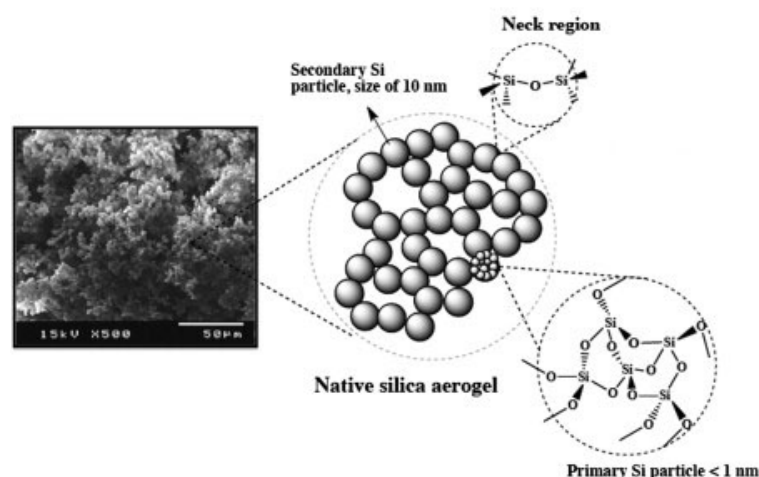
Figure 2.1: Typical Scanning Electron Microscopy (SEM) image of silica aerogels with a schematic representation of primary and secondary silica particles. Reprinted from [15], Copyright (2014), with permission from Elsevier.

When the gel point is reached, it is assumed that the reactions of hydrolysis and condensation of the silicon alkoxide are complete [14, 15]. This change from a liquid to a solid phase is called the sol–gel transition. A representation of the sol–gel chemistry of alkoxysilanes is shown in Scheme 2.1.

The hydrolysis and condensation reactions are normally controlled by the solution pH, which has a major influence on the microstructure of the obtained gels. Therefore, the sol–gel polymerization is usually catalyzed by an acid and/or a base. Hydrochloric acid is the most used acid catalyst, whereas ammonium, sodium and potassium hydroxides are generally applied as basic catalysts. The hydrolysis is faster than the condensation in the

Hydrolysis

$$\begin{array}{c} RO \\ RO \end{array} Si-OR \ + \ H_2O \ \rightleftharpoons \ \begin{array}{c} RO \\ RO \end{array} Si-OH \ + \ ROH \qquad \text{(Equation 1)}$$

Water Condensation

$$\begin{array}{c} RO \\ RO \end{array} Si-OH \ + \ \begin{array}{c} RO \\ RO \end{array} Si-OH \ \rightleftharpoons \ \begin{array}{c} RO \\ RO \end{array} Si-O-Si \begin{array}{c} OR \\ OR \end{array} + \ H_2O \qquad \text{(Equation 2)}$$

Alcohol Condensation

$$\begin{array}{c} RO \\ RO \end{array} Si-OH \ + \ \begin{array}{c} RO \\ RO \end{array} Si-OR \ \rightleftharpoons \ \begin{array}{c} RO \\ RO \end{array} Si-O-Si \begin{array}{c} OR \\ OR \end{array} + \ ROH \qquad \text{(Equation 3)}$$
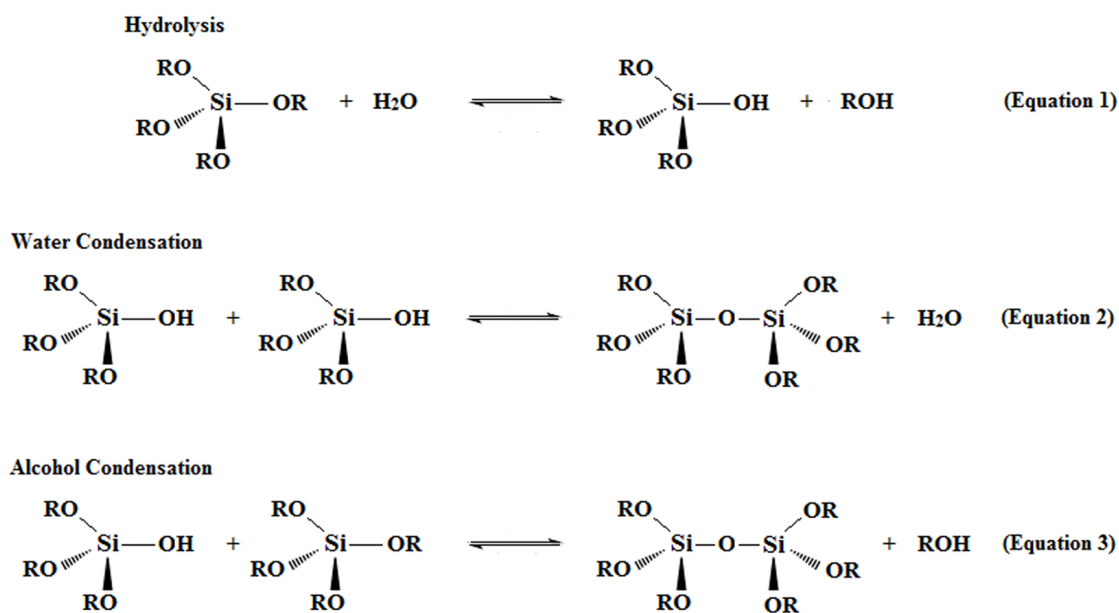
Scheme 2.1: Overview of the sol-gel chemistry with tetraalkoxysilanes. The initial step is the hydrolysis (1) of the alkoxysilane, which is followed by water condensation (2) and alcohol condensation (3) of the newly formed silanols.

acid-catalyzed system, leading to the formation of a less branched network structure, while, for the base-catalyzed system, the condensation step is favored, resulting in a highly condensed network (extent of 80–90%) and fewer residual alkoxide and silanol groups than under acid conditions (extent of 65–75%) [116, 117]. The degree of condensation will contribute to the material polarity and its surface properties. With a higher level of condensation, the base-catalyzed gels are more hydrophobic (with fewer Si–OH groups) than those prepared under acid conditions [117, 118].

Besides the acid and base catalysts, other factors can influence the rates of hydrolysis and condensation and, thus, the silica gel structure. The presence of organic solvents can lead to an improvement in the homogeneity of the mixture (since many silicon alkoxides are not miscible with water) or to a direct interaction between the solvent molecules and the silicon center. The increase of the molar ratio between the solvent and the precursors leads to the increase of the gelation time, for example, Rao *et al*. [80] verified that changing the methanol:methyltrimethoxysilane (MTMS) molar ratio from 14 to 35 induced the increase of the gelation time from 2 to 16 h. In fact, the increase in this molar ratio increases the separation between the monomers and between the reacting silica oligomers in the sol.

The water amount is another important factor, and the water:alkoxide ratio must be high enough to guarantee the hydrolysis reaction completeness [119]. Rao *et al*. [120] synthesized hydrophobic silica aerogels by a two-step acid–base catalyzed sol–gel process. The authors showed that by changing the molar ratio between acid and/or basic water and the silica precursor, it was possible to modify the gel density. For example, for molar ratios

of acid and basic water:precursor higher than 3.75 and 2.25, respectively, the gel density was higher, since the water separates the silanol molecules and partially inhibits the cross-linking of the silane chain (effect of dilution). Consequently, due to the network fragility, the gel shrinks during the drying step forming a dense aerogel. For values lower than those indicated above, the hydrolysis step is limited, leading to unhydrolyzed groups at the silica network surface.

The majority of materials obtained by the sol–gel methodology derives from monomers with three or four alkoxide substituents (OR) bonded to the silicon atom, which may present different polymerization rates. Each pendant organic group (R') will contribute to a network with lower cross-linking density and rate, for example, the processing of $Si(OR)_4$ results in four network-forming Si–O–Si bonds per silicon, but only three will result when $R'Si(OR)_3$ is used [37] (Scheme 2.2). Several organic groups R' can be employed, the group should only be hydrolytically stable. The substituents may produce electronic effects and induce steric hindrance that influence the hydrolysis and condensation reactions of alkoxysilane groups [118].
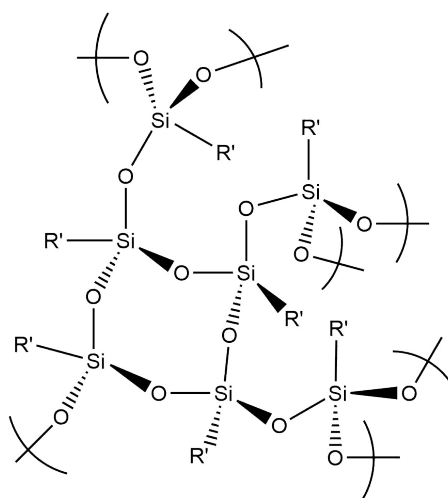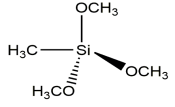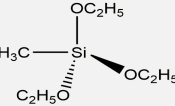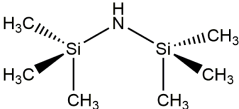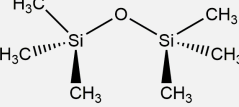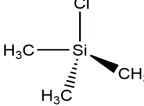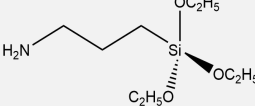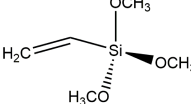
Scheme 2.2: Representation of a silica skeleton obtained from precursors that present a non-reactive side chain, R'.

The sol–gel process provides the possibility of surface modifications, enlarging the applications of the aerogels. The objective of an organic modification is to achieve new properties arising from the organic groups without losing the original properties of the aerogels such as high porosity and very low density [121]. Modifying the functional groups or the ratio between the precursors can result in interesting hybrid materials. The addition of organosilane reagents, like MTMS, methyltriethoxysilane (MTES), hexamethyldisilazane (HMDZ), hexamethyldisiloxane (HMDSO), trimethylchlorosilane (TMCS), aminopropyltriethoxysilane (APTES) or vinyltrimethoxysilane (VTMS),

represented in Table 2.1, is the most dominant route for modifying the surface groups of the sol–gel-derived materials [122].

Table 2.1: Some of the co-precursors and/or modifying agents used in the synthesis of organically modified silica aerogels.

Co-precursors and/or modifying agents	Chemical formula	Abbreviation	Chemical structure
Methyltrimethoxysilane	$Si(OCH_3)_3CH_3$	MTMS	
Methyltriethoxysilane	$Si(OC_2H_5)_3CH_3$	MTES	
Hexamethyldisilazane	$HN(Si(CH_3)_3)_2$	HMDZ	
Hexamethyldisiloxane	$O(Si(CH_3)_3)_2$	HMDSO	
Trimethylchlorosilane	$Si(CH_3)_3Cl$	TMCS	
Aminopropyltriethoxysilane	$H_2N(CH_2)_3Si(OC_2H_5)_3$	APTES	
Vinyltrimethoxysilane	$H_2C{=}CHSi(OCH_3)_3$	VTMS	

In general, there are two different methodologies for the surface modification of silica aerogels: the co-precursor method and surface derivatization. In the first methodology, the surface-modifying agent is added to the silica sol before the gelation. In the second one, the gel is obtained first and, then, the inorganic or organic network is placed into a mixture containing a solvent and the surface modifying agent [14].

Li and co-workers [38] carried out a study for the comparison of modification strategies, namely the co-precursor and surface derivatization methods and also a two-step method (a combination of the other two methodologies). Tetraethylorthosilicate (TEOS), MTMS, and TMCS were used as the precursor, co-precursor and modifying agent, respectively. For the derivatization and two-step methods, a solvent exchange with *n*-hexane was performed after gelation, followed by surface modification with a 10% TMCS/*n*-hexane solution. The authors described how the modification occurred in each one of the methods, as schematized in Figure 2.2. The material obtained by the co-precursor method presented the smallest specific surface area (635.41 m^2.g^{-1}), pore

volume (0.89 cm^3.g^{-1}) and average pore size (3.93 nm), while the aerogel from the derivatization method had the most uniform pore size distribution with an average diameter of 12 nm. The samples from the two-step method had the highest specific surface area (865.09 m^2.g^{-1}) and the lowest intensity of $\equiv$Si–OH groups, which justifies the higher value obtained for the contact angle (162°).
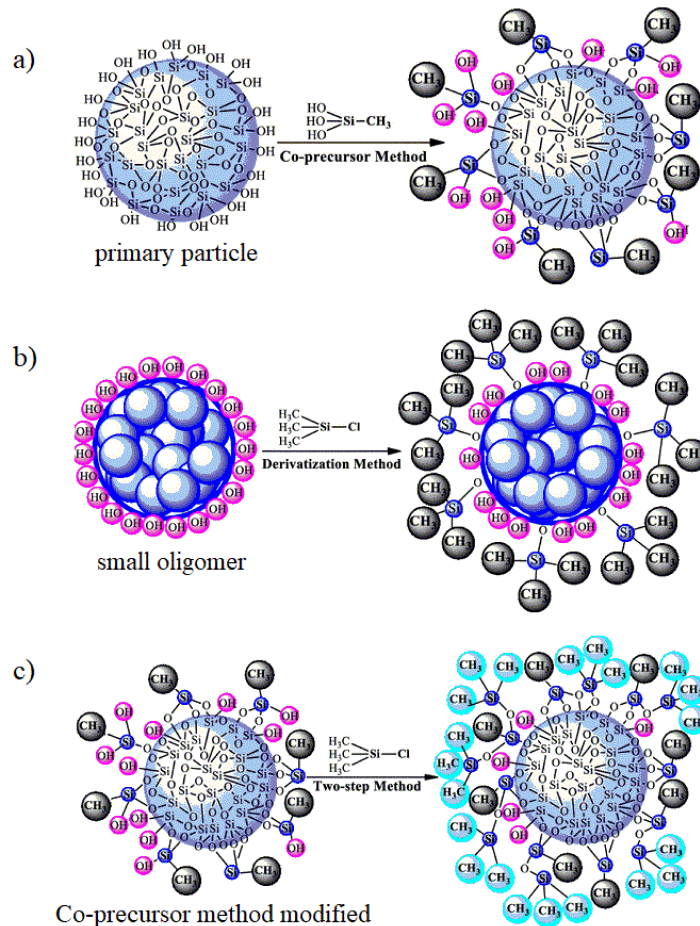
Figure 2.2: Representation of chemical reactions of the three different modification methods: (a) co-precursor; (b) surface derivatization and (c) two-step methods. Reprinted with permission from Springer Nature, reference [38], Copyright (2015).

All subsequent processing stages (described in the following sections) depend on the initial structure of the gel, and the characteristics of the materials obtained by the sol–gel process can be controlled and/or modulated by modifying the parameters and the precursors of the synthesis.

2.2.2 Aging

The second step for obtaining an aerogel is aging, which will strengthen the solid skeleton of the silica gel. In this stage, the polycondensation reactions continue to occur within the gel network, as long as the silanols are close enough to react. This process contributes to the thickening of the connecting points (neck regions, Figure 2.1) between

the secondary particles. A spontaneous shrinkage due to the network strengthening will also happen, named syneresis, and results in the expulsion of some liquid from the pores [115].

During the aging, two main mechanisms occur simultaneously. The first consists of the neck growth from re-precipitation of dissolved silica from the surface of the secondary particles onto the inter-particle bridges, thickening these connection points; the second occurs with the dissolution of the smaller particles and precipitation onto larger ones, the so-called Ostwald ripening [123]. Both mechanisms make the gel structure more rigid and cohesive with increasing aging time [15, 115].

2.2.3 Drying

The final stage consists of drying the wet gel, wherein the solvent is removed leaving only the solid silica network. There are three methods of drying that are commonly used: (1) evaporative drying; (2) freeze drying; and (3) supercritical drying [115]. The materials obtained by each drying method are normally termed xerogels, cryogels and aerogels, respectively, the latter having a more extensive pore network.

Drying of the gels under subcritical conditions is based on the evaporation of the solvent. Contrarily to the other drying methods, there is the formation of a liquid–vapor interface. Therefore, when the solvent within the gel pores evaporates, these are subjected to high surface tension effects which might cause partial collapse of the structure. In order to reduce the capillary forces responsible for the partial destruction of the porous matrix, before evaporating polar solvents, a solvent exchange may be accomplished [124]. In addition, the referred shrinkage can be avoided if a surface modification is performed in the silica skeleton. When hydrophobic groups are present on the aerogel surface, the repulsion between these groups and their low interaction with the organic polar solvents lead to a significant reduction of the capillary forces and shrinkage, originating the so called "spring-back effect" [125]. In this case, aerogel-like materials are obtained. If the different variables of the subcritical evaporation (evaporation temperature, gas entrainment during evaporation, use of vacuum, solvent type, etc.) are selected properly, it is also possible to control the texture of the pores [126, 127]. Moreover, the partial shrinkage of the structure may not be relevant if the desired texture is composed of only micropores (diameter below 2 nm) and mesopores (diameter between 2 nm and 50 nm) [128].

The method of lyophilization, which results in cryogels, is based on freezing and subsequent solvent removal by sublimation. This method is effective in the drying of hydrogels with controlled pore structure. In fact, the main advantage of this type of

drying is the possibility to obtain a large amount of mesopores [129]. This method can lead to dramatic changes in the density of cryogels after freezing, mainly due to large voids resulting from the formation of crystals within the structure of the gels [130]. To prevent the formation of these crystals, which can deform the nanostructured network, the solvent can be replaced before drying [131]; *t*-butanol is the most common solvent used for exchange with water [132], since it suffers a smaller change in density than water and reduces the drying time due to the higher vapor pressure. However, the difficulty in preparing monoliths and the necessity to change the solvent to avoid the formation of megapores (pores with diameters greater than 10 μm) [133] are some of the disadvantages of this method.

The most widely used drying method is supercritical fluid drying (SCD). In one of the routes, the removal of the solvent is accomplished at elevated temperatures and pressures (above the critical point of the solvent), and this is the best way to preserve the porous network and structural properties created during the gel synthesis. In order to avoid the high temperature of this protocol, in another route the organic solvent may be replaced with CO_2 before its elimination under supercritical conditions. The critical temperature of CO_2 (31 ^{o}C) is lower than those of organic solvents, due to its low surface tension. Thus, the supercritical region has mild temperature conditions in this case. The main problem refers to the fact that when the solvent used in the synthesis is water, it must be replaced by an organic solvent, since water is poorly soluble in supercritical CO_2. Solvent washing is also advisable in the case of using alkoxides as precursors, since there is also some water in the system resulting from the water condensation reactions and the addition of acid or basic water for the catalysis. This will increase the number of processing steps. Other disadvantages of this method are performing the process under high pressure and with CO_2 feed, which increases the costs and equipment maintenance when compared to other drying methods [134, 135].

The choice of the drying method will determine the structural properties of the final material. All three methods have advantages and disadvantages, and the selection of the method to be used will depend on the chemical system and the final application of the dried material.

2.2.4 Common additive phases in silica aerogels

In terms of properties, silica aerogels have very attractive characteristics such as porosity higher than 90%, specific surface area between 250 and 800 $m^2.g^{-1}$, bulk density ranging from 0.003 to 0.3 $g.cm^{-3}$, and low thermal conductivity ($\sim 15 - 40$ $mW.m^{-1}.K^{-1}$) [8]. In contrast, they have limitations in their mechanical strength, and are complicated

to process without causing fractures in the material [88]. Woignier and Phalippou [136] assessed the mechanical properties of silica aerogels from tetramethylorthosilicate (TMOS), and found that these aerogels, with porosity greater than 95% and density of 0.1 g.cm^{-3}, have a maximum flexural strength of around 0.02 MPa and a compression strength of ~0.015 MPa. Their intrinsic brittleness imposes severe restrictions on the ability to support loads [15]. Therefore, improving the mechanical properties of silica aerogels has been a challenge in order to develop a material that can fully maintain its attractive properties for new applications.

Silica aerogels allow the incorporation of other types of compounds into the network, which can contribute to different/improved characteristics of the formed composite materials when compared to those presented by the native silica aerogels. Several strategies have been investigated for the modification of silica aerogels by this route, and the addition of particles, polymers or fibers is one of the methodologies for improving different properties of the aerogels, such as mechanical, thermal, electrical, magnetic or optical properties, which enables their wider application. In the following, one example for each type of these additive phases is given to illustrate these modifications.

The incorporation of nanoparticles into silica aerogels can provide some desired functional properties. Lee *et al*. [90] developed a study in which magnetite (Fe$_3$O$_4$) nanoparticles were embedded in a spherical silica aerogel to provide magnetic properties to the composite. The silica matrix had almost no impact on the magnetic properties, and the Fe$_3$O$_4$:SiO$_2$ nanocomposite retained the superparamagnetic behavior of the Fe$_3$O$_4$ nanoparticles. The saturation magnetization values decreased with the decrease of Fe$_3$O$_4$ wt% in the nanocomposite, varying from 34.5 emu.g^{-1} for 90 wt% to 8.3 emu.g^{-1} for 50 wt%.

A common method for aerogel mechanical reinforcement is the incorporation of polymers into the silica backbone. As an example, in a study developed by Maleki *et al*. [53], the effect of the incorporation of 1,6-bis(trimethoxysilyl)hexane (BTMSH) or 1,4-bis(triethoxysilyl)-benzene (BTESB) into the TMOS-derived underlying structure of tri-methacrylate cross-linked silica aerogels was studied. Figure 2.3 presents the proposed molecular structures of the surface modified silica aerogels. The polymer reinforced silica aerogels exhibited density values ranging from 0.13 to 0.39 g.cm^{-3}, compression strengths from 0.011 to 0.4 MPa and thermal conductivities of 39 to 93 mW.m^{-1}.K^{-1}. Thus, the combination of organically bridged bis-silanes with a covalently linked polymer phase provided lower densities when compared to other polymer reinforced aerogels, and higher mechanical strength than the non-crosslinked aerogels.
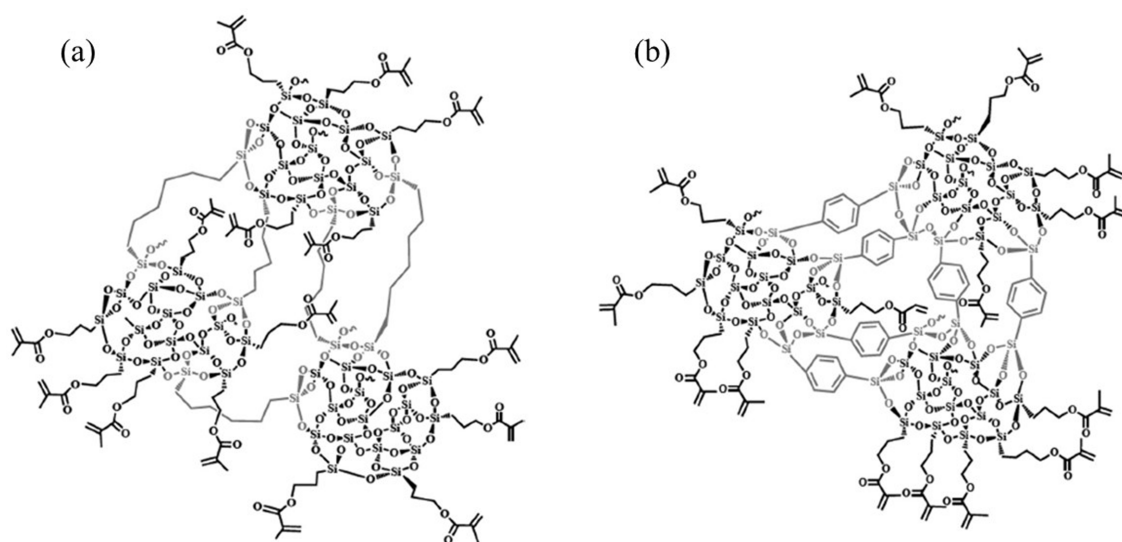
Figure 2.3: Proposed molecular structure of a (a) methacrylate-modified aerogel with a part of the total silicon derived from BTMSH and (b) methacrylate-modified aerogel with a part of the total silicon derived from BTESB. Adapted from reference [53], Copyright (2014), with permission from Elsevier.

a. run 5, d = 0.071 g/cm³

b. run 1; d = 0.088 g/cm³

c. run 12, d = 0.394 g/cm³

d. run 13, d = 0.321 g/cm³
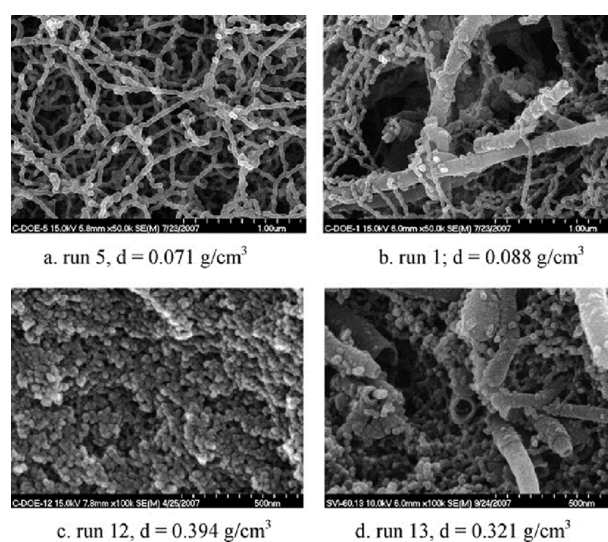
Figure 2.4: Scanning electron micrographs of silica aerogel monoliths without carbon fibers (left) and with fibers (right). Micrographs (a) and (b) are both lower density monoliths, while (c) and (d) are both higher density aerogels. Reproduced from reference [137] with permission of The Royal Society of Chemistry, Copyright (2008).

The incorporation of fibers into silica aerogels can also modify some properties of these materials. For example, Meador *et al.* [137] achieved good strength results by including carbon nanofibers in the silica backbone of di-isocyanate cross-linked silica aerogels. Figure 2.4 shows the SEM images of the synthesized materials. In Figures 2.4a and b low density materials without and with 5% of fibers, respectively, are presented, and it is possible to observe the similarity between the sample microstructures. For comparison, samples with higher densities are shown in Figures 2.4c and d. The effect of di-isocyanate and fiber content on the material density is almost negligible, with the total silane concentration being the most influential variable. When 5% of carbon nanofibers were added to the lowest

density aerogels, the compressive modulus increased by 3-fold, from 0.2 MPa to 0.6 MPa, and the tensile strength from 0.07 MPa to 0.36 MPa, without modifying the density or porosity. The presence of carbon fibers also improved the strength of the gels before cross-linking.

2.3 Carbon nanostructures – properties and preparation

Carbon nanomaterials are intensively studied due to their unique and outstanding properties. Some of these nanomaterials, from one-dimensional (carbon nanotubes and carbon nanofibers) and two-dimensional (graphene) materials to three dimensional structures (carbon aerogels), were already used to synthesize composites in association with silica aerogels. In the next sections, the properties of these carbon materials as well as the most common methodologies for their synthesis will be presented.

2.3.1 Carbon nanotubes

Carbon nanotubes can be multi-walled (MWCNTs), with a central tube of nanometric diameter surrounded by other graphene layers, or single-walled nanotubes (SWCNTs), constituted by only one layer. Both CNT types were discovered by Iijima in 1991 and 1993, respectively [138, 139]. They are considered one-dimensional (1D) nanomaterials, independently of the number of walls.

The cylindrical geometry, the singularities of curvature and the quantum confinement of CNTs have a significant impact on their properties. Depending on their diameter and helicity, CNTs can be metallic or semiconducting [140]. The electron transport in CNTs occurs through quantum effects; hence, this carbon nanomaterial can conduct electric current without scattering and dissipation of heat. The unique band structure of CNTs imparts them with high current transport capacity and high thermal conductivity. On the other hand, the covalent bonding between individual carbon atoms puts the CNTs among the strongest and stiffest materials. They have excellent mechanical properties, like high compressibility and high strength in the axial direction, which can be attributed to their high Young's modulus and tensile strength [141].

CNTs present unique properties, different from those found in three-dimensional (3D) graphite, two-dimensional (2D) graphene and other 1D fibrillar carbon allotropes. Table 2.2 shows some of the main physical properties of both single and multi-walled carbon nanotubes and their comparison with 1D carbon nanofibers (CNFs), 2D graphene and 3D graphite (highly oriented pyrolytic graphite – HOPG).

Table 2.2: Physical properties of carbon sp^2 allotropes.

Properties	SWCNTs	MWCNTs	CNFs[a]	Graphene	Graphite (HOPG)
Young's modulus (TPa)	0.9-1.7 [142]	1.0-1.28 [143]	0.04-0.06 [144]	1.04 [145]	0.028-0.031 [146]
Tensile strength (GPa)	25-135 [143]	11-63 [143]	0.3-0.6 [144]	130 [143]	0.11 [146]
Thermal conductivity (W.m^{-1}.K^{-1})	3500-5800 [147]	>3000 [147]	0.07 [148] to 1600 [149] (graphitic CNFs)	~4840-5300 [147]	1-3 [146] (c direction), 190-390 [146] (ab direction)
Theoretical specific surface area (m^2.g^{-1})	~1315 [150]	680-850 [151] (2 walls CNTs), 295-430 [151] (5 walls CNTs)	-	2630 [152]	-
Specific surface area (m^2.g^{-1})	577 [153]	448 [153]	20-2500 [154]	-	-
Electrical conductivity (S.m^{-1})	10^6 [143]	10^6 [143]	10^{-7} to 10^3 [154]	10^6 [143]	2.0 x 10^5 to 2.5 x 10^5 [146]

[a] Electrospun carbon nanofibers

The uncommon properties of CNTs attract great interest for several applications, namely for chemical sensors, electronic devices, adsorbent materials for gases and heavy metals, lithium batteries, hydrogen storage, supports for catalysts and as a mechanical reinforcement phase in composites.

CNTs can be synthesized using several techniques, for example: by arc discharge, in which MWCNTs with high crystallinity are obtained; by plasma arc jet, where the product will be a mixture of CNTs with different percentages of amorphous carbon and fullerene; by laser ablation, which produces CNTs with the highest degree of purity; and by chemical vapor deposition (CVD), by which bulk quantities of CNTs can be obtained. Due to the possibility of synthesizing nanotubes in bulk, associated with its simplicity and low cost, CVD is now the standard method for CNT production [155].

The general CVD mechanism for obtaining nanotubes involves the following steps: (1) adsorption of a precursor gas in the catalyst particles; (2) dissociation of precursor molecules forming C_xH_y species; (3) dissolution and diffusion of carbon species in the catalyst particles; (4) carbon saturation and structure precipitation; and (5) reformatting of the metal particles and successive incorporation of carbon into the CNT growth structure [156] (Figure 2.5). The precipitation of carbon from the saturated metal contributes to the formation of tubular carbon solids with sp^2 structure. Tube formation is favored over other forms of carbon because a tube contains no dangling bonds and therefore is in a low energy form [155].
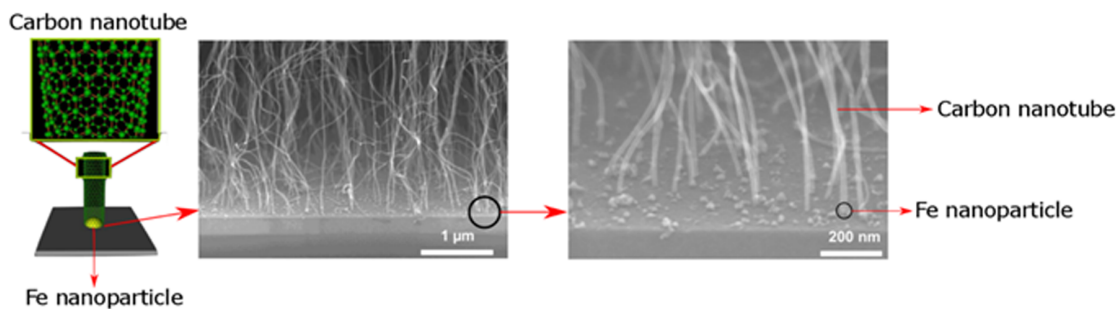
Figure 2.5: Schematic and SEM images of CVD growth of a CNT forest on a silicon wafer coated with Fe catalyst nanoparticles.

The carbon sources most preferred in CVD are hydrocarbons like methane, ethylene, xylene, acetylene, carbon monoxide or their mixtures. The growth temperature is typically in the range of 550–750 ^{o}C and the most commonly used substrates are nickel, quartz, silicon, silicon carbide, silica, alumina, stainless steel or glass. The catalytic system consists of transition metals, such as iron, nickel, copper and cobalt, dispersed on the support [155].

In the CVD process, the chemical reactions of the precursor species can be initiated by different methods, for example by heat, as in hot filament CVD (HFCVD) [157] and thermal CVD (TCVD) [158], or by plasma, in the case of plasma-enhanced CVD (PECVD) [159]. HFCVD uses a metallic filament (usually Ta) heated up to 2000–2500 ^{o}C [160], which causes the thermal dissociation of the carbon precursor. This technique presents higher yields and is less costly than the PECVD. In the TCVD, a simple furnace, running in the temperature range of 600–1200 ^{o}C, is sufficient to fully activate the gas mixture. The catalyst-supported TCVD provides superior versatility/yields and the purest CNTs (∼99.98%) [143]. In PECVD, the initiation of the reaction is accomplished by electrical energy. This method allows the obtainment of high-quality nano-filaments at low temperatures [161], however, it produces low yields and is very expensive due to the plasma power source.

2.3.2 Carbon nanofibers

Carbon nanofibers (CNFs) are 1D carbon nanomaterials, as in the case of carbon nanotubes [162], and can be defined as sp^2-based linear filaments [163]. Even though some methodologies to obtain the CNFs have similar conditions to the ones used in the growth conditions for CNTs, those materials are different from the latter [138, 163, 164]. The main distinction between these two types of nanomaterials is the stacking of the graphene sheets in various ways, leading to more edge sites on the outer wall of the CNFs than the CNTs [164–166]. These fibers have a diameter of *ca*. 100 nm and are

characterized by an aspect ratio greater than 100 and their high flexibility [163, 167]. They also present high surface area to volume ratio, high thermal conductivities and good mechanical properties (Table 2.2), leading to great potential in applications such as energy storage, electrochemical biosensors, catalysts, composite production and selective adsorbents [164, 168–170].

The CNF structure is mostly dependent on the synthesis process, for example the diameter of CNFs can be controlled by the size of the used catalyst particles ranging from 2 to 100 nm, and presenting lengths in the range of 5–100 μm [169]. The two most common methodologies of synthesis to obtain carbon nanofibers are CVD and the carbonization of polymer nanofibers obtained by electrospinning [167, 171].

CVD is one of the most frequent processes used to synthesize CNFs. In this methodology, the decomposition of a hydrocarbon gas takes place on a catalytic particle, which can be of iron, nickel, cobalt or copper, at temperatures ranging from 500 to 1200 ^{o}C, leading to the formation of well-organized tubular filaments of hexagonal sp^2 carbon [163, 167, 168]. Some advantages of this method are that the fibers thickness can be controlled, as already mentioned before, and the orientation of the graphite plane can be oriented by the growth temperature and/or nature of the metallic catalyst [168]. But some disadvantages are also verified in the CVD technique, such as high associated costs, complex chemical and physical processes and the possibility of only producing relatively short fibers [144].

Another route for the production of CNFs is electrospinning [144, 167, 168, 171], which is an effective technique to synthesize polymeric nanofibers [168]. The procedure to obtain the nanofibers is described by Inagaki *et al*. [172], in which a viscoelastic solution of polymers is charged by a DC or AC high voltage due to the potential difference between the syringe and grounded target. When the surface charge repulsion is dominant, critical conditions are achieved and a jet is drawn from the spinneret under a constant flow rate. The jet solidifies, as the solvent evaporates, and forms thin fibers that are deposited on the collector.

The types of polymer nanofibers which have been converted to carbon nanofibers are limited, such as polyacrylonitrile (PAN), cellulose, phenolic resins, polyimide (PI), poly-(vinylalcohol) (PVA), poly(vinylidenefluoride) (PVDF) and pitch, if compared with the more than 100 kinds of polymers that have been used to produce nanofibers by this methodology [167, 168, 172].

As PAN is the most used polymeric precursor due to its higher carbon yield and strength [163], the steps of oxidative stabilization and carbonization are going to be described based on this material. The stabilization of PAN is a necessary procedure to

prevent the melting during the carbonization and to produce good quality carbon nanofibers. This process occurs by heating the PAN fibers around 280 ^{o}C [163] in an atmosphere containing oxygen, which induces the cyclization of nitrile groups and the cross-linking of the chain molecules in the form of –C=N–C=N– [173]. In the carbonization step, the polymeric fibers are submitted to temperatures around 1000 ^{o}C [172] in inert atmospheres, in order to remove non-carbonized components selectively in the form of gases, for example H_2O, NH_3, CO_2 and N_2. After this procedure, the yield of carbon nanofibers is about 50–57% of the mass of the original PAN [173].

2.3.3 Graphene

Graphene is a 2D material comprising layers of carbon atoms arranged in six-membered rings. Its honeycomb network is the elementary building block of other allotropes, such as three-dimensional graphite, nanotubes, and fullerenes. Ideally, graphene is a material with a single-layer, however three different types of graphene were described: single-layer graphene (SG), bilayer graphene (BG), and few-layer graphene (FG, number of layers ~10) [174]. Although scientists knew that one-atom-thick 2D crystal graphene existed and had been theoretically studied for sixty years [175], only in 2004 Geim and Novoselov were able to isolate and characterize the material [176]. Even though graphene is the basic block of carbon allotropes, the extra quantum confinement of the electrons, due to the lack of a third dimension, gives graphene various novel properties, different from those of other carbon nanostructures. Due to the two-dimensional structure, it is the only form of carbon in which every atom is available for chemical reaction from two sides and the defects within a sheet increase its chemical reactivity [177].

Graphene is the strongest material ever tested, and it presents outstanding mechanical properties, Table 2.2. It has a specific strength of 48 MN.m.kg^{-1} (*i.e.* force per unit area at failure divided by density) before breaking; for steel it is equal to 154 kN.m.kg^{-1} [178, 179]. Its electronic mobility is also high, with a reported value of 15 000 cm^2.V^{-1}.s^{-1} and a theoretical potential limit of 200 000 cm^2.V^{-1}.s^{-1}, with these values being limited by the scattering of acoustic photons [180].

The method for obtaining graphene has a great impact on the material final properties, with consequences in its applications. Therefore, depending on the desired features of graphene, a different synthesis method can be more appropriate. The several distinct methodologies to obtain this material can be separated in two categories: physical methods and chemical methods, as shown in Table 2.3 [181].

CVD onto transition-metal substrates is the most promising and accessible method for

the synthesis of graphene with high quality. In this process, the substrate is exposed to gaseous precursors that will decompose on the surface to grow a thin film, while the by-products evaporate. There are different methodologies to achieve this, for example, by heating the sample with a filament or by a plasma. Distinct metal substrates can also be used, such as Ni, Pd, Ru, Ir and Cu [180].

Kim *et al.* [43] were able to grow high-quality stretchable graphene films using CVD on nickel layers. A mixture of H_2, CH_4 and Ar was used, and the process temperature was about 1000 ^{o}C. The methane decomposes on the surface, and the carbon diffuses into the Ni substrate. The system is refrigerated with Ar and a graphene layer grows on the surface of the substrate. The number of the graphene layers can be controlled with the variation of parameters such as the thickness of the catalytic metals and/or the growth time. A fast cooling rate is critical for suppressing the formation of multiple layers and for allowing efficient separation of the graphene layers from the substrate in the later stage.

Varying the used substrate, from nickel to copper, leads to the formation of single-layer graphene with less than 5% of few-layer graphene. The number of layers will not rise even with time increase; this probably happens due to the low solubility of carbon in the copper substrate providing a pathway for growing self-limited graphene films [182].

Table 2.3: Comparison of different methods for graphene synthesis. Adapted from reference [181] with permission of The Royal Society of Chemistry, Copyright (2001).

Categories	Synthesis methods	Precursors	Advantages	Disadvantages
Physical methods	Micromechanical exfoliation	Graphite	Simplicity; high quality; low cost	Time-consuming; low yields
	Epitaxial growth on silicon carbide (SiC)	SiC wafer	Uniform; high quality	High cost; high temperature; high vacuum
	Arc discharge	Graphite	Low cost; easy doping; good crystallinity	Non-uniform; impure
Chemical methods	Chemical vapor deposition (CVD)	Hydrocarbon gases	High quality; uniform; large-scale	High temperature; high cost
	Chemical reduction of graphene oxide	Graphite	High yields; low cost; large-scale	Low quality
	Unzipping CNTs	CNTs	Low cost; large-scale	Time-consuming; complex process
	Electrochemical method	Graphite	Low cost; high quality	Low yields
	Total organic synthesis	Polycyclic aromatic hydrocarbons	High quality precisely defined structures	High cost; limited size range; complex process

2.3.4 Carbon aerogels

Inorganic gels were the dominant theme in the sol–gel literature until the late 1980s when Pekala and his colleagues used organic polymers to obtain organic and carbon aerogels [183]. The aerogel obtained by Pekala was produced using the sol–gel method, by polymerizing resorcinol with formaldehyde under alkaline conditions, followed by supercritical drying. The obtained material, called organic aerogel, consisted of interconnected colloidal particles having a diameter of approximately 10 nm. Properties such as low density, high porosity and sol–gel process versatility make carbon aerogels promising materials for numerous applications such as adsorbents [184], electrodes [185, 186], supports for catalysts [187], and thermal insulation for high temperatures [188].

The most commonly used monomers for obtaining organic gels are resorcinol-formaldehyde (RF) and melamine-formaldehyde (MF), but other compounds can also be used for this purpose, such as phenol-formaldehyde, cresol-formaldehyde, phenol-furfural, and also polyacrylonitriles, polyacrylates, polystyrenes and polyurethanes, among many others [130, 189].

The process for obtaining carbon aerogels can be divided into three stages: synthesis of organic gels, drying and carbonization. Each step has a certain role in the final properties of the material, and the three steps will be described in the next subsections.

Synthesis of organic gels

The synthesis process that will be described in this section will be based on the resorcinol-formaldehyde precursors, since they are the most used/studied in the literature. The reactions of polymerization and cross-linking, also mentioned as gelation and curing processes, happen during the sol–gel reactions between the precursors [190].

The major reactions of resorcinol-formaldehyde include: (1) the addition reaction to form the hydroxymethyl groups ($-CH_2OH$) derived from formaldehyde on resorcinol; (2) the condensation of the resultant molecules to form methylene ($-CH_2$) and ether–methylene ($-CH_2OCH_2$) bridged compounds; and (3) the disproportionation of ether–methylene bridges to form methylene bridges and formaldehyde as a by-product [191–193]. Resorcinol is a trifunctional phenolic compound that allows the addition of molecules, in this case formaldehyde, at 2-, 4- and/or 6-positions, but these molecules are less reactive than their corresponding anions. Thus, in the presence of OH^- anions, the hydrogen of the resorcinol is removed, leading to the formation of hydroxymethyl derivatives [134, 190].

The condensation of the products (hydroxymethyl derivatives) occurs under acidic conditions. Both steps of this mechanism lead to the formation of a highly cross-linked cluster, displayed in Scheme 2.3, ranging from 7 to 10 nm in diameter [190]. At the end of this step, colloidal particles start to aggregate and form an interconnected structure that occupies all the aqueous solution original volume [190], building the gel's three-dimensional open network [194].
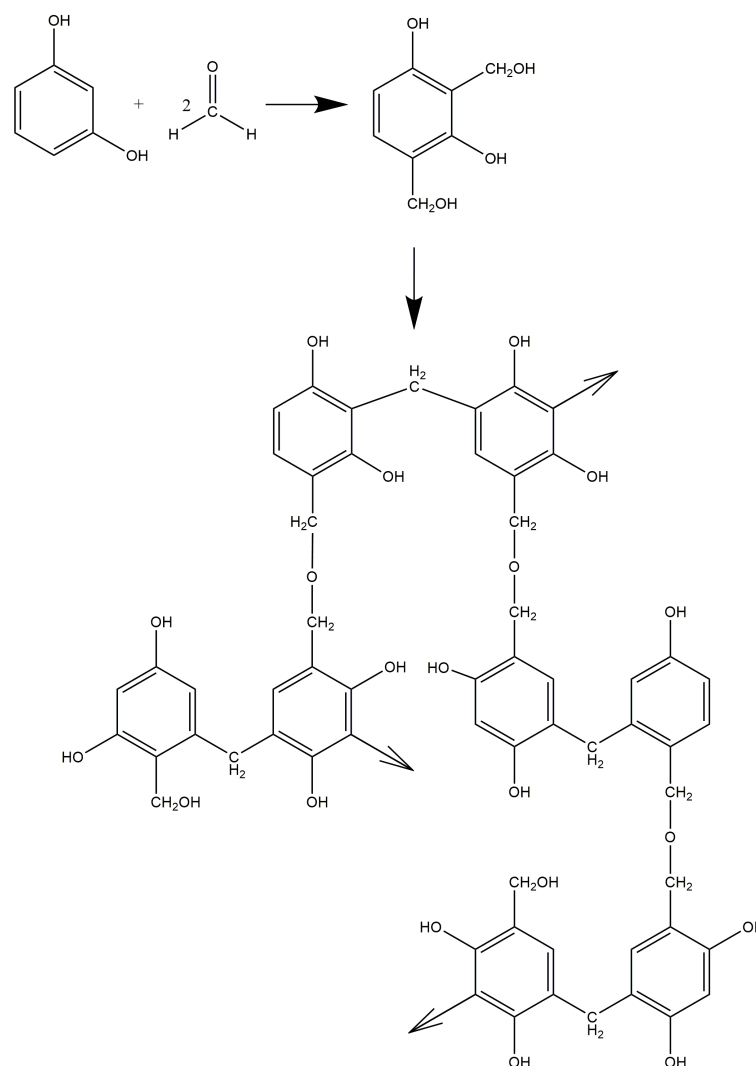
Scheme 2.3: Schematic diagram of the reaction of resorcinol with formaldehyde. Adapted with permission from reference [193]. Copyright (1997) Elsevier.

The final pore texture of carbon gels is determined by the solution initial pH, since this parameter controls the polymerization, and the subsequent cross-linking. As verified by Lin and co-authors [193], RF gels synthesized with initial pH higher than 7.0 showed a weak pore structure, as fewer structure-forming condensation reactions happen. These gels do not resist the drying and pyrolysis steps; the extreme conditions lead to the collapse of the nanostructure, forming materials with residual pore volume and surface area. In contrast, when lower values of pH are used, as the condensation reactions are promoted,

highly cross-linked gels are formed with strong structures, that will remain intact even after high temperature treatment.

To obtain high surface area materials resulting from the organic gels a narrow range of pH values are required, with slightly acidic condition [193]. This is achieved by the controlled addition of diluted nitric acid and weak bases, such as sodium carbonate (Na_2CO_3), as reaction catalysts. However, Job [195] has shown that not all bases are equally effective, at the same pH value, in promoting high surface areas, and that both the concentration and type of basic catalysts (anionic and cationic) modify the final properties of the gel.

The resorcinol/catalyst (R/C) ratio is one of the main factors that determines the structures and final properties of the gels [196, 197]. For catalysts such as sodium carbonate, a R/C molar ratio between 50 and 300 is commonly used [190, 192]. Pekala *et al*. [192] reported that low R/C ratios, *i.e.* high catalyst conditions (R/C = 50), lead to small particles ($\sim$3–5 nm) that are linked together with large necks. On the other hand, high R/C ratios (*i.e.* R/C = 200) result in larger polymer particles (11–14 nm) connected in a "string of pearls". These two types of gels are usually described as polymeric and colloidal, respectively, and the colloidal RF aerogels exhibit little shrinkage during supercritical drying, lower surface area and weak mechanical properties, while the polymeric gels present opposite characteristics.

Another important parameter for the preparation of carbon gels is the reaction medium, and various solvents may be used. Some examples are deionized water [183, 198, 199], acetone [200, 201] or methanol [126]. While water is the cheapest among the solvents, the others may be preferred to obtain specific final properties.

Upon completion of the polymerization step, an organic gel of covalent nature is formed and, as a consequence, the initial solution loses its fluidity, producing a gel. The aging time of the gel is an extension of the process in which the cross-linking of the polymeric aggregates, previously formed in the gelation phase, is favored, so that a three-dimensional cross-linked polymer is obtained.

Drying of organic gels

One critical step of the process to obtain aerogels is the drying step, as already referred to in Part 2 of this review when explaining the synthesis of the silica aerogels. In this step, the solvent used as a reaction medium is removed leaving only the solid polymer network. Three drying techniques are commonly employed: (1) supercritical, the elimination of the solvent occurs under supercritical conditions; (2) lyophilization, in which the solvent is frozen and removed by sublimation and (3) subcritical drying of the

gel by simple evaporation of the solvent [190]. Further details on these three types of drying modes can be found in Section 2.2.3.

Carbonization process

For obtaining carbon aerogels, a thermal treatment of the earlier described organic aerogels is required. This procedure, also known as carbonization, leads to a thermally stable nanostructured material mainly composed of carbon, as other constituents such as labile oxygen, non-cross-linked organic chains and hydrogen surface groups are removed by the high temperatures used in this stage [190, 194]. Usually the carbonization step is performed in a tube furnace under a constant flow of inert gas, for example argon, N_2 or He, at temperatures between 500 ^oC and 2500 ^oC [187, 190, 194].

The pyrolysis temperature causes considerable changes in the properties of RF aerogels. The main objectives of the carbonization step are to obtain thermally stable carbonaceous materials and to develop micro- and mesoporosity in the aerogels and xerogels, which can lead to the increment of the surface area, particularly at low pyrolysis temperatures. If higher temperatures are used, the surface area and pore volume of these carbon materials tend to decrease [190]. Nevertheless, these carbon aerogels do not present electrical conductivity unless carbonized above 750 ^oC, and the maximum of the electrochemical double layer capacitance is verified between 800 and 900 ^oC [185].

The nature of the gas used during carbonization may also influence the structural properties and pore sizes of the aerogels. The use of nitrogen (N_2) during this step results in materials with specific surface areas of approximately 600–700 $m^2.g^{-1}$ [133]. However, Kang *et al*. [202] reported the use of ammonia gas during the carbonization of organic xerogels and obtained materials with specific surface areas greater than 1000 $m^2.g^{-1}$. These variations show the great influence of the carbonization step on the final properties of carbon aerogels. As in the case of the synthesis variables, modifications in the heat treatment conditions allow the obtaining of materials with specific chemical and textural properties, as presented in Table 2.4.

Table 2.4: Properties of different organic/carbon aerogels.

Properties	Resorcinol-formaldehyde aerogels	Carbon aerogels
Bulk density (g.cm^{-3})	0.04–0.10 [26]	0.05–1.00 [33]
Specific surface area (m^2.g^{-1})	∼800 (base-catalyzed) [189] ∼300 (acid-catalyzed) [189]	400 [34] to 1100 [35]
Pore size (nm)	10–20 [189]	0.5–50 [33]
Particle size (nm)	3–5 (high catalyst conditions) [189] 11–14 (low catalyst conditions) [189]	-
Porosity (%)	>80 [190]	80–98 [35]
Electrical conductivity (S.m^{-1})	-	25–100 [35]

2.4 Carbon nanostructure-silica aerogel composites - synthesis and applications

The possibility of transferring some of the individual properties of carbon nanostructures presented in the previous section to a bulk material, associated with the differentiated characteristics of silica aerogels, has opened the way for using these carbon nanomaterials in an even larger number of applications, including electronic and optoelectronic devices, thermal insulation and adsorption.

2.4.1 CNT–silica aerogel composites

The chemical systems and experimental methodologies used in the published studies for preparing aerogel composites involving carbon nanotubes and silica matrices are reported in Table 2.5.

Table 2.5: Literature studies in which carbon nanotubes and silica were used to synthesize aerogel composites.

Reference	Chemical system	Experimental methodology
Song *et al*. [203]	Silica precursor: TEOS Carbon material: MWCNTs	1st step – silica aerogel preparation: TEOS was mixed with water, alcohol and catalyst; CO_2 supercritical drying 2nd step A – synthesis of the composite material – 1st methodology: carbon deposition –> decomposition of acetylene, in a tube furnace, at 550 ^{o}C; post-treatment –> inert atmosphere at 670 ^{o}C for 0.5 h 2nd step B – synthesis of the composite material – 2nd methodology: carbon and iron deposition –> decomposition of ferrocene at 120 ^{o}C for around 20 h in a helium atmosphere (∼200 Torr); inert atmosphere at 700 ^{o}C for about 1 h

Table 2.5 – Literature studies in which CNTs and silica were used to synthesize aerogel composites. (*Continued*)

Reference	Chemical system	Experimental methodology
Bargozin *et al*. [94]	Silica precursor: water glass Carbon material: MWCNTs	Synthesis of the composite material: water glass was diluted in triple deionized water (volume ratio 1:4); 0.05 g of MWCNTs were dispersed, by ultrasonic stirring for 15 min, in 12 cm^3 of diluted water glass; the solution was stirred with an amberlite ion exchange resin; addition of ammonia hydroxide until the pH became 4; sol transferred into a Teflon vessel, and kept under airtight conditions until gelation; after gelation, hydrogels were aged for 3 h under airtight conditions; gels were first kept in isopropyl alcohol for 4 h at 60 ^oC and, then, in *n*-hexane for 3 h at 60 ^oC; for surface modification: addition of 20% of TMCS to the *n*-hexane solution (2 h at 60 ^oC); ambient pressure drying (APD): room temperature for 10 h, 50 ^oC for 2 h and 200 ^oC for 2 h
Duque *et al*. [92]	Silica precursor: TMOS Carbon material: SWCNTs	1st step – SWCNT preparation: 10 mg of raw SWCNTs were dispersed in water with sodium dodecylsulfate (SDS) or sodium deoxycholate (DOC); homogenization at 19000 rpm for 2 h, sonication for 4 min; ultra-centrifuged for 4 h 2nd step – synthesis of the composite material: by chemical vapor-into-liquid sol–gel: two vessels, one with SWCNT suspension and one with TMOS, were placed in a sealed container for 1–6 h at room temperature; by liquid-phase sol–gel: mixture of SWCNTs suspension and TMOS. 48 h aging; solvent exchange –> methanol; CO_2 supercritical drying –> 24 h at 10 ^oC and 51 atm, then heated to 40 ^oC and pressure increased to 90 atm
Bangi *et al*. [204]	Silica precursor: water glass Carbon material: MWCNTs	1st step – MWCNTs preparation: MWCNTs were dispersed in water (10 mL) by coating with Tween 80 (1.9 wt%); after the adsorption of Tween 80 on the MWCNTs surface, ultrasonication for 4 h 2nd step – synthesis of the composite material: the aqueous dispersion of MWCNTs was added to sodium silicate solution (molar ratio of 146.67 for $H_2O:Na_2SiO_3$); addition of citric acid (3 M) to form the gel; aging –> 3 h; gels washed with water by shaking at 150 rpm and 50 ^oC for 4 h; solvent exchange –> methanol for 24 h; silylation –> methanol:TMCS:hexane for 24 h (1:1:1 volume ratio); gels washed with hexane; APD: 50 ^oC and 200 ^oC for 1 h each
Wang *et al*. [205]	Silica precursor: water glass Carbon material: MWCNTs	Synthesis of the composite material: water glass was diluted in water; the solution went through an amberlite ion exchange resin column; addition of MWCNTs suspension (0–15 vol%) dispersed by arabic gum in the silica sol; addition of ammonia hydroxide; 48 h aging –> 24 h in ethanol/water and 24 h, at 50 ^oC, in ethanol/TMCS/*n*-hexane; APD –> room temperature for 20 h; heat-treatment –> 50 ^oC for 2 h, 80 ^oC for 2 h, 120 ^oC for 1 h and 150 ^oC for 1 h

Table 2.5 – Literature studies in which CNTs and silica were used to synthesize aerogel composites. (*Continued*)

Reference	Chemical system	Experimental methodology
Sun *et al.* [95]	Silica precursor: TEOS Carbon material: COOH-MWCNTs	1st step – MWCNT modification: 500 mg of CNTs were immersed in a mixture of concentrated HNO_3 and H_2SO_4 (3:1 in volume) at 100 ^oC for 6 h; after cooling to room temperature, the mixture was poured into cold deionized water (1 L) and then vacuum-filtered through a 0.22 μm polycarbonate membrane; the solid was filtered and washed with deionized water until neutral pH, and then re-suspended in 100 mL of HCl (12 M) for 12 h at 100 ^oC; the suspension was finally vacuum-filtered through a 0.22 μm polycarbonate membrane and dried under vacuum for 10 h at 100 ^oC 2nd step – synthesis of the composite material: 400 mg of COOH-MWCNTs were ultrasonically dispersed in the mixture of 2 mL of TEOS, 20 mL of ethanol and 4 mL of water; addition of HCl aqueous solution; after intensely stirring at room temperature for 4 h, addition of ammonia aqueous solution; 12 h aging –> room temperature; solvent exchange –> ethanol 3 times, followed by the mixture of *n*-hexane and TMCS 3 times; APD –> 150 ^oC for 10 h
Sachithanadam and Joshi [96]	Silica precursor: commercial silica aerogel Carbon material: COOH-MWCNTs (FMWNTs)	Synthesis of the composite material – 1st methodology [206]: gelatin in water –> sonication for 1 h; addition of SDS –> frothed into foam; addition of the silica aerogel and FMWNTs (0.042 to 0.082 wt%); air drying at room temperature with a relative humidity of 60% Synthesis of the composite material – 2nd methodology: gelatin in water –> sonication for 1 h; addition of SDS, silica aerogel and FMWNTs (from 0.017 to 0.050 wt%); freeze-drying
Chernov *et al.* [93]	Silica precursor: TEOS Carbon material: MWCNTs	1st step – MWCNT synthesis: MWCNTs were produced *via* catalytic chemical vapor deposition using the preformed Fe–Co catalyst at 680 ^oC 2nd step – synthesis of the composite material: TEOS was diluted with methanol; after alcohol removal, the silica–organic oligomers (1.9 mL) were diluted with ethane nitrile; nanotube suspension obtained in dimethylformamide (DMF) (0.01 mg.mL^{-1} of DMF); the liquid phase of each sample was increased up to 5 mL by DMF and water addition; sol condensation –> promoted by NH_3; gel aged for 2–3 days, and further acetonitrile was exchanged with isopropanol; supercritical drying (236 ^oC, 5.38 MPa)
Huang *et al.* [63]	Silica precursor: TEOS Carbon material: COOH-MWCNTs	1st step – preparation of carboxylic carbon nanotubes: pristine MWCNTs were added to HNO_3 –> stirring at 90 ^oC for 6 h; the generated solid was centrifuged, washed and dried under vacuum; 2nd step – synthesis of the composite material: COOH–MWCNTs (mass fraction from 7 to 9%) were mixed with TEOS; HCl and ammonia were added; after gelation –> solvent exchange with a mixture of TMCS and *n*-hexane; drying at 65 ^oC (4 h), 80 ^oC (2 h) and 120 ^oC (2 h)

Continued on next page

Table 2.5 – Literature studies in which CNTs and silica were used to synthesize aerogel composites. (*Continued*)

Reference	Chemical system	Experimental methodology
Piñero *et al*. [97]	Silica precursor: TEOS Carbon material: MWCNTs	Synthesis of the composite material: 2.5 mL of TEOS was mixed with 2.0 mL of ethanol; 1 mL of HNO_3 (pH 1) was added and the solution submitted to 1 min of ultrasounds; addition of 6.5 mL of ethanol; 3.25 mL of a basic solution (NH_4OH and CNTs - pH 12) was added into the silica sol while being submitted to 30 s of ultrasounds; after gelation –> aging at 80 ^oC for 48 h; washing –> 7 days in ethanol; ethanol supercritical drying –> temperature raised until 260 ^oC (1 $^oC.min^{-1}C$) and pressure of 8 MPa, maintained for 30 min

Among the studies presented in Table 2.5 only one was developed using SWCNTs. The others referred to materials synthesized using MWCNTs, mostly carboxylic carbon nanotubes, since the CNT functionalization improves their dispersion in the silica matrix [207]. The silica precursor is the point in which the studies differ the most; water glass and TEOS were the most used precursors (three and five times, respectively), while TMOS and commercial silica aerogels were used only once. For the drying step, the preferred method was ambient pressure drying (APD) to obtain the composite materials, while supercritical drying was used in four cases and freeze drying in one. This confirms that the three drying strategies are viable routes to dry these composite materials. Some of the most relevant properties of these materials are compiled in Table 2.6.

Table 2.6: Some relevant properties of the synthesized composite materials with carbon nanotubes and silica.

Reference	Aerogel composite materials	Optimum amount of carbon for the chosen application	Specific surface area $(m^2.g^{-1})$	Pore volume $(cm^3.g^{-1})$	Bulk density $(g.cm^{-3})$	Average pore size (nm)	Tested application
Bargozin et al. [94]	Silica aerogel–MWCNTs	0.05 g of MWCNTs	802.0	3.6	0.230	2.5	Adsorbent
Duque et al. [92]	SWCNTs–silica	10 mg of raw SWCNTs	∼1400.0	-	∼0.057	∼6.0	-
Bangi et al. [204]	Silica aerogel doped with MWCNTs	0.5 mL	706.0	2.13	0.053	12.1	-
Wang et al. [205]	MWCNTs doped silica	5 vol%	-	-	0.193	2.0-50.0	-
Sun et al. [95]	CNT/silica	400 mg	-	2.92	0.062	-	Adsorbent
Sachithanadam and Joshi [96]	Gelatin silica aerogel doped with FMWNTs	0.042 wt%	-	-	-	-	Thermal insulator
Chernov et al. [93]	Silica aerogel with incorporated MWCNTs	Maximum of 0.8 wt%	-	-	0.250	3.0-20.0	-
Huang et al. [63]	MWCNTs–silica	Mass fraction of 8%	-	4.58^a 21.83^b	0.201^a 0.045^b	∼20.0	Adsorbent
Piñero et al. [97]	Silica-CNT hybrid aerogels	0.5 wt%	540	4.1	0.069	20	-

[a] Values of pore volume and density for the monolithic aerogel. [b] Values of the volume of pores in the aerogel and the interspace between aerogel fragments and density of aerogel fragments.

2.4.2 CNFs–silica aerogel composites

The synthesis and characterization of composite materials developed with fibers, such as mineral, ceramic, aramid and carbon, and silica aerogels were already addressed in a literature study by Ślosarczyk [208]. However, as the focus of this review is on the composites obtained by the mixture of carbon nanostructures with silica aerogels, it is still relevant to present in this section studies in which carbon nanofibers were used in these composite systems. The chemical systems and experimental methodologies used to obtain the found CNFs–silica aerogel composites are presented in Table 2.7.

Table 2.7: Literature studies in which carbon nanofibers and silica were used to synthesize aerogel composites

Reference	Chemical system	Experimental methodology
Lu *et al.* [209]	Silica precursor: TMOS Carbon material: graphitic carbon nanofibers	1st step – preparation of graphitic carbon nanofibers (GCNFs): narrow herringbone GCNFs were prepared by the procedure of Anderson and Rodriguez (vapor-phase growth processes) [210] 2nd step – preparation of GCNFs/silica aerogel composites by sol–gel process: addition of 1.0 mL of TMOS and 0.0161 g of surface-enhanced GCNFs into a solution of 1.21 mL of water, 2.72 mL of ethanol and 0.52 mL of dimethylformamide; addition of 0.48 mL of a 0.1% solution of NH_4OH; the wet alcogel was soaked 8 times in 250–300 mL of ethanol and aged at room temperature for 72 h; supercritical drying
Meador *et al.* [137]	Silica precursor: TMOS and APTES Carbon material: carbon nanofibers	Preparation of the aerogel composites: solution A: 0.055 g of fibers, 47 mL of CH_3CN, 2.25 mL of TMOS and 0.75 mL of APTES –> sonication for 30 min; solution B: 47.67 mL of acetonitrile and 2.33 mL of water; solution B was poured into solution A, shaken vigorously, allowed to gel and aged for 24 h; gels –> washing with acetonitrile 4 times at 24 h intervals; replacement of acetonitrile with a 6% di-isocyanate bath for 24 h with intermittent agitation; decantation of the monomer solution, exchange with acetonitrile, and the monoliths were allowed to react for 72 h in an oven at 71 ^{o}C; oven-cured gels cooled to room temperature, and the acetonitrile was replaced 4 more times in 24 h intervals; CO_2 supercritical drying ($\sim$100 bar, 25 ^{o}C – 5 cycles of 2 h/ $\sim$ 215 bar, 45 ^{o}C)
Wei *et al.* [211]	Silica precursor: TEOS Carbon material: carbon nanofibers	Preparation of carbon fiber–silica aerogel composites: solution of TEOS (20.8 g), ethanol (13.8 g) and HCl (1.8 g of 0.14 wt% HCl/H_2O solution) –> stirring for 1.5 h; addition of ethanolic carbon nanofibers suspension; 0.2 mL of 5M NH_4OH added to the solution, and after 30 min, another 1.1 mL; after 2 days of aging –> washing with ethanol (3 times every 24 h); CO_2 supercritical drying
Ślosarczyk [208]	Silica precursor: TEOS Carbon material: carbon nanofibers	Preparation of carbon fiber–silica aerogel composites: solution of TEOS, ethanol and 0.1 M HCl; addition of carbon nanofibers –> stirring for 15 min; NH_4OH (1.5 M) –> quick gelation; aging in ethanol for 7 days; surface modification –> TMCS/*n*-hexane (volume ratio of 1/10) at 50 ^{o}C for 48 h; drying in air

The articles presented in Table 2.7 report composites of carbon nanofibers–silica, being the diameter of the used fibers from 30 to 150 nm. As silica precursors, TEOS was used in two studies, while TMOS by itself in one study and together with APTES in another. All the described studies used the sol–gel methodology to obtain the composite materials, and the majority used supercritical procedures in the drying step; only the work developed by Ślosarczyk [208] used ambient pressure drying. The composite properties are summarized in Table 2.8.

Table 2.8: Some relevant properties of the synthesized composite materials with carbon nanofibers and silica.

Reference	Aerogel composite materials	Optimum amount of carbon for the chosen application	Specific surface area $(m^2.g^{-1})$	Pore volume $(cm^3.g^{-1})$	Bulk density $(g.cm^{-3})$	Average pore size (nm)	Tested application
Lu *et al.* [209]	GCNFs/silica	0.0161 g	182.0	-	-	-	-
Meador *et al.* [137]	Carbon nanofibers in di-isocyanate cross-linked silica	5% (w/w)	89.8	-	0.088	29	-
Wei *et al.* [211]	Carbon nanofibers/SiO_2	10 wt%	829.0	4.80	0.109	-	Thermal insulation
Ślosarczyk [208]	Silica aerogel–carbon nanofibers	10 volume%	589.8	-	0.195	10.3	-

2.4.3 Graphene–silica aerogel composites

The chemical systems/experimental methodologies found in the published studies in which composite materials were synthesized with graphene and silica aerogel matrices are presented in Table 2.9. The corresponding properties of these materials are summarized in Table 2.10.

Table 2.9: Literature studies in which graphene or graphene oxide (GO) and silica were used to synthesize aerogel composites

Reference	Chemical system	Experimental methodology
Kabiri *et al.* [100]	Silica precursor: APTES and DE[1] Carbon material: GO	1st step – surface modification of DE: silanization process with APTES 2nd step – preparation of GO: oxidation of natural graphite by an improved Hummers method 3rd step – synthesis of the composite material: GO (20 mg) and 10 mL of water –> sonication for 1 h; addition of APTES–DE (5 mg) to the mixture –> another 1 h of sonication; addition of $FeSO_4.7H_2O$; 90 ^{o}C for 6–8 h; freeze-drying for 24 h
Meng *et al.* [75]	Silica precursor: TEOS Carbon material: GO	1st step – preparation of GO: oxidation of natural graphite by a modified Hummers method 2nd step – synthesis of the composite material: 17.5 mL of GO solution (3.6 mg.mL^{-1}) in ethanol –> sonication for 1 h; addition of TEOS –> sonication for 1 h; 180 ^{o}C for 24 h; wet gels hydrothermally treated in ammonia (10 v/v%) for 3 h at 120 ^{o}C; freeze-drying
Loche *et al.* [99]	Silica precursor: TEOS Carbon material: Graphene	1st step – preparation of graphene in DMF dispersion: dispersion of 5.0 g in 100 g of DMF; sonication of the mixture in an ultrasonic bath at room temperature for 24 h; centrifugation for 30 min at 4000 rpm, and removal of residual solid graphite; filtration –> polyvinylidene fluoride filters

Continued on next page

Table 2.9 – Literature studies in which graphene or GO and silica were used to synthesize composites (*Continued*)

Reference	Chemical system	Experimental methodology
		2nd step – synthesis of the composite material: 3.95 mL of TEOS added to ethanol; pre-hydrolysis under acidic conditions using 1.965 mL of acidic stock solution (2 mL of HNO_3, 80 mL of ethanol and 130 mL of distilled water); addition of graphene dispersion in DMF (2.985 mL); a hydro-alcoholic solution of urea was added and kept under reflux at 85 ^oC; after 40 min –> addition of lithium borohydride solution; the gel was kept in an oven at 40 ^oC for 3 h; high temperature supercritical drying at up to 330 ^oC and 70 atm
Tajik *et al.* [212]	Silica precursor: water glass Carbon material: Graphene	1st step – synthesis of silica aerogel: mixture of 20 mL sodium silicate with 2 mL citric acid (3 M); after 3 h at 50 ^oC, the gel was washed with water; immersion in methanol for 24 h at 50 ^oC; washing with hexane and drying at 200 ^oC for 1 h 2nd step – synthesis of the composite material: silica aerogel powder was placed on a quartz boat and annealed in a horizontal tube in the presence of H_2 (600 sccm) at 600 ^oC (5 ^oC.min^{-1}) for 2 h; acetylene was injected into the reactor (100 sccm) for 30 min; cool down to room temperature under a N_2 atmosphere
Lei *et al.* [98]	Silica precursor: TEOS Carbon material: GO	1st step – preparation of GO: oxidation of graphite powder by a modified Hummers method 2nd step – synthesis of the composite material: TEOS, ethanol and oxalic acid solution under stirring; addition of GO suspension (0 to 10 wt%) –> ultrasonic treated for 15 min; solution was hydrolyzed for 24 h; addition of ammonia –> sol into gel; solvent exchange –> ethanol; supercritical drying
Dervin *et al.* [213]	Silica precursor: water glass Carbon material: GO	1st step – synthesis of graphite oxide (GtO): GtO was prepared from natural graphite following the improved method developed by Marcano *et al.* [214] 2nd step – synthesis of the GO solution: different amounts of GtO added to 7.04 mL of deionized water; dispersed GtO sheets exfoliated via ultrasonication for 1 h 3rd step – synthesis of the composite material: 5.93 mL of sodium silicate diluted with 7.035 mL of deionized water; solution passed through an ion-exchange resin; addition of GO solution and NH_4OH until a pH of 6–7; sols were kept at 50 ^oC for gelation, and aged for 3 h at 50 ^oC; 24 h solvent exchange – methanol; 24 h surface modification – methanol:TMCS:hexane = 1:1:2 v/v; gels washed 4 times in 24 h with hexane, ambient pressure drying: 80 ^oC for 5 h, 150 ^oC for 1 h and 200 ^oC for 1 h
Hong-li *et al.* [215]	Silica precursor: TEOS Carbon material: GO	1st step – preparation of GO aqueous solution: modified Hummers' method 2nd step – synthesis of the composite material: TEOS, ethanol and GO solution were added into a flask; addition of HCl to obtain a solution with pH of 2.5 - 3.0 –> stirring for 30 min at 35 ^oC; addition of concentrated NH_4OH until sol reached a pH of 6.0 - 7.0 –> maintained at 35 ^oC until gelation; aging –> 3 h at 50 ^oC; surface modification –> HMDZ for 8 h; washing –> hexane (3 times); APD –> 80 ^oC (4 h); 100 ^oC (4 h) and 200 ^oC (1 h)

Table 2.9 – Literature studies in which graphene or GO and silica were used to synthesize composites (*Continued*)

Reference	Chemical system	Experimental methodology
Zhu *et al*. [216]	Silica precursor: TEOS Carbon material: Graphene	Synthesis of the composite material: Mixture of H_2O, ethanol and TEOS (1:4:1 volume ratio); addition of HCl as catalyst –> stirring for 90 min; graphene dispersion was added into the solution –> ultrasounds for 25 min; addition of NH_4OH 0.2 M until pH was 6 - 7; aging and ethanol washing –> room temperature; CO_2 supercritical drying
Oikawa *et al*. [217]	Silica precursor: water glass Carbon material: reduced GO	Synthesis of the composite material: water glass was diluted in ultrapure water; reduced GO (rGO) was added into the solution; concentrated HCl was used as acid catalyst; immersion of the hydrogel, first in a HCl solution (1 h), then in a solution of 6.8 wt% octamethyltrisiloxane and 2-propanol (60 ^{o}C, 6 h); APD –> 150 ^{o}C for 2 h
Thakkar *et al*. [218]	Silica precursor: TEOS Carbon material: GO	Synthesis of the composite material: TEOS was hydrolyzed by an acid solution (HNO_3 in ethanol and water); GO was dispersed in ethanol by ultrasonic treatment then added to the silica sol; addition of a hydro-alcoholic solution of urea –> refluxed at 85 ^{o}C; aging –> overnight at 40 ^{o}C; ethanol supercritical drying –> up to 330 ^{o}C, 70 atm
Zhang *et al*. [219]	Silica precursor: TEOS Carbon material: GO	1st step – synthesis of GO: GO was prepared by a modified Hummers method 2nd step – synthesis of the composite material: TEOS, ethanol and water were mixed (1:7:2 molar ratio); HCl was used to adjust the pH to 3; solution was stirred for 24 h at room temperature; addition of DMF and GO to the sol and stirred for 1 h; NH_4OH was added until pH was 7.5; hydrosol was placed into a ultrasonic cleaner to gelify; aging, solvent replacement, surface modification and drying were performed under ambient conditions

For the studies reported in Table 2.9, the majority used graphene oxide as a carbon source for the composite systems, with only three studies using graphene. The use of graphene oxide (GO) is justified by the fact that, unlike graphene with a bare surface, it possesses a large quantity of oxygen-containing groups (epoxide and hydroxyl groups, for example), which improve the graphene solubility in solvents and the interaction with the silica network [98]. Among the studies that used GO, the majority obtained this carbon material by using a modified Hummers method, in which, originally, the graphite oxidation occurs by adding potassium permanganate ($KMnO_4$) and sodium nitrate ($NaNO_3$) into concentrated H_2SO_4 [220]. The most common silica precursor used by the authors was TEOS, being used in seven studies, and, for the drying step, the three methodologies, APD, freeze-drying and supercritical drying, were used.

As seen in Tables 2.5, 2.7 and 2.9, the authors designated the materials as aerogels,

---

[1]APTES – 3-aminopropyl-triethoxysilane; DE – diatomaceous earth; GO - graphene oxide.

even though some of them were dried by freeze-drying and APD. The aerogel designation was probably used due to the obtained properties of the final materials, since the developed materials exhibited characteristics similar to the ones obtained for aerogels, such as very high surface areas and low densities. This is in agreement with a very recent communication that was published regarding the use of the term "aerogel" [36].

Table 2.10: Some relevant properties of the synthesized composite materials with graphene oxide and silica.

Reference	Aerogel composite materials	Optimum amount of carbon for the chosen application	Specific surface area $(m^2.g^{-1})$	Pore volume $(cm^3.g^{-1})$	Bulk density $(g.cm^{-3})$	Average pore size (nm)	Tested application
Kabiri *et al.* [100]	Graphene-DE	20 mg of GO	368.0	-	-	-	Adsorbent
Meng *et al.* [75]	SiO$_2$-graphene	Solution with 3.6 mg.mL^{-1} of GO	396.9	0.67	-	6.8-8.2	Anode material
Loche *et al.* [99]	Graphene/silica	0.1 wt%	473.0	4.23	-	30.0	Adsorbent
Tajik *et al.* [212]	Silica-graphene	16 wt%	843.6	-	-	22.0	Stabilizer of emulsion
Lei *et al.* [98]	SiO$_2$/GO	0.4 wt%	960.8	5.12	$\sim$0.08	-	Thermal insulator
Dervin *et al.* [213]	GO/SiO$_2$	0.5 wt%	700.0	0.99	0.14	5.3	-
Hong-li *et al.* [215]	GO/silica composite aerogel	1.5 wt%	740.0	2.83	0.16	15.3	Thermal insulator
Zhu *et al.* [216]	G/SiO$_2$ composite aerogel	0.1 wt%	1096	2.67	-	-	Thermal insulator
Oikawa *et al.* [217]	rGO-silica xerogel nanocomposite	2.5 wt%	403	0.98	-	18	-
Thakkar *et al.* [218]	rGO/SiO$_2$ nanocomposite aerogel	5 wt%	510	4.26	-	25	Adsorbent
Zhang *et al.* [219]	GO/SiO$_2$ hybrid aerogel	0.5 wt%	948	3.12	-	14.8	Thermal insulator

2.4.4   C/SiO$_2$ aerogel composites with RF as a carbon source

Here we focus on carbon/silica composite aerogels, obtained by the pyrolysis of organic/silica materials at temperatures of about 800 ^{o}C, and not on those composed of carbon and silicon carbide (not containing silica), in which the composites were subjected to temperatures, usually, above 1500 ^{o}C. In particular, we close the framework of this review by also reporting 3D interpenetrating C–SiO$_2$ networks. For more details on C/SiC composites, the readers should refer to a recent review of Fei *et al.* [221]. Thus, in the following tables (Tables 2.11 and 2.12), we present the synthetic routes and properties described by several authors related to C/SiO$_2$ aerogels where the carbon source is RF-based organic aerogels.

Table 2.11: Literature studies in which resorcinol-formaldehyde and silica were used to synthesize C/SiO_2 aerogel composites

Reference	Chemical system	Experimental methodology
Chen *et al.*[222]	Silica precursor: silica nanoparticles Carbon material: RF	1st step – preparation of RF/silica aerogel composites: resorcinol (13 g) and formaldehyde (19 g) added to 50 g of silica sol (30 wt%); addition of 100 mL of distilled water and pH adjusted to 9; the solution was placed in a water bath at 85 ^{o}C for 5 days; washing with ethanol; supercritical drying 2nd step – preparation of carbon/silica aerogel composites: carbonization of the dried aerogels in N_2 at 800 ^{o}C for 3 h
Ye *et al.*[223]	Silica precursor: APTES Carbon material: RF	1st step – preparation of RF/silica aerogel composites: mixture of resorcinol, formaldehyde, ethanol and APTES in a flask, with a F/R molar ratio of 2; addition of water to start the sol–gel reactions (H_2O/APTES molar ratio = 2); the solution was transferred to a glass vial and placed in an oven at 50 ^{o}C for 7 days; CO_2 supercritical drying 2nd step – preparation of carbon/silica aerogel composites: carbonization of the dried aerogels in N_2 at 800 ^{o}C (heating rate = 1 ^{o}C.min^{-1}) and a soaking time of 2 h
Chen *et al.*[224]	Silica precursor: TEOS Carbon material: RF	1st step – preparation of RF/silica aerogel composites: preparation and stirring of a solution composed of 0.8 g of resorcinol, 1.1 g of formaldehyde solution, 4.0 g of CH_3CN and 30 mg of 38 wt% HCl, for 30 min at 27 ^{o}C; preparation of a second solution with 4.2 g of TEOS, 0.6 g of H_2O and 4.0 g of CH_3CN; before the gel point –> addition of the first solution to the second, and stirring until a light red transparent binary sol was obtained; addition of 0.2 g of HF –> second acidic catalyst; the sol was poured into polypropylene ampoules, undergoing gelation at 27 ^{o}C within 30 min (or at 80 ^{o}C in 15 min); aging gels for 24 h at room temperature; washing gels with acetone every 8 h for 6 times; CO_2 supercritical drying 2nd step – preparation of carbon/silica aerogel composites: pyrolysis of the RF/SiO_2 aerogel –> 700 ^{o}C (1 ^{o}C.min^{-1} heating rate) for 2 h, under N_2 flow (150 mL.min^{-1})
Chen *et al.*[225]	Silica precursor: TEOS Carbon material: RF	1st step – preparation of RF/silica aerogel composites: mixing of resorcinol (1.1 g), formaldehyde (1.5 g), CH_3CN (5.0 g) and 38 wt% HCl (0.03 g) at 25 ^{o}C for 1 h; addition of TEOS (4.2 g), HC_3CN (5.0 g) and deionized water (0.1 g) to the RF sol; HF used as a second catalyst; the sol was transferred into polypropylene molds for gelation; aging gels for 24 h at room temperature; washing with acetone every 8 h for 6 times; CO_2 supercritical drying 2nd step – preparation of carbon/silica aerogel composites: pyrolysis of the RF/SiO_2 aerogel –> 800 ^{o}C for 2 h, in a N_2 atmosphere
Kong *et al.*[226]	Silica precursor: APTES Carbon material: RF	1st step – preparation of RF/silica aerogel composites: mixture of resorcinol, formaldehyde, APTES and ethanol at a molar ratio of 1:2:1:60; the solution was transferred to polypropylene molds and placed into an air oven at 60 ^{o}C; after gelation –> aging at 75 ^{o}C for 24 h and simultaneous washing with ethanol every 8 h; CO_2 supercritical drying 2nd step – preparation of carbon/silica aerogel composites: carbonization of the RF/SiO_2 aerogel –> 800 ^{o}C for 3 h, under N_2 flow (150 mL.min^{-1})

Table 2.11 presents several studies developed with resorcinol and formaldehyde as a carbon source for the composite material, however, different silica sources can be applied. Normally the R/F source is chosen because of the characteristics it can provide to the final material. In the cited articles, silica nanoparticles, TEOS and APTES were the used precursors. For the drying step, supercritical fluid drying was the only applied methodology. To obtain C/SiO$_2$ aerogels, thermal treatments at temperatures between 700 ^{o}C and 800 ^{o}C were performed, in N$_2$ atmospheres. The differences caused by these treatments can be observed in the composite properties displayed in Table 2.12. For example, for these composites, the specific surface area and densities showed an increase after the pyrolysis, continuing the expected shrinkage of the samples and in agreement with the reduction of pore size (Table 2.12).

Table 2.12: Some relevant properties of the synthesized composite materials with RF or C and silica

Reference	Aerogel composite materials	Specific surface area (m^2.g^{-1})	Pore volume (cm^3.g^{-1})	Bulk density (g.cm^{-3})	Average pore size (nm)	Tested application
Chen *et al.* [222]	Carbon/silica	311.0	1.90	0.540	16.1	-
Ye *et al.* [223]	RF/silica Carbon/silica	87.0 166.0	0.35 0.39	0.082 0.096	16.14 9.27	-
Chen *et al.* [224]	RF/SiO$_2$ C/SiO$_2$	554.0 985.0	- -	0.173 0.182	16.4 11.9	- -
Chen *et al.* [225]	RF/SiO$_2$ C/SiO$_2$	596.0 769.0	- -	0.160 0.190	14.3 24.3	Thermal insulator Thermal insulator
Kong *et al.* [226]	RF/SiO$_2$ C/SiO$_2$	384.0 430.0	- -	0.101 0.139	- -	- -

2.4.5 Applications of carbon nanostructure–silica aerogel composite materials

The improved or even new properties presented by silica aerogels after the addition of carbon nanomaterials have opened up numerous possibilities for the applications of these composite materials. Among the several areas in which these materials can be applied, these are mostly being used in optical applications, as anodic materials, in thermal insulation and as adsorbents. The studies developed so far in this context will be presented in the next subsections.

It is worth noting that only seven studies referred to in Sections 2.4.1 to 2.4.4 measured the mechanical properties of the composites. An emphasis on the obtained results will also be presented in the next subsections, along with other relevant properties for the sought application. Regarding the works of Piñero *et al.* [97] (Tables 2.5 and 2.6) and Meador *et*

al. [137] (Tables 2.7 and 2.8), their only purpose was to improve the mechanical properties by adding carbon nanostructures. In the work of Piñero *et al.* [97], the addition of only 0.5 wt% of CNTs into a TEOS matrix allowed a significant enhancement of the mechanical parameters. The pure silica aerogel collapsed upon 0.2 MPa stress and resisted less than 50% deformation, while the composite achieved a compressive strength of 0.9 MPa and reached a maximum deformation of 74%. Meador *et al.* [137] added CNFs to polymer–silica aerogel composites, but without a significant increase in density. In this work, it is clear that the increase of the amount of CNFs in the composites leads to an increase of their mechanical strength. More details on the obtained values are already presented in Section 2.2.4.

Optical

One of the first studies on the composite system of carbon nanotubes and silica aerogels was developed by Duque *et al.* [92], in which the authors presented an innovative approach to obtain highly fluorescent solution-free SWCNT–silica aerogels. The composite materials were synthesized as reported in Table 2.5, and exhibited optical transparency, a good percolation of the SWCNTs throughout the silica matrix, minimal shrinkage and retained many of the photo-luminescence (PL) characteristics observed in the initial surfactant/nanotube suspensions, as shown in Figure 2.6.
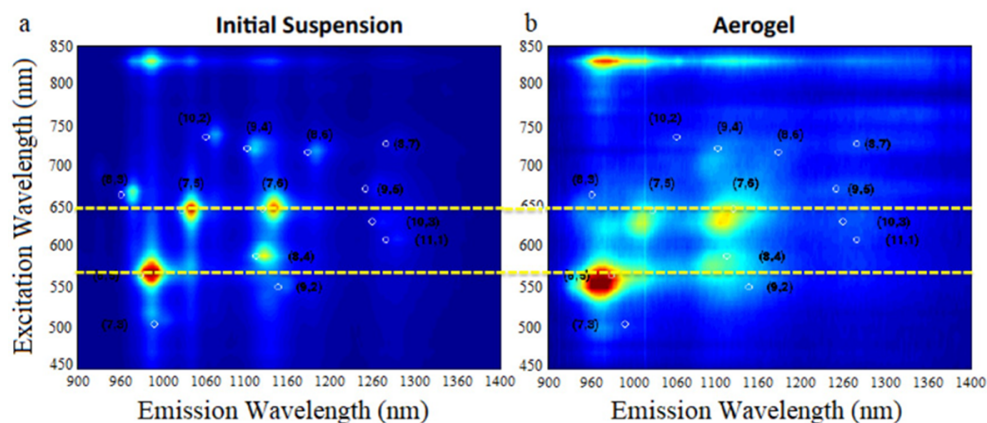
Figure 2.6: Emission profile as a function of excitation wavelength for: (a) the initial SWCNT suspension in sodium deoxycholate (DOC) and (b) the corresponding SWCNT–silica aerogel. Reprinted with permission from reference [92]. Copyright (2011) American Chemical Society.

The aerogels presented an overall blueshift in emission and excitation of respectively 35 and 20 nm after calcination, if compared to the initial dispersion. Besides, the PL intensity at cryogenic temperatures was three times higher than that observed at room temperature. These characteristics indicate a reduction in the interactions between SWCNTs and the matrix, consistent with the nanotubes in a surfactant-free environment. The strong PL

achieved from this nanocomposite, coupled with tunable interactions and optical density led to a new material with potential applications in several areas, such as in sensing, photonics and optoelectronics.

Chernov and co-authors [93] were also able to develop a solution-free environment for nanotubes. The silica aerogel, synthesized with TEOS (Tables 2.5 and 2.6), provided a solution-free matrix, in which the MWCNTs get trapped in the aerogel pores, since all the liquid phase gets removed during the drying step. The optical properties shown by the aerogel–MWCNTs composites are mostly influenced by the MWCNTs, and the transmission value can be controlled by the quantity of added carbon nanotubes. The composite material exhibits a saturated absorption for 200 fs laser pulses at 515 nm. Due to these optical properties, associated with the thermal stability of silica aerogels, the developed composite can be applied as an optical element in several photonic devices.

Anode materials

With the aim of developing a new composite to be applied as an anode material for lithium ion batteries (LIBs), Meng *et al*. [75] synthesized a three-dimensional amorphous SiO_2@graphene aerogel (SiO_2@GA) (Tables 2.9 and 2.10). Due to the intended application, the material electrochemical properties were studied. The discharge–charge behavior was evaluated for the first three cycles and the obtained results for the composite were compared with those of the SiO_2 and graphene aerogel (GA). The coulombic efficiencies of the materials, SiO_2, GA and SiO_2@GA, were 46.4%, 42.3% and 43.5%, respectively. For the second and third cycles, the coulombic efficiency improved for all the materials, with the values obtained for the SiO_2@GA (93.9%; 97.4%) being higher than the ones for SiO_2 and GA. The results of cyclic voltammetry show that the SiO_2@GA has a similar behavior to SiO_2, suggesting that the composite is also electroactive for lithium storage. The materials showed an excellent stability even for 300 cycles and their rate capability was tested at several current densities (100–5000 mA.g^{-1}), Figure 2.7. Although the GA has a superior specific charge capacity and cycling performance at low current densities, the SiO_2@GA exhibits better results at high current densities and is always superior to SiO_2. With these characterizations, the SiO_2@GA composite displays very good electrochemical performance, being a promising anode material for lithium-ion batteries.
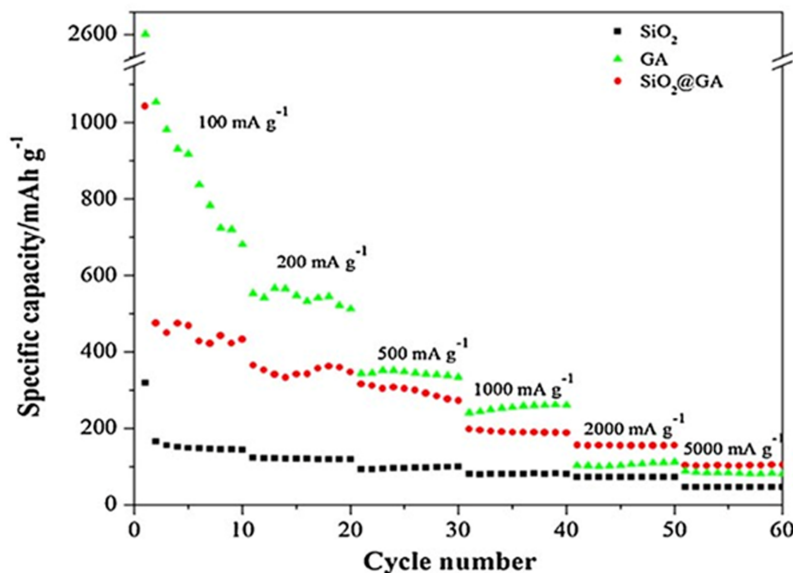
Figure 2.7: Rate capability of SiO_2, GA and SiO_2@GA composites at current densities from 100 to 5000 mA.g^{-1}. Reprinted from reference [75], Copyright (2015), with permission from Elsevier.

Besides the studied graphene–silica composite system, it is possible to obtain anodes for LIBs using silicon nanoparticles and graphene as developed by Xu *et al*. [227] and Hu *et al*. [228]. Xu and co-authors [227] prepared a reduced graphene oxide (RGO) aerogel wrapped silicon nanoparticle (SiNP) (RGO–AG/Si) composite, while Hu *et al*. [228] synthesized a free-standing graphene-encapsulated silicon nanoparticle aerogel (G@Si aerogel) with the same objective as Meng *et al*.[75] and Xu *et al*.[227]. In addition to graphene, carbon nanotubes can also be used to obtain composite materials with silicon nanoparticles as demonstrated by Shim *et al*. [229]. These authors synthesized CNTs aerogel–silicon (CA@Si) nano-hybrid structures comprising silicon–CNTs aerogels via freeze-drying. However, as these studies use silicon instead of silica, further details are not given here since these composites are out of the scope of this review.

Thermal insulators

Thermal insulation is another possible application for these composite materials. Silica aerogels are well known for their extremely low thermal conductivity, however, as mentioned before, they present limitations in their mechanical strength [15]. The work of Sachithanadam and Joshi [96] presented the thermal conductivity of composite materials. In this case, the authors studied the variations in the thermal conductivity, using the Lee's Disc method, of gelatin silica aerogel–sodium dodecyl sulfate (GSA–SDS) composite blocks doped with COOH-functionalized MWCNTs (FMWCNTs) - *vide* Table 2.5. The lowest value of the thermal conductivity (16 mW.m^{-1}.K^{-1}) was achieved when 0.042 wt% of FMWCNTs were incorporated into a gelatin–silica aerogel (gelatin:silica mass ratio of

1:9) without SDS. Based on numerous experiments carried out, thermal conductivity prediction models were developed as a function of the aerogel granular size and temperature, Figure 2.8.
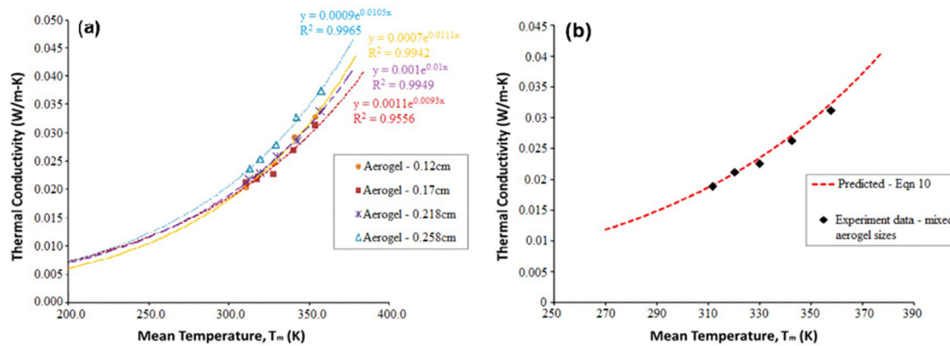
Figure 2.8: (a) Thermal conductivity of hydrophobic translucent silica aerogel granules (Lumira LA1000 from Cabot Corp® (USA)) of various sizes as a function of temperature; (b) experimental vs. predicted results. Reprinted from reference [96], Copyright (2015), with permission from Elsevier.

The synthesized material featured very good thermal insulation, with a thermal conductivity of 16 mW.m^{-1}.K^{-1}, when compared to several commercially available thermal insulators, for example, glass wool (40 mW.m^{-1}.K^{-1}), styrofoam (30 mW.m^{-1}.K^{-1}), and polyurethane foam (26 mW.m^{-1}.K^{-1}) [230].

The thermal conductivity was also assessed by Bangi *et al*. [204], who were able to successfully incorporate MWCNTs into silica aerogels. The silica aerogels were synthesized with sodium silicate and dried by APD (Tables 2.5 and 2.6). The scanning electron microscopy analysis allowed the visualization of the MWCNTs and silica particle interaction, in which the silica gets capped on the side walls of MWCNTs, indicating an enhancement in its toughness (Figure 2.9). The coupling among the materials is considerably strong, due to hydrogen bonding between the surface OH groups on the modified MWCNTs and the silanols, and cannot be easily detached. When 0.5 mL of MWCNTs solution was added to the silica sol, the obtained aerogel showed the lowest density and highest surface area, Table 2.6. This sample presented values of thermal conductivity that can be as low as 67 mW.m^{-1}.K^{-1}, high porosity (97.2%) and a hydrophobic character up to a temperature of 435 ^{o}C.
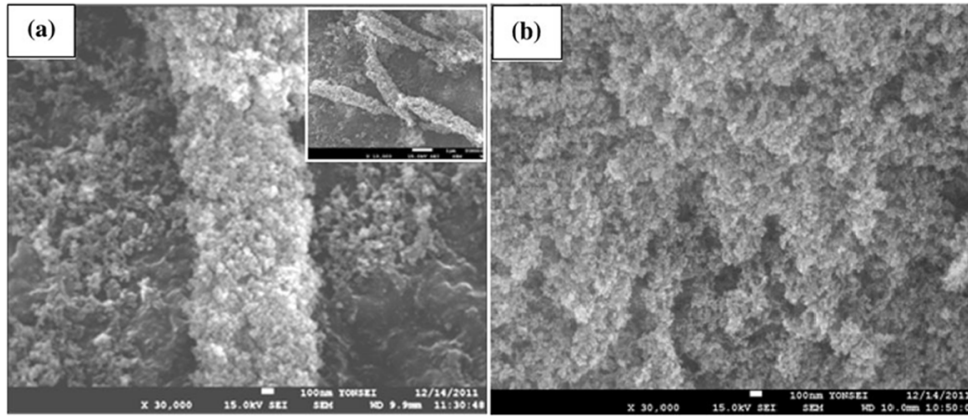
Figure 2.9: SEM images of (a) MWCNTs doped silica aerogel and (b) undoped silica aerogel. Reprinted with permission from Springer Nature, reference [204], Copyright (2012).

Another composite system was studied by Wang *et al.* [205], who fabricated a MWCNTs doped silica aerogel (MWCNTs–SA) (see Table 2.5), and investigated the properties of this new material. The MWCNTs–SA exhibited an anisotropic macroporous honeycomb structure. When 5% of MWCNTs were added, the composite material showed the least shrinkage (8.9%) and highest porosity (91.23%). Its hydrophobic behavior was maintained up to 400–500 ^{o}C. The developed material presented a good thermal stability and mechanical integrity, while maintaining low density (0.193 g.cm^{-3}) and high surface area, which allows the material to be applied as a thermal insulator.

The composites synthesized with carbon nanofibers and silica aerogels can also be applied as thermal insulators. Wei *et al.* [211] developed opacified monolithic aerogels (Tables 2.7 and 2.8) to be applied at high temperatures. The authors were able to incorporate up to 20 wt% of carbon nanofibers into the mesoporous network of silica aerogels. The increase of 0.5 to 20 wt% of carbon nanofibers in the composite material led to a slight decrease in the porosity (95.9% to 94.8%) and in the pore volume from 5.23 to 4.43 cm^3.g^{-1}. In agreement, the room temperature thermal conductivity increased from 29.5 to 38.0 mW.m^{-1}.K^{-1}. For the tests at 500 ^{o}C, an increase in the thermal conductivities was verified with the temperature rise (inset of Figure 2.10a). The increase was most pronounced for the silica aerogel without carbon, indicating an effective suppression of thermal radiation by the incorporation of carbon nanofibers. Figure 2.10a also shows a strong decrease in the thermal conductivity at 500 ^{o}C, with the increase of carbon nanofiber amount, which stabilizes with the load of 10 wt% (50 mW.m^{-1}.K^{-1}). In the following, the thermal stability of the composite was tested by holding the samples at 500 ^{o}C for a period of 600 h (Figure 2.10b). An increase in the thermal conductivity was verified in the time period of 100–150 h that may be due to the volume shrinkage of the samples. However, after this interval the values remained almost constant (55 mW.m^{-1}.K^{-1}), demonstrating an excellent thermal stability of the composite.
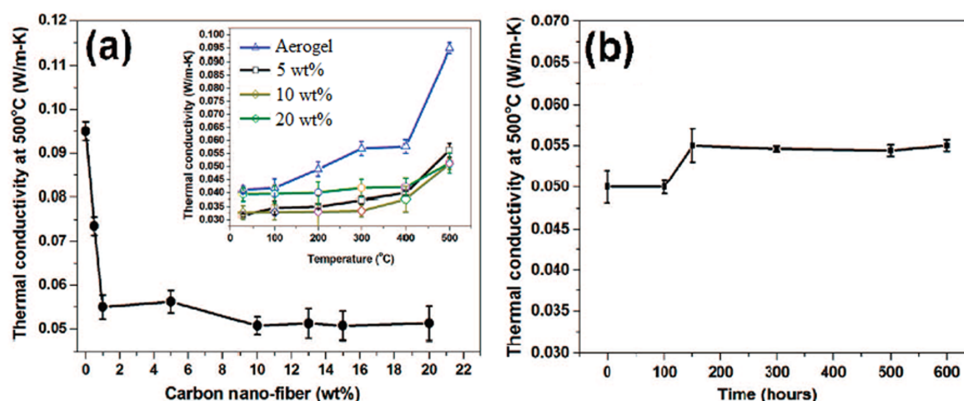
Figure 2.10: (a) Thermal conductivities of composite silica aerogels at 500 ^oC as a function of the carbon nanofiber loading. The inset shows the thermal conductivity versus temperature for the composite silica aerogels with increasing carbon nanofiber loading: 0, 5, 10, and 20 wt%. (b) Stability of a composite of the silica aerogel with 10 wt% of fibers in terms of the thermal conductivity at 500 ^oC, tested for a long time period of 25 days. Reprinted with permission from reference [211]. Copyright (2009) American Chemical Society.

With the aim of enhancing both properties, thermal insulation and mechanical strength, Lei and co-authors [98] added graphene oxide as a nano-filler into the silica aerogel matrix (*vide* Tables 2.9 and 2.10). As the content of GO increases from 0.0 wt% to 10.0 wt%, the material density also increases from 0.074 g.cm^{-3} to 0.179 g.cm^{-3}, and more sharply above 1 wt% of GO. This is accompanied by a general trend of decrease in the surface area, as seen in Table 2.13. The obtained composites also reveal a hydrophobic behavior, Table 2.13. The inclusion of graphene oxide improved the compressive strength of silica aerogel composites by a maximum of 65% (5 wt% of GO) and reduced their thermal conductivity by ~13–19% (Table 2.13). The strength increase can be attributed to the anchoring effect of GO nano-sheets in the silica network, which results in a blocking of crack propagation. Regarding the thermal conductivity, the addition of GO makes the pores of silica aerogels more uniform and with a higher amount of smaller pores. As a result, the degree of constriction of free-molecule-movement is higher, so the contribution of gas heat transfer decreases. However, the thermal conductivities of the composites with 1.0 wt% and 5.0 wt% of GO are slightly higher than that with 0.4 wt% of GO, and thus the solid heat conductivity must also be taken into account, as this is density-dependent. The results obtained by these SiO$_2$/GO aerogel composites for thermal conductivity are exceptional, being lower than the values obtained by silica aerogels based on MTMS/water glass (22.6 mW.m^{-1}.K^{-1}) [231], by the aerogel/fibrous ceramic composite (52.4 mW.m^{-1}.K^{-1}) [232], by silica–cellulose hybrid aerogels (40 mW.m^{-1}.K^{-1}) [233], and by graphene aerogels (32.7 mW.m^{-1}.K^{-1}) [234]. With these improved properties, the new material has great potential to be applied as a thermal insulator.

Table 2.13: Properties of GO/SiO$_2$ composite aerogels [98].

Samples	Specific surface area (m^2.g^{-1})	Water contact angle (^{o})	Compressive strength (MPa)	Thermal conductivity (W.m^{-1}.K^{-1})
0.0 wt% GO	837.4	136	0.238	0.0089
0.4 wt% GO	960.8	137	0.356	0.0072
1.0 wt% GO	867.7	140	0.361	0.0077
5.0 wt% GO	560.4	151	0.394	0.0075

It is worth noting that the improvement of the compressive and/or tensile strength of silica-based composites due to the incorporation of reinforcing nanomaterials of 1-D type usually leads to an increase in the thermal conductivity [235, 236]. As an example, Wong *et al*. [235] observed that nano-fibrillated cellulose-reinforced silica composites present 25–40% higher tensile strength than the silica aerogel of the same density, but the thermal conductivity of the composite material increased by 11% (from 13.8 to 15.3 mW.m^{-1}.K^{-1} with 0 to 4.56 mg.mL^{-1} of fibers in the sol). In fact, these 1-D materials do not cause much constriction on the free-molecule-movement of air from one pore to another as in the case of the 2-D structure of graphene [237].

With the same goals that Lei *et al*. [98], enhancing mechanical and thermal properties, Hong-li and co-authors [215] developed novel GO/silica composite aerogels. By changing the GO content, from 0 wt% to 3 wt% in the TEOS-based silica aerogels, the authors were able to significantly improve the mechanical strength of these materials, increasing their compression strength from 0.04 MPa to 0.65 MPa. The best result of thermal conductivity was achieved when adding 1.5 wt% of GO (18 mW.m^{-1}.K^{-1}). The developed composites have great properties and have a good potential for being used in thermal insulation applications.

Zhu *et al*. [216] were able to prepare an opacified graphene/SiO$_2$ composite aerogels with improved thermal conductivity. The addition of small amounts of the carbon nanostructure (0.1 wt%) caused a reduction in the specific surface area, from 1576 to 1096 m^2.g^{-1}, and in the pore volume, from 4.13 to 2.67 cm^3.g^{-1}, if compared to the silica aerogel. However, the presence of GO leads to an enhancement in thermal insulation property, with the composite achieving values of 18.4 mW.m^{-1}.K^{-1}.

A novel heat-insulation composite phase change material (PCM) was developed by Zhang *et al*. [219] by adsorbing n-octadecanol (OD) into a graphene oxide/silica hybrid aerogel, as described in Table 2.9. The OD/GO/silica hybrid aerogel showed a higher heat storage capacity (145.6 J.g^{-1}) than the OD/silica aerogel, and lower thermal conductivity (81 mW.m^{-1}.K^{-1}) when compared with pure OD (301.5 mW.m^{-1}.K^{-1}).

Chen *et al*. [225] developed a one-pot acid-catalyzed synthesis, as described in Table

2.11, to obtain a resorcinol/formaldehyde cross-linked silica aerogel. Both materials, RF/SiO$_2$ and derived C/SiO$_2$ aerogel composites, showed low densities and high surface areas (Table 2.12). The mechanical properties were tested with the RF/SiO$_2$ and C/SiO$_2$ composites, presenting values of 2.4 and 8.2 MPa for the Young's modulus and 0.21 and 0.63 MPa for the compressive yield strength, respectively. This confirms the high capability of the C network to reinforce the composites, when compared to polymer-reinforcement. The storage modulus for the RF/SiO$_2$ aerogel increased with the temperature (2.1 MPa at room temperature and 3.3 MPa at 300 ^{o}C), while for the C/SiO$_2$ no evident change was verified (near 10 MPa between room temperature and 300 ^{o}C). Thermal properties were also tested for these composites, with RF/SiO$_2$ showing a thermal conductivity of 39 mW.m^{-1}.K^{-1} and C/SiO$_2$ of 53 mW.m^{-1}.K^{-1}. For this property, it appears that the C network connectivity plays a major role in the thermal conduction. These values are very close to the ones presented by insulating materials, for example glass wool (40 mW.m^{-1}.K^{-1}), showing the potentiality of these aerogels to be applied as thermal insulators.

Adsorbents

The use as adsorbents is another possible application of aerogels synthesized with carbon nanostructures and silica. Both carbon nanotubes and graphene can be used for the adsorption of different compounds such as oils, heavy metals, phenolic compounds and gases.

The choice of using MWCNTs may be justified by the fact that this carbon material generates a stable composite without altering the nanostructure of the silica aerogels, and this material was the one used by Bargozin *et al*. [94] to develop silica aerogel–MWCNTs nanocomposites with a water glass precursor and using APD (vide Table 2.5). The synthesized material showed high surface area, nanometric pores (Table 2.6), good hydrophobicity (above 140 ^{o}) and better mechanical properties (300 N maximum pressure) when compared with the pure silica aerogels. The adsorption capacity of the nanocomposite material was tested for different compounds (benzene, toluene, xylene, n-hexane, kerosene, gasoline and petroleum) and the acquired results were compared with the ones obtained for the silica aerogel and activated carbon. Under the same experimental conditions, the silica aerogel–MWCNT nanocomposite presented better results for all the pollutants if compared with the activated carbon; for kerosene and petroleum, the adsorption capacities of the composite were 11 and 47 times better than those of activated carbon, respectively. The results demonstrate that the monolithic nanocomposite has an adsorption capacity 5 times its weight, and the synthesis

methodology allows its regeneration several times without any reduction in the adsorption performance. However, when compared with the pure silica aerogel, the nanocomposite showed lower adsorption capacities for the tested adsorbates, for example, the silica aerogel presented an adsorption capacity of 7.0 g.g^{-1} for toluene while the composite showed an adsorption capacity of 5.0 g.g^{-1}.

Sun and co-workers [95] also synthesized a silica aerogel reinforced with carbon nanotubes for adsorption purposes. The composite material was synthesized via a sol–gel process (*vide* Table 2.5), presenting a three-dimensional network structure and hydrophobic properties (water contact angle of 150°). The addition of the carbon nanostructure improved the compressive strength, leading to an aerogel composite that can bear a load of 12.6 MPa (90 times greater than that of the silica aerogel). Several solvents and oils were used in this work to investigate the adsorption properties of the CNT/silica aerogel, revealing uptake capacities higher than 11 g.g^{-1} for all the tested pollutants and achieving 15 g.g^{-1} for the best case (lube-oil), as demonstrated in Figure 2.11a. The adsorption capacity of the aerogel composite was higher than that of the pure silica aerogel, for example the CNT/silica aerogel presented an adsorption capacity of 15.6 g.g^{-1} for the lube oil, while, for the same compound, the value for the silica aerogel was 14.9 g.g^{-1}. The capability of regeneration of the material was also tested, with the CNT/silica aerogel still showing high levels of adsorption capacities even after 30 regeneration cycles (Figure 2.11b), proving its potential use for chemical accident remediation and cleaning organic pollutants.
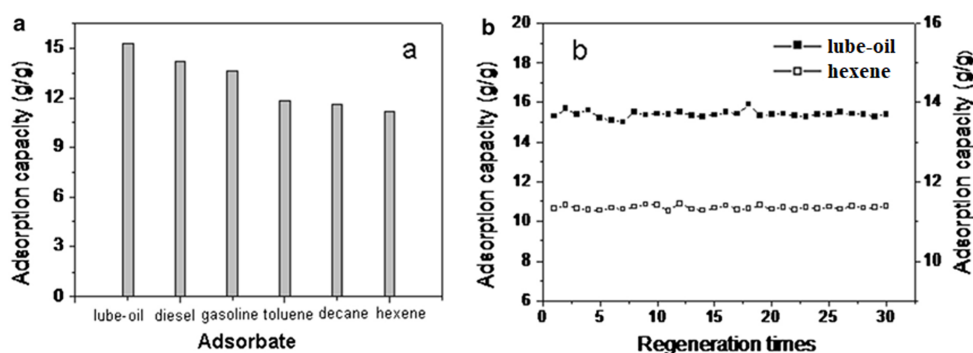
Figure 2.11: (a) Adsorption capacities of the CNT/silica aerogel for a selection of organic solvents and oils; (b) regeneration capacity of the CNT/silica aerogel. The materials have been kept at 200 ^{o}C for about 60 min for regeneration. Reprinted with permission from Springer Nature, reference [95], Copyright (2014).

Huang *et al.* [63] developed MWCNTs–silica aerogels (MSA) using the sol–gel methodology as reported in Table 2.5. The composite shows an oleophilic character, with a water contact angle of 154°, and with the addition of CNTs a decrease in the bulk density of the monolithic aerogels was achieved. For diesel adsorption, the composite had an

adsorption capacity of 28.48 cm^3(oil) per g, showing a synergistic effect between the MWCNTs and silica aerogel in oil adsorption, which showed 19.2 cm^3(oil) per g and 9.70 cm^3(oil) per g as adsorption capacities, respectively. The reusable performance of the MSA was also tested; direct combustion in air was used to remove the adsorbed oil. Four kinds of oil were used as adsorbates during these tests and the composite material still exhibited high adsorption capacities even after 15 removal cycles, Figure 2.12. In continuous oily water treatment, in which the concentration of oily water was set at 2600 $mg.L^{-1}$ for the first 10 h and then reduced to 1000 $mg.L^{-1}$, the material presented a removal efficiency of 98% in the first 24 h. In this experiment, the MSA had a total adsorption capacity of 15.13 $g.g^{-1}$ and reached its saturation after 56 h, for the adsorption of diesel oil. The results of the composite material for static adsorption of diesel oil exhibited an adsorption capacity as high as 24.42 $g.g^{-1}$, which is higher than the values obtained for the MTMS-derived silica aerogel (18.55 $g.g^{-1}$) [238] and for silica aerogels reinforced with 0.3% of polyacrylonitrile fibers ($\sim$10.5 $g.g^{-1}$) [45]. For kerosene, the MSA also presented superior results to the MTMS-derived silica aerogel, with adsorption capacity values of $\sim$22.5 $g.g^{-1}$ and 16.45 $g.g^{-1}$ [238], respectively. These results show new perspectives for an effective method of oil adsorption, with application in environmental protection.
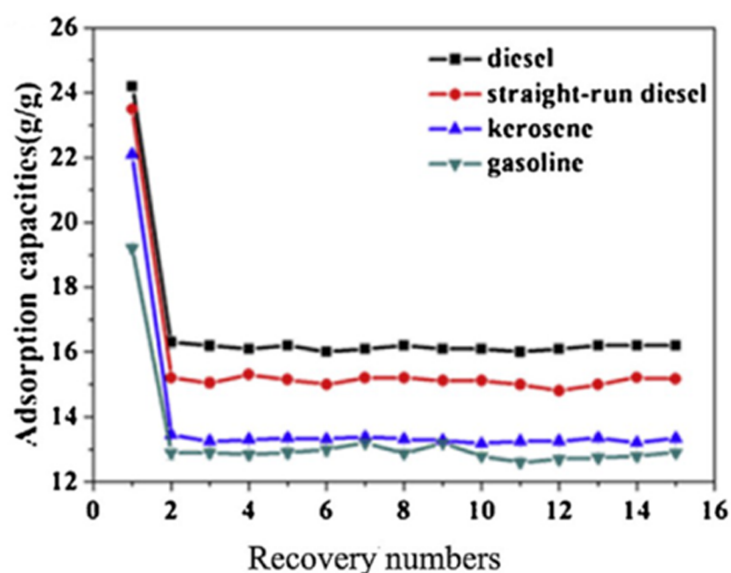
Figure 2.12: Oil adsorption capacity of MSA during repeated adsorption–desorption cycles. Reprinted from reference [63], Copyright (2016), with permission from Elsevier.

Loche *et al*. [99] developed graphene/silica nanocomposites suitable to be applied as oil sorbents for water remediation. The authors chose the sol–gel procedure to incorporate graphene at the early stages of gel formation (Table 2.9), obtaining a porous texture that is characteristic of aerogels which enclose dispersed graphene sheets. Even though the

addition of 0.1 wt% of graphene reduces the material surface area from 530 $m^2.g^{-1}$ (undoped silica aerogel) to 473 $m^2.g^{-1}$, the presence of this quantity of carbon nanomaterial improves the aerogel adsorption capacity (K) of mineral oil in more than 20% when compared to the SiO_2 aerogel, Figure 2.13a. If the adsorption capacities are normalized in relation to the surface area (K/S), the enhancement is up to 35% for the 0.1 wt% nanocomposite, Figure 2.13b. As the authors pointed out, the developed materials have great potential for water remediation from oil spills, since their adsorption capacities for crude oil are around 7 $g.g^{-1}$ and they are fire-resistant, which can prevent fires that are a major threat connected to oil spills.
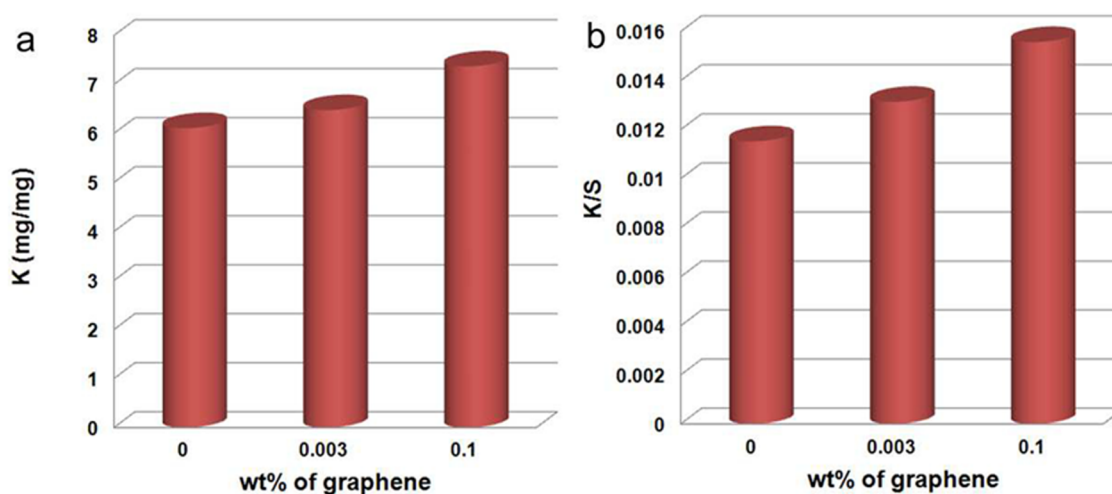
Figure 2.13: (a) Adsorption capacities for mineral oil by the undoped SiO_2 aerogel and by graphene/SiO_2 aerogel nanocomposites with different graphene loadings after a contact time of 3 minutes (k error $\pm$ 0.6) and (b) adsorption capacity values normalized over the surface area. Reproduced from reference [99] with permission of The Royal Society of Chemistry, Copyright (2016).

The work developed by Kabiri *et al*. [100] used a graphene–diatomaceous earth (GN–DE) aerogel (*vide* Tables 2.9 and 2.10) for the removal of mercury ions. The authors studied the influence of the solution pH on the Hg^{2+} removal, and the results showed that the adsorption capacity increases from pH 2 to 6.5. An adsorption capacity of 528 $m^2.g^{-1}$ was observed for the GN–DE, at an initial concentration of mercury equal to 400 $mg.L^{-1}$; the composite material also presented a fast kinetics of Hg^{2+} adsorption, with about 60% of the metal removed during the first 5 min and about 90% in 30 min, before reaching equilibrium, Figure 2.14. A study was also performed to confirm the practical application of the composite material for removing mercury ions from different water sources. The experiments were conducted on water samples (tap and river water) with 100 $mg.L^{-1}$ of Hg^{2+} and the results were compared with those of Milli-Q water. The maximum adsorption capacities obtained were 362 $mg.g^{-1}$, 308 $mg.g^{-1}$ and 336 $mg.g^{-1}$, for Milli-Q, river and tap water, respectively. The slightly lower value verified for the river water is

attributed to its complex matrix, in which several ions are in competition with Hg^{2+}. When comparing the mercury adsorption of the graphene–DE aerogel with that of other adsorbents, the results obtained by this composite material can be described as outstanding, for example the GN–DE presented an adsorption capacity of 528 mg.g^{-1}, while silica aerogels modified with mercapto functional groups showed values of 181.81 mg.g^{-1} [239] and the resorcinol-formaldehyde (RF) aerogel modified with amine had a maximum adsorption capacity of 158.73 mg.g^{-1} [240].
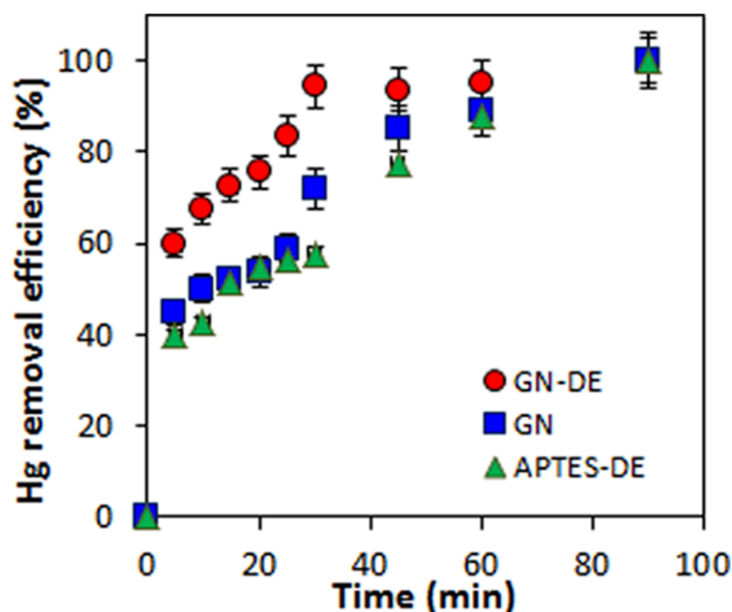
Figure 2.14: Time dependence of Hg^{2+} adsorption on the graphene–DE (GN–DE) aerogel, graphene (GN) aerogel (with αFeOOH nanoparticles), and APTES modified diatom (APTES-DE). Conditions: Hg concentration = 200 mg.L^{-1}; pH = 6.5. Reprinted with permission from reference [100]. Copyright (2015) American Chemical Society.

The use of rGO-silica composite as oil adsorbent was tested by Thakkar *et al.* [218]. The experiments showed that the composite aerogels were highly active oil sorbents, achieving sorption capacities up to 11 times the mass of the sorbent. Overall, the best results were achieved when 5 wt% of rGO was loaded into the silica aerogel, with the material showing a much higher selectivity towards oil rather than water if compared to plain SiO$_2$. The composite also shows more durable and reliable behavior over time, leading to a longer shelf-life than the silica aerogel. With these characteristics, the rGO-silica composites are effective for application in environmental remediation.

Another possibility is to use graphene aerogels containing silica as adsorbents. Wang and co-authors [76] developed 3D graphene aerogel–mesoporous silica frameworks (GAs–MS) for the adsorption of phenolic compounds. For the phenol case, the GAs–MS presented q values of $\sim$90 mg.g^{-1}, however, when compared with other aerogels the result obtained by this material is lower. For example, hydrophobic granular silica aerogels can

achieve an adsorption capacity of 142 mg.g^{-1} when the equilibrium concentration of phenol was equal to 290 mg.L^{-1} [82], and the maximum adsorption capacity of clay-hybrid aerogels towards phenol was 116.75 mg.g^{-1} [241]. On the other hand, there are other reported silica aerogels which have lower performance than the GA–MS composite, for example MTMS-derived and sodium silicate hydrophobized aerogels (21.1 mg.g^{-1} [242] and 13 mg.g^{-1} [243]). Also, Yun *et al.* [77] developed a 3D macroporous, silica and nitrogen-incorporated reduced graphene oxide aerogel (SN-rGOA) for gas adsorption. The material adsorption capacities were assessed for two acidic gases, CO_2 and SO_2. For the experiments with CO_2, the adsorption capacity was 2.38 mmol.g^{-1} at 1000 kPa. The tests with SO_2 were performed under atmospheric pressure, and the SN-rGOA presented a value of 2.19 mmol.g^{-1}.

Other applications

Another application has already been developed for these composite materials, as shown by Tajik and co-authors [212], who used a silica–graphene nano-hybrid as a stabilizer of emulsions. In their work, they obtained a material with single and few stacked graphene sheets in the silica aerogel by chemical vapour deposition, as described in Table 2.9. A sample was prepared under the predicted optimum conditions, as shown in Figure 2.15. The stability of the nano-hybrid was determined by measuring the zeta potential that was found to be about -21 mV. The interfacial tension of the water/decalin emulsion, determined by the Wilhelmy plate method, showed a considerable decline in the presence of the silica–graphene nano-hybrid, changing from 55 to 30.12 mN.m^{-1}. The obtained results show that the developed material is a promising nano-additive to improve the stabilization of oil–water emulsions.
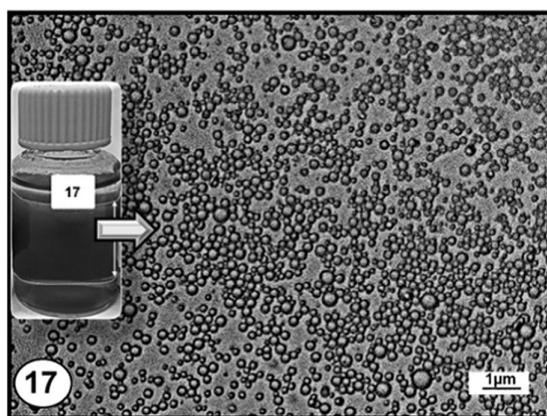
Figure 2.15: Microscopy image of the silica–graphene emulsion's stabilizer prepared under the predicted optimum conditions (migration time of particles to the interface = 72 h; sonication time = 90 min; nanohybrid particle concentration = 0.15 wt%; oil = decalin; surfactant = SDS) by Tajik and co-workers (Reprinted from reference [212], Copyright (2016), with permission from Elsevier.

2.5   Conclusion

Even though silica aerogels have exceptional properties such as low bulk density and thermal conductivity, and high specific surface area, an effort has been made in the last decade to obtain materials with distinctive characteristics when compared to the native silica aerogels. Several strategies were already studied for the modification of aerogels, such as the addition of particles, polymers, or fibers as some of the possible additives for providing and/or improving different properties of silica aerogels. As reported in this review, a new approach for the modification of these aerogels has been developed by the insertion of carbon nanostructures, such as carbon nanotubes, carbon nanofibers, graphene and carbon aerogels. These carbon materials have well-known characteristics, such as high electrical conductivity, high mechanical strength and high specific surface area. The newly developed materials maintain some of the excellent properties verified for silica aerogels, namely specific surface areas higher than 300 $m^2.g^{-1}$, low densities and average pore size in the range of mesopores. Moreover, unique properties were obtained for carbon nanomaterial–silica aerogel composites, such as improved insulation performance, with materials that can achieve thermal conductivities as low as 7.2 $mW.m^{-1}.K^{-1}$, or good adsorption capacities for environmental pollutants, like mercury ions and diesel, or even optical or electrochemical properties. Due to these outstanding properties, the carbon nanomaterial–silica aerogel composites have the potential to be applied as optical or anode materials, as thermal insulators or adsorbents. Although only seven studies measured the mechanical properties of the obtained composites, it is clear from the reported studies that the incorporation of carbon nanostructures into the silica network improves their mechanical properties. In this regard, and since the mechanical strength is the weakest feature of silica aerogels, there is still large room for further studies.

Chapter 3

Polysilsesquioxane-based silica aerogel monoliths with embedded CNTs

Part of this chapter is based on the work *Polysilsesquioxane-based silica aerogel monoliths with embedded CNTs* published in the journal Microporous and Mesoporous Materials (2019), 288, 109575, by Alyne Lamy-Mendes, Ana V. Girão, Rui F. Silva and Luísa Durães.

3.1 Objective and novelty of the work

Inspired by the new promising properties observed in the composite systems reviewed in Chapter 2, the main objective of the work presented in the current chapter was to develop new multi-walled carbon nanotubes (MWCNTs)-silica aerogel composites based in a methyltrimethoxysilane (MTMS)-derived silica matrix. The influence of (3-aminopropyl)trimethoxysilane (APTMS) as silica co-precursor was studied and the obtained physical, chemical and microstructural properties were discussed. The authors were able to prepare monolithic materials applying APD as drying methodology and using an ambient friendly mixture of solvents (50% ethanol/50% water). The addition of silane-modified carbon nanotubes to the silica system allowed their better dispersion, with composites showing lower thermal conductivities and densities, when compared to the corresponding silica aerogel counterpart without CNTs, while improving the final mechanical properties.

To the best of our knowledge, the synthesis of CNTs-silica aerogel composites using these silica precursors, in particular with MTMS as the main matrix builder, has not yet

been reported. Moreover, the obtained gels were dried at ambient pressure and achieved similar properties when compared to aerogels dried in supercritical conditions.

3.2 Experimental Section

3.2.1 Materials

Methyltrimethoxysilane (MTMS; purity $\geq$98%, *Aldrich*; $CH_3Si(OCH_3)_3$), (3-aminopropyl)trimethoxysilane (APTMS; purity $\geq$97%, *Aldrich*; $H_2N(CH_2)_3Si(OCH_3)_3$), tetramethylorthosilicate (TMOS; purity $\geq$99%, *Aldrich*; $Si(OCH_3)_4$), ethanol (absolute, *Fluka*; C_2H_5OH), oxalic acid anhydrous (purity $\geq$99%, *Fluka*; $C_2H_2O_4$), ammonium hydroxide (25% NH_3 in H_2O, *Fluka Analytical*; NH_4OH), hexadecyltrimethylammonium bromide (CTAB; purity $\geq$99%, *Sigma*; $C_{19}H_{42}BrN$), commercial multi-walled carbon nanotubes (CNTs; purity 90%, *Nanocyl*, average diameter of 9.5 nm, average length of 1.5 μm, surface area of 250–300 $m^2.g^{-1}$), sulfuric acid (purity 95%, *Sigma Aldrich*; H_2SO_4), peracetic acid (38-40%, *Merck*; CH_3CO_3H), hydrogen peroxide (30 wt% in H_2O, *Merck*; H_2O_2) and nitric acid (purity 70%, *Sigma Aldrich*; HNO_3) were used in this work without any further purification.

3.2.2 Surface modification of carbon nanotubes

For the development of MWCNTs-silica aerogel composites, a good interaction between the silica matrix and the carbon nanostructure is imperative. In their pristine form, commercial MWCNTs present a significant amount of impurities, such as Al, Fe and Co, which can have a negative influence in their properties. The contamination of these MWCNTs was assessed in another work of the research group [244], in which commercial nanotubes (NC7000) showed a residue of 11.6 wt%. The presence of these contaminants was also confirmed here by transmission electron microscopy (TEM) images (Figure 3.1), as a significant number of embedded metallic impurities (dark contrast dots) were observed.

In this regard, the purification and modification of these carbon nanostructures becomes essential to remove their impurities and to improve their chemical reactivity and the interaction with the silica network. Different methodologies were applied in order to achieve these goals, from treatments with acids (nitric acid, sulfuric acid and peracetic acid), hydrogen peroxide and a silane (tetramethylorthosilicate - TMOS), to plasma treatments with ammonia and oxygen, as reported in Table 3.1. The modification conditions are presented in the same table.
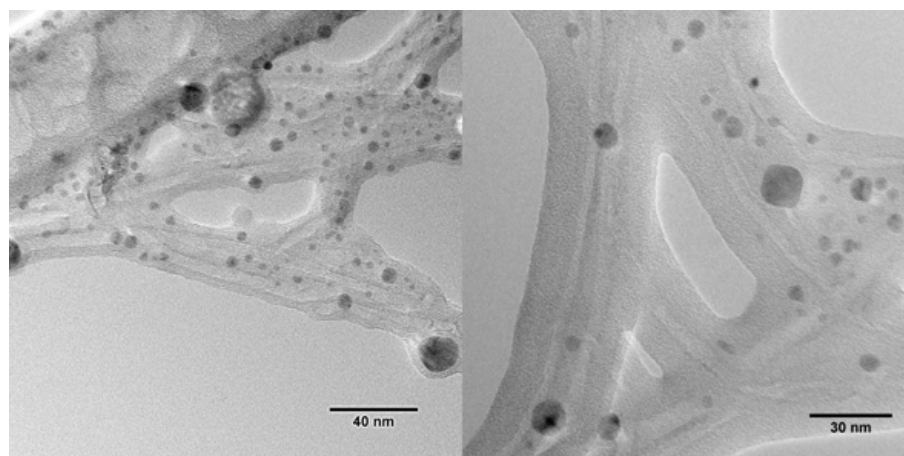
Figure 3.1: TEM images of commercial multi-walled carbon nanotubes (MWCNTs).

After characterization of all modified CNTs, it was concluded that the Sample 22 (Table 3.1) was the most appropriate for the composites development. So, a more detailed description of the modification process is here provided. The multi-walled carbon nanotubes were submitted to acidic and silanization treatments. The chosen procedure was based in the methodology presented by Kim *et al*. [245]. The first step consisted in the surface modification of CNTs by refluxing them with concentrated HNO_3 for 20 hours at 50 °C, followed by filtering and washing with water. The CNTs were then dried at 60 °C overnight. These CNTs were denominated as CNTs-HNO_3. The second modification step was the silane treatment, in which the nanotubes were submitted to a reflux with a 10% silane solution (TMOS in a mixture of 70% ethanol/30% water) for 4 hours at 70 °C, then filtered and dried at 60 °C for 1 day. These CNTs were denominated as CNTs-TMOS.

Table 3.1: Modifications made to the multi-walled commercial carbon nanotubes.

Sample	First step	Second step
01	Reflux - H_2SO_4 + HNO_3 (3:1 v/v, 85 °C, 4h)	-
02	Ultrasound - H_2SO_4 + HNO_3 (3:1 v/v, 4h)	-
03	Stirring - CH_3CO_3H (25 °C, 4h)	-
04	Ultrasound - HNO_3 + H_2O_2 30% (3:1 v/v, 3h)	-
05	Reflux - HNO_3 (50 °C, 20h)	-
06	Plasma NH_3 (30 min 70W - 50 sccm)	-
07	Plasma NH_3 (30 min 30W - 50 sccm)	-
08	Plasma NH_3 (15 min 70W - 50 sccm)	-
09	Plasma NH_3 (15 min 30W - 50 sccm)	-
10	Plasma NH_3 (30 min 100W - 10 sccm)	-
11	Plasma NH_3 (15 min 100W - 10 sccm)	-
12	Plasma NH_3 (30 min 70W - 10 sccm)	-
13	Plasma NH_3 (15 min 70W - 10 sccm)	-

Continued on next page

Table 3.1 – Modifications made to the multi-walled commercial carbon nanotubes. (*Continued*)

Sample	First step	Second step
14	Plasma O_2 (10 min 100W - 10 sccm)	-
15	Plasma O_2 (2 min 100W - 10 sccm)	-
16	Plasma O_2 (2 min 70W - 10 sccm)	-
17	Reflux - HNO_3 (50 °C, 20h)	Stirring - H_2O_2 30% (3h)
18	Reflux - HNO_3 (50 °C, 20h)	Reflux - H_2O_2 30% (60 °C, 3h)
19	Reflux - HNO_3 (50 °C, 20h)	Ultrasound - H_2O_2 30%
20	Reflux - HNO_3 (50 °C, 20h)	Reflux - TMOS (5% v/v):EtOH (70 °C, 4h)
21	Reflux - HNO_3 (50 °C, 20h)	Reflux - TMOS (10% v/v):EtOH (70 °C, 4h)
22	Reflux - HNO_3 (50 °C, 20h)	Reflux - TMOS (10% v/v):(70% EtOH: 30% H_2O) (70 °C, 4h)

3.2.3   Synthesis of CNTs-silica aerogel composites

The silica materials in this work were prepared based on MTMS as main precursor, taking advantage of the previous experience with earlier works [54, 246], but with adjusted incorporation of a co-precursor (APTMS) and overall conditions optimization, described as follows. MTMS was chosen as it allows the synthesis of highly flexible and superhydrophobic aerogels. APTMS was selected to reduce significantly the gelation time and, consequently, avoid the settling of CNTs during gelation.

The dispersion of CNTs in the system was a key factor to obtain homogeneous samples, being the addition of a surfactant essential to achieve this goal. CTAB was the selected surfactant, as it is a good surfactant for CNTs dispersion even in basic conditions [247]. The addition of CTAB also allows obtaining a more controlled microstructure of the silica network and promotes the miscibility between water and the organic moieties of the silanes [248, 249]. The first quantity of CTAB added to the system was 0.25 g (0.83 wt% of gel), based in the study of Li *et al.* [250], in which the authors determined that the critical micelle concentration of CTAB in a 50%/50% ethanol-water mixture was 0.022 M. Thus, the amount of CTAB added is just below that value. The second amount of surfactant used was based in previous works of our research group [251], in which, for an aerogel derived from 100% MTMS, the best properties were obtained by adding 1.25 g of CTAB ($\sim$4.0 wt% of gel).

In order to avoid leaching of the carbon nanomaterial from the system, ambient pressure drying was the chosen methodology instead of continuous supercritical CO_2 drying. Silica aerogel samples and corresponding composites were synthesized with a mixture of ethanol/water (50%/50% v/v) as solvent, which prevented shrinkage during APD. This solvent mixture also allows a better interaction between CNTs and the silica

sol.

All the materials were synthesized by a two-step acid–base catalyzed sol–gel process, with oxalic acid (0.01 M) as acid catalyst and ammonium hydroxide (1 M) as basic catalyst. The samples were prepared with different proportions of silica precursors (MTMS and APTMS), according to Table 3.2. The synthesized silica aerogels are denoted as xMyA_S or xMyA_S1, where x in xM is the mol percentage of Si from MTMS, y in yA corresponds to the mol percentage of Si from APTMS, S and S1 are indicative of the amount of surfactant added in the samples, with S corresponding to 0.83 wt% of CTAB and S1 to 4.0 wt%. For the composites with CNTs, the designations xMyA_CNT_S or xMyA_CNT_S1 are used.

Table 3.2: Chemical systems nomenclature, silica precursors proportion, quantities of CTAB and CNTs used, as well as gelation time and linear shrinkage (diameter) observed for each sample.

Samples	CNTs (wt%)	CTAB (g)	MTMS (% mol of Si)	APTMS (% mol of Si)	Gelation time (min)	Linear Shrinkage (%)
100M_S	-	0.25	100	0	11	2.8 ± 0.2
100M_CNT_S	0.03	0.25	100	0	10	1.9 ± 0.4
90M10A_S	-	0.25	90	10	3	0.8 ± 0.2
90M10A_CNT_S	0.03	0.25	90	10	2	0.6 ± 0.2
80M20A_S	-	0.25	80	20	3	8.2 ± 1.0
80M20A_CNT_S	0.03	0.25	80	20	2	14.4 ± 1.8
100M_S1	-	1.25	100	0	12	6.1 ± 0.3
100M_CNT_S1	0.03	1.25	100	0	11	6.3 ± 0.4
90M10A_S1	-	1.25	90	10	4	1.5 ± 0.2
90M10A_CNT_S1	0.03	1.25	90	10	3	1.1 ± 0.4
80M20A_S1	-	1.25	80	20	5	[a]
80M20A_CNT_S1	0.03	1.25	80	20	4	[a]

(a) Fractured samples.

The synthesis was carried out with CTAB, added onto the solvent mixture, along with MTMS. The acid catalyst was then added to promote the hydrolysis reaction. After five minutes, APTMS was added, followed by the ammonium hydroxide solution to increase the pH, favoring the condensation/polycondensation reactions. The process was carried out under thermal control, at 27 °C, until complete addition of the basic catalyst. Gelation of all samples occurred within twelve minutes. In order to improve cohesion of the solid three-dimensional network, a subsequent step of aging was carried out by keeping the samples at 27 °C for seven days. During this period, further condensation reactions, syneresis and coarsening processes took place. CTAB removal was carried out by diffusional ethanol washing, performing eight changes, whilst the samples were kept in an oven at 60 °C. Finally, the obtained materials were dried at 60 °C for three days and then at 100 °C for three hours.

The CNTs-silica aerogel composites were prepared as previously described for the silica

aerogels, with the difference of adding the CNTs (0.03 wt% of the gel) to the solvent mixture with CTAB and submitting it to 30 minutes of sonication before MTMS addition.

3.2.4 Characterization

Carbon nanotubes characterization

Possible changes on the morphology of the carbon nanotubes during the surface functionalization step and the elemental composition of the modified carbon nanotubes were assessed using scanning transmission electron microscopy with energy-dispersive X-ray spectroscopy (TEM-EDX; *STEM Hitachi 2700, EDS detector Bruker*), operated at 200 kV. The dried powders were dispersed in ethanol P.A. and a drop of such suspension was placed on top of a continuous conductive carbon thin film copper grid, left to dry in air.

Fourier-Transform (FT) Raman spectra were acquired (*Horiba Jobin-Yvon LabRAM HR-UV 800, micro-FTRaman* spectrometer) using a laser excitation of 442 nm. The measurements were performed in the wavenumber range from 100 to 3000 cm^{-1}, exposure time of 20 seconds and up to 10 accumulations. From the Raman spectra the positions of D and G bands were obtained, as well as the I_D/I_G ratio.

Fourier Transform Infrared (FTIR) transmission spectroscopy (*Jasco FTIR 4200*) was used in order to confirm if the chemical surface modification of the carbon nanotubes was successful. Spectra were collected using the potassium bromide (KBr) pellet method, the pellets being prepared with 78–80 mg of KBr and ∼0.1 mg of each CNT, CNTs-HNO$_3$ and CNTs-TMOS samples. A total of 256 scans were recorded from 4000 to 400 cm^{-1} with a resolution of 4 cm^{-1}.

In order to obtain the hydrodynamic size distribution of MWCNTs, dynamic light scattering (DLS) measurements were performed. The carbon nanotubes were dispersed in ultrapure water with CTAB and sonicated for 30 min before the analysis. To assess the dispersion status of CNTs in the sol, zeta potential technique was applied. Zeta potential measurement was carried out in the solution containing MTMS, solvent mixture (EtOH/H$_2$O), surfactant, acid catalyst and CNTs-TMOS. DLS and zeta potential measurements were performed, at 25 °C, on a *Malvern Instruments Zetasizer Nano-ZS (Malvern Instruments Ltd.)*. The average hydrodynamic diameter and zeta potential were evaluated with *Zetasizer 7.11* software.

Chemical characterization of the aerogels

Fourier Transform Infrared (FTIR) transmission spectroscopy (*Jasco FTIR 4200*) was used to provide information on the chemical groups present in the aerogels structure.

Spectra were collected using the potassium bromide (KBr) pellet method, the pellets being prepared with 78-80 mg of KBr and 0.2–0.3 mg of each aerogel. Fourier-Transform (FT) Raman spectra were also acquired (*Horiba Jobin-Yvon LabRAM HR-UV 800, micro-FTRaman* spectrometer). The applied operating conditions for both techniques were the same as described in the previous section.

The crystalline structure of the samples was assessed using powder X-ray diffraction (XRD - *Philips X'PERT-PRO* Diffractometer system), by collecting information from 2-70° (2θ), with a step size of 0.02°, at room temperature, and operated at 40 kV/50 mA.

The hydrophobicity of the aerogel monoliths was obtained via contact angle measurement (*OCA 20, Dataphysics*), using the sessile drop technique with high purity water as test liquid.

Microstructural characterization of the aerogels

Linear shrinkage was calculated using the diameter of the samples before (d_0) and after drying (d), as described by Equation (3.1).

$$\text{Linear shrinkage (\%)} = \frac{d - d_0}{d_0} \times 100 \tag{3.1}$$

Bulk density (ρ_b) was assessed by measuring/weighing regular parts of the monolithic aerogels/composites. Helium pycnometry (*Accupyc 1330, Micromeritics*) was used to evaluate the aerogel skeletal density (ρ_s). The determination of the samples porosity used both the bulk and skeletal densities, according to Equation (3.2).

$$\text{Porosity (\%)} = \left(1 - \frac{\rho_b}{\rho_s}\right) \times 100 \tag{3.2}$$

The specific surface area (S_{BET}) was determined by nitrogen gas adsorption at 77 K (*Gemini V2.00, Micromeritics Instrument Corp.*), applying the BET theory in the relative pressure interval 0.05–0.25 of the adsorption isotherm. The Barrett–Johner–Halendar (BJH) theory was used for pore volumes, pore size distribution and average pore size determination, but limited to the size range of 1.7 nm to 300 nm. Overall size range pore volume (V_P) and average pore size were also estimated using Equations (3.3) and (3.4), usually applied to aerogels exhibiting a highly constrained network [252].

$$V_P \text{ (cm}^3\text{.g}^{-1}) = \frac{1}{\rho_b} - \frac{1}{\rho_s} \tag{3.3}$$

$$\text{Average pore diameter (nm)} = \frac{4(V_{\mathrm{P}})}{S_{\mathrm{BET}}} \tag{3.4}$$

Morphology and microstructure of the silica aerogels and corresponding composites were assessed using scanning electron microscopy (SEM; *Hitachi, SU-70*), operated at 15 kV, and scanning/transmission electron microscopy (STEM; *STEM Hitachi 2700* and *TEM JEOL, 2200FS*), operated at 200 kV. Silica aerogel-based materials are electron beam sensitive and, consequently, demand a careful sample preparation procedure. For SEM, the powders were dropped directly onto a double-sided carbon tape, and the excess of material was removed under gentile nitrogen gas flow; then, a carbon thin film was deposited on top of the specimens using a carbon rod coater (*Emitech K950X*). For TEM, samples were dispersed in ultra-pure water, manually shaken, and a drop of this suspension was then placed on a copper grid containing a continuous conductive carbon thin film, and left to dry in air prior to analysis.

Thermo-mechanical characterization of the aerogels

Thermal properties of the samples were determined by a Simultaneous Differential Scanning Calorimeter, combining thermogravimetry analysis and differential scanning calorimetry (TGA/DSC) (*SDT Q500, TA Instruments*). The samples were placed inside an alumina crucible and heated from room temperature up to 1200 °C, at a constant rate of 10 °C.min^{-1}, under a nitrogen flow. Thermal conductivity was assessed by the transient plane source technique, at 20 °C (*Thermal Constants Analyzer TPS 2500S, Hot Disk*).

For mechanical evaluation, simple uniaxial compression tests on samples with approximately 15 x 15 x 10 mm^3 were performed using a load cell of 3 kN, at a rate of 0.5 mm.min^{-1} [253, 254], until sample break or equipment limit (*Inspekt mini* equipment, *Hegewald & Peschke*). Also, uniaxial compression-decompression tests were run using a load cell of 50 N, from a strain of 0% to 20% at a rate of 0.5 mm.min^{-1} [253], and then back to 0% by removing the load at the same speed.

3.3   Results and discussion

3.3.1   Characterization of Carbon Nanotubes

The purpose of treating the MWCNTs with acids is to generate active groups on the nanotubes' surface. Although the oxidation treatments with the mixture of concentrated sulphuric and nitric acids (Samples 1 and 2 - Table 3.1) were effective, and functional

groups, such as carboxylic (-COOH), hydroxyl (-OH) and carbonyl (-C=O), were formed on the surface of MWCNTs, both approaches were very aggressive, causing the breaking of the CNTs into smaller ones, as showed in Figure 3.2. In fact, it is observed that CNTs present much shorter lengths than the initial ones (average length of 1.5 μm). As one of the goals is to improve the mechanical properties of the composite materials, these CNTs are not appropriate and other approaches were tested.
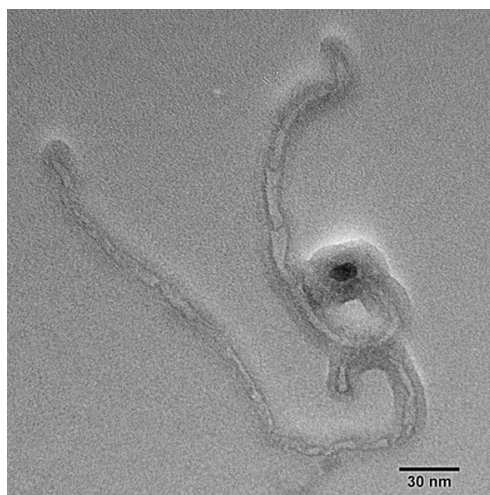
Figure 3.2: TEM image of MWCNTs treated with a mixture of concentrated sulfuric and nitric acids.

The next step was to test modifications with different acids, particularly peracetic acid, nitric acid and a mixture of nitric acid and hydrogen peroxide, to try to avoid the MWCNTs breaking. To establish if the modifications were effective, Raman analyses were performed, as shown in Figure 3.3.

As observed in the Raman spectra, in the region of 1000–2000 cm^{-1}, the characteristic bands of MWCNTs, namely the D band at around 1360 cm^{-1} and the G band near 1570 cm^{-1}, are identified. The G band arises from the vibrational mode E$_{2g}$ in the symmetry group D$_{6h}^4$ of the crystal planes of graphite and is found in all sp^2 carbons. On the other hand, the D band occurs due to reduced symmetry or near crystalline ends, meaning that the D band is induced by defects. All kinds of graphitic materials also exhibit a strong Raman band appearing in the range 2500–2800 cm^{-1} and this characteristic band corresponds to the overtone of the D band (G'). The band at about 2950 cm^{-1} is associated with a D + G combination mode and also is induced by disorder [255–258].
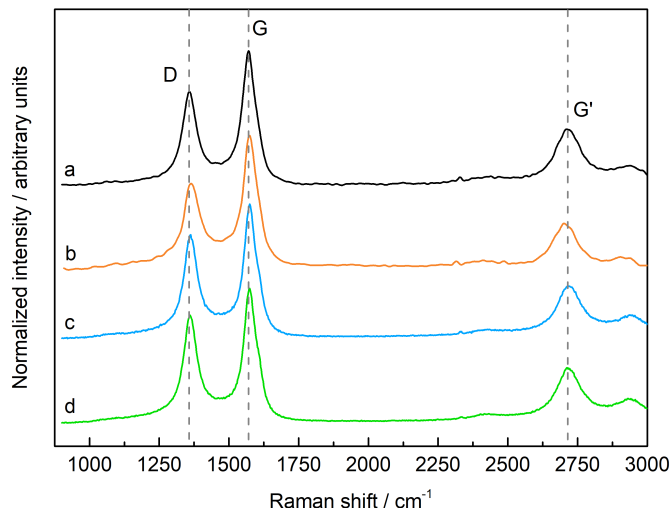
Figure 3.3: Raman spectra of a) pristine commercial MWCNTs and MWCNTs submitted to different treatments: b) stirred in CH_3CO_3H (sample 3, Table 3.1), c) mixture of HNO_3 and H_2O_2 in the ultrasounds (sample 4, Table 3.1) and d) refluxed in HNO_3 at 50 °C (sample 5, Table 3.1).

The intensity ratio of D and G bands (I_D/I_G) is a way to estimate the proportion of amorphous/disordered carbon (sp^3) relative to graphitic carbon (sp^2), so an increase in the I_D/I_G means a higher amount of sp^3 carbons. Alterations in this ratio usually indicate the presence of new defects in the MWCNTs, along with changes in the carbon nanotubes geometry that are caused by the introduction of new functional groups [259–261]. This ratio has been calculated for these different samples from the Raman data, and the values are listed in Table 3.3, as well as the positions of the main identified bands.

Table 3.3: Raman spectral positions and I_D/I_G intensity ratios for the commercial MWCNTs without treatment and modified MWCNTs (Samples 3, 4 and 5, Table 3.1).

Samples	Position of D band (cm^{-1})	Position of G band (cm^{-1})	Position of G' band (cm^{-1})	I_D/I_G
Without treatment	1358.0	1570.8	2715.0	0.68
03	1360.4	1576.2	2720.2	0.72
04	1362.7	1575.9	2720.1	0.71
05	1361.1	1575.7	2716.8	0.77

From Figure 3.3 and Table 3.3, it is possible to observe that the D and G bands shifted to higher wavenumbers (around 3 and 5 cm^{-1}, respectively), if compared with the same bands for the commercial MWCNTs without modification. This upshift could be induced by the insertion of chemical groups, which can be interpreted as defects on the nanotubes structure [261, 262].

By comparing the I_D/I_G values of commercial MWCNTs without any treatment and the ones submitted to acidic treatments an increase is observed. These variations indicate that

the three processes lead to an increment in the amount of defects in the carbon nanotubes as well as changes in the MWCNTs geometry due to the binding of new functional groups [262, 263]. The most substantial changes were achieved by the reflux with nitric acid, while the amount of defects created by the other two treatments was not high enough to produce a significant alteration in the I_D/I_G ratio.

As the most significant changes were obtained for Sample 5, transmission electron microscopy was performed for these CNTs, Figure 3.4. This technique allowed the confirmation that, besides inserting defects in the CNTs as indicated by Raman spectroscopy, the treatment with nitric acid was also effective in removing the impurities present in the commercial MWCNTs (Figure 3.1), since none dark contrast spot was observed in the images. Contrary to the treatment with strong acids (mixture of concentrated sulfuric and nitric acids), this chemical attack was able to purify the carbon nanotubes without damaging the CNTs lengths, as observed in the lower magnification image (Figure 3.4), which can enable the mechanical reinforcement of the silica aerogel composites.
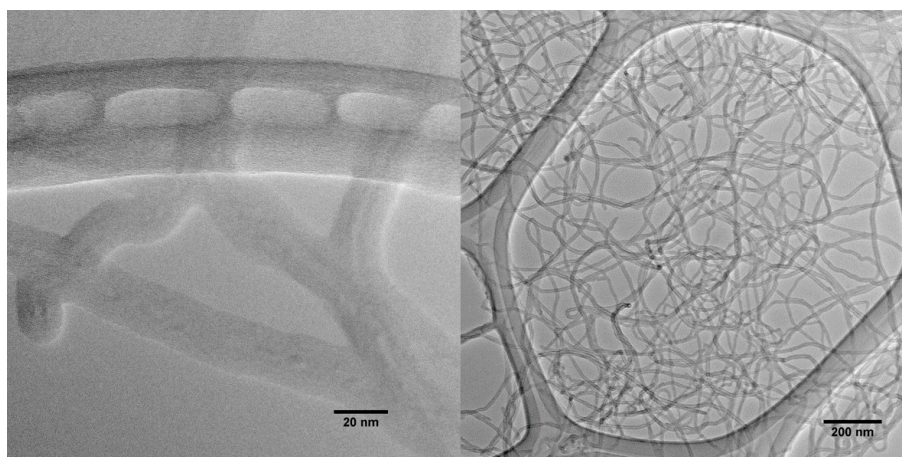
Figure 3.4: TEM images of MWCNTs treated under reflux with concentrated nitric acid at 50 °C for 20 h.

At the same time that these acid treatments were performed, alternative modifications with two types of plasma (NH_3 and O_2) were also tested (Table 3.1 - Samples 06 to 16). The objective of these plasma treatments was to reduce the time needed to obtain modified MWCNTs. Different powers, times and volumetric flows were used to optimize the purification and modification of the nanotubes. However, plasma oxidation treatments have proved to be temporary [264–266], as confirmed by the results obtained by energy-dispersive X-Ray (EDX) displayed in Table 3.4 for the samples in which higher power and longer times were applied (Samples 6 and 14). It is possible to see that, even though some of the impurities were reduced in the carbon nanotubes, no significant

variation was observed in the amount of nitrogen and oxygen if compared with the pristine MWCNTs. As the modifications were only temporary, these carbon nanotubes are not suitable to be used in the development of carbon nanostructure-silica aerogel composites.

Table 3.4: Chemical analysis of the energy-dispersive X-Ray (EDX) spectra.

Element	Pristine MWCNTs (Atomic Percent)	Sample 06 (Atomic Percent)	Sample 14 (Atomic Percent)
Carbon	93.58 ± 1.69	95.04 ± 0.37	92.7 ± 1.36
Nitrogen	2.40 ± 0.25	2.24 ± 0.23	2.37 ± 0.29
Oxygen	3.11 ± 1.65	1.87 ± 0.08	3.99 ± 1.26
Sodium	0.04 ± 0.02	0.01 ± 0.01	0.01 ± 0.01
Aluminium	0.81 ± 0.16	0.81 ± 0.12	0.91 ± 0.26
Iron	0.06 ± 0.03	0.03 ± 0.03	0.02 ± 0.01

So, even though the procedures using nitric acid require more time to be performed, it was the method that showed better results so far. Thus, these modified carbon nanotubes (CNTs-HNO$_3$) were used as base to subsequent modifications, in order to improve even further the interaction between the carbon structure and the silica matrix. As H$_2$O$_2$ is a relatively mild oxidant and can be used under neutral conditions [267], it was chosen to be applied in the second step of the MWCNTs modifications to increment the amount of functional groups in these nanostructures (Table 3.1 - Samples 17 to 19). The second methodology was the modification of these carbon nanostructures with TMOS (Table 3.1 - Samples 20 to 22), as a silane can help enhance their dispersion and their interfacial strength with the silica network [245]. All these six modifications were tested in MWCNTs-silica aerogel composites, and, among these, Sample 22 showed the best results regarding the dispersion in the solvent mixture used during the synthesis and the interaction with the silica matrix. Therefore, the carbon nanotubes modified with HNO$_3$ in the first step, and with TMOS (10% v/v) in a solvent solution of 70% EtOH:30% H$_2$O, in the second part (CNTs-TMOS), were the ones used for the development of the carbon nanotubes-silica aerogel composites. The characterization of these MWCNTs will be described in the sequence.

From DLS measurements, for the pristine CNTs, an average hydrodynamic size of 238.9 ± 28.5 nm was obtained. After the oxidation treatment (CNTs-HNO$_3$), the hydrodynamic diameter did not change significantly, with a value of 229.8 ± 13.5 nm. However, after the silanization process (CNTs-TMOS), a value of 270.1 ± 5.03 nm was recorded. This increase is certainly due to the surface modification performed in the carbon nanotubes, since the silica layer grows attached to the CNTs surface which leads

to a higher overall diameter.

Infrared spectroscopy measurements were also performed for the carbon nanomaterials, as seen in Figure 3.5a. For the commercial CNTs, one band attributed to O–H groups was observed at 3430 cm^{-1}. In this spectrum, bands regarding the stretching vibration of C–H groups also appeared between 2960 and 2860 cm^{-1}, as well as that corresponding to the stretching of C=C groups of the backbone of the carbon nanotubes, at 1560, 1350 and between 1000 and 500 cm^{-1} [268–271]. For the CNTs-HNO$_3$, the same vibrational bands regarding the stretching of C–H groups between 2960 and 2860 cm^{-1} were seen [268, 269, 271]. Different bands regarding the carboxylic groups were also observed in this spectrum, one around 1750 cm^{-1} that corresponds to the stretching vibration of the C=O bond [272], another for the CNT–COOH, H bonded (1630 cm^{-1}) [271, 273] and a third band associated to the stretching vibration of the C–O bond (1040 cm^{-1}) [271, 274]. After performing treatment with TMOS on the CNTs-HNO$_3$, several silica related bands appeared in the spectrum. The bands at *ca.* 1200 and 1090 cm^{-1} are associated with the longitudinal and transversal-optical components of the asymmetric stretching vibration of Si–O–Si bonds, respectively [275]. Absorption bands regarding the stretching vibration of the Si–O group were also observed at 960, 800 and around 560 cm^{-1}. The presence of these bands strongly indicates that the silanization of the carbon nanotubes takes place.

Transmission electron microscopy was performed in order to confirm the presence of silica around the carbon nanotubes. From the obtained image in Figure 3.5b, it was possible to see a condensate around CNTs. Nevertheless, one could say that the surrounding layer on the CNTs can be due to an easily condensate layer of amorphous carbon. Therefore, energy-dispersive X-ray spectroscopy was performed, confirming, indeed, the silica modification on the CNTs, as seen on the EDX spectrum shown in Figure 3.5c. Finally, zeta potential provided data regarding the dispersion of the carbon nanomaterials in the silica sol. The obtained value was 60.1 $\pm$ 6.0 mV, indicating an excellent dispersion of the CNTs-TMOS in the silica solution just before gelation.
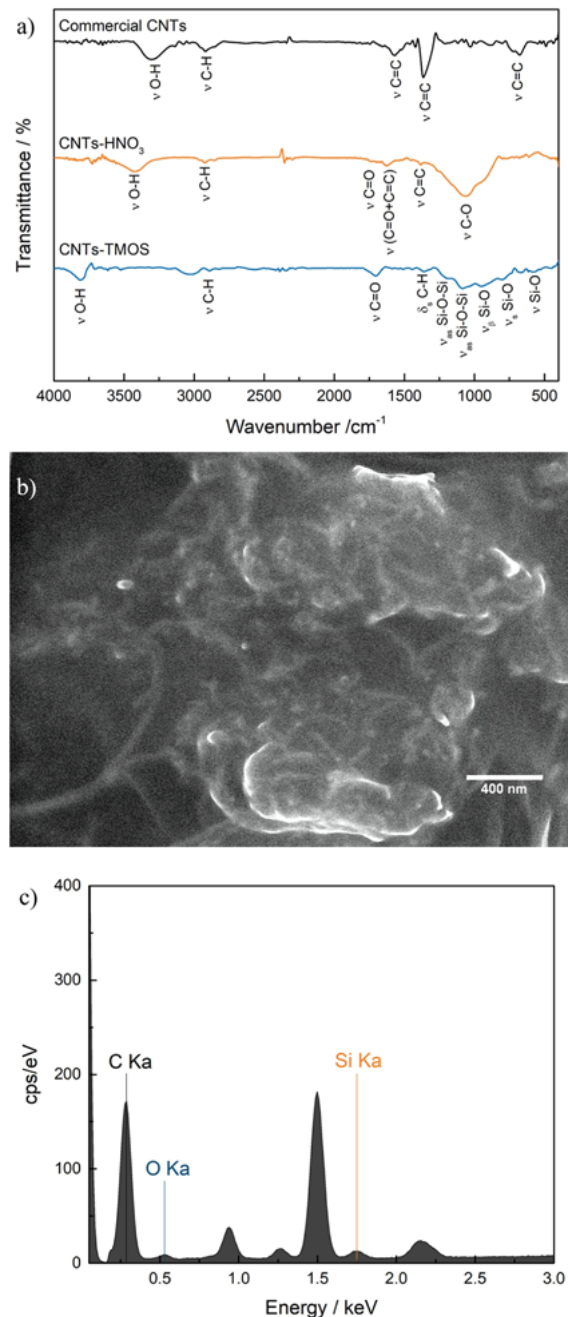
Figure 3.5: Characterization of carbon nanotubes. a) FTIR spectra, b) TEM image of CNTs-TMOS and c) EDX analysis of CNTs-TMOS. υ – stretching vibration; υ_s – symmetric stretching vibration; υ_{as} – asymmetric stretching vibration; υ_β – in-plane stretching vibration; δ – deformation vibration; δ_s – symmetric deformation vibration (bending); δ_{as} – asymmetric deformation vibration (bending).

3.3.2 Aerogels selection based on experimental observations: effect of amine group and surfactant amounts

As observed in Table 3.2, APTMS addition causes a significant reduction of the gelation time, due to the basic properties of amine functional groups [276]. One would expect that increasing the APTMS proportion in the system, it would even further reduce the gelation time. However, the opposite was observed for the tested amounts, and this is in agreement with the work reported by Hüsing *et al.* [276], when using an organo(trialkoxy)silane with

an organic group containing a strong basic substituent. This probably occurs due to two opposite effects caused by higher concentration of APTMS. First, the amine groups act as a basic catalyst, favoring gelation, thus decreasing the gelation time. Secondly, the increase of amine groups also leads to more hydrogen-bond acceptors, resulting in less free network-forming units (silanols), which increases the gelation time. The steric hindrance caused by the aminopropyl group also contributes to this tendency [276].

The presence of CNTs in the solution acted as good surface sites for gel growth and appears to have accelerated the solid structure formation [94], possibly playing a role of structuring agent in the gel formation. CTAB also influences the time required to obtain a cohesive gel, since, when used in lower quantities, it allows the decrease of phase separation, resulting in a faster condensation rate. On the other hand, if used in a higher amount, the surfactant causes steric hindrance and affects the network formation [249], slightly increasing the gelation time.

Figure 3.6 gives a complete set of macroscopic views of the silica aerogels and corresponding CNTs-silica aerogel composites prepared with different proportions of precursors and surfactant (according to Table 3.2).
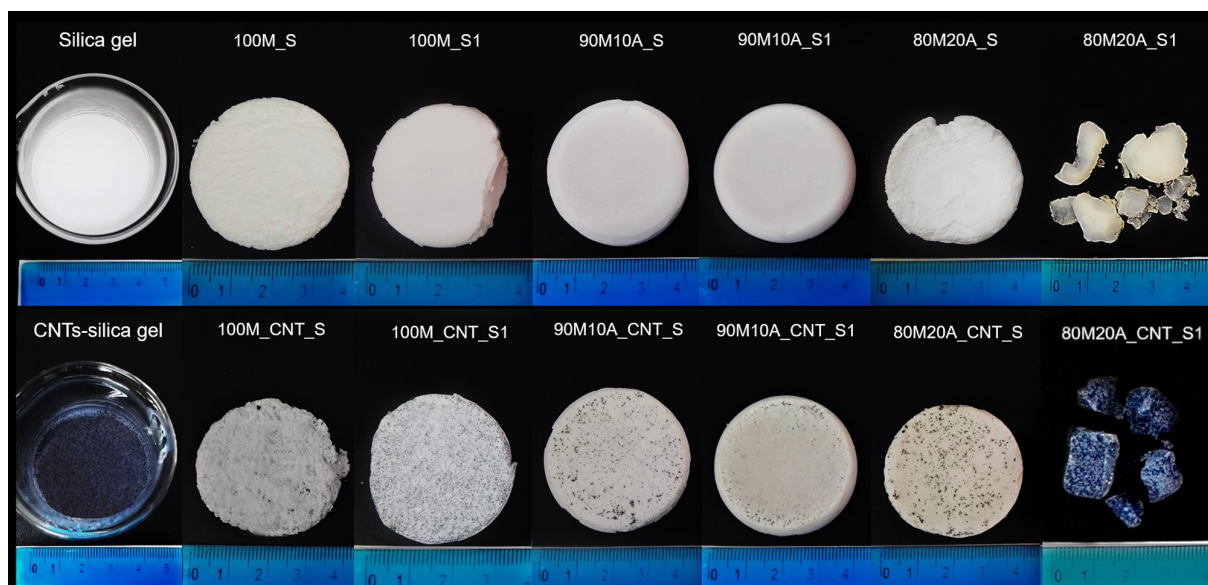
Figure 3.6: Macro-photographs of silica and CNTs-silica gels with 100% of MTMS and 4.0 wt% of CTAB, silica aerogels and CNTs-silica aerogel composites with different proportions of precursors and surfactant.

A large shrinkage was observed for the samples with 20% of Si content from APTMS (Table 3.2), and it was not possible to obtain monoliths of this silica system in the presence of 4.0 wt% of CTAB (Figure 3.6). Therefore, their characterization is mainly presented as supporting information. Nevertheless, data obtained for the samples 80M20A will be addressed hereafter whenever it enables a better understanding of the results discussed in the main text.

Regarding the samples' linear shrinkage (Table 3.2), the 90% MTMS/10% APTMS aerogels (Figure 3.6) present the lowest value for both quantities of surfactant. Since shrinkage is related to the gel network stability [276], it is concluded that the systems developed with 10% of APTMS appear to have a more cohesive silica network than the other materials. Even though higher concentrations of APTMS might yield more sites for reaction, the excess of amine groups in the solution can result in steric interferences during gelation producing a weaker silica skeleton [277], leading to larger shrinkage of the gel during the aging and drying steps. A larger amount of CTAB (4.0 wt%) in the system also interfered with the silica network formation, causing a low level of cross-linking among the secondary particles [249], consequently leading to higher shrinkage in the drying stage (Table 3.2).

The presence of higher amounts of APTMS in the system, associated with an excess of surfactant, may justify the 80M20A samples shatter. Again, it is likely that a synergistic effect between the increase of amine groups and CTAB in the system results in higher steric hindrance during gelation, causing a higher interference in the network formation [249, 277]. The association of higher quantities of these two compounds results in weaker silica networks, inducing the structure collapse during the drying step.

3.3.3 Chemical characterization of the obtained aerogels and composites

To assess the chemical structure of the prepared materials, FTIR spectra of the samples were collected and shown in Figure 3.7, and the characteristics vibrational frequencies (cm^{-1}) are reported in Tables A1 and A2.
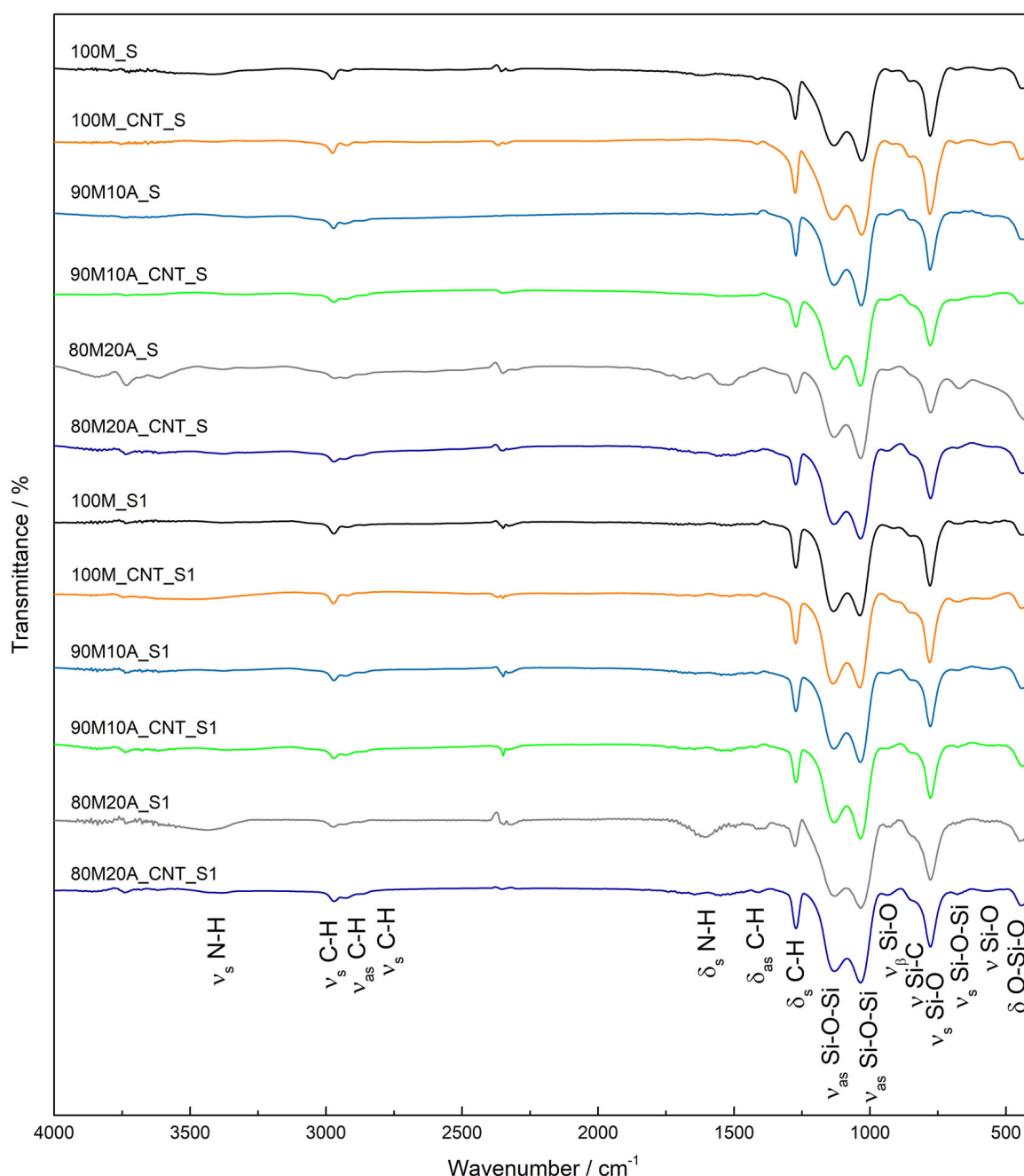
Figure 3.7: FTIR spectra of silica aerogels and corresponding CNTs-silica aerogel composites. υ – stretching vibration; υ_s – symmetric stretching vibration; υ_{as} – asymmetric stretching vibration; υ_β – in-plane stretching vibration; δ – deformation vibration; δ_s – symmetric deformation vibration (bending); δ_{as} – asymmetric deformation vibration (bending).

Overall, the obtained spectra are very similar, and in the samples containing APTMS, the presence of the band corresponding to the group –NH_2 is clearly observed. The bands at *ca.* 1140 and 1040 cm^{-1} are associated to the longitudinal and transversal-optical components of the asymmetric stretching vibration of Si-O-Si, respectively. The Si-C stretching vibration from the methyl group of MTMS appears around 835 cm^{-1}. The symmetric stretching vibrations of the Si-O-Si bonds are observed near 760 cm^{-1}. The band near 400 cm^{-1} corresponds to the deformation vibrations of O-Si-O bonds [275].

Thus, the presence of such bonds between silicon and oxygen indicates that the precursors have efficiently originated a silica network.

FT-Raman spectra for the silica aerogels and corresponding CNTs-silica aerogel composites are presented in Figures 3.8a and 3.8d. Analysis of these spectra allowed a better understanding regarding the structure of the obtained aerogels. Usually, in the typical region of SiO-networks (wavenumbers lower than 1200 cm^{-1}), two defect bands of silica are observed. These bands are D_1 ($\sim$490 cm^{-1} for fused silica and $\sim$475 cm^{-1} for silica aerogel [278]) and D_2 ($\sim$600 cm^{-1}), assigned to eight-membered rings (4-SiO) and to planar six-membered rings (3-SiO), respectively [279–283]. For all the materials, only a band near 475 cm^{-1} is observed, indicating that the eight membered rings are predominant [278] and also that the presence of the carbon nanomaterial does not affect the formation of the silica network at primary particles scale.

Another characteristic silica band is observed at 790 cm^{-1}, referent to the symmetric mode of the Si-O-Si vibration [284]. For wavenumbers superior to 1200 cm^{-1} only bands related to the $-$CH groups from the modified silica network are identified, assigned to the CH_3 asymmetric deformation (around 1420 cm^{-1}), and CH_3 asymmetric and symmetric stretching (at 2916 cm^{-1} and 2979 cm^{-1}, respectively) [284, 285]. For the samples containing APTMS, a small shoulder around 2885 cm^{-1}, corresponding to CH_2 asymmetric stretching, was observed. In the CNTs-silica aerogel composites, two bands, D and G related to the carbon nanotubes are observed, confirming the formation of the aerogel composite. The first band is the D band centered around 1350 cm^{-1}, associated to the distortion caused in the carbon structure by sp^2 hybridization. The second one is the G vibration around 1560 cm^{-1}, which arises from the doubly degenerate phonon mode (E_{2g} symmetry) and Raman active for sp^2 carbon networks [255, 256, 286, 287].
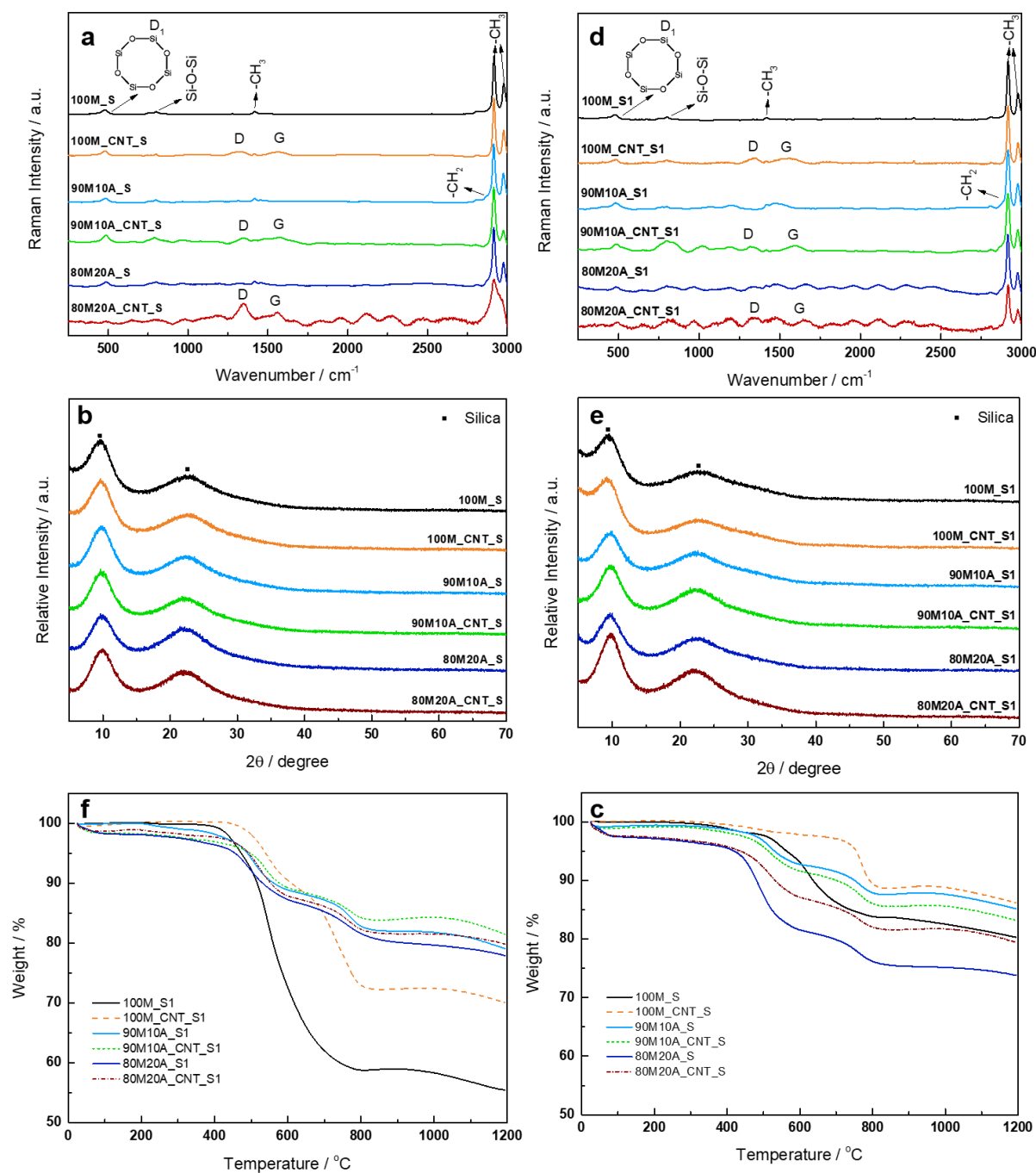
Figure 3.8: Chemical and thermal characterizations of silica aerogels and corresponding CNTs-silica aerogel composites. Samples with 0.83 wt% g of CTAB: a) Raman spectra, b) Powder X-ray diffraction patterns and c) Thermogravimetric curves. Samples with 4.0 wt% of CTAB: d) Raman spectra, e) Powder X-ray diffraction patterns and f) Thermogravimetric curves.

Figures 3.8b and 3.8e shows the powder XRD patterns obtained for the synthesized aerogels and corresponding CNTs composites. For all the samples, two broad diffraction bands are observed around 9° and 22° (2θ), characteristic of silica materials with very low crystallinity, which is in agreement with previous results obtained for similar aerogels [246, 288, 289]. The band at lower angle, around 9° (2θ), is usually attributed to the d-spacing between silicon atoms linked to alkyl groups (methyl or propyl), possibly indicating alkyl group channels in the structure. In the presence of APTMS, this reflection appears

with higher relative intensity, due to the length of the alkyl groups. Thus, this might be an indication that the propyl group channels are probably contributing to the material structure more than those formed by methyl groups [246, 288]. The second band around $22°$ (2θ) is related to the spacing between Si atoms and the angle of the group Si-O-Si [246, 288]. Comparing these results to those from previous works, it appears that APTMS might induce a higher degree of crystallinity in the obtained materials since the silica network diffraction appears slightly more intense and less broad in this case. Moreover, CNTs corresponding bands in the composite patterns are not detected, since their main reflection around $25°$ (2θ) is overlapped by that of the silica network and the remaining bands are not observable possibly due to the low content of carbon nanomaterial in the composites. Finally, the characteristic crystalline peaks of CTAB (Figure 3.9) are not observed at any point of the diffractograms of Figures 3.8b and 3.8e, confirming an efficient surfactant removal during the washing step.
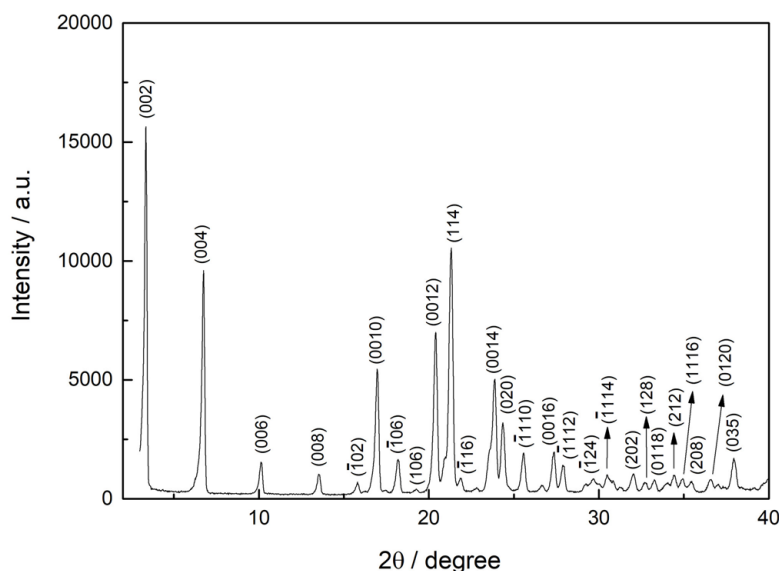
Figure 3.9: Powder X-ray diffraction pattern of the surfactant cetyl trimethylammonium bromide (CTAB).

Wetting properties of the aerogels and corresponding CNTs-silica aerogel composites were determined by contact angle measurements between a drop of ultra-pure water and the sample, as seen in Figure 3.10. The samples show a super-hydrophobic character, with contact angles between 150° and 180° [290], independently of the adopted synthesis conditions. These results are consistent with the predominant structure-builder precursor, *i.e.* MTMS, since the $-CH_3$ groups of MTMS remain oriented towards the surface, during condensation, conferring hydrophobic properties to the material. In the composites, it appears that the presence of the carbon nanotubes enhanced the hydrophobic behavior of the samples. The aerogels synthesized with larger amounts of

CTAB (4.0 wt%) present slightly higher contact angles, probably due to different roughness profiles at their surface, as superhydrophobicity is usually enhanced by surface roughness at the micro- and nanoscale [291].
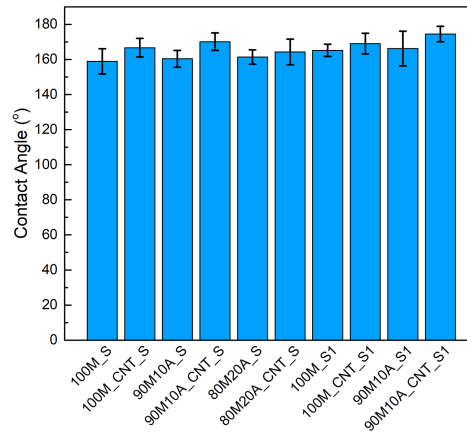
Figure 3.10: Contact angles of silica aerogels and CNTs-silica aerogel composites.

3.3.4 Microstructural characterization of the obtained aerogels and composites

Table 3.5 summarizes the physical and microstructural properties evaluated for silica aerogels and corresponding CNTs-silica aerogel composites.

Table 3.5: Summary of physical and microstructural properties of the synthesized silica aerogels and CNTs-silica aerogel composites.

Samples	Bulk density	Skeletal density	Porosity	Pore volume[a]	Specific surface area	Average pore size[b]
	$(kg.m^{-3})$	$(kg.m^{-3})$	(%)	$(cm^3.g^{-1})$	$(m^2.g^{-1})$	(nm)
100M_S	75.6 ± 2.8	1457.6 ± 49.1	94.8 ± 0.1	12.5 ± 0.5 (0.13)	444.6 ± 4.3	112.9 ± 3.4 (2.6)
100M_CNT_S	61.3 ± 5.3	1462.5 ± 44.1	95.8 ± 0.2	15.6 ± 1.4 (0.14)	463.4 ± 4.5	134.9 ± 10.1 (2.7)
90M10A_S	79.3 ± 11.1	1458.8 ± 17.8	94.6 ± 0.7	11.9 ± 1.8 (0.01)	11.3 ± 0.2	4220.6 ± 546.2 (5.8)
90M10A_CNT_S	76.2 ± 5.6	1571.8 ± 20.5	95.1 ± 0.3	12.5 ± 1.0 (0.02)	18.4 ± 0.3	2713.5 ± 179.8 (5.4)
80M20A_S	76.0 ± 8.2	1468.6 ± 79.9	94.8 ± 0.3	12.5 ± 1.3 (0.14)	97.4 ± 2.4	512.3 ± 42.7 (6.7)
80M20A_CNT_S	75.3 ± 10.3	1650.0 ± 46.4	95.4 ± 0.5	12.7 ± 1.8 (0.05)	45.2 ± 1.2	1121.6 ± 126.1 (6.3)
100M_S1	75.3 ± 5.1	1610.2 ± 74.7	95.3 ± 0.1	12.6 ± 0.9 (0.40)	458.1 ± 2.2	110.5 ± 6.9 (6.6)
100M_CNT_S1	75.6 ± 8.3	1703.0 ± 85.7	95.6 ± 0.2	12.7 ± 1.4 (0.60)	492.4 ± 4.0	102.7 ± 10.3 (7.2)
90M10A_S1	80.9 ± 7.2	1478.9 ± 51.8	94.5 ± 0.3	11.7 ± 1.0 (0.10)	72.2 ± 1.3	647.4 ± 46.1 (6.8)
90M10A_CNT_S1	84.6 ± 5.1	1560.9 ± 78.2	94.6 ± 0.1	11.2 ± 0.7 (0.16)	118.2 ± 2.1	378.3 ± 15.6 (7.4)
80M20A_S1	381.7 ± 24.2	1378.9 ± 5.7	72.3 ± 1.6	1.9 ± 0.2 (0.50)	311.9 ± 7.7	24.3 ± 1.5 (6.4)
80M20A_CNT_S1	142.2 ± 0.5	1417.7 ± 27.5	89.9 ± 0.2	6.3 ± 0.1 (0.23)	245.6 ± 3.2	103.0 ± 0.8 (5.8)

[a] The values in the parenthesis are the pore volume obtained by BJH adsorption between 1.7 nm and 300 nm. [b] The values in the parenthesis are the average pore diameter obtained from N_2 adsorption isotherm.

The bulk densities for all the samples, except for those with 20% mol of Si from APTMS and 4.0 wt% of CTAB that collapsed during drying, are in good agreement with

those found by Durães *et al.* [54] for MTMS xerogels and aerogels prepared in the absence of CTAB. When APTMS is added to the system, a slight increase in the bulk densities is observed. This variation can be justified by the presence of the aminopropyl groups, larger when compared to the methyl groups of MTMS, that lead to a higher extent of condensation. Even though this increase was verified, most of the samples still present values below 85 kg.m^{-3}. The lowest density was observed for the 100M_CNT_S sample, with a bulk density of *ca.* 61 kg.m^{-3}. In general, these bulk densities are lower than those determined for CNTs-silica aerogel composites synthesized with different precursors, such as TEOS [63] and water glass [94, 205], but dried in similar conditions. Moreover, the bulk densities obtained in this study are similar to those measured by Piñero *et al.* [97] (dried TEOS-based composites under supercritical conditions), indicating the efficiency of the gel processing and drying methodology adopted in this work.

The skeletal densities of silica aerogels are, usually, in the range of 2000–2200 kg.m^{-3} [8, 276, 292]. However, for samples synthesized with only MTMS, the value was found to be 1900 kg.m^{-3} [80]. According to Hüsing and Schubert [276], organically modified silica presented lower values, with an average skeletal density of 1430 kg.m^{-3}. Thus, our results, with values below 1800 kg.m^{-3}, are very consistent with the expected ones, as seen in Table 3.5. The skeletal density of the composites is slightly higher when compared to those for the corresponding silica aerogels. The CNTs skeletal density, around 2100 kg.m^{-3} [293], possibly contributed to the increase of the overall skeletal density of the composites.

The aerogel porosity was obtained from the density values. Porosity can be related to the network shrinkage extent [36], and the obtained results agree with the samples' shrinkage, as the materials that show low shrinkage have high porosities. The majority of the samples presented values above 94.5%, which are very similar, or even higher, than the ones reported for MTMS-based aerogels dried under supercritical conditions [54, 251, 294, 295], as well as those for CNTs-silica aerogel composites in the literature [63, 204, 205, 296].

In this work, the samples' pore volume was determined by two methodologies, and a significant discrepancy was observed between the two final values, as seen in Table 3.5. The difference is due to the fact that the nitrogen adsorption-desorption method only measures a very restricted fraction of the total pore volume, taking into account pore sizes below 300 nm and only contemplating around 10% of the total pore volume [297, 298]. If the pore volume is determined using data from the BJH adsorption curves, there is a correlation between the pore volume and the surface area, showing that when the pore volume (only micro and mesopores) increases, the same trend is followed by the specific surface area. Generally, the pore volume determined by the BJH methodology increases

for a higher amount of CTAB (Table 3.5). The presence of CNTs also seems to promote a small increase in the volume of small pores. Nevertheless, a significant decrease in the micropore/mesopore volume (BJH) was verified when 10% of APTMS was added to the system, especially for the lower amount of surfactant. This trend is also confirmed by the low specific surface areas and much higher values of calculated average pore sizes (Table 3.5), which may be due to a higher extent of condensation and filling of these small pores. For the samples containing 20% of APTMS, as significant shrinkage during the drying step occurs, it is not possible to delineate a definitive conclusion regarding the pore volume obtained by BJH. When the pore volumes were determined using the bulk and skeletal densities (Equation (3.3)), the obtained values were, generally, very close. The proximity of the values can be justified by the lower sensitivity of this method to the micro and mesopore variations, since the fraction of macropores is much more significative than the others. However, an increase of the pore volume with the introduction of CNTs is noticed, which confirms the effect of CNTs also in the larger pores structure.

As seen in Table 3.5, the specific surface areas determined for the samples using only MTMS as silica precursor are in good agreement to those reported for MTMS aerogels synthesized in the presence of CTAB and dried by the supercritical method [251]. On the other hand, the specific surface areas are higher than those found in the literature for MTMS-based silica materials dried at ambient pressure [54, 299]. However, it should be noted that, in some situations, data may not be accurate due to the nitrogen adsorption technique limitations when evaluating this type of materials [300, 301], in particular when they have, to a certain point, a flexible structure.

Regarding the samples containing 10% of APTMS and prepared with 0.83 wt% of CTAB, their specific surface areas dramatically decrease when compared to those for aerogels synthesized without APTMS (Table 3.5) or generally expected for aerogels [8]. A possible explanation for this is that our samples present large secondary particle radii [276] and a significant quantity of macropores, as mentioned before and later confirmed by SEM images. With the same proportion of APTMS and when the amount of CTAB is increased to 4.0 wt%, the samples show specific surface areas quite higher than those prepared with less amount of surfactant. This indicates that the surfactant presence causes a meaningful rearrangement of the porous structure, suggesting a higher number of micro and mesopores in the samples, since a reduction in the calculated average pore size, combined with an increase in the specific surface area, was observed for all the samples. The CNTs composites presented higher surface areas than the corresponding aerogels. This is possibly due to stereological reasons, since the CNTs might provide points of nucleation for the silica network to evolve, modifying the aerogel microstructure

and/or morphology. However, the specific surface areas are lower when compared with other silica-carbon nanotubes systems obtained from orthosilicate and sodium silicate [94, 97, 298].

In general, duplicating the APTMS amount, the aerogels specific surface area increases (Table 3.5), probably due to the higher shrinkage in these samples, which narrows the pore size and increases the amount of micro- and mesopores in the aerogels. Additionally, when the amount of CTAB is also increased, the samples surface area also increases considerably. In the case of the corresponding CNTs composites (with higher amounts of APTMS and CTAB), the specific surface area does not increase so much, most likely due to the collapse of the structure.

Correlating the pore volume data with the specific surface area and bulk density data, it appears that the macroporous structure has a significant role and contribution to the high pore volume and low density, with consequent decreasing of the specific surface area, especially in the samples containing APTMS. Finally, regarding the average pore size (Table 3.5), the BJH method only considers pore size below 300 nm, which is an underestimation of the global average pore size. On the other hand, Equation (3.4) estimates the average pore size taking into account the overall pore size range. Therefore, electron microscopy can give a more accurate insight on the pore size as well as on the morphology of the silica network. Figure 3.11 shows SEM images of the synthesized aerogels and corresponding CNTs composites.

All the samples synthesized with 0.83 wt% of CTAB show spherical shaped secondary particles with a diameter around 1 μm, or slightly higher, with observable macroporosity and rough agglomerates, as illustrated in Figure 3.11. These large particles and pores were expected for these aerogels, especially for the ones containing amine groups, since under more basic conditions, silica growth is not restricted by cluster hydrolysis [276, 302]. During surfactant removal, the aging process continues to take place and silica becomes more soluble in basic alcoholic solutions, at elevated temperatures. This leads to re-dissolution of smaller particles and re-precipitation of silica at the surface of larger particles, with consequent decreasing of the specific surface area [303]. In the corresponding CNTs composites, it was not possible to observe the carbon nanotubes due to the large dimension of the silica particles and also because the silica network is formed around the carbon nanomaterials.

As Figure 3.11 demonstrates, it was possible to observe a significant difference in the microstructure of the samples containing higher quantities of CTAB. The higher amount of surfactant leads to a reduction of the size of the secondary particles and a more uniform porous network. In the aerogels synthesized with 100% MTMS, a microstructure

composed of very small structural units is observed (Figure 3.11). In contrast, the samples 90M10A_S1 and 90M10A_CNT_S1 (Figure 3.11) show slightly larger structural units. For the sample 80M20A_S1, it was observed an almost continuum of matter, composed of very large silica clusters. The significantly different morphology observed for this sample is probably due to the collapse of the silica network and the sample's high level of densification, which also reflects in the highest value of bulk density among the developed samples (Table 3.5). Some degree of shrinkage was also observed for the sample 80M20A_CNT_S1, however not so extensive as for the sample without the CNT, since it was still possible to identify the silica structural units and with the sample's density being less than half of the value of their silica counterpart. Structural units of approximately the same size of the samples with 10% of APTMS were observed for the 80M20A_CNT_S1 sample.
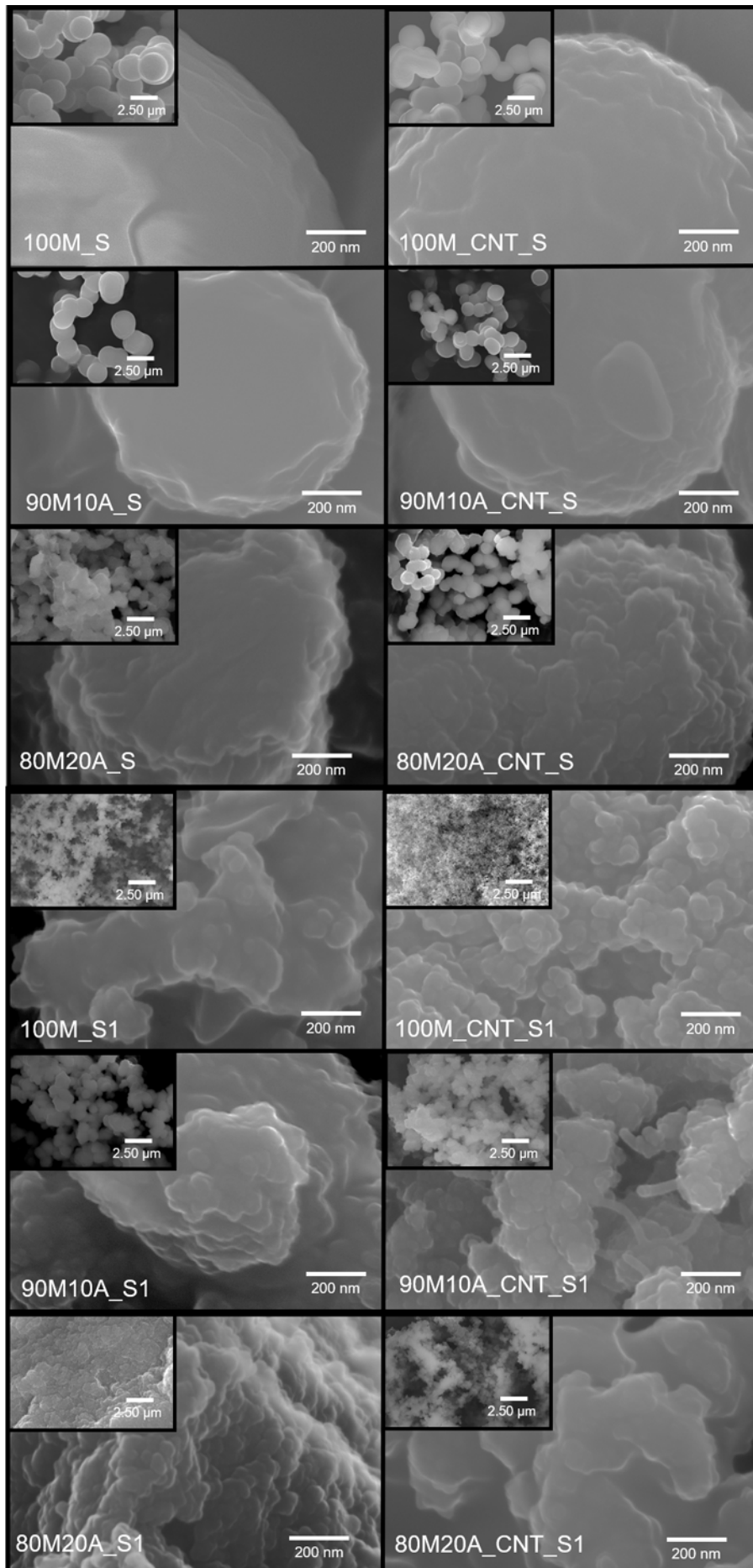
Figure 3.11: Low-magnification (inset) and higher-magnification SEM images of the prepared silica aerogels and corresponding CNTs-silica aerogel composites.

In the 90M10A_CNT_S1 sample, it was possible to confirm the presence of carbon nanotubes, linking silica clusters and/or emerging from within the silica network. Similar observations have been reported for different composites prepared with CNTs and distinct silica precursors [63, 94, 97]. As previously stated, it appears that the silanized carbon nanotubes act as a nucleating agent/site enabling the silica network to be formed around these nanomaterials. This has been confirmed by further TEM inspections, as Figure 3.12 illustrates.
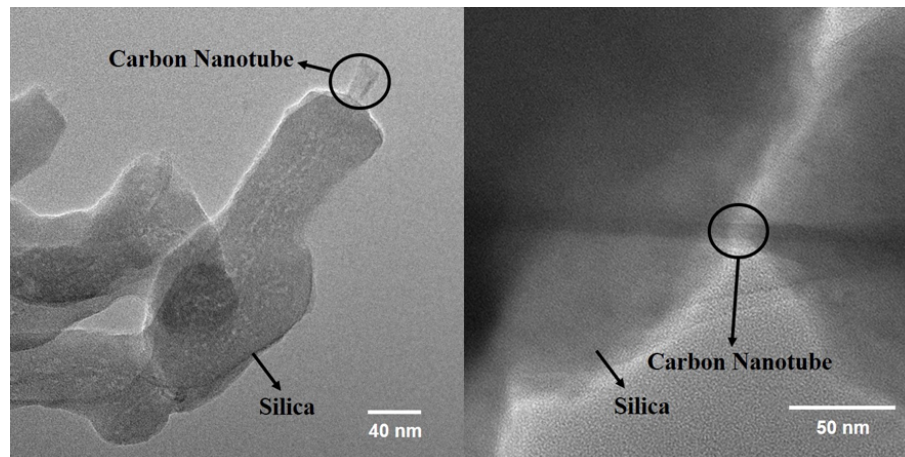
Figure 3.12: TEM images of CNTs-silica aerogel composite.

A distinctive silica structure surrounding the CNTs is observed, with the silica particles changing from spherical to more cylindrical and/or rod-like shapes following the elongated shape of the CNT. This orderly arrangement indicates that the chemical binding between the silica modified CNTs and the silica precursors takes place during the synthesis, leading to a cohesive composite network. Moreover, due to the superior mechanical properties of carbon nanotubes, this probably results in the reinforcement of the silica aerogels, avoiding cracking of the samples during their manufacturing and improving the poor mechanical properties normally observed in these silica materials. Consequently, the thermo-mechanical properties of the obtained materials were assessed and will be presented in the next section.

3.3.5 Thermo-mechanical properties of the obtained aerogels and composites

The thermal behavior of the materials was first evaluated using TGA. The obtained thermogravimetric curves are shown in Figures 3.10d and 3.10f, and the corresponding temperatures and weight losses for the observed thermal phenomena are indicated in Table A3. TGA results show that, up to 1200 °C, the higher mass loss occurs for the

samples with 100% MTMS and 4.0 wt% of CTAB, which is due to a more ramified network, with more Si–OH end groups. The thermograms obtained for the aerogels did not show a significant weight loss relative to CTAB degradation (near 200 °C), indicating an efficient surfactant removal during the washing procedure. The samples 90M10A_S1 and 90M10A_CNT_S1 showed an almost negligible weight loss (less than 1.5%) before 300 °C, which can be attributed to residual solvents and/or CTAB. Two weight losses were detected for the aerogels synthesized only with MTMS, corresponding to the first and second stages of the thermal decomposition of the methyl groups linked to silicon [246], under a non-oxidizing atmosphere. For the samples containing propylamine groups, the losses before 500 °C are a combination of the first thermal decomposition of the methyl groups and the amine decomposition, justifying the higher values of weight loss at lower temperatures. For most of the composites, the CNTs presence reduces the total weight loss, indicating an improvement on the aerogels' thermal resistance. The TGA curves for higher amount of APTMS (Figures 3.10d and 3.10f) show higher mass loss in the initial temperatures (< 100 °C) due to the removal of adsorbed moisture on amine terminal groups (linked by hydrogen bonding).

Thermal conductivity of the silica aerogels and corresponding CNTs-silica aerogel composites was also assessed, as Table 3.6 shows. The presence of amines in the aerogels leads to an increase in the materials' thermal conductivity when compared with the aerogels prepared with only MTMS. This variation can be associated with the higher density of the samples with APTMS, as the heat transferred by the solid part of the samples is a density dependent property [98], as well as the presence of less micro and mesopores in these systems, which favors an increase of the contribution of the gaseous thermal conductivity. Generally, the addition of carbon nanotubes to the aerogels causes a decrease of the thermal conductivity, with the exception of 100M_CNT_S sample in which the opposite is verified. However, as reported by Jelle *et al*. [304], the thermal conductivity of silica aerogels presents a typical minimum as function of density, and for values of density below this optimum, pores with higher diameters are obtained, leading to an increase of the gas thermal conductivity, as observed for this particular sample (100M_CNT_S). Thus, the optimum density value for the synthesized samples is possibly around 75 kg.m^{-3}, since the three aerogels showing densities near this value (100M_S, 100M_S1 and 100M_CNT_S1) have conductivities lower than 40 mW.m^{-1}.K^{-1}. The thermal conductivity values found in this work are higher than those obtained for CNTs-silica aerogel composites dried using a freeze-drying methodology [96]. Nevertheless, our experimental thermal conductivities are much lower when compared with those for composite systems also dried in ambient conditions (67 mW.m^{-1}.K^{-1} or

higher) [204]. It is also worth mentioning that when MTMS-based aerogels have superinsulating properties, a significant increase is verified in the materials densities, as demonstrated by Hayase *et al.* [253] whose materials showed conductivities of 15 and 17 mW.m^{-1}.K^{-1}, but presented densities of 270 and 290 kg.m^{-3}, respectively. So, in this work, we were able to develop materials with low values of conductivity without compromising their densities, with these remaining in the order of 75 kg.m^{-3}.

Table 3.6: Thermal conductivity and mechanical properties of the synthesized aerogels with and without carbon nanotubes.

Samples	Thermal conductivity (mW.m^{-1}.K^{-1})	Stress at maximum load[a] (MPa)	Strain at maximum load[a] (%)	Young's modulus[b] (kPa)	Recovery ratio[b] (%)
100M_S	38.7 ± 0.3	13.0 ± 1.9	60.1 ± 2.0	22.3 ± 0.3	94.0
100M_CNT_S	41.6 ± 0.4	21.5 ± 1.4	42.8 ± 2.8	64.7 ± 0.4	98.8
90M10A_S	43.5 ± 0.3	22.7 ± 2.6	61.4 ± 2.5	104.9 ± 0.7	98.0
90M10A_CNT_S	41.8 ± 0.1	23.9 ± 1.3	54.8 ± 1.1	201.5 ± 1.6	99.8
80M20A_S	56.2 ± 1.4	23.8 ± 0.5	84.0 ± 3.5	309.5 ± 0.4	69.5
80M20A_CNT_S	51.5 ± 1.1	23.9 ± 1.4	66.9 ± 5.7	123.0 ± 0.1	41.6
100M_S1	36.8 ± 0.7	23.1 ± 1.6	90.9 ± 0.4	40.1 ± 0.2	100.0
100M_CNT_S1	31.2 ± 0.1	35.0 ± 4.1	65.6 ± 0.9	50.2 ± 0.3	100.0
90M10A_S1	44.1 ± 0.3	12.4 ± 0.3	87.0 ± 1.2	68.7 ± 0.2	99.8
90M10A_CNT_S1	43.7 ± 0.6	13.5 ± 3.7	58.2 ± 2.8	191.3 ± 0.1	100.0

[a] These tests were performed with a load cell of 3 kN. [b] These tests were performed with a load cell of 50 N.

Uniaxial compression tests were performed on the prepared monolithic materials in order to study the effect of incorporating carbon nanotubes into the silica skeleton, as well as the addition of APTMS and CTAB. Figures 3.13a and 3.13b shows the plots obtained for the samples when submitted to high loads (3 kN), until collapsing. The curves are almost horizontal until a certain strain (from 30% to 70% depending on the sample) and suddenly increase until the ultimate values. The samples were compressed without observable fracture to strains up to ∼90%. However, the samples did not recover their original shape after the applied loads were removed. Similar behavior was observed by Wong *et al.* [305] for samples presenting densities lower than 0.1 g.cm^{-3}. The authors attributed the higher compressibility of these low-density materials to the increased aspect ratio of the silica necks, which allows the aerogels to bend instead of fracture when submitted to compressive loads. The silica necks could elastically recover to their original dimensions, until some degree of strain. However, beyond that value, the aerogel samples suffer significant plastic deformation [305]. The curves final regime corresponds to the materials' densification after compaction [137, 230]. This set of experiments allowed to obtain stress and strain values at maximum load, as given in Table 3.6. In all cases, the

addition of CNTs increases the stress at maximum load at the same time that decreases the strain in that limit. The reinforcing effect of CNTs is thus effective and corresponds to an increase of stiffness of the materials.
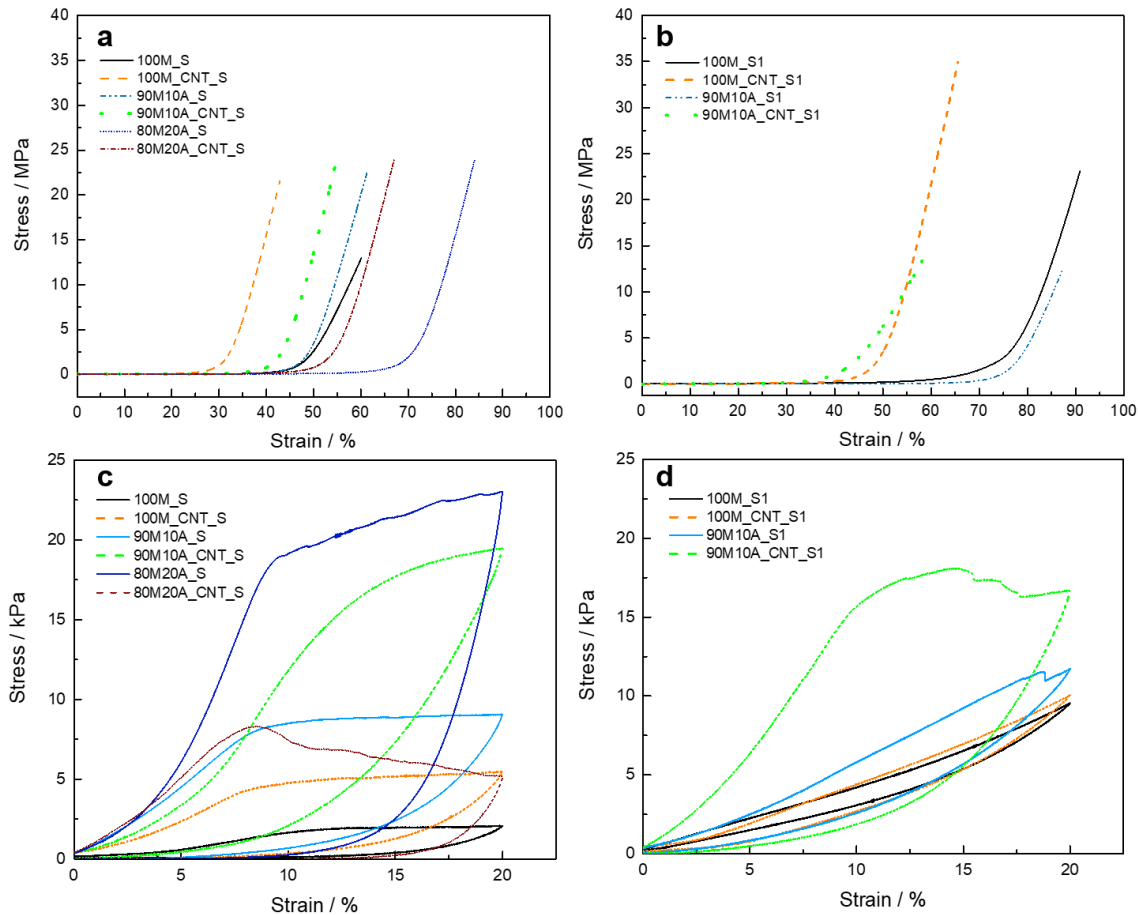
Figure 3.13: Stress-strain curves for silica aerogels and corresponding CNTs-silica aerogel composites obtained a) and b) by uniaxial compression with a load cell of 3 kN and c) and d) by compression-decompression with a load cell of 50 N.

Figures 3.13c and 3.13d shows the obtained curves when the aerogels were tested under a much lower load (50 N), in compression-decompression conditions. These graphs allow the visualization of the initial non-linear regime until about 2%, followed by a linear elastic response until approximately 8% and, finally, the compaction regime until application of the reverse load. This last regime tends to a horizontal line, as observed in the previous performed tests, before densification (Figures 3.13a and 3.13b). These tests under 50 N give a more accurate determination of the Young's modulus (E) than those performed with higher loads (3 kN). The Young's moduli (Table 3.6) were obtained by the slope determined in the linear elastic regime below 8% strain. Generally, the presence of CNTs caused an increase in the Young's modulus and when APTMS was added to the system, a more significant improvement in the Young's modulus was verified. A synergistic effect was observed in the samples' stiffness when amine groups were added to

the system together with CNTs, as an even more meaningful increase in the Young's modulus was verified. These results confirm the reinforcing effect of CNTs, as well as the influence of amine groups, on the mechanical properties of silica aerogels. Moreover, the Young's moduli here observed are much higher than those obtained for MTMS aerogels dried in supercritical conditions (1.5 kPa) [251] and, for the samples with amine and CNTs, they are higher than those for VTMS–MTMS–TMOS-derived aerogels without reinforcement (57 kPa) or reinforced with polybutylacrylate (25 kPa) or with polystyrene (91 kPa) [306], for example.

The recovery ratio of the samples was also assessed (Figures 3.13c and 3.13d, and Table 3.6). The aerogels were compressed until 20% strain and then decompressed until the detected force became less than 0.05 N. All samples show very high recovery ratios (Table 3.6), with total recovery or almost complete recovery for the samples synthesized with 4.0 wt% of CTAB, indicating an improvement in their elasticity. In the case of samples in which a lower amount of CTAB was used, the ones with CNTs also show almost complete recovery.

3.4   Conclusion

We were able to obtain monolithic polysilsesquioxane-based aerogel composites with CNTs using ambient pressure drying, without significant shrinkage. APTMS and CTAB were added to the system in order to improve physical and mechanical properties. All the samples presented silica eight-membered rings, indicating that the presence of these modifiers did not affect the formation of the silica network at primary particles scale. The presence of a higher amount of surfactant (4.0 wt%) allowed a more effective control of the pore structure, while the addition of amine groups caused an increase in the secondary particles size. When carbon nanotubes were incorporated in the system, a distinctive silica structure was obtained, with the silica particles following the format of the CNT, changing from spherical to more cylindrical shapes. This variation indicates that a chemical binding between the carbon nanostructure and silica precursors occurs during the synthesis. The final materials showed high porosities, low densities and superhydrophobicity, as well as low thermal conductivities and improved mechanical properties. The flexibility of the sol-gel process allows the tailoring of the CNTs-silica aerogel composites depending of the desired application, as, for example, more rigid samples can be obtained by reducing the amount of surfactant and adding amine groups, while samples with high recovery rates and low thermal conductivities can be synthesized by increasing the CTAB quantity in the absence of APTMS. The CNTs-silica aerogel

composites here obtained can be proposed for a wide range of applications where porosity, surface area, hydrophobicity, thermal conductivity and mechanical properties are selection criteria, for instance as adsorbents and thermal insulators.

Chapter 4

Influence of 1D and 2D carbon nanostructures in silica-based aerogels

This chapter comprises the work *Influence of 1D and 2D carbon nanostructures in silica-based aerogels* by Alyne Lamy-Mendes, Wim J. Malfait, Amin Sadeghpour, Ana V. Girão, Rui F. Silva and Luísa Durães that is ready for submission.

4.1   Objective and novelty of the work

Enhancing the unique properties of silica aerogels, as well as providing different characteristics by modifying their structure with distinct compounds, greatly relies on the chemical and physical characterization and the understanding of their micro- and nanostructure [307]. Until now, most studies combining carbon nanostructures with silica aerogels were carried out for composites with TEOS or water-glass as silica precursors. To the best of our knowledge, and with the exception of our group's work [308], research using methyltrimethoxysilane (MTMS) for developing carbon nanostructures-silica aerogel composites has not been reported, despite the evident importance of MTMS as a precursor for silica aerogels and foams [54, 80, 309–312]. Moreover, comparison studies of the impact of different carbon nanostructures in the same silica aerogel system are yet to be performed. Hence, the goal of this work is to provide better understanding on the effect of 1D (carbon nanotubes) and 2D (graphene oxide) carbon nanomaterials on the chemical, physical and structural properties of MTMS-based silica aerogels, and enabling a direct comparison of their influence in the final aerogel characteristics, particularly in their fine

chemical structure, thermo-mechanical properties and electrochemical performance. The addition of APTMS was also considered as co-precursor in small amounts, in order to decrease the gelation time and avoid settling of the carbon phase. This parameter significantly influenced in the silica network features, and its study is equally an important contribution of this study to the progress of the state-of-the-art.

4.2 Experimental Section

4.2.1 Materials

Methyltrimethoxysilane (MTMS; purity $\geq 98\%$, *Aldrich*; $CH_3Si(OCH_3)_3$), (3-aminopropyl)trimethoxysilane (APTMS; purity $\geq 97\%$, *Aldrich*; $H_2N(CH_2)_3Si(OCH_3)_3$), ethanol (absolute, *Fluka*; C_2H_5OH), oxalic acid anhydrous (purity $\geq 99\%$, *Fluka*; $C_2H_2O_4$), ammonium hydroxide (25% NH_3 in H_2O, *Fluka Analytical*; NH_4OH), hexadecyltrimethylammonium bromide (CTAB; purity $\geq 99\%$, *Sigma*; $C_{19}H_{42}BrN$), poly(ethylene glycol) 600 (PEG; purity $\geq 99\%$, *Sigma*; $H(OCH_2CH_2)nOH$), commercial multi-walled carbon nanotubes (CNTs; purity 90%, *Nanocyl*, average diameter of 9.5 nm, average length of 1.5 μm, surface area of 250–300 $m^2.g^{-1}$), graphene oxide (GO; *Graphenea*, concentration 0.4 wt%, monolayer content (at 0.05 wt%) $\geq 95\%$), nitric acid (purity 70%, *Sigma Aldrich*; HNO_3) and tetramethyl orthosilicate (TMOS; purity $\geq 99\%$, *Aldrich*; $Si(OCH_3)_4$) were used in this work. Graphite powder (*Sigma–Aldrich*), mineral oil (*Sigma–Aldrich*), iron(III) chloride hexahydrate (purity 97%, *Sigma Aldrich*, $FeCl_3 \cdot 6 H_2O$), potassium hydroxide (*Merck*, KOH) and ultra-pure water were also used. All reagents were used without prior purification.

4.2.2 Surface modification of carbon nanotubes

The multi-walled carbon nanotubes were submitted to two different surface modifications, as described in a previous work [308]. Briefly, MWCNTs were refluxed with concentrated HNO_3 for 20 hours at 50 °C, followed by filtering and washing with distilled water, then dried at 60 °C overnight. These MWCNTs were designated as CNTs-HNO_3. In the second surface modification protocol, the CNTs-HNO_3 were submitted to a reflux with a 10% silane solution (TMOS in a mixture of 70% ethanol/30% water) for 4 hours at 70 °C, then filtered and dried at 60 °C for 1 day; these carbon nanotubes were denominated as CNTs-TMOS.

4.2.3 Synthesis of carbon nanomaterial-silica aerogel composites

The composite materials were prepared by a two-step acid–base catalyzed sol–gel process with oxalic acid (0.01 M in water) as acid catalyst, ammonium hydroxide (1 M in water) as basic catalyst, ethanol-water as the solvent. The samples were prepared with different proportions of silica precursors (MTMS, as main precursor and APTMS, as co-precursor). The synthesized silica aerogels are denoted as xMyA, where x in xM is the mol percentage of Si from MTMS, y in yA corresponds to the mol percentage of Si from APTMS. For the composites with CNTs (1D composites) and graphene oxide (GO) (2D composites), the designations xMyA_CNT_z or xMyA_GO_z were applied, where z is the amount in mg of carbon nanomaterial added to the system.

The use of surfactants was considered from the onset of this work to promote the dispersion of the carbon nanostructures in the silica sol. For the carbon nanotubes-silica aerogel composites, CTAB was the selected surfactant, as it ensures a good dispersion of the CNTs even in basic conditions [247]. The same surfactant was tested for the GO-silica aerogel composites, however, when CTAB was added in the solution containing ethanol-water solvent and GO, a phase separation was observed (Figure B1). Thus, it was not possible to effectively disperse the GO with CTAB. It was also tried to obtain the GO-silica aerogel composites without surfactant. Even though monolithic samples were obtained, SEM images showed that in this case, the GO was not evenly distributed in the samples, agglomerating in some parts of the silica matrix (Figure B2). So, it was necessary to use a different type of surfactant, PEG, for the GO composite samples, in order to obtain materials with better distribution of the carbon nanomaterial in the silica matrix.

The synthesis process started with the addition of a surfactant, CTAB for the CNTs samples and PEG for the GO samples (~4.0 wt% of the sol), into the solvent mixture (ethanol:water 50%/50% v/v), along with MTMS, followed by the addition of the acid catalyst. For the CNTs-silica aerogel composites, the suspension was sonicated for 30 minutes before MTMS addition. For the GO-silica aerogel composites, the suspension was stirred for 5 min before MTMS addition. After 30 minutes of the optional stirring, APTMS was added to the solution, followed by the ammonium hydroxide. The synthesis procedure was performed under thermal control at 27 °C, gelation occurred within 15 minutes and the samples were aged for 7 days, at 27 °C. Surfactant removal was carried out by diffusional ethanol washing, performing 8 changes, while the samples were kept in an oven at 60 °C. The aerogel composites were dried at ambient pressure at 60 °C, for 3 days, and then at 100 °C, for 3 hours.

Different quantities of carbon nanomaterials were added to the composites: up to 200 mg for carbon nanotubes ($\sim$0.6 wt% of the sol) and up to 100 mg for graphene oxide ($\sim$0.3 wt% of the sol). For the composites containing CNTs, it was possible to obtain monolithic samples with higher amounts of carbon nanomaterial (400 mg), but they could not be dispersed homogeneously in the ethanol/water solvent mixture, leading to the formation of large aggregates of CNTs. For the GO composites it was not possible to obtain materials using only MTMS, since these samples did not gel, remaining completely liquid even after one-week.

4.2.4 Characterization of the aerogel composites

As the main goal of this study is to compare the influence of 1D and 2D carbon nanomaterials in the silica aerogel matrix, several characterization techniques were employed to provide better understanding of the synthesized 1D and 2D silica aerogel composites.

Chemical characterization

Detailed information regarding the chemical structure of the aerogels network was obtained from Fourier Transform (FT) Infrared (IR) transmission spectroscopy. For FTIR analysis, a *Jasco FTIR 4200* equipment was used, recording a total of 256 scans from 4000 to 400 cm^{-1} with a resolution of 4 cm^{-1}. The spectra were collected using the potassium bromide (KBr) pellet method, the pellets being prepared with 78-80 mg of KBr and 0.2–0.3 mg of each aerogel. FT-Raman spectra were acquired with a *Horiba Jobin-Yvon LabRAM HR-UV 800, micro-FT Raman* spectrometer, using a laser excitation of 442 nm. The measurements were performed in the wavenumber range between 100 and 3000 cm^{-1}, exposure times of 20 seconds and up to 10 accumulations.

Solid-state nuclear magnetic resonance (SS-NMR) analysis was performed to assess the surface chemistry of the synthesized materials and to verify possible changes in the silica matrix caused by the addition of the 1D and 2D carbon nanomaterials. The spectra were collected as previously described by Malfait *et al*. [299, 313]. In summary, spectra were acquired with magic angle spinning (MAS) on a *Bruker* spectrometer equipped with a wide-bore 9.4 T magnet, corresponding to Larmor frequencies of 400.2 MHz for ^{1}H, 100.6 MHz for ^{13}C, and 79.5 MHz for ^{29}Si. To increase sensitivity, ^{1}H–^{13}C and ^{1}H–^{29}Si cross-polarization (CP) spectra were collected with 7 mm zirconia rotors, a spinning rate of 4500 Hz $\pm$ 2 Hz, and contact times of 2000 and 5000 μs, respectively. The spectra were acquired with a recycle delay of 2 s, *i.e.* between 1.3 and 4 times the ^{1}H *T1* relaxation times typically observed for silica aerogels (0.5 to 1.5 s). The samples were ground and

compressed before analysis and the zirconia rotors were filled completely to maximize sensitivity. The chemical shifts are referenced to tetramethylsilane using adamantane and Si rubber as secondary chemical shift standards.

Structural characterization

The crystalline structure of the samples was evaluated using powder X-ray diffraction (XRD - *Philips X'PERT-PRO* Diffractometer system), by collecting information from 2-70° (2θ) with step size of 0.02°, at room temperature, using Cu$K\alpha$ radiation (λ = 1.54 Å) and operated at 40 kV/50 mA.

Bulk density (ρ_b) was determined by measuring and weighing the monolithic aerogels/composites, and the aerogel skeletal density (ρ_s) was measured by Helium pycnometry (*Accupyc 1330, Micromeritics*). The specific surface area (S_{BET}) was assessed by nitrogen gas adsorption at 77 K (*Gemini V2.00, Micromeritics Instrument Corp.*), applying Brunauer-Emmett-Teller (BET) theory in the relative pressure interval 0.05–0.25 of the adsorption isotherm.

The porosity (equation 4.1) and pore volume (equation 4.2) were calculated using bulk and skeletal densities. The average pore size was estimated using the obtained values for pore volume and specific surface area (equation 4.3).

$$\text{Porosity (\%)} = (1 - \frac{\rho_b}{\rho_s}) \times 100 \tag{4.1}$$

$$V_P \text{ (cm}^3.\text{g}^{-1}) = \frac{1}{\rho_b} - \frac{1}{\rho_s} \tag{4.2}$$

$$\text{Average pore diameter (nm)} = \frac{4(V_P)}{S_{BET}} \tag{4.3}$$

The morphology and microstructure of the developed materials was assessed by scanning electron microscopy (SEM; *Hitachi, SU-70*), operated at 15 kV, and scanning/transmission electron microscopy (STEM; *STEM Hitachi 2700* and *TEM JEOL, 2200FS*), operated at 200 kV. For SEM, powders were dropped directly onto a double-sided carbon tape, material excess was removed under gentile nitrogen gas flow, and a conductive carbon thin film was deposited onto the specimens using a carbon rod coater (*Emitech K950X*). For TEM, the samples were dispersed in ethanol p.a., hand-shook for a few minutes and a drop of the dispersion was placed onto a 400 mesh copper grid with a

continuous carbon film and left to dry in air. High-resolution (HR) TEM images were processed using software *Digital Micrograph 3.42*.

Small angle X-ray scattering (SAXS) was used to provide insight of the materials at the nanoscale, obtain information about primary and secondary silica particles, and study the influence of carbon nanomaterials' addition on the nanopores formation. The SAXS analysis was performed using a *NanoStar* instrument (*Bruker AXS GmbH*, Karlsruhe, Germany). The instrument was equipped with a microfocused X-ray source (*Incoatec GmbH*, Geesthacht, Germany), with a beam spot size of about 400 μm and Cu Kα radiation (λ = 0.154 nm). The scattering intensities from both background and samples were acquired for 60 s at 107 cm detector distance. A *VÅNTEC-2000* Xe-based gas avalanche detector with 2048x2048 pixels and the pixel size of 68x68 μm was used. The minimum reliably measured scattering vector magnitude, q_{min}, is 0.1 nm^{-1}, with q = $(4\pi/\lambda)$ sin θ, where 2θ is the scattering angle. All experiments were carried out under vacuum ($\sim$ 0.01 mbar) to minimize the background scattering from air. Powder samples were used for the measurements, with the samples being placed in a holder and secured with Kapton film. The background scattering from Kapton was subtracted from the experimental data prior to the data analysis.

Thermo-mechanical characterization

Thermal conductivity was assessed by the transient plane source (TPS) technique, at 20 °C (*Thermal Constants Analyzer TPS 2500S*, *Hot Disk*). For selected samples, this analysis was also carried out at different temperatures within the range of -25 °C to 150 °C. For mechanical evaluation, uniaxial compression-decompression tests, on samples with approximately 15 x 15 x 10 mm^3, were run using a load cell of 50 N, up to 10% strain at a deformation rate of 0.5 mm.min^{-1} [253, 314], and then back to residual strain by removing the load at the same speed.

Electrochemical characterization

Potentiodynamic electrochemical cyclic voltammetry (CV) and electrochemical impedance spectroscopy (EIS) measurements were performed by using a *PalmSens* portable potentiostat/galvanostat, *PalmSens4*, integrating an EIS analyser module. This device was controlled by the *PSTrace 5.5* software (*PalmSens*, Netherlands). The cyclic voltammograms were recorded within the potential range of -0.5 to 0.2 V and scan rates from 5 up to 400 mV.s^{-1}. EIS measurements were performed at an open circuit potential, using a sinusoidal wave with an amplitude of 0.01 V and 73 data points logarithmically distributed over 0.01 –10000.0 Hz frequency range. A modified carbon paste electrode was

the working electrode, a Pt wire the counter electrode and Ag/AgCl the reference electrode. The carbon paste (100 mg) electrode was prepared by carefully mixing graphite powder (50% (w/w)) with aerogel samples (25% (w/w)) and subsequently adding mineral oil (25% (w/w)). The components were mixed manually in a mortar until complete homogenization. The obtained material was packed into an adequate support of electrode consisting of a plastic cylindrical tube (internal diameter 5 mm) with a copper rod inside used as an external electric contact [315]. The electrochemical experiments were carried out in a KOH 6M solution, using a three-electrode system in one-compartment electrochemical cell of 5 mL capacity at 25 °C.

The specific capacitances obtained from the CV were calculated by the equation (4.4) [316–318].

$$C_\mathrm{S} = \frac{\int I \mathrm{d}V}{2(v\,m\,\Delta V)} \tag{4.4}$$

where C_S is the specific capacitance, $\int I \mathrm{d}V$ represents the area under voltammetric curve, v is the scan rate, m is the mass of aerogels used in the working electrode and ΔV is the potential window.

4.3   Results and discussion

4.3.1   Chemical characterization

FTIR analysis showed that the presence of carbon nanomaterials was not detected in the spectra, even when higher amounts were used in the samples, with only the typical silica bands being identified. These findings were expected, as previously observed for carbon nanotubes-silica aerogel composites [308]. In both examples of FTIR spectra shown in Figure 4.1a, bonding between silicon and oxygen are observed, indicating that the precursors have originated a silica network. The symmetric stretching vibrations of the Si–O–Si bonds, the Si–C stretching vibration from the methyl group of MTMS and the bands associated to the longitudinal and transversal-optical components of the asymmetric stretching vibration of Si–O–Si appears around 760 cm^{-1}, 835 cm^{-1}, 1040 cm^{-1} and 1140 cm^{-1}, respectively [275]. Regarding the use of different surfactants, such as PEG or CTAB, both composites aerogels present similar silica bands, indicating that the use of these different compounds in the synthesis do not have major effects on the chemical structure of the silica network.
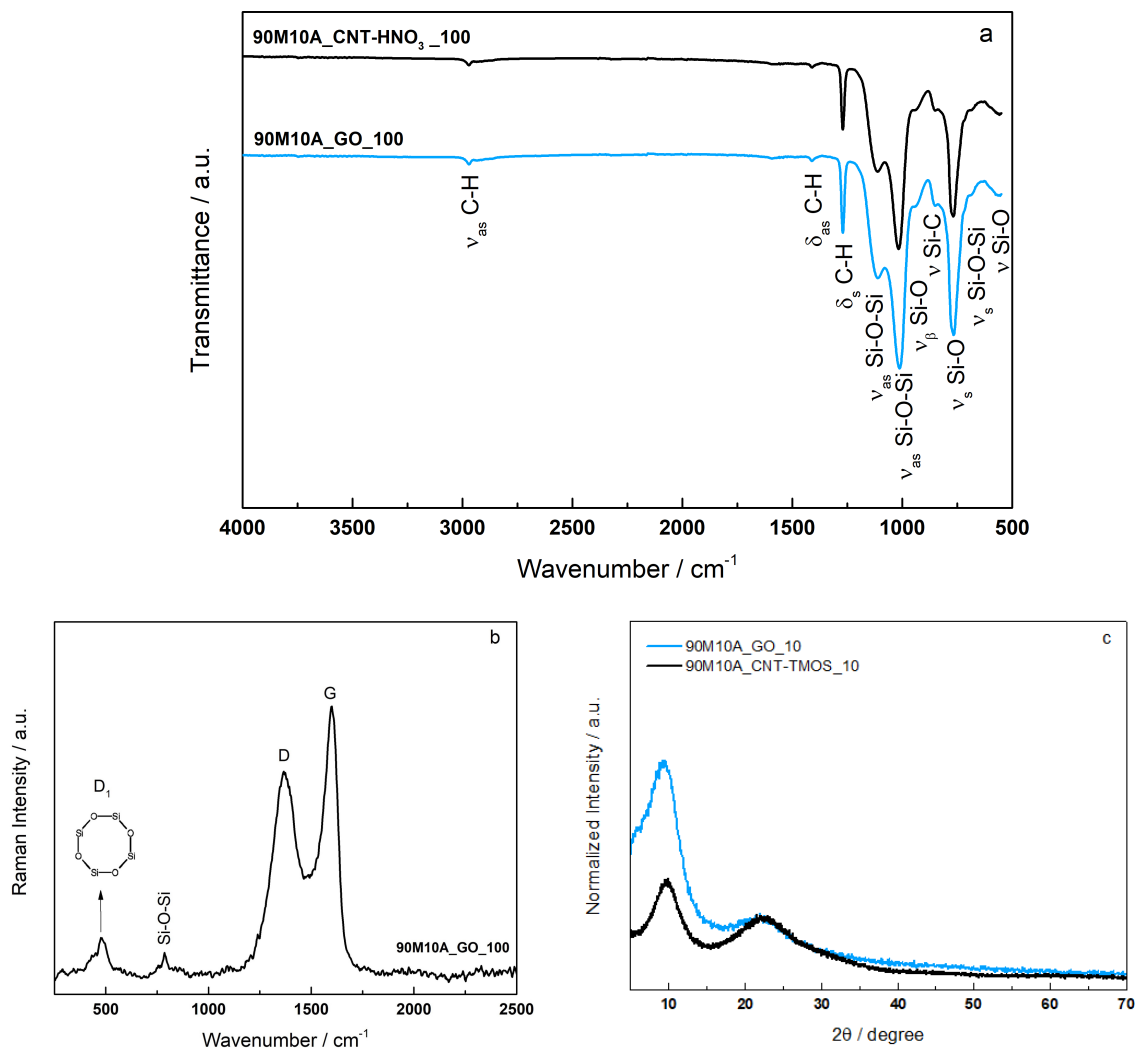
Figure 4.1: Chemical and structural characterizations of carbon nanomaterials-silica aerogel composites: a) FTIR spectra, b) Raman spectra and c) powder X-ray diffraction patterns (normalized).

The presence of carbon nanomaterials in the composites was then confirmed by Raman spectroscopy. The spectra for the aerogels synthesized with both 1D and 2D nanomaterials, carbon nanotubes [308] and graphene oxide (Figure 4.1b), exhibit the two characteristic absorption bands, D band (around 1350 cm^{-1}) and G band. For the GO composite the G band is at approximately 1597 cm^{-1}, which is in agreement with the literature for GO with high levels of oxidation [319–321]. A broad signal near 500 cm^{-1}, assigned to Si-O-Si bending vibrations and rings with 4 -Si-O- units (D1) [279–283, 322, 323] and a signal near 790 cm^{-1}, also assigned to Si-O-Si vibrations, are observed in all composites, independent of the presence or concentration of 1D and 2D carbon nanostructures.

The effect of APTMS addition into the MTMS-based silica aerogel was studied by solid-state MAS NMR, as illustrated in Figure 4.2. The ^{29}Si spectra (Figure 4.2a) display the T^n resonances arising from Si atoms originating from the hydrolysis and condensation of MTMS and APTMS, with T^3 corresponding to Si atoms with one carbon neighbor and three

bridging oxygen atoms (BO) and T^2 to Si atoms with one carbon neighbor, two BO and one non-bridging oxygen (NBO) atom [324]. The ^{29}Si spectra are very similar for all aerogels, with the T^2 band (-58 ppm) accounting for only around 10% of the T^3 (-67 ppm) intensity [324], indicating a high degree of condensation of the trifunctional silane during aerogel synthesis.

More significant differences between the samples were observed in the ^{13}C spectra (Figure 4.2b). When APTMS is added to the MTMS based aerogels, the carbons from aminopropyl chain are clearly visible in the spectra (at 11, 27 and 45 ppm with increasing distance from the amino group), and their intensity scales with the APTMS content used during synthesis. The position and width of the main Si-CH$_3$ signal at -3 ppm remains unchanged upon APTMS addition.

The use of different surfactants (CTAB and PEG) in the synthesis process and its influence in the final chemical structure of the silica aerogels was also assessed. The ^1H–^{29}Si CP MAS NMR spectra are near-identical when using PEG versus CTAB (Figure B3a). Even though the ^1H–^{13}C CP MAS NMR spectra are also quite similar, a small additional peak around 73 ppm is observed for the sample synthesized with PEG, indicating the retention of a small amount of PEG in the system (Figure 4.2c). It is possible that the retention of this surfactant is caused by the hydrogen bond interactions between the oxygen atoms and terminal OH groups of PEG with the amino groups of the APTMS precursor or residual silanol groups in the silica network. Alternatively, some PEG may be covalently bonded to the silica network through alcoholysis between the PEG terminal OH and residual silanol. Due to these strong interactions, it was evidently not possible to completely remove PEG from the system using only diffusional washing. However, the presence of this surfactant is very minor (based on its low NMR intensity) and does not affect the chemical structure of the silica network as the ^1H–^{29}Si CP spectra obtained for these samples are very similar to those obtained for the composites synthesized using CTAB.
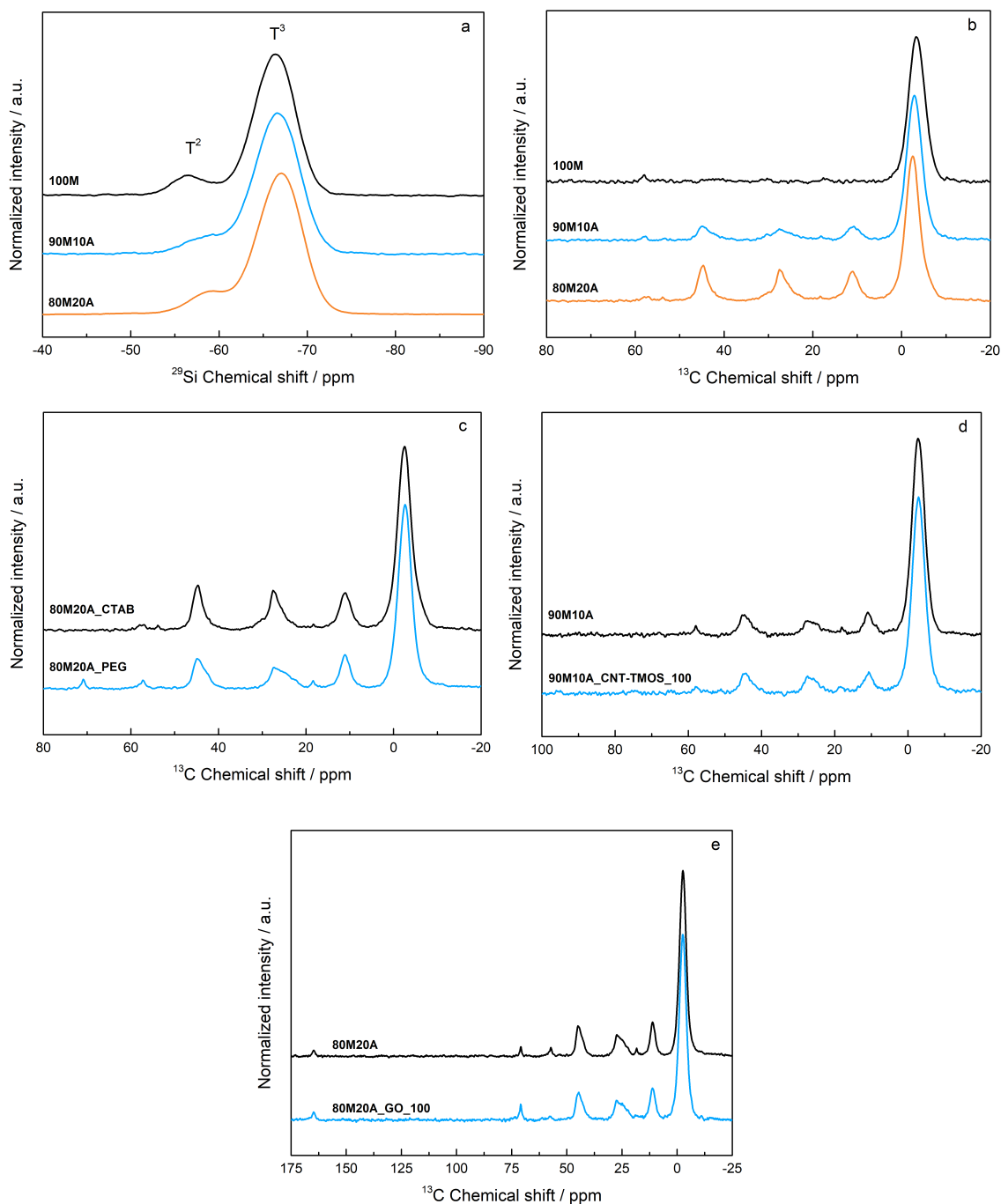
Figure 4.2: a) ^{1}H–^{29}Si solid-state MAS NMR spectra of MTMS based aerogels synthesized with variable APTMS content (0, 10 and 20% of total Si atoms from top to bottom); b) ^{1}H–^{13}C solid-state MAS NMR spectra of MTMS based aerogels synthesized with variable APTMS content (0, 10 and 20% of total Si atoms from top to bottom); c) ^{1}H–^{13}C solid-state MAS NMR spectra of 80%MTMS/20%APTMS silica aerogels synthesized with CTAB versus PEG as surfactant; d) ^{1}H–^{13}C solid-state MAS NMR spectra of 90%MTMS/10%APTMS silica aerogels synthesized with and without CNTs; and e) ^{1}H–^{13}C solid-state MAS NMR spectra of 80%MTMS/20%APTMS silica aerogels synthesized with and without GO.

The presence of carbon nanotubes has only minor effects on the ^{1}H–^{29}Si CP MAS NMR (Figure B3b) and ^{1}H–^{13}C CP MAS NMR spectra (Figure 4.2d). The ^{29}Si spectra are nearly identical, indicating no major chemical changes in Si-O-Si condensation with or without carbon nanotubes, even though some differences between them are observed by the structure-based analytical techniques such as TEM, SEM, SAXS and BET (see below). A

direct detection of the used carbon nanomaterials with ^{1}H–^{13}C CP MAS NMR is not possible due to the low loading of these materials and relatively low sensitivity of SS-NMR. When graphene oxide was added into the silica matrix, some small differences could be observed: a broadening of the main CH_3 peak (-2.6 ppm), as well as an intensity decrease and slight broadening of the APTMS peaks (Figure 4.2e). These differences indicate that more variations in the local environment around the methyl and aminopropyl groups occur in the presence of the GO sheets.

Therefore, solid state MAS NMR results demonstrate that both 1D and 2D carbon nanomaterials do not prevent or significantly affect the condensation of the silica precursors into the three-dimensional network. However, the presence of carbon nanostructures with two dimensions (2D), in this case graphene oxide, has a small, but measurable impact on the local chemical environment of the organic groups.

4.3.2 Structural characterization

Powder X-ray diffractions patterns were obtained for the 1D and 2D carbon structures-silica aerogel composites. The broad XRD patterns indicate the amorphous nature of the materials. Two broad reflections are observed for both the GO and CNT composite samples. These peaks are typical for sol-gel derived materials from MTMS [288] and have been previously reported for 1D carbon nanotubes-silica aerogel composites [308]. The bands can be attributed to the d-spacing between silicon atoms linked to alkyl groups (methyl or propyl) (around 9°) and to those of the Si-O-Si network, similar to silica glass (around 22°) [246, 288, 308]. As presented in Figure 4.1c, in the normalized patterns, the band around 9° for the 2D (GO) composites has higher relative intensity than the 1D (CNTs) composites. A possible explanation is the fact that GO has a typical reflection in this region assigned to the interlayer d-spacing around 0.87 nm [214, 319, 325–329], but it is unlikely that the relatively low amount of GO can account for the large difference.

The physical and microstructural properties of the reference silica aerogels and their corresponding 1D and 2D carbon composites are summarized in Tables 4.1 and 4.2. The references samples (without carbon nanostructures), independent of the surfactant type, have densities (75.3 to 88.4 kg.m^{-3}) similar to the ones obtained for other MTMS-based xerogels and aerogels in the literature [54, 330, 331], with the exception of the material containing 20% of APTMS synthesized with CTAB, that displays a higher value of bulk density (381.7 kg.m^{-3}). The high density for this particular sample is related to the significant shrinkage suffered by this material during the drying step.

Contrary to the bulk density, systematic variations in specific surface area are observed for the reference aerogels. The aerogels synthesized with CTAB as surfactant

(Table 4.1), even for the higher density 20% APTMS material, have higher surfaces areas than the aerogels produced with PEG as surfactant (Table 4.2). The difference in surface area reflects the distinct microstructures, as observed by SEM (Figure 4.3). The materials synthesized with CTAB have a finer microstructure, which leads to higher values of specific surface area, while the samples obtained with PEG have a coarser structure, with significant larger particles and pores, and, consequently, lower surface areas.

The increase of amine amount added in the MTMS system with CTAB as surfactant, first results in a significant reduction (with 10% of APTMS), followed by an increase in the specific surface area (with 20% of APTMS), but not fully reaching the value of the 100M system. These variations can be related to the different particle radii obtained for these networks, as also observed for the different surfactants. As expected, the addition of amine groups leads to an increase in the particle radii, since the silica growth is not limited by cluster hydrolysis under more basic conditions [276, 302, 308], and therefore, lower values of specific surface area are obtained for the resultant material. However, for the sample with 20% of APTMS and CTAB, a decrease in the secondary particles' diameters, associated with higher values of surface area, was observed. There are two possible explanations for this. First the higher amount of APTMS in the system can favor nucleation, so the silica particles growth is more distributed through the whole solution in a higher number of nuclei, leading to smaller particles. The second reason may be the combination of higher amounts of APTMS and CTAB, which causes higher steric barriers against particle aggregation, leading to the stabilization of smaller particles [276].

For the samples synthesized with PEG, it is likely that PEG is only assisting the dispersion of graphene oxide in the solution, but not effectively controlling/preventing silica particle growth. Similar large secondary particles were found in works where no surfactant was used, and higher amounts of water were added into the system [332, 333]. The explanations for these larger particles are mainly related to the presence of excess water in the system without a surfactant that is able to control the silica growth. For H_2O/MTMS molar ratios higher than 8, the hydrolysis and condensation reactions can be complete due to the over-stoichiometric conditions, not limiting the particles growth [332]. Also, the increase of aqueous equivalents changes the solvent to an anti-solvent ratio, which causes the silica particles to grow more separately, leading to larger sizes and the presence of macropores [333]. Under these particular conditions, the microstructure of the synthesized materials shows larger pores and spherical shaped particles, as observed in the SEM images (Figure 4.3).

Table 4.1: Summary of physical and microstructural properties of the synthesized silica aerogels and CNTs-silica aerogel composites.

Samples	Bulk density (kg.m^{-3})	Porosity (%)	Pore volume (cm^3.g^{-1})	Specific surface area (m^2.g^{-1})	Average pore size (nm)
100M [308]	75.3 ± 5.1	95.3 ± 0.1	12.6 ± 0.9	458.1 ± 2.2	110.5 ± 6.9
100M_CNT-HNO$_3$_10	72.8 ± 3.9	94.6 ± 0.1	13.0 ± 0.7	477.7 ± 1.7	108.8 ± 6.2
100M_CNT-HNO$_3$_50	90.7 ± 8.2	94.7 ± 0.1	10.4 ± 0.5	438.5 ± 2.4	95.2 ± 5.4
100M_CNT-HNO$_3$_100	92.1 ± 4.9	94.6 ± 0.1	10.3 ± 0.6	485.1 ± 2.6	84.7 ± 4.9
100M_CNT-HNO$_3$_200	96.6 ± 7.7	94.3 ± 0.2	9.8 ± 0.1	463.0 ± 2.5	84.4 ± 1.5
100M_CNT-TMOS_10 [308]	75.6 ± 5.1	95.6 ± 0.2	12.7 ± 1.4	492.4 ± 4.0	102.7 ± 10.3
100M_CNT-TMOS_50	65.4 ± 4.0	96.1 ± 0.1	14.7 ± 0.9	422.2 ± 6.8	139.3 ± 10.8
100M_CNT-TMOS_100	77.8 ± 1.6	95.4 ± 0.2	12.3 ± 0.2	486.3 ± 2.1	100.9 ± 2.4
100M_CNT-TMOS_200	82.9 ± 2.4	95.1 ± 0.1	11.5 ± 0.3	430.6 ± 7.3	106.5 ± 4.7
90M10A [308]	80.9 ± 7.2	94.5 ± 0.3	11.7 ± 1.0	72.2 ± 1.3	647.4 ± 46.1
90M10A_CNT-HNO$_3$_10	81.9 ± 4.3	93.2 ± 0.2	11.4 ± 0.6	306.9 ± 4.3	148.4 ± 9.6
90M10A_CNT-HNO$_3$_50	95.6 ± 6.7	93.8 ± 0.1	9.8 ± 0.7	131.1 ± 1.6	299.6 ± 25.0
90M10A_CNT-HNO$_3$_100	92.1 ± 7.6	94.1 ± 0.2	10.2 ± 0.9	134.9 ± 1.7	303.0 ± 29.4
90M10A_CNT-HNO$_3$_200	101.4 ± 7.3	93.5 ± 0.1	9.2 ± 0.7	90.8 ± 2.5	406.2 ± 41.5
90M10A_CNT-TMOS_10 [308]	84.6 ± 5.1	94.6 ± 0.1	11.2 ± 0.7	118.2 ± 2.1	387.3 ± 15.6
90M10A_CNT-TMOS_50	81.9 ± 5.1	94.8 ± 0.2	11.6 ± 0.4	79.1 ± 1.1	669.7 ± 33.8
90M10A_CNT-TMOS_100	86.9 ± 2.8	94.4 ± 0.1	10.9 ± 0.5	54.3 ± 0.8	800.5 ± 46.5
90M10A_CNT-TMOS_200	83.1 ± 4.8	94.7 ± 0.1	11.4 ± 0.7	115.9 ± 2.4	393.2 ± 31.0
80M20A [308]	381.7 ± 24.2	72.3 ± 1.6	1.9 ± 0.2	311.9 ± 7.7	24.3 ± 1.5
80M20A_CNT-HNO$_3$_10	474.6 ± 21.3	66.5 ± 0.8	1.4 ± 0.1	268.1 ± 5.2	20.9 ± 1.6
80M20A_CNT-HNO$_3$_50	381.1 ± 13.8	73.1 ± 0.4	1.9 ± 0.1	132.2 ± 1.7	58.1 ± 3.2
80M20A_CNT-HNO$_3$_100	437.7 ± 9.5	69.1 ± 0.1	1.6 ± 0.1	180.8 ± 2.4	34.9 ± 1.3
80M20A_CNT-HNO$_3$_200	427.4 ± 4.8	69.8 ± 0.1	1.6 ± 0.1	208.9 ± 2.7	31.3 ± 1.2
80M20A_CNT-TMOS_10 [308]	142.2 ± 0.5	89.9 ± 0.2	6.3 ± 0.1	245.6 ± 3.2	103.0 ± 0.8
80M20A_CNT-TMOS_50	386.4 ± 5.8	72.7 ± 0.1	1.9 ± 0.1	175.3 ± 2.4	43.0 ± 1.2
80M20A_CNT-TMOS_100	355.3 ± 1.1	74.9 ± 0.4	2.1 ± 0.1	313.1 ± 4.3	26.9 ± 0.3
80M20A_CNT-TMOS_200	305.1 ± 11.1	78.5 ± 0.4	2.6 ± 0.1	340.5 ± 3.8	30.2 ± 1.6

Table 4.2: Summary of physical and microstructural properties of the synthesized silica aerogels and GO-silica aerogel composites.

Samples	Bulk density (kg.m^{-3})	Porosity (%)	Pore volume (cm^3.g^{-1})	Specific surface area (m^2.g^{-1})	Average pore size (μm)
90M10A	88.4 ± 3.0	93.7 ± 0.1	10.6 ± 0.4	9.4 ± 0.4	4.5 ± 0.2
90M10A_GO_10	82.9 ± 4.2	94.1 ± 0.2	11.4 ± 0.6	5.5 ± 0.5	8.3 ± 0.7
90M10A_GO_50	80.4 ± 3.3	94.3 ± 0.2	11.7 ± 0.5	25.8 ± 1.1	1.8 ± 0.1
90M10A_GO_100	86.8 ± 3.4	93.8 ± 0.2	10.8 ± 0.4	34.3 ± 1.2	1.3 ± 0.1
80M20A	79.2 ± 5.1	94.6 ± 0.1	11.9 ± 0.5	20.4 ± 0.5	2.3 ± 0.1
80M20A_GO_10	76.1 ± 2.6	94.8 ± 0.1	12.5 ± 0.4	22.4 ± 0.8	2.2 ± 0.1
80M20A_GO_50	73.8 ± 1.7	95.0 ± 0.2	12.9 ± 0.8	29.3 ± 0.9	1.7 ± 0.1
80M20A_GO_100	73.5 ± 2.8	95.0 ± 0.1	12.9 ± 0.3	71.9 ± 1.1	0.7 ± 0.1
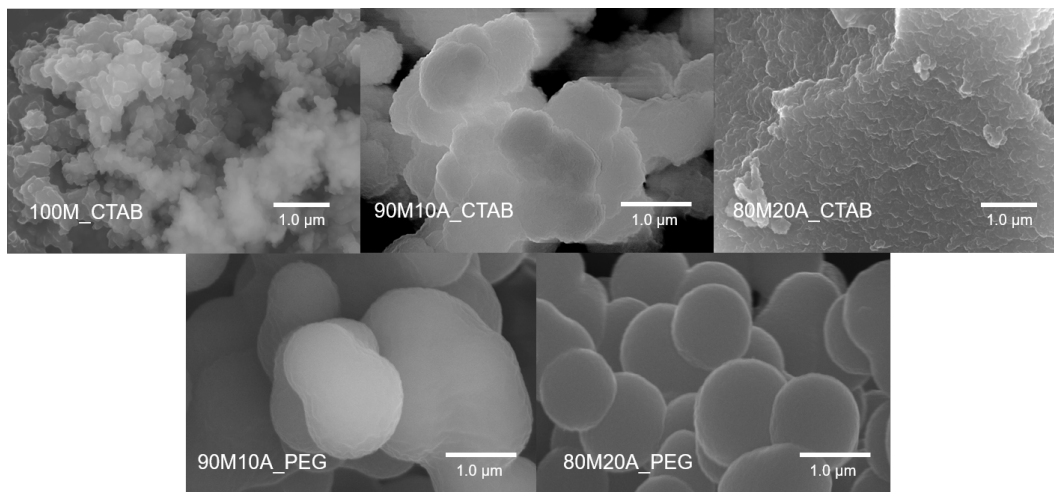
Figure 4.3: SEM images of the prepared silica aerogel with different surfactants (CTAB or PEG).

Regarding the composite materials, with the exception of the samples with carbon nanotubes and 20% of APTMS in the matrix, all materials show similar values for bulk density (65.4 to 101.4 kg.m^{-3}). Moreover, some samples presented even lower bulk density than those observed for MTMS xerogels and aerogels [54, 330, 331], or for carbon nanostructure-silica aerogel composites obtained with different precursors, dried under ambient pressure conditions [1, 63, 94, 205, 215].

For the 1D composites, most of the samples synthesized with CNT-HNO$_3$ show higher values of bulk density than their counterpart prepared with CNT-TMOS, indicating that higher shrinkage occurs for these samples during the drying step. One possible explanation is that a better interaction between the silica matrix and the silane-modified carbon nanotubes is achieved, with these materials showing a better support to the silica skeleton than those only submitted to the acid surface modification. In general, for the composites 100M and 90M10A obtained with CNT-HNO$_3$, the increasing amount of carbon nanotubes increases the bulk density, along a linear trend. For the same systems with CNT-TMOS, bulk densities are similar and do not show significant variations with the increase of carbon nanotubes in the samples. Regarding the 80M20A systems, much higher density values are obtained for the composites, similar to the CNT free reference sample. Nevertheless, it is important to mention that when the added amount of CNTs was equal or higher than 50 mg, and regardless of their high-level shrinkages, the final 1D composites remained monolithic, in contrast to what is observed for lower quantities of CNTs, independent of their surface modification. This indicates that when the carbon nanotubes start to connect to each other, they are able to sustain the silica matrix, avoiding the fracture of the final samples during drying.

For the 2D composites (shown in Table 4.2) no significant bulk density variations were noticed, including for the 80M20A, GO free reference sample, in contrast to the 80M20A

reference sample from the CNT batch. Samples with higher amount of amine precursor show slightly lower values than those obtained with 10% of APTMS, and the GO-composites always have lower bulk density than their reference silica aerogel counterparts. A possible explanation for these results is that the presence of a carbon nanostructure, such as GO, with a significant different shape than the silica matrix may have some physical influence during the development of the 3D aerogel network. In the end, the 2D nanostructure helps prevent the shrinkage of these composites even when prepared with higher quantity of APTMS.

In terms of porosity, again with the exception of the samples synthesized with CNTs and 20% of APTMS with values between 65 and 90%, the remaining matrices and composites present similar porosities, with values higher than 93%. These porosity values are similar or even higher than those reported for MTMS-based aerogels dried with supercritical fluids [54, 251, 294, 295], or those for carbon nanostructures-silica aerogel composites [63, 204, 205, 296]. The pore volume is also very similar, although these materials present a large amount of macropores in their structure and the method is not sensitive enough to micro and mesopores variations.

Regarding the specific surface area, all samples synthesized only using MTMS as precursor show values consistent with those in the literature (420 - 500 $m^2.g^{-1}$). Aerogels usually present specific surface areas between 250 and 800 $m^2.g^{-1}$ [79], and some of our systems show even higher values than those reported for MTMS-based silica materials dried under similar conditions [54, 299]. Nonetheless, when amine groups are included in the structure, a decrease of the specific surface area is observed in all systems.

The presence of CNTs also influences the specific surface area, as observed for most of the 90M10A samples, whose 1D composites show higher values independently of the CNTs surface modification process. This is most probably due to stereological reasons, as CNTs provide points of nucleation for the silica growth, altering the network morphology [308]. In contrast, for the 80M20A samples, most of their composites present lower values of specific surface area. A possible justification for these, is that, as mentioned for the 90M10A samples, the presence of CNTs favors the silica growth, which can lead to larger secondary particles than the reference sample.

The 2D composites present lower values for specific surface area, if compared with the 1D composites, which can be due to large particle radii, in the micrometers order formed in the overall network, as confirmed by SEM imaging (Figure 4.5). Regarding the specific surface area values determined for the 2D composites, the highest values are observed for those containing 100 mg of GO ($\sim$ 4 wt% of the aerogel), but these may have a contribution of the exposed GO high surface area, and not from the aerogel silica matrix itself.

SEM images of the 1D and 2D composites (100 mg of carbon material) are shown in Figures 4.4 and 4.5, respectively. Generally, the images show the typical silica network morphology of secondary particles, also known as pearl-necklace-like structure [8]. It is also possible to observe that the samples with 90M10A and CNTs, and all 2D composites, present much larger pores and secondary particles than the remaining materials. The presence of such large particles is expected for the samples with APTMS as co-precursor [276, 302, 308], as mentioned for the reference samples. Another factor contributing to the growth of secondary particles is the fact that, during the washing steps, the aging process continues to happen, which leads to the re-dissolution and re-precipitation of silica, resulting in the decrease of the specific surface area [303], which is in agreement with previous observations.

Moreover, the calculated average pore sizes in Tables 4.1 and 4.2 are also in good agreement with what is observed from SEM analysis. The influence of using carbon nanostructures with different surface treatments on the silica network formation was not detected by SEM imaging, since all samples present very similar silica matrices. Furthermore, due to the significant difference in size between the carbon nanostructures and the overall silica network, especially those presenting large secondary units, it was not possible to clearly distinguish the 1D/2D structures within the aerogel matrix. Thus, TEM analysis was performed to better assess the carbon nanostructures presence in such composites, as illustrated in Figures 4.4 and 4.5.
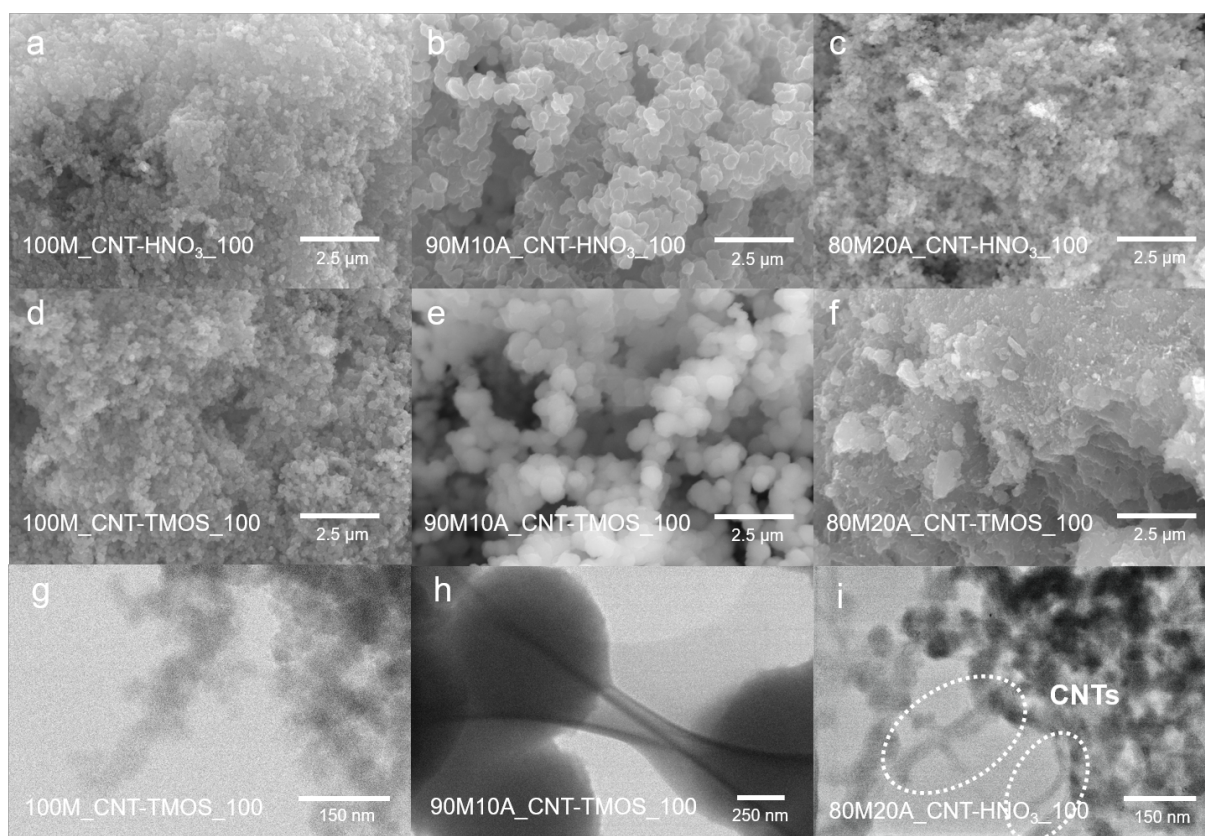
Figure 4.4: SEM (a to f) and TEM (g to i) images of the prepared carbon nanotubes-silica aerogel composites with 100 mg of the CNTs.

The microstructure of the CNT-silica composite aerogel synthesized with 100% MTMS (Figure 4.4g) is composed of very small structural units, with the silica nanoparticles clearly decorating the interlinked carbon nanotubes. In the 90M10A_CNT-TMOS_100 composite (Figure 4.4h), the silica matrix evolved around the carbon nanotube, ending in a more elongated shape linked to the remaining network. The CNTs modification with a silane precursor most probably improves the chemical interaction between the two distinct materials, with the 1D nanostructure clearly connecting the silica clusters. In contrast to the CNTs-TMOS composites, where it was not possible to differentiate the two phases, the 80M20A_CNT-HNO$_3$_100 sample (Figure 4.4i) undoubtedly show a few disconnected carbon nanotubes. These observations were expected since the interaction between CNTs modified with nitric acid and the silica matrix is certainly weaker than that between silanized CNTs and the silica network.

Regarding the 2D composites, it is possible to observe a small part of the graphene oxide sheet next to the silica matrix (sample 90M10A_GO_100 - Figure 4.5c), with larger secondary silica particles as observed in the corresponding SEM image (Figure 4.5a). HRTEM imaging analysis mostly revealed single or a few layers GO involved within the silica framework. Nevertheless, detailed inspection also exposed a few areas where a small number of fragmented GO sheets have agglomerated. The generated Fourier

transform diffraction pattern (inset of Figure 4.5e) shows a ring like pattern and spots typical of polycrystalline nature with crystallographic orientation between the sheets, respectively [321, 334]. Most of the graphene oxide identified in the aerogel matrix clearly shows diffraction spots for short-range order over a length scale, like those of graphite/graphite oxide [321]. These images illustrate the GO crystalline structure confirmed by the generated diffraction spots with a six-fold pattern [319, 321, 334]. HRTEM images also demonstrate the characteristic high transparency of the GO layer deposited onto the carbon film of the grid [321]. These findings are in very good agreement with those from powder XRD and Raman spectroscopy.
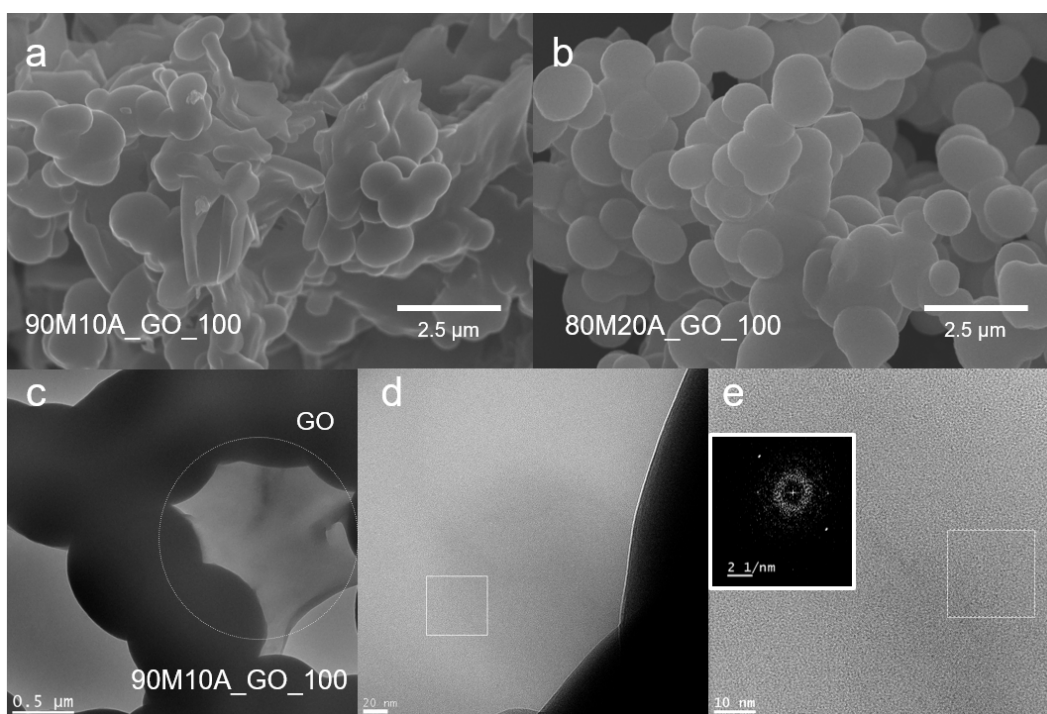
Figure 4.5: SEM images (a and b) and HRTEM images (c and d) of the prepared graphene oxide-silica aerogel composites with 100 mg of the GO and generated Fourier transform image (e).

To investigate more in detail the morphology and porosity of the composite materials, SAXS measurements were performed on samples with and without carbon nanotubes (Figure B4). This technique was also performed in graphene oxide-silica aerogel composites, however, only a plateau was observed due to the large particle sizes of these samples, and an ultra-small angles setup would be necessary. X-ray scattering patterns were analyzed to reveal two important structural features [335]. The first one is associated with the decay of scattering intensity at small angles, best explained by the classical Porod analysis. In this approach, the decay rate of scattering intensity follows $1/q^\alpha$ with α known as Porod exponent. For three-dimensional particles and perfectly smooth surfaces, a Porod exponent of 4 is expected. For particles with surface roughness,

this exponent decrease to a minimal value of 3. The rougher the particle surface is, the smaller is the Porod exponent. We have analyzed the initial decay rate by the slope of scattering intensity versus q curve in log-log scale. The results are summarized in Figure 4.6. The comparison of Porod slope values for three different matrices indicates only small variations around -3.72 $\pm$ 0.06, with the sample 90M10A displaying highest surface roughness (lowest Porod exponent). The addition of carbon nanotubes caused an increase in the Porod exponent (reduction of absolute values), so that both CNTs-silica aerogel composites indicate the Porod exponent of -3.6. This variation confirms the fact that CNTs effectively modify the formation of the silica network, *i.e.* the microstructure of the aerogels, and this higher surface roughness demonstrates a good agreement with morphology observed in TEM images (Figure 4.4).
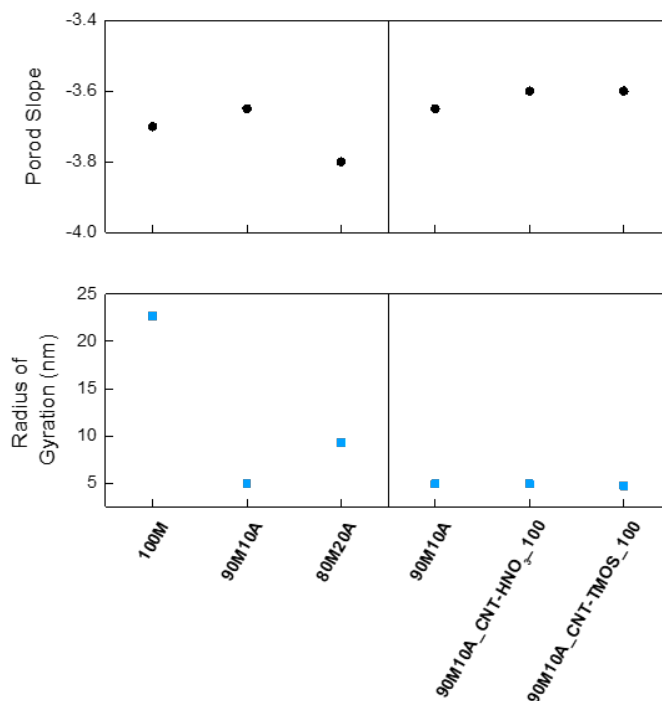
Figure 4.6: Porod slope values and Radius of gyration (R_g) obtained from silica aerogels and carbon nanotubes-silica aerogel composites with 100 mg of CNTs.

The second feature obtained from scattering curves is associated to nanometer-sized pores within the silica particles. This appears as a broad hump at larger scattering angles, *e.g.* shown in Figure 4.7 at the q values between 0.5 and 1.0 nm^{-1}. The position and intensity of this hump explains the size and the number density of pores. To acquire a quantitative measure of these pores, the previously obtained Porod decay function was subtracted from the experimental data and the resulting curve is interpreted as the scattering signal from internal pores. Further analysis of the deduced curves by indirect

Fourier transformation [336] leads to the identification of pair-distance distribution function (PDDF) and the average radius of gyration of pores. Similar approaches have been applied previously to reveal the pore size and surface roughness of the silica particles from SAXS data [335, 337].
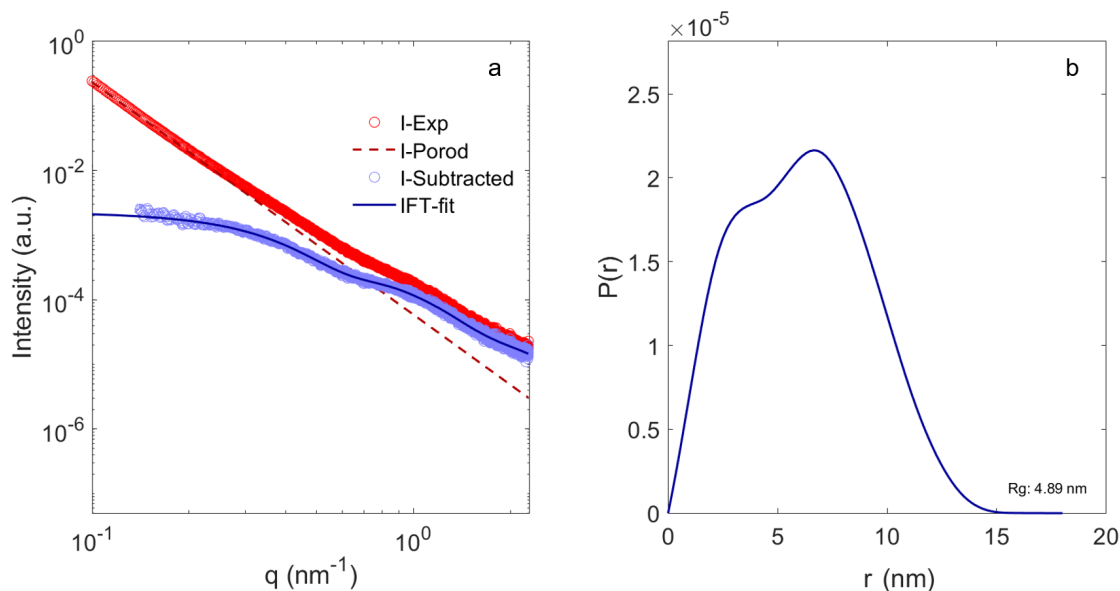
Figure 4.7: a) Experimental scattering patterns and their relevant residual scattering obtained from subtraction of Porod line are shown together with the indirect Fourier transformation (IFT) evaluation of residual scattering. b) Pair-distance distribution function, $P(r)$, obtained from IFT analysis of residual scattering from pores for the sample 90M10A_CNT-HNO$_3$_100.

The determined radii of gyration by the SAXS study (Figure 4.6) are significantly lower than the pore sizes estimated by the average pore diameter (P_d) equation ($P_d = 4V_P/S_{BET}$) (Table 4.1). This discrepancy can be explained by the fact that SAXS is not sensitive to structural features around or larger than 100 nanometers (depending on the instrument resolution). In other words, the radius of gyration determined by SAXS corresponds to nanometer sized length scales of smaller primary particles, which are not accurately determined by P_d equation or visible by microscopic techniques.

From the SAXS data, a significant reduction of the radius of gyration of pores was observed by the addition of amine groups, with values changing from 22.7 $\pm$ 2.52 nm (100M) to 4.89 $\pm$ 0.68 nm (90M10A) and 9.33 $\pm$ 0.46 nm (80M20A). Then, the addition of CNTs causes only a slight decrease if compared with the 90M10A silica matrix.

4.3.3   Thermo-mechanical characterization

The effect of the 1D and 2D carbon nanomaterials on the typical thermal insulation of the prepared silica aerogels was assessed through measurement of the thermal conductivity of the monolithic materials, as presented in Table 4.3.

Table 4.3: Thermal conductivity of the monolithic silica aerogels without carbon nanostructures and with different amounts of CNTs-HNO$_3$, CNTs-TMOS and GO.

Amount of carbon nanostructure	Thermal conductivity (mW.m^{-1}.K^{-1})		
	100M_CNTs-HNO$_3$	90M10A_CNTs-HNO$_3$	80M20A_CNTs-HNO$_3$
0 mg [308]	36.8 $\pm$ 0.7	44.1 $\pm$ 0.3	-
10 mg	35.2 $\pm$ 0.1	43.2 $\pm$ 0.1	-
50 mg	34.7 $\pm$ 0.2	46.9 $\pm$ 0.1	67.1 $\pm$ 0.2
100 mg	36.4 $\pm$ 0.1	48.7 $\pm$ 0.1	80.7 $\pm$ 0.7
200 mg	43.5 $\pm$ 0.1	55.2 $\pm$ 0.1	80.6 $\pm$ 0.4
	100M_CNTs-TMOS	90M10A_CNTs-TMOS	80M20A_CNTs-TMOS
0 mg [308]	36.8 $\pm$ 0.7	44.1 $\pm$ 0.3	-
10 mg [308]	31.2 $\pm$ 0.1	43.7 $\pm$ 0.6	-
50 mg	33.3 $\pm$ 0.1	47.3 $\pm$ 0.1	62.1 $\pm$ 0.5
100 mg	33.1 $\pm$ 0.1	47.7 $\pm$ 0.1	64.7 $\pm$ 0.3
200 mg	36.1 $\pm$ 0.1	48.6 $\pm$ 0.2	68.2 $\pm$ 0.1
		90M10A_GO	80M20A_GO
0 mg	-	48.0 $\pm$ 0.1	49.3 $\pm$ 0.1
10 mg	-	43.6 $\pm$ 0.3	50.0 $\pm$ 0.2
50 mg	-	46.3 $\pm$ 0.1	49.6 $\pm$ 0.1
100 mg	-	45.4 $\pm$ 0.1	48.8 $\pm$ 0.2

The results in Table 4.3 indicate that the nature of the silica matrix has a significant impact on the thermal conductivity. It appears that, increasing the amount of APTMS in the system, leads to a significant increase in the values of thermal conductivity, with the samples containing 20% of APTMS presenting the highest values. This variation can also be attributed to the higher values of density verified for these samples (Table 4.1), since thermal conductivity of aerogels highly depend on their bulk density. Several authors [8, 196, 298, 305, 338] have demonstrated that this dependence has typically a U-shape, with the solid thermal conductivity being favored by higher densities. On the contrary, the gaseous thermal conductivity has a higher impact for aerogels with lower densities, since the presence of larger pores do not contribute to Knudsen effect [298].

Moreover, the carbon nanostructures also have an impact in the thermal conductivity of the aerogels. The addition of low amounts of the 1D and 2D carbon materials may lead to a reduction in the total thermal conductivity. In the case of 1D composites, the most considerable reduction ($\sim$ 15 %) was observed for the sample 100M_CNT-TMOS_10, if compared with the corresponding pristine sample. Nevertheless, an increase in the thermal conductivity is observed for all silica systems with the addition of higher quantities of CNTs to the network. This trend can be explained by the potential of percolation threshold in these materials, where the carbon nanostructures increasingly

become in contact with each other. Thus, there is an increase in the solid thermal conductivity, since preferential paths of heat transfer are formed and CNTs are well known for their high thermal conductivities. Due to the significant shrinkage observed in the 1D composites with higher APTMS content, this effect is most probably enhanced, as observed by SEM imaging (Figure 4.8), that clearly shows CNTs in close contact with each other.
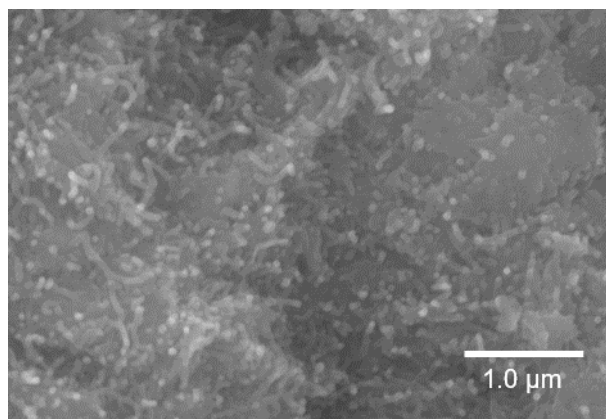
Figure 4.8: SEM image of the 80M20A aerogels with 200 mg of CNTs-HNO$_3$.

Considering the different types of surface modification of the carbon nanotubes, lower values of thermal conductivity were obtained for the samples with CNTs-TMOS, probably due to the fact that the silica particles grow around these nanotubes, as previously seen the TEM imaging (Figures 4.4). Thus, preventing the contact between the carbon nanotubes and simultaneously altering the silica network, which leads to a reduction of the solid thermal conductivity. The addition of CNTs-HNO$_3$ also caused a decrease in the thermal conductivity of the 1D composites, probably due to the same reasons. Nonetheless, the found values are higher than those for silanized CNTs, since chemical interaction between the silica network and 1D nanostructures is not so considerable, and it has been verified that these CNTs are further exposed in the aerogel matrix.

As a result of not being able to obtain a cohesive gel for 100% MTMS, lower values of thermal conductivity were not achieved by the samples with graphene oxide, as the presence of APTMS always causes an increase in this property, as previously mentioned. For the composites made with GO, even though a small reduction in the thermal conductivity is observed for the sample 90M10A_GO_10, the remaining materials all showed very similar values regarding this property. It was expected that the presence of GO would lead to some variability in thermal conductivity, since, with the addition of small amounts of this carbon nanomaterial, a tendency to decrease the thermal conductivity was observed in the literature [98, 215], however, no significant variation

was here observed. This can be explained by the pore size of the silica matrix. The reduction in thermal conductivity by the addition of GO occurs because this material makes the pore distribution of the silica matrix more uniform, with a higher amount of pores smaller than 70 nm [98, 215], which leads to the constriction of free-molecule-movement. In the case of the silica matrix here developed (MTMS/APTMS using PEG as surfactant), even with addition of GO, the pores do not achieve this low size, always remaining in the macropores range (Table 4.2 and Figure 4.5), with the GO even causing the increase of the average pore size in some samples, thus originating an increase of the gaseous contribution to the thermal conductivity.

The effect of temperature on thermal conductivity was determined within a range of temperatures, from -25 °C to 125 °C, for the samples 100M and 100M_CNT-TMOS_10, with the latter being the sample with the lowest value of thermal conductivity (Table 4.3). The obtained results are illustrated in Figure 4.9. As expected, there is a linear increase between temperature and measured thermal conductivity, with the 1D composite showing a smaller increase rate. The main difference between the two samples is observed when both were submitted to a temperature of 125 °C, with the silica aerogel presenting a value of 59.2 mW.m^{-1}.K^{-1} and the CNT-silica aerogel composite with nearly 30% lower thermal conductivity value (42.8 mW.m^{-1}.K^{-1}). This difference indicates a significant improvement in the thermal insulation performance of the silica aerogel, as the 1D composite shows lower thermal conductivities in the overall temperature range, especially for temperatures above 50 °C. This is possibly due to the opacifying effect of CNTs, which limits the radiative contribution on thermal conductivity, as the radiative conductivity becomes increasingly significant at temperatures above 300 K (27 °C) [8].
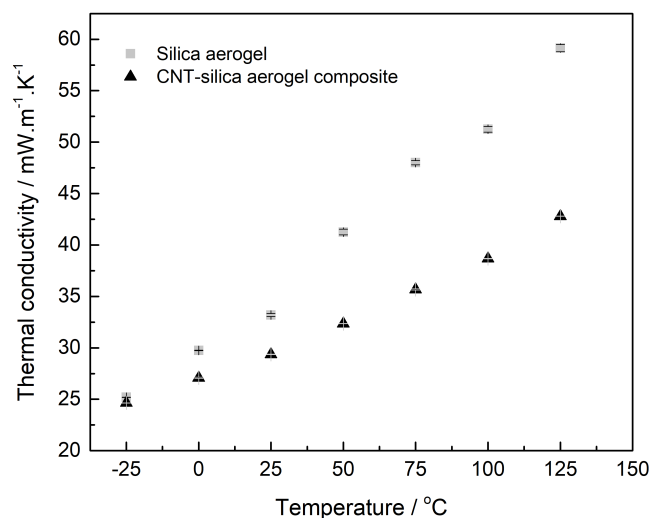
Figure 4.9: Thermal conductivity of the 100M and 100M_CNT-TMOS_10 aerogels in different temperatures.

The mechanical behavior of the silica aerogels and 1D and 2D composites was also evaluated by uniaxial compression tests, as shown in Figure 4.10. For the 100M materials, the Young's modulus is low and approximately the same (in the order of tens of kPa - Table B2) with the most significant variation being observed for the samples with higher amount of CNTs, which showed values of 154 kPa, for the 100M_CNT-HNO$_3$_200, and 72 kPa, for the 100M_CNT-TMOS_200. Although small variations took place, all the samples are flexible, as they showed high recovery rates. Higher variability is observed for the 90M10A samples with 1D carbon nanostructure, with the Young's modulus appearing to vary randomly. These systems are still relatively flexible, as Young's modulus in the order of tens of kPa were once again obtained, however, these composites have lower recovery rates than the corresponding 100M samples. Even though there are some differences in their microstructure, these samples present larger pores than the other 1D composites systems, which can be a possible explanation for these meaningless variations. Besides that, it is also worth mentioning that, due to the inherent variability of the compression tests, these tests are not sensitive enough to detect small variations in the samples structure. For the 80M20A composites with carbon nanotubes, the highest values were obtained, with the Young's modulus in the order of MPa (between 1 and 14 MPa - Table B2), and these results are probably due to the significant shrinkage observed for these samples during the drying step, leading to higher bulk densities. In contrast to what is observed for 100M-based aerogels, these samples are not flexible.
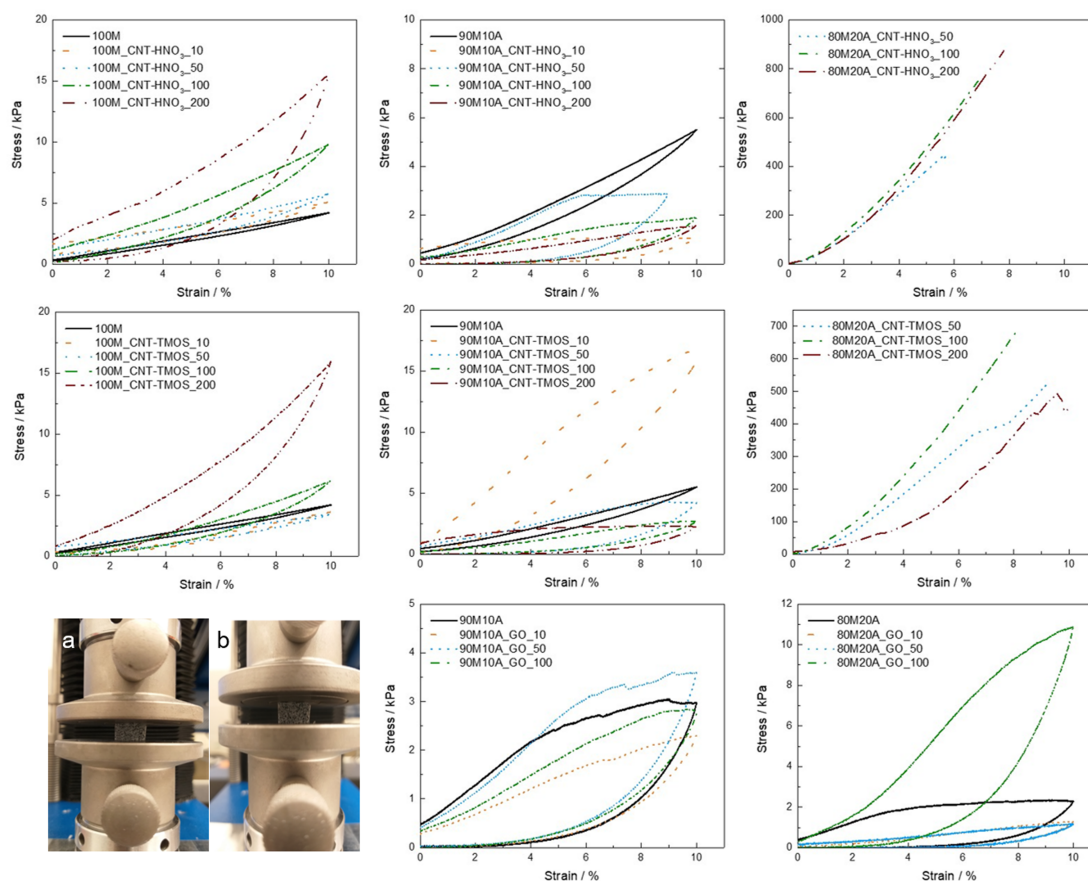
Figure 4.10: Stress-strain curves for silica aerogels and corresponding carbon nanomaterials-silica aerogel composites obtained by compression-decompression with a load cell of 50 N. a) Sample 100M_CNT-TMOS_10 under compression; b) Sample 100M_CNT-TMOS_10 after load release.

The 2D composite systems present similar mechanical behavior, with Young's modulus values below 50 kPa, with the exception of 80M20A_GO_200 that showed a Young's modulus of 150 kPa. The substantial presence of large pores within these materials is probably the main responsible for these findings, since only small variations in the measurements were detected with the addition of GO to the systems. Moreover, these results are also in agreement with the ones obtained for the 90M10A samples with CNTs, which also present pores in the macropore range.

4.3.4 Electrochemical characterization

The electrochemical performance of the aerogels and corresponding 1D and 2D composites were investigated by CV and EIS. In order to quantitatively evaluate the charge storage capacity, the specific capacitance was determined using the equation 4.4, with the results summarized in Table 4.4. In general, the presence of amine groups has a significant impact on the specific capacitance, since these systems show higher values

than the 100% MTMS composites.

Table 4.4: Calculated specific capacitance of silica aerogels without carbon nanostructures and with different amounts of CNTs-HNO$_3$, CNTs-TMOS and GO from the CV curves at 50 mV.s^{-1}.

Amount of carbon nanostructure	Specific capacitance (μA.g^{-1})		
	100M_CNTs-HNO$_3$	90M10A_CNTs-HNO$_3$	80M20A_CNTs-HNO$_3$
0 mg	98.3	906.8	184.2
10 mg	222.9	537.4	287.1
50 mg	260.0	519.4	383.7
100 mg	395.8	715.0	434.7
200 mg	1108.9	442.7	943.7
	100M_CNTs-TMOS	90M10A_CNTs-TMOS	80M20A_CNTs-TMOS
0 mg	98.3	906.8	184.2
10 mg	212.0	990.7	287.3
50 mg	242.4	1419.3	340.4
100 mg	566.5	8307.2	635.7
200 mg	877.6	4230.2	701.6
		90M10A_GO	80M20A_GO
0 mg	-	450.1	343.0
10 mg	-	307.1	845.7
50 mg	-	588.6	948.4
100 mg	-	1541.6	1279.2

The cyclic voltammograms performed for the carbon nanostructures-silica aerogel composites samples are shown in Figures B5 to B15 in Appendix A.

For most of the systems, increasing the carbon content in the composite leads to an increase in the specific capacitance of the materials. In the 90M10A systems with carbon nanotubes, the variation was not linear, and the highest values for these composites were achieved for an amount of 100 mg of CNTs. These systems also showed the highest values of specific capacitance, and these can be correlated with the different type of porosities, as these samples show significant larger macropores than the remaining 1D composites (Figure 4.4). Even though smaller pores (micro- and mesopores) can significantly increase the specific surface area of aerogels, their presence can have a negative effect in the electrical properties. In porous materials, the electrical double layer (EDL) is formed inside the material pores and not adjacent to the electrode surface. Thus, when the pore size is in the same magnitude order as the EDL thickness, the electrical double layers inside the pore overlap, causing a reduction in their electrical capacities [339, 340]. As this overlapping effect exists only in microporous and in a part of mesoporous region, the 90M10A samples do not show this effect, which can explain the superior values obtained for these aerogels. The same explanation can be used for the 2D composites, if compared

with their CNTs equivalent, especially for the 80M20A systems, as the composites show significant different average pore sizes (Tables 4.1 and 4.2), which supports the fact that the GO composites present higher specific capacitance values.

Regarding EIS analysis presented in Figure 4.11, the spectra were fitted with the same electrical equivalent circuit consisting of the cell resistance (R_Ω - R1) in series with a parallel combination of a constant phase element, (CPE - Q1), and a charge transfer resistance (R_{ct} - R2), as shown in Figure 4.11. The CPE is assumed as a non-ideal capacitor according to the relation CPE = $-1/(Ci\omega)^\alpha$, where C is the capacitance, which describes the charge separation at the double layer interface, ω is the angular frequency and α is the roughness factor (due to heterogeneity of the surface), that varies from 0.5 to 1, where an α value of 1 represents a perfectly smooth surface [341, 342].
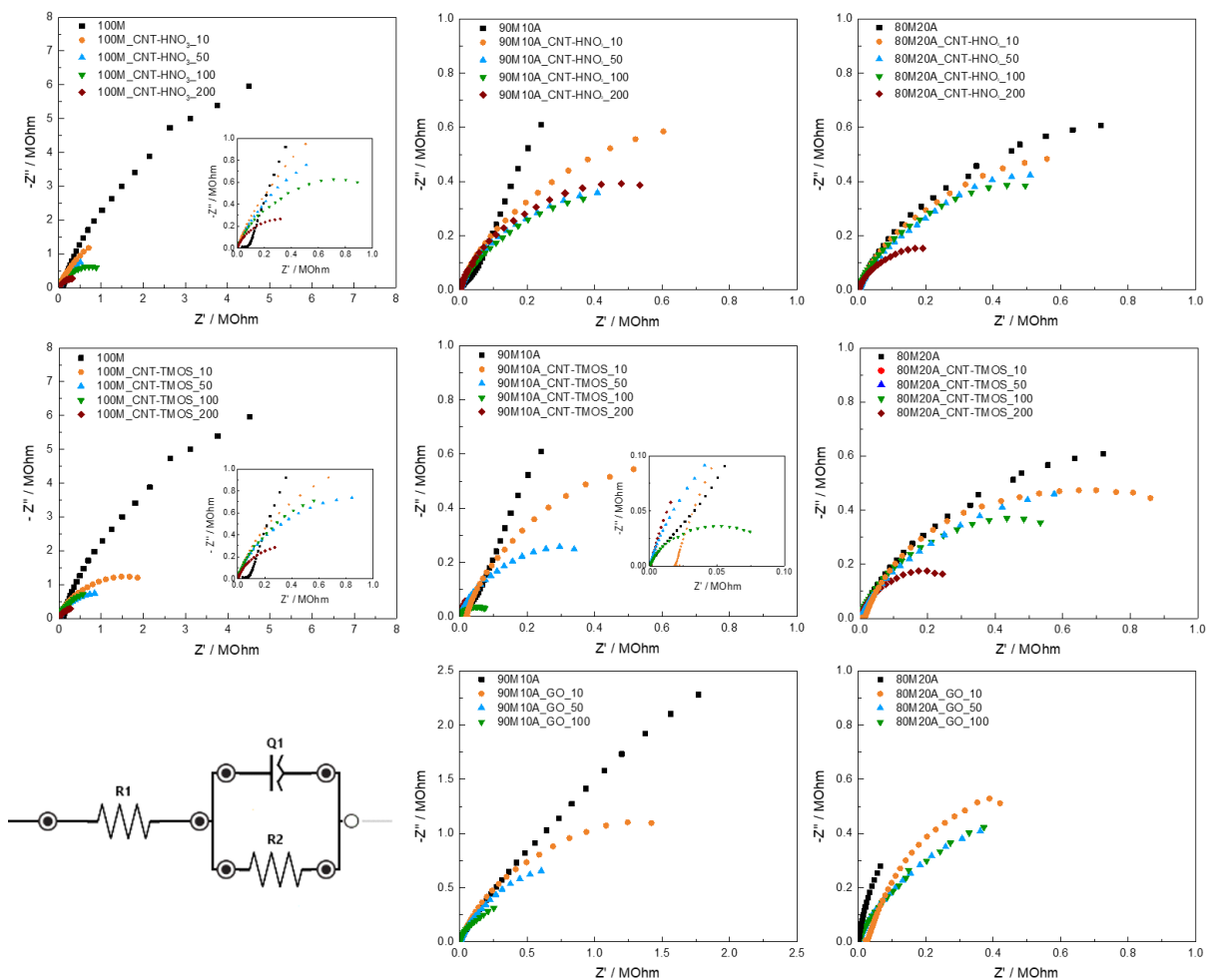
Figure 4.11: The Nyquist plots of the silica aerogels and carbon nanomaterial-silica aerogel composites electrodes and their equivalent circuit.

All EIS Nyquist plots present a single region, a semicircular part, probably corresponding to the electron transfer process. For the electrodes composed of the pristine aerogels, the semicircle shows larger diameters, and, as the semicircle diameter is directly

proportional to the resistance of the electrons flow at the interface, these results indicate that in these samples the electron transfer is not very effective. The presence of 1D and 2D carbon nanostructures leads to a decrease of the imaginary part of the impedance (-Z"), suggesting the increase of the capacitance, which in its turn, improves the electrochemical response. This is in agreement with the results obtained by the cyclic voltammograms for these electrodes.

For most of the systems, as the amount of carbon material increased, further reductions in the impedance were observed, and this decrease indicates that the electrons could be transferred faster with lower loss, which could lead to higher electrochemical performances. These results were expected considering that the carbon nanostructures possess high electrical conductivity and decrease the R_{ct}, allowing a quick electron transfer through the 3D structure. Again, the exception for this continuous decreasing trend in impedance was the 90M10A with CNTs. The samples with 200 mg of CNTs show higher impedance values than those containing 100 mg. These variations are probably due to the materials porosities, as previously discussed regarding the specific capacitances determined by CV. Finally, the presence of amine groups in the silica matrix also caused a significant change in the samples resistance. The aerogels developed with APTMS present a smaller semicircle than the 100M samples. There are two factors which may explain the cause for this difference; first, the different porous structure which may enhance the electron transport at electrode/electrolyte interface leading to higher values of capacitance [343], and, second, the introduction of nitrogen which endows the electron donor characteristics and provides electrochemically active sites for pseudo-capacitive reactions [344].

4.4   Conclusion

The influence of adding different 1D and 2D carbon nanostructures in the properties of MTMS-based silica aerogels was here evaluated. The composite materials consisting of carbon nanotubes or graphene oxide and silica aerogels have been prepared by using an acid-base-catalyzed sol–gel process. The presence of these carbon materials did not prevent the formation of the silica three-dimensional network; however, the addition of GO caused more impact in the aerogels' chemical structure than CNTs. The physical properties were also affected by their addition, with variations being observed mainly in the specific surface area and average pore sizes, but the presence of APTMS in the silica matrix proved to be more influential than the carbon nanomaterials.

The CNTs have a more significant impact in the microstructure of the materials than the GO. As observed in SEM and TEM images, the silica matrix can grow around the 1D nanomaterials and follow their shape, especially for the CNTs modified with TMOS. Regarding the thermal properties, it was proven that the presence of GO did not have a meaningful influence in the thermal conductivity, however this is probably due to the presence of pores in the micrometers order, that have a larger impact in this property than the GO. On the other hand, the addition of small amounts of CNTs leads to a decrease in the thermal conductivity of the silica aerogels, with this effect being more significant in temperatures above 50 °C, achieving reductions of up to 30%, if compared with the silica aerogel, at 125 °C. The addition of CNTs also led to an improvement on the aerogels' thermal resistance, as previously determined [308]. The combination of these excellent thermal properties indicates that the CNTs-silica aerogel composites have a great potential to be applied in the thermal insulation field, especially in high-temperature environments.

The addition of these carbon nanomaterials also has a significant effect in the electrochemical properties of silica aerogels, leading to an increase in the specific capacitance and a decrease of the resistance of the electrons flow at the interface of these materials. The higher specific capacitances were achieved by the 90M10A systems with 100 mg of CNTs-TMOS and GO. For most of the systems, the lowest resistances were obtained for the composites with the higher amounts of carbon nanostructures, as expected.

In summary, for MTMS-APTMS silica aerogel systems, CNTs have a more significant impact in the aerogels' features than GO, and it is possible to change both the silica matrix and the amount of carbon nanostructure to achieve the desired characteristics. The possibility of tailoring the properties of these materials gives them a wide application potential in different areas, such as thermal insulation, adsorption and energy related applications.

Chapter 5

Effect of carbon nanostructures addition in silica aerogel's adsorption of organic pollutants

Part of this chapter comprises the work *Amine Modification of Silica Aerogels/Xerogels for Removal of Relevant Environmental Pollutants* published in the journal Molecules (2019), 24, 3701, by Alyne Lamy-Mendes, Rafael B. Torres, João P. Vareda, David Lopes, Marco Ferreira, Vanessa Valente, Ana V. Girão, Artur J. M. Valente, and Luísa Durães; and on the work *Carbon nanostructures-silica aerogel composites for adsorption of organic pollutants* by Alyne Lamy-Mendes, David Lopes, Ana V. Girão, Rui F. Silva and Luísa Durães that will be submitted.

5.1   Introduction

The growth of industrial complexes has led to a considerable contamination increase in aquatic environments, as a significant amount of different pollutants, both organic and inorganic, are released with wastewater, reaching natural aquifers [345, 346].   For example, substantial quantities of aromatic compounds are employed as industrial solvents and are present in petroleum and gasoline [347–349], and due to their toxicity, associated with carcinogenic and mutagenic effects in some cases, there is a growing interest and need to remove these pollutants from industrial effluents, from health and environmental perspectives [346, 350, 351]. Phenol, for example, is highly toxic even at low concentrations [352] and the exposure to pollutants such as benzene and xylene for long periods of time leads to several negative effects on human health, from skin

irritation to cancer and liver lesions [353]. In addition, the removal process of volatile organic compounds (VOCs) is a recurrent challenge due to their highly volatile nature and persistency in the environment [354].

Besides these well-known contaminants, pharmaceutical active compounds (PhACs) have been recently identified as emerging pollutants and, due to their consumption growth, they are continuously entering in the environment media, particularly in aquatic ones, due to the effluents from industrial, urban or hospital wastewater treatment plants [355–357]. From the 150 pharmaceuticals daily used in significant amounts worldwide, 55 of them are detected in relevant concentrations [358–360]. Amoxicillin (AMX), a broad-spectrum β-lactam antibiotic, is one of the largely produced drugs and most commonly used antibiotics [361], while Naproxen (NPX) is a non-steroidal anti-inflammatory drug, being one of the most prescribed among this category [362]. As consequence, both drugs have been detected in water resources [363–367] and wastewater sewers [368–372]. The presence of these PhACs can lead to the thrive and expansion of antibiotic resistance genes (ARGs), as even non-antibiotic pharmaceuticals, including NPX, contribute to the horizontal transfer of ARGs [373], and lower effectiveness in treating the original diseases [374]. Besides, as these PhACs are designed to induce a physiological response, their presence in the aquatic environment is problematic since they can potentially affect both aquatic and human lives [355, 375].

For all the aforementioned reasons, the more conventional wastewater treatments need to be improved, due to increasing difficulty to comply with regulations [376]. Among the different treatment technologies available as, for example, biological treatment, chemical oxidation, coagulation, precipitation and membrane separation, the adsorption process has aroused special interest [377, 378]. Its effectiveness, easy adaptation, simple operation and the availability of different adsorbents make adsorption a viable method for a wide range of applications [379, 380]. For the removal of pollutants from aqueous solutions, materials such as activated carbon, mesoporous SiO_2, alumina, zeolites or clays are commonly applied [352, 381, 382]. However, the use of these predominant industrial sorbents is limited due to some drawbacks, including poor adsorption capacities, low removal efficiency and slow kinetics [101, 383].

Silica aerogels are a good alternative to overcome these limitations via manipulation of sol-gel technology. A combination of high porosity, small pores and a versatile surface chemistry results in capable adsorbents [101, 384]. In fact, a higher surface area favors adsorption performance and the latter can be further enhanced with surface functional groups or charge [385]. By changing the aerogels' degree of hydrophobicity, Štandeker *et al*. [81], through the incorporation of methyltrimethoxysilane (MTMS) or trimethylethoxy-

silane (TMES) in tetramethoxysilane (TMOS) based aerogels, were able to improve the removal of toxic organic compounds from water, such as benzene, toluene, chloroform and chlorobenzene. The synthesized superhydrophobic materials showed adsorption capacities 15 to 400 times higher than the values obtained by granulated active carbon. Qin *et al.* [82] changed the hydrophilic character of tetraethylorthosilicate (TEOS) based aerogel by modifying these materials with trimethylchlorosilane (TMCS). With these aerogels, it was possible to achieve high removal rates of phenol from water, with a maximum adsorption capacity of 142 mg.g^{-1} when the equilibrium concentration of phenol was 290 mg.L^{-1}.

From the examples reported above, the interaction between silica aerogels and the pollutants can be improved by modifying the aerogels' surface chemistry. Apart from the presence of methyl groups, the presence of amino and carboxyl functional groups can also result in strong affinities towards specific contaminants [386, 387]. However, some of these modifications result in the decrease of the specific surface area [388, 389]. Even though specific surface area is a key factor in the pollutants removal, several factors can be adjusted to enhance the overall adsorption rate, such as pH, contact time and contaminant concentration [390, 391]. Another possible modification that can be made in the silica aerogels, to further improve their adsorption capacities, is the addition of carbon nanostructures, which are highly efficient adsorbents for water treatments due to their various morphologies and high specific surface area [392]. Moreover, these materials also allow chemical modification and functionalization [392, 393], which can enhance their affinity with emerging chemical contaminants.

Due to the enhanced affinity/interaction of amino groups and carbon nanomaterials with several pollutants, the aim of this part of the work is to show the influence of the amino functionalization and the addition of carbon nanotubes or graphene oxide into silica aerogels built from MTMS regarding their removal capacities for different contaminants in aqueous solutions. The chosen pollutants, benzene, toluene, xylene, phenol, amoxicillin and naproxen, have high environmental relevance, owing to their toxicity and persistency, and are also commonly found in different wastewaters. The obtained results are compared against other adsorbents reported in the literature for these pollutants.

5.2 Experimental Section

5.2.1 Synthesis of carbon nanomaterial-silica aerogel composites

The silica materials tested in this chapter were prepared as described in previous chapters (Chapters 3 and 4). Briefly, the composite materials were prepared by a two-step acid–base catalyzed sol–gel process with oxalic acid (0.01 M) as acid catalyst, ammonium

hydroxide (1 M) as basic catalyst. In the case of the composites with CNTs, hexadecyltrimethylammonium bromide (CTAB) was used as surfactant, while for the GO-silica aerogel composites, the surfactant was Poly(ethylene glycol) 600 (PEG). Initially, two amounts of these compounds were tested, 0.83 wt% and 4.0 wt%, for the silica aerogels. These materials were denoted as xMyA, where x in xM is the mol percentage of Si from MTMS, y in yA corresponds to the mol percentage of Si from APTMS. Two types of carbon nanotubes were here added to the silica matrix, CNT-HNO$_3$ and CNT-TMOS, with the modification procedure being described in Section 4.2.2. For the composites with CNTs and GO, the designations xMyA_CNT_z or xMyA_GO_z were applied, where z is the amount in mg of carbon nanomaterial added to the system (up to 50 mg).

Samples containing 20 % of APTMS were also tested as adsorbents, however, for most of the pollutants, there were no significant improvements in the removal efficiencies. Only in the case of amoxicillin the presence of higher amounts of amine groups was beneficial, so the results of the adsorption tests of these samples will only be presented in this particular case.

5.2.2 Characterization

In order to assess the incorporation of the amine groups into the silica structure, elemental analysis of previously grounded samples (*EA 1108* CHNS-O, *Fision Instruments*), in terms of C, H and N elements, was performed.

Bulk density was calculated by measuring the mass and volume of portions of the sample. For samples that can be cut into regular forms, the volume was assessed by measuring their dimensions in the three axes; for irregular pieces, it was obtained by liquid displacement. The Brunauer-Emmett-Teller (BET) specific surface area was obtained through nitrogen adsorption (*ASAP 2000*, *Micrometrics*).

The microstructures of the prepared samples were analyzed through scanning electron microscopy (SEM) using a *Hitachi FEG-SEM SU70*, after being coated with a conductive carbon thin layer, and *Compact/VPCompact FESEM* (*Zeiss Merlin*), after being coated with a thin gold layer.

Solid-State Nuclear Magnetic Resonance (SSNMR) analysis was performed to assess if any modification in the surface chemistry of the synthesized materials occurs after the adsorption of both drugs, amoxicillin and naproxen. The SSNMR spectra were collected as described in Chapter 4.

5.2.3 Adsorption Experiments

The adsorbents were obtained from the prepared materials after milling and sieving to obtain particles of 75–250 μm. The adsorbate solutions were prepared with high purity water. The adsorption tests were conducted by placing the adsorbent in contact with the adsorbate solution in a test flask under shaking — *Heidolph–REAX 20* shaker, at 16 rpm and 20 °C. The adsorbent concentration in the test flask was kept at 2 g.L^{-1}. In the equilibrium tests, the initial concentrations of the solutions varied between 10–500 mg.L^{-1} for benzene and its derivatives, and between 10-50 mg.L^{-1} for the drugs. The used concentrations were chosen to be representative of the organic compounds concentration range in an industrial wastewater [394–396]. All the solutions were shaken for 24 h to ensure equilibrium conditions. The kinetic experiments were conducted at different time intervals, from 2 min to 360 min. For benzene and its derivatives, the solutions had an initial concentration of 100 mg.L^{-1}, while for the drugs the initial concentration was 25 mg.L^{-1}.

After each test was concluded, the solutions were filtered, and their concentration determined by Ultraviolet–visible (UV-Vis) spectrophotometer (*T70*, *PG Instruments*) using specific wavelengths: 255, 262, 265, 270, nm for benzene, toluene, xylene and phenol, respectively, and 273 and 272 nm, for amoxicillin and naproxen, respectively.

The equilibrium adsorption capacity, q_e (mg.g^{-1}), is defined by Equation (5.1), where C_0 (mg.L^{-1}) and C_e (mg.L^{-1}) are the initial and equilibrium adsorbate concentrations, respectively, m (g) is the mass of the adsorbent and V (L) the volume of the solution:

$$q_e = \frac{V(C_0 - C_e)}{m} \tag{5.1}$$

The removal efficiency (*RE*) of the pollutants was calculated by Equation (5.2):

$$RE\,(\%) = \frac{(C_0 - C_e)}{C_0} \times 100 \tag{5.2}$$

In order to understand the interaction at equilibrium between the adsorbent and adsorbate, three models were studied in this work, the Langmuir, Freundlich and Brunauer–Emmett–Teller (BET) isotherm models. The models were fitted to the data using non-linear fitting algorithms.

The Langmuir isotherm is described by Equation (5.3), where q_{max} is the monolayer adsorption capacity of the adsorbent (mg.g^{-1}) and K_L is the Langmuir equilibrium constant (L.mg^{-1}):

$$q_e = \frac{q_{max} K_L C_e}{1 + K_L C_e} \tag{5.3}$$

The Langmuir adsorption isotherm model considers that the thickness of the adsorbed layer is one molecule, *i.e.* a monolayer adsorption, and that the adsorption process on the surface occurs at specific sites. The following premises are also assumed for this model: no lateral interaction occurs between the adsorbed molecules, all sites should have equal affinity regarding the adsorbate and that the surface is homogeneous [397]. The features of the Langmuir isotherm can be indicated by the dimensionless constant called separation factor (R_L), also known as equilibrium parameter, that is defined by equation (5.4):

$$R_L = \frac{1}{1 + K_L C_0} \tag{5.4}$$

where C_0 is the initial concentration of the adsorbate in mg.L^{-1}. The value of R_L indicates the shape of the isotherms to be either irreversible ($R_L = 0$), favorable ($0 < R_L < 1$), linear ($R_L = 1$) or unfavorable ($R_L > 1$) [397, 398].

The Freundlich isotherm is described by Equation (5.5). The parameters K_F and n_F refer to the Freundlich constant ((mg.g^{-1}) (L.mg^{-1})$^{1/n_F}$) and to the heterogeneity factor, respectively:

$$q_e = K_F \, C_e^{\,1/n_F} \tag{5.5}$$

Freundlich model is used to describe the reversible and non-ideal adsorption process, and, on contrary to Langmuir, a multilayer adsorption is possible. This model is also able to provide information about the adsorption mechanism, when the heterogeneity factor is higher than 1, a cooperative adsorption occurs (multilayer), while if the $1/n_F$ is lower than 1, the process is favorable and the mechanism of sorption is mainly chemisorption [397, 398].

The BET extinction model related to liquid–solid interface, which is characterized by the formation of an initial monolayer followed by a multilayer physical-based sorption [349, 399], is exhibited in Equation (5.6), where C_{BET}, C_S, q_S and q_e are the BET adsorption isotherm (L.mg^{-1}), adsorbate monolayer saturation concentration (mg.L^{-1}),

theoretical isotherm saturation capacity ($mg.g^{-1}$) and equilibrium adsorption capacity ($mg.g^{-1}$), respectively [400].

$$q_{e} = \frac{q_{S} C_{BET} C_{e}}{(C_{S} - C_{e}) \left[1 + (C_{BET} - 1) \left(\frac{C_{e}}{C_{S}} \right) \right]} \qquad (5.6)$$

The BET model is considered a particular form of the Langmuir model, and the same suppositions are here applied, with the addition of the assumption that same adsorption energy is found in the second, third and higher layers. However, the first layer has a different energy than the other layers [397].

The rate of the adsorption process was evaluated by fitting two empirical kinetic models to the kinetic data, namely the pseudo-first and pseudo-second order models, as described by Equations (5.7) and (5.8) (after integration with appropriate boundary conditions) [401]:

$$q_{t} = q_{e} \left(1 - e^{-tk_{1}} \right) \qquad (5.7)$$

$$q_{t} = \frac{q_{e}^{2} k_{2} t}{q_{e} k_{2} t + 1}, \qquad (5.8)$$

where k_{1} ($1.min^{-1}$) and k_{2} ($g.(mg.min)^{-1}$) are the pseudo-first and pseudo-second order rate constants, respectively.

The Akaike's information criteria (AIC), Equation (5.9), was the chosen methodology for the evaluation of the best model [402]:

$$\text{AIC} = n\log \left(\frac{s^{2}}{n} \right) + 2K + \frac{2K(K+1)}{n - K - 1}, \qquad (5.9)$$

where s^{2} is the residual sum of squares, n is the number of experimental data points and K is the number of model parameters. The last term in AIC equation is added when the sample size is small (n/K < 40) to prevent an overfit [403].

Considering that individual AIC values are not interpretable, the following re-scaling allows the comparison between models

$$\Delta_{i} = AIC_{i} - AIC_{min}, \qquad (5.10)$$

where AIC_{min} is the minimum of the different AIC values. The Δ_{i} allows a meaningful interpretation: models with $\Delta_{i} \leq 2$ have a substantial support, those with $3 \leq \Delta_{i} \leq 7$ have considerably less support, and the ones with $\Delta_{i} \geq 10$ have essentially no support [403, 404].

5.3 Results and discussion

5.3.1 Silica Aerogels Selection Based on Preliminary Adsorption Tests

The first step for the adsorbents screening was to determine which quantity of surfactant used during the synthesis procedures would lead to better removal rates for each pollutant. At the same time, the influence of amine groups in the silica matrix, with the addition of 10 mol percentage of APTMS, in the adsorption process was also tested. For these studies, only CTAB was used as surfactant, in order to reduce the number of experiments. These preliminary results are presented in Table 5.1.

Table 5.1: Silica precursor system, amounts of CTAB used during the synthesis, and the removal efficiency of the materials for the studied pollutants.

| Pollutant | C_0 | Removal Efficiency (%) | | | |
| | | MTMS | | 90MTMS/10APTMS | |
	(mg.L^{-1})	0.83 wt%	4.0 wt%	0.83 wt%	4.0 wt%
Benzene		72.1 ± 2.1	51.0 ± 1.3	50.0 ± 2.0	15.4 ± 1.2
Toluene	200	81.1 ± 0.7	68.9 ± 2.3	48.7 ± 2.4	51.7 ± 1.9
Xylene		96.9 ± 1.4	86.7 ± 0.1	66.9 ± 0.8	74.8 ± 0.7
Phenol		20.0 ± 2.4	8.4 ± 1.7	25.9 ± 1.2	19.1 ± 1.8
Amoxicillin	25	5.3 ± 2.0	5.0 ± 2.3	15.6 ± 1.3	19.4 ± 2.5
Naproxen		84.2 ± 0.7	69.0 ± 0.9	79.0 ± 1.8	93.8 ± 0.3

For most of the adsorbate-adsorbent systems the lower amount of CTAB (0.83 wt%) presented better adsorption performance, so, based in these data, from now on, only samples with this quantity of surfactant will be characterized and used for the remaining adsorption tests. Regarding the silica systems, three organic compounds (benzene, toluene and xylene) were better removed by the material with only MTMS in the matrix, probably due to their non-polar nature and the matrix super-hydrophobicity (contact angles higher than 150°), which allows an hydrophobic interaction between the methyl groups derived from MTMS and these molecules.

For phenol and amoxicillin, the presence of amine leads to an improvement in the removal efficiency, which can be justified by the interaction of the amine group in the matrix with the hydroxyl group of these pollutants molecules by hydrogen bonding. For the naproxen, both matrices presented similar results, so, for this particular drug, the remaining tests will be performed with both silica systems, while for the other pollutants, only the best system will be used as adsorbent.

5.3.2 Properties of the Adsorbents

Elemental analysis was performed to assess the mass fraction of specific chemical elements, namely C, H and N. This technique can provide information about the incorporation of amine groups in the adsorbents and about the extent of the sol-gel reactions (incomplete or complete condensation) [405]. The theoretical weight percentages of Si + O, C, H and N were calculated on the assumptions that: (1) all hydrolyzable groups, from all the silica precursors, reacted—complete condensation; (2) one hydroxyl group per hydrolyzed precursor did not react—incomplete condensation 1OH; and (3) two hydroxyl groups per hydrolyzed precursor did not react—incomplete condensation 2OH. For the theoretical data, it is also considered a complete hydrolysis of the precursors and that all precursors molecules condensed. The experimental values from elemental analysis and theoretical results related to these elements are shown in Table 5.2.

Table 5.2: Experimental and theoretical percentages of chemical elements in the samples.

Samples		wt% Si + O ^{a}	wt% C	wt% H	wt% N
100M	Experimental	74.60	20.30 ± 0.39	4.70 ± 0.04	0.41 ± 0.03
	Complete condensation	77.60	17.90	4.51	0.00
	Incomplete condensation 1OH	78.93	15.78	5.30	0.00
	Incomplete condensation 2OH	79.97	14.11	5.92	0.00
90M10A	Experimental	74.17	18.81 ± 0.35	5.05 ± 0.10	1.96 ± 0.02
	Complete condensation	72.92	20.18	4.94	1.96
	Incomplete condensation 1OH	74.70	17.92	5.64	1.74
	Incomplete condensation 2OH	76.12	16.11	6.20	1.57

$^{(a)}$ The values indicated for Si + O are the differences between the sum of the other elements and 100%.

For the adsorbents developed without amine precursors, the experimental data are closer to the theoretical scenario of the complete condensation, while in the presence of amine groups, the experimental data indicate that an incomplete condensation occurs (Table 5.2). That incomplete condensation can be justified by the steric hindrance caused by the aminopropyl group, preventing the formation of siloxane bridges. Higher values of C were observed, indicating that not all precursors underwent complete hydrolysis. This discrepancy was expected, since the hydrolysis step is accomplished in very short periods. The presence of traces of N on the samples without the amine precursor (100M) is due to residues of ammonia catalyst [405]. The agreement between the experimental and theoretical amounts of N element for the samples synthesized with APTMS confirms the complete incorporation of this precursor in the silica network, proving a successful modification of the matrix.

The physical and microstructural properties of these materials are reported in Table

5.3. The addition of a 10 mol% Si from silica precursor containing the aminopropyl groups into MTMS-silica materials leads to a small increase in the bulk density, as observed in Table 5.3. However, all the carbon-nanotubes silica aerogels composite materials still have bulk density values lower than 80 $kg.m^{-3}$. While the addition of GO does not have a significant influence in this property, the presence of carbon nanotubes alters the bulk density, with small amounts of CNTs (10 mg) leading to a decrease in these values (Table 5.3).

Table 5.3: Summary of physical and microstructural properties of the synthesized silica aerogels and carbon nanostructures-silica aerogel composites with 0.83 wt% of surfactant.

Samples	Bulk density	Porosity	Pore volume	Specific surface area	Average pore size
	$(kg.m^{-3})$	(%)	$(cm^3.g^{-1})$	$(m^2.g^{-1})$	(nm)
100M	75.6 ± 2.8	94.8 ± 0.1	12.5 ± 0.5	444.6 ± 4.3	112.9 ± 3.4
100M_CNT-HNO$_3$_10	73.1 ± 2.8	93.9 ± 0.3	12.8 ± 0.7	465.4 ± 5.7	110.4 ± 7.7
100M_CNT-TMOS_10	61.3 ± 5.3	95.8 ± 0.2	15.6 ± 1.4	463.4 ± 4.5	134.9 ± 10.1
90M10A	79.3 ± 11.1	94.6 ± 0.7	11.9 ± 1.8	11.3 ± 0.2	4221 ± 546
90M10A_CNT-HNO$_3$_10	76.3 ± 2.5	95.2 ± 0.1	12.5 ± 0.4	293.7 ± 3.0	170.0 ± 7.3
90M10A_CNT-TMOS_10	76.2 ± 5.6	95.1 ± 0.3	12.5 ± 1.0	18.4 ± 0.3	2713 ± 180
90M10A	83.0 ± 2.8	93.9 ± 0.2	11.3 ± 0.4	5.02 ± 0.9	9021 ± 1929
90M10A_GO_10	79.2 ± 1.2	94.3 ± 0.1	11.9 ± 0.2	11.2 ± 0.2	4250 ± 140

All the samples show porosities superior to 93% and pore volume up to 15.6 $cm^3.g^{-1}$, with these results being similar to the ones obtained for their equivalents with 4.0 wt% of surfactants. The specific surface areas are the highest between the developed samples for the materials synthesized with only MTMS, being the obtained values consistent with the literature, as organically modified silica (ORMOSIL) aerogels usually have values between 250 and 800 $m^2.g^{-1}$ [79].

For all the samples with APTMS, the addition of amine groups caused a significant decrease in the specific surface areas, independently of the amount of surfactant (Table 4.2). The highest value among the 90M10A materials was obtained for the sample synthesized with CNT-HNO$_3$, and one possible explanation for this variation can be the fact that these carbon nanotubes are not being completely surrounded by the silica matrix, contrary to the observed for CNT-TMOS, and their surface area is probably also contributing to the overall value. The lowest values were obtained for the GO samples, independently of the amount of PEG.

Regarding the average pore sizes, the samples with lower surface areas presented the highest values as expected, with the samples with 10% of amine having pores in the micrometers order, with the exception of 90M10A_CNT-HNO$_3$_10. However, this

particular result can not be very accurate, as the average pore size is calculated from other properties (Equation 3.4), inclusive the specific surface area. In the case of 90M10A_CNT-HNO$_3$_10 sample, a higher value of specific surface area was obtained, nonetheless, as already explained, this value probably has a contribution of the CNTs surface area, but the carbon nanotubes do not contribute to the formation of new pores or reduction of the existing ones, which leads to a underestimation of the pore sizes. Higher values of pore size are, in fact, supported by the SEM images (Figure 5.1), as this sample presents pore sizes in the same order than the other materials.

In the SEM images, Figure 5.1, it is possible to observe a significant amount of macropores in all the samples, which is in agreement with the high values of pore sizes. For all composite materials the characteristic structure of aerogels (pearl-necklace) is observed. In the presence of carbon nanotubes, the samples synthesized with CNT-TMOS appear to have bigger secondary units than the composites obtained with CNT-HNO$_3$. These differences probably occur due to the fact that silica matrix is able to grow around the silanized CNTs, as mentioned in prior chapters, while this is not verified for the samples with CNT-HNO$_3$. Comparing the composites with CNT-HNO$_3$, the one with only MTMS in the matrix seems to have smaller secondary particles than the 90M10A samples and appears to have a more uniform pore distribution. The larger secondary units were obtained for the GO composite, with them having almost double the size than the samples synthesized with CNTs. This sample also has the largest pores among the composite materials, which is in agreement with the results of surface area and average pore size presented in Table 5.3.
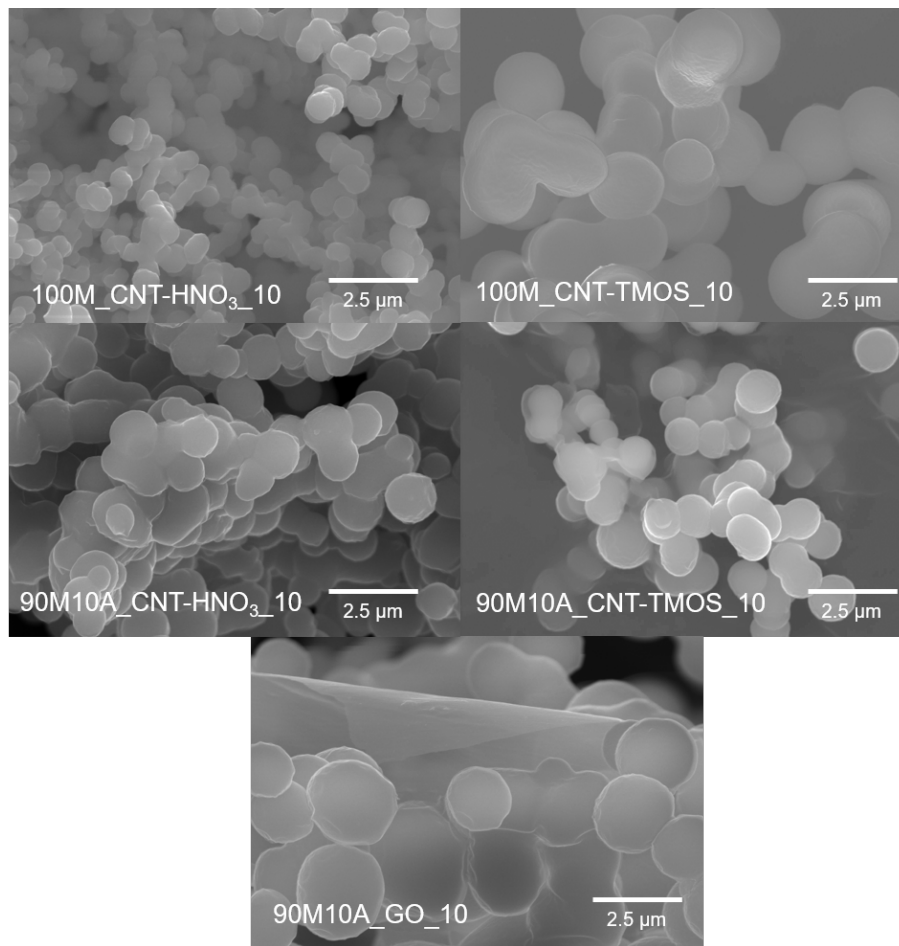
Figure 5.1: SEM images of the samples with 10 mg of CNTs-HNO$_3$ or CNT-TMOS and with 10 mg of GO obtained with 0.83 wt% of surfactant.

5.3.3   Study of adsorption of pollutants on the selected aerogels

Benzene

The parameters of the Langmuir, Freundlich and BET isotherm models, as well as the pseudo-first and pseudo-second order kinetic models, are presented in Table 5.4 for the adsorbent-adsorbate pairs tested. The AIC was used as the estimator of the models' relative quality. Experimental equilibrium and kinetic data, and the best isotherm/kinetic models for each material, are plotted in Figure 5.2.

For the sample 100M the best fit was achieved by Freundlich, which describes adsorption for heterogeneous surfaces, and the heterogeneity factor obtained for the 100M sample indicates that the adsorption of this pollutant is favorable in this case, as also perceived by the shape of the isotherm.

Table 5.4: Parameters of non-linear isotherms and kinetic models for benzene adsorption on the silica-based aerogels.

Isotherm Model	Parameters	100M	100M_CNT-TMOS_10	100M_CNT-HNO$_3$_10
Langmuir	q_m (mg.g^{-1})	88.1 ± 5.4	70.7 ± 6.0	78.5 ± 5.8
	K_L (L.mg^{-1})	0.13 ± 0.07	0.12 ± 0.02	0.05 ± 0.01
	R_L	0.015 - 0.43	0.016 - 0.45	0.038 - 0.67
	AIC	42.8	31.8	27.6
Freundlich	$1/n_F$	0.4 ± 0.03	0.3 ± 0.02	0.4 ± 0.02
	K_F ((mg.g^{-1}) (L.mg^{-1})$^{1/n_F}$)	12.7 ± 2.0	15.3 ± 1.0	7.6 ± 0.7
	AIC	32.7	32.6	29.0
BET	q_S (mg.g^{-1})	62.2 ± 3.8	44.1 ± 4.3	53.7 ± 5.9
	C_{BET} (L.mg^{-1})	135.7 ± 38.2	144.4 ± 18.1	62.8 ± 8.8
	C_S (mg.L^{-1})	587.6 ± 75.3	550.3 ± 77.6	698.2 ± 157.2
	AIC	34.8	27.0	27.0
	Maximum experimental q_e (mg.g^{-1})	114.4 ± 2.1	111.4 ± 3.9	103.0 ± 4.8
	Removal Efficiency (%, C_0 = 200 mg.L^{-1})	72.1 ± 2.0	53.9 ± 2.4	60.0 ± 3.0
Kinetic Model	Parameters	100M	100M_CNT-TMOS_10	100M_CNT-HNO$_3$_10
Pseudo-First Order	k_1 (1.min^{-1})	0.3 ± 0.2	0.3 ± 0.1	0.05 ± 0.01
	q_e (mg.g^{-1})	34.1 ± 0.5	34.7 ± 0.2	30.5 ± 0.6
	AIC	45.5	33.7	35.6
Pseudo-Second Order	k_2 x 10^3 (g.(mg.min^{-1}))	17.3 ± 6.7	30.6 ± 7.2	2.3 ± 0.2
	q_e (mg.g^{-1})	35.1 ± 0.5	35.1 ± 0.2	33.8 ± 0.4
	AIC	40.1	27.5	16.3
	Experimental q_e at C_0 of 100 ppm (mg.g^{-1})	41.0 ± 1.6	41.7 ± 1.5	37.7 ± 1.4
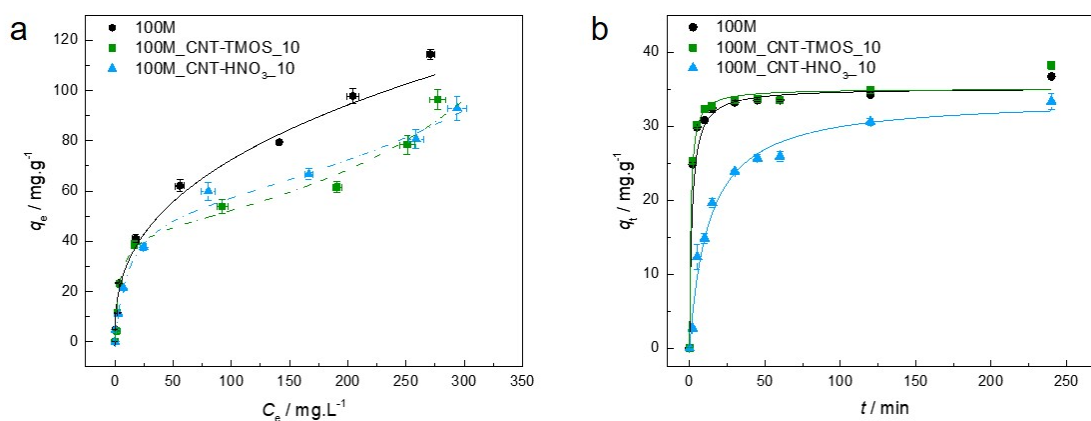
Figure 5.2: (a) - Experimental equilibrium data and the best fitted isotherm model for adsorption of benzene into the studied aerogels (solid line - Freundlich; dashed line - BET). (b) - Representative plots of the fit of non-linearized form of pseudo-second order equation (solid line) to the data of experimental adsorption capacity as function of time, for the studied adsorbents towards benzene (C_0 = 100 ppm, 15 rpm, 20 °C).

When CNTs were added into the silica matrix the BET model provided the most adequate results, indicating a multilayer adsorption. However, in the case of sample

100M_CNT-HNO$_3$_10 the difference between AIC values of Langmuir and BET was lower than two, indicating that both models have statistical support. In order to choose the best model between these, the Akaike weights were determined, with the results providing the probability that the candidate model is the best among the set of models [406]. In this circumstance, the Akaike weight for Langmuir is 0.428 and for BET is 0.572, indicating that BET isotherm model is 1.33 times more likely to be correct. Nevertheless, it cannot be ruled out that the poor fitting of Langmuir equation might be due to the fact that q_e was not experimentally reached, so it would be necessary to test higher concentrations of benzene to confirm the adjust. However, due to the toxicity of this compound, it was decided not to pursue the adsorption tests with concentrations higher than 500 ppm.

The adsorption mechanism for this pollutant is probably based on the hydrophobic interaction (physical adsorption) between the methyl groups derived from MTMS and the benzene molecule (Scheme 5.1).
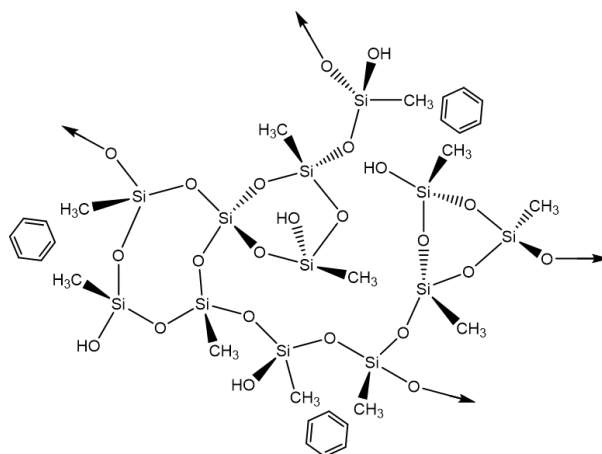
Scheme 5.1: Proposed adsorption mechanisms between silica aerogels and benzene.

As reported by Perdigoto *et al*. [242] the preparation method of adsorbent materials can highly influence their adsorption capacities, as different synthesis procedures lead to different pore structures. Comparing the benzene adsorption capacity of MTMS material (100M) here developed with the ones obtained by Perdigoto *et al*. [242] and Štandeker *et al*. [81], this influence is clear. The lower adsorption capacities among the three works were obtained by Štandeker *et al*. [81], whose material presented low values of surface area combined with an average pore size of 4.8 nm. The ambient pressure dried (APD) aerogel developed in this work has similar surface area value to that obtained by Perdigoto *et al*. [242]. Nevertheless, the adsorption capacities herein reported were inferior to the ones reported there, which can be attributed to the different pore structures, as our average pore size is of 112.9 nm (Table 3.5), and the reported material of Ref. [242] has a bimodal

distribution of micropores and mesopores. Thus, for benzene adsorption, the presence of a significant amount of both micropores and mesopores seems to be an important factor to achieve higher removal rates in MTMS-based materials.

For the samples with CNTs, BET was the best isotherm model. The underlying mechanism of BET model (multilayer adsorption) can be justified on the basis of the ability of benzene to form aggregates via π-π stacking interactions [407]. For the carbon nanotubes-silica aerogel composites, the materials' adsorption capacity shows a dependency of the pollutant's initial concentration, with the q_e value increasing with the increase of the initial concentration of adsorbate. These variations are in agreement with the occurrence of multilayer adsorption characterized by short-range interactions [349].

The addition of carbon nanotubes in the matrix caused a decrease in the removal efficiency of the MTMS-based matrix, which was not expected, since modified CNTs have already been used for the removal of this pollutant and showed good performance [394, 408]. One justification for the decrease in the removal capability, when CNT-TMOS were added into the composite, can be the fact that these nanotubes are surrounded by silica, since the matrix grows around these materials, as shown in Chapter 3 and 4, so most of the CNTs are not really exposed, and, as consequence, they are not able to be in contact with the benzene solution. This supposition was reinforced as, for most of the pollutants here tested, no significant variation was observed when the silanized carbon nanotubes were added into the matrix, if compared with the silica aerogels. The presence of CNT-HNO$_3$ did not have a significant effect in the benzene removal, however the presence of these CNTs leads to better results in the case of other pollutants as will be shown in the following sections.

Regarding the kinetics, the 100M and 100M_CNT-TMOS_10 showed very similar profiles, however, the samples with the CNTs showed a shorter time to achieve the equilibrium (lower k_2 - Table 5.4). When CNT-HNO$_3$ was used in the composite, a slower adsorption rate was obtained, and the equilibrium is reached with higher times than the other samples. The experimental kinetic data of benzene adsorption in these silica-based aerogel composites was better explained by the pseudo-second order (PSO) model. The PSO kinetic model is used to describe chemical adsorption as well as physical adsorptions [409, 410], as the isotherm models indicates that a physical adsorption occurs, it is a good indicative that physisorption might dominate the adsorption process in this case, as suggested in Scheme 5.1. However thermodynamic analyses are more appropriate for determining which process takes place (physisorption or chemisorption) [410], so additional information, such as activation energies, is necessary to conclude which one is the kinetic mechanism [411].

Toluene

The parameters of the Langmuir, Freundlich and BET isotherm models, as well as the kinetic models, are presented in Table 5.5, and the experimental equilibrium and kinetic data, and the best isotherm/kinetic models for each material regarding the adsorption of toluene, are plotted in Figure 5.3.

Table 5.5: Parameters of non-linear isotherms and kinetic models for toluene adsorption on the silica-based aerogels.

Isotherm Model	Parameters	100M	100M_CNT-TMOS_10	100M_CNT-HNO$_3$_10
Langmuir	q_m (mg.g^{-1})	206.0 ± 10.7	306.4 ± 69.4	183.7 ± 11.1
	K_L (L.mg^{-1})	0.02 ± 0.01	0.0 ± 0.003	0.04 ± 0.01
	R_L	0.09 - 0.83	0.22 - 0.93	0.051 - 0.73
	AIC	23.7	45.4	26.7
Freundlich	$1/n_F$	0.47 ± 0.03	0.61 ± 0.06	0.35 ± 0.03
	K_F ((mg.g^{-1}) (L.mg^{-1})$^{1/n_F}$)	14.2 ± 2.0	7.4 ± 2.1	28.3 ± 4.2
	AIC	27.2	39.9	26.1
BET	q_S (mg.g^{-1})	147.8 ± 23.7	86.3 ± 9.6	123.2 ± 8.3
	C_{BET} (L.mg^{-1})	24.8 ± 6.3	21.7 ± 8.7	49.5 ± 6.5
	C_S (mg.L^{-1})	862.8 ± 421.1	305.3 ± 33.6	547.2 ± 86.0
	AIC	27.9	41.7	20.6
	Maximum experimental q_e (mg.g^{-1})	159.6 ± 2.6	169.6 ± 1.3	168.3 ± 2.8

| Kinetic Model	Parameters	100M	100M_CNT-TMOS_10	100M_CNT-HNO$_3$_10
Pseudo-First Order	k_1 (1.min^{-1})	0.18 ± 0.11	0.10 ± 0.01	0.078 ± 0.007
	q_e (mg.g^{-1})	44.3 ± 0.4	46.2 ± 0.1	46.3 ± 0.5
	AIC	52.9	36.5	30.0
Pseudo-Second Order	k_2 x 10^3 (g.(mg.min^{-1}))	6.3 ± 0.8	8.6 ± 1.0	6.8 ± 0.8
	q_e (mg.g^{-1})	46.8 ± 0.3	47.2 ± 0.1	47.6 ± 0.3
	AIC	25.4	29.4	16.3
	Experimental q_e at C_0 of 100 ppm (mg.g^{-1})	44.3 ± 0.4	43.2 ± 0.8	45.9 ± 0.2
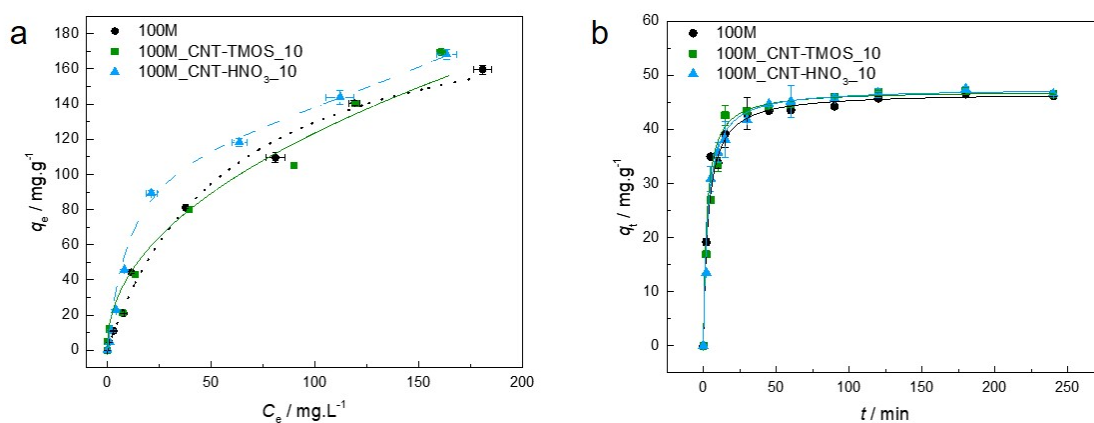
Figure 5.3: (a) - Experimental equilibrium data and the best fitted isotherm model for adsorption of toluene into the studied aerogels (dotted line - Langmuir; solid line - Freundlich; dashed line - BET). (b) - Representative plots of the fit of non-linearized form of pseudo-second order equation (solid line) to the data of experimental adsorption capacity as function of time, for the studied adsorbents towards toluene (C_0 = 100 ppm, 15 rpm, 20 °C).

Regarding the adsorption of toluene, each material has a different isotherm model that provides a better fit: for the 100M was Langmuir, suggesting a that the adsorption occurs into a homogeneous surface and a monolayer of the sorbate is formed [398] and for the 100M_CNT-HNO$_3$_10 was BET, indicating that a multilayer adsorption takes place [397]. For the 100M_CNT-TMOS_10 the difference between the AIC values of Freundlich and BET was lower than two, so once again the Akaike weights were used. The Freundlich model has an Akaike weight of 0.715, while BET has a value of 0.285, so Freundlich is 2.51 times more likely to be the correct model in this case, with this model indicating that a favorable ($1/n_F$ < 1) adsorption on heterogeneous surfaces happens [398].

The results presented in Table 5.5 demonstrate that the addition of CNTs leads to higher experimental adsorption capacities than the MTMS-silica aerogel. The kinetic model that fitted better all the samples, was again the pseudo-second order. As in benzene case, the removal of toluene from water by the silica materials is probably a physisorption process, as weak electrostatic interactions such as hydrophobic interactions are most likely occurring between the silica matrix and the pollutant, as represented in Scheme 5.2.
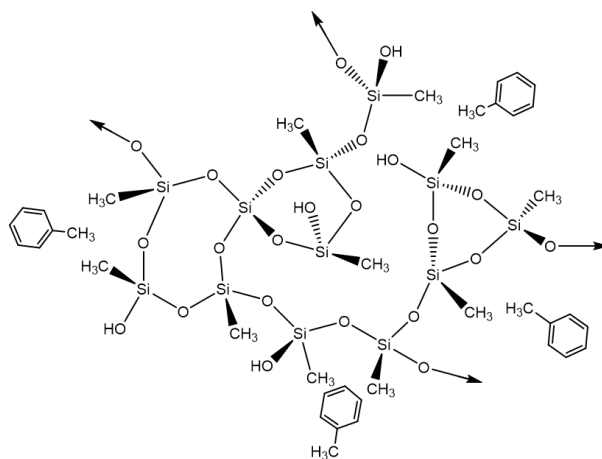
Scheme 5.2: Proposed adsorption mechanisms between silica aerogels and toluene.

By observing the shape of all the adsorption curves in Figure 5.3, it can be concluded that all materials have favorable adsorption isotherms. The same favorable behavior was observed in the work of Perdigoto *et al*. [242], that used MTMS aerogels and xerogel for toluene removal from water solutions. Other hydrophobic adsorbents, such as MTMS-derived aerogels and TMES/TMOS-derived aerogels obtained by Štandeker *et al*. [81] and silica aerogel granules (Cabot Nanogel®) used by Wang *et al*. [412], presented unfavorable adsorption isotherms. It is important to mention that mostly unfavorable isotherms are related to the adsorbents' heterogeneous surfaces, which is directly correlated to the synthesis and drying of these materials [242].

For a better comparison, Wang and co-authors [412] estimated the adsorption capacity values for different materials when the C_e was 200 mg/L. The Nanogel used in their work showed the lowest q (37 mg.g^{-1}) among the analyzed materials, and the granulated activated carbon the highest (268 mg.g^{-1}). The MTMS-based aerogels developed by Štandeker *et al*. [81] and by Perdigoto *et al*. [242] showed results of 87 mg.g^{-1} and 114 mg.g^{-1}, respectively. For the same C_e, the 100M_CNT-TMOS_10 has a value of 186 mg.g^{-1}, which shows a significant improvement if compared with the other hydrophobic aerogels, however, is still lower than the results presented by the activated carbon.

As the best results were achieved by the composite materials, two more samples were developed with higher quantities of CNTs (50 mg), to determine if the amount of this carbon material would affect the removal efficiency of toluene from the aqueous solutions. The obtained results for four different initial concentrations are reported in Table 5.6.

Table 5.6: Removal efficiency of the carbon nanotubes-silica aerogel composites with two amounts of carbon nanostructure for different initial concentrations of toluene.

	Removal Efficiency (%)			
Sample	$C_0 = 50$ mg.L^{-1}	$C_0 = 100$ mg.L^{-1}	$C_0 = 200$ mg.L^{-1}	$C_0 = 400$ mg.L^{-1}
100M_CNT-TMOS_10	85.2 ± 1.3	86.4 ± 1.4	80.2 ± 0.7	70.1 ± 0.3
100M_CNT-TMOS_50	88.5 ± 0.2	92.8 ± 0.3	85.6 ± 0.1	71.9 ± 0.5
100M_CNT-HNO$_3$_10	91.7 ± 0.4	91.8 ± 0.4	89.4 ± 1.3	71.9 ± 1.7
100M_CNT-HNO$_3$_50	91.9 ± 0.3	90.6 ± 0.9	85.0 ± 0.8	70.7 ± 0.5

For all concentrations, an increase in the toluene's removal from the solution was observed when the amount of silanized CNTs was raised to 50 mg, while for the CNT-HNO$_3$ a slight decrease in the efficiency was noticed. In these cases, the increase of carbon nanotubes in the systems does not have a significant effect in the adsorbent's capacity, indicating that the variation in adsorption efficiency is probably more correlated with the impact that these carbon nanostructures have on the structure of the silica network, leading to a more branched network which can affect the average pore size and specific surface area, than with the presence of the carbon materials themselves.

Xylene

The parameters of isotherm and kinetic models are presented in Table 5.7, and the experimental equilibrium and kinetic data, and the best isotherm/kinetic models for each material regarding the adsorption of xylene, are plotted in Figure 5.4. Once again, for each material, the AIC indicates a different model as the best fitting; for the 100M was BET, suggesting a multilayer adsorption, and for the 100M_CNT-TMOS_10 was Freundlich, implying a favorable adsorption into an heterogeneous surface [397, 398]. For the 100M_CNT-HNO$_3$_10, Langmuir showed the lower AIC value, however the Δ_i is lower than two when comparing with both other models, so the Akaike weight was assessed. As Langmuir has the lower AIC values, Freundlich and BET were compared with it. For Langmuir and Freundlich, the Akaike weights were 0.631 and 0.369, respectively, so Langmuir is 1.7 more probable to be correct. When comparing Langmuir with BET, the results were 0.549 and 0.451, respectively, and once again Langmuir showed the best probability to be the correct model. As Langmuir provided the best fit to the data, that indicates that the adsorption of xylene by 100M_CNT-HNO$_3$_10 is favorable ($0 < R_L < 1$) and a monolayer is formed.

Regarding the kinetics, pseudo-second order model presented the best results for the silica aerogel, which was confirmed by the Akaike weights, with the PSO being 2.26 times more likely to be the most appropriated model, while both materials containing CNTs showed a best fit with the pseudo-first order (PFO), which indicates that the

external/internal diffusion is the rate limiting step [398]. The differences in the models that better described the kinetic data can be correlated to the different porous structure of the materials, as the addition of carbon nanotubes affects the silica aerogel network, as previously described, leading to distinct adsorption mechanisms [413]. The influence of structural difference was more evident in the kinetic mechanism of xylene, as PSO was the most appropriate model for benzene and toluene, and this can probably be explained by the differences in the kinetic energy, polarity and spatial structure of this pollutant when compared to the other two.

Table 5.7: Parameters of non-linear isotherms and kinetic models for xylene adsorption on the silica-based aerogels.

Isotherm Model	Parameters	100M	100M_CNT-TMOS_10	100M_CNT-HNO$_3$_10
Langmuir	q_{m} (mg.g^{-1})	185.9 ± 7.3	190.0 ± 9.2	175.2 ± 6.7
	K_{L} (L.mg^{-1})	0.12 ± 0.03	0.096 ± 0.026	0.24 ± 0.09
	R_{L}	0.016 - 0.46	0.020 - 0.51	0.008 - 0.29
	AIC	28.9	32.9	29.2
Freundlich	$1/n_{\mathrm{F}}$	0.2 ± 0.7	0.2 ± 0.1	0.2 ± 0.1
	K_{F} ((mg.g^{-1}) (L.mg^{-1})$^{1/n_{\mathrm{F}}}$)	81.5 ± 185.6	64.7 ± 7.7	74.1 ± 12.6
	AIC	91.0	27.2	30.3
BET	q_{S} (mg.g^{-1})	142.8 ± 5.4	136.8 ± 11.0	142.2 ± 12.5
	C_{BET} (L.mg^{-1})	254.4 ± 75.7	191.9 ± 96.5	272.8 ± 159.9
	C_{S} (mg.L^{-1})	531.2 ± 70.4	517.7 ± 122.0	456.8 ± 173.1
	AIC	20.8	32.8	29.6
	Maximum experimental q_{e} (mg.g^{-1})	187.3 ± 2.3	184.3 ± 1.8	200.5 ± 4.9
Kinetic Model	Parameters	100M	100M_CNT-TMOS_10	100M_CNT-HNO$_3$_10
Pseudo-First Order	k_1 (1.min^{-1})	0.09 ± 0.01	0.10 ± 0.01	0.10 ± 0.01
	q_{e} (mg.g^{-1})	48.1 ± 0.2	48.1 ± 0.04	47.8 ± 0.4
	AIC	40.7	22.9	12.5
Pseudo-Second Order	k_2 x 10^3 (g.(mg.min^{-1}))	6.6 ± 0.9	10.4 ± 2.6	3.8 ± 1.1
	q_{e} (mg.g^{-1})	49.1 ± 0.2	48.7 ± 0.2	50.3 ± 1.1
	AIC	39.0	42.0	24.7
	Experimental q_{e} at C_0 of 100 ppm (mg.g^{-1})	49.9 ± 0.05	49.8 ± 0.07	48.7 ± 0.3
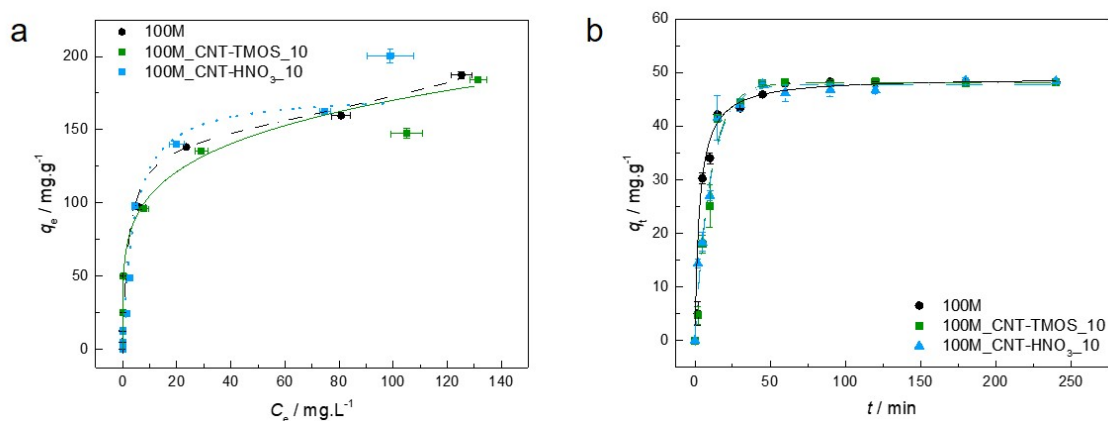
Figure 5.4: (a) - Experimental equilibrium data and the best fitted isotherm model for adsorption of xylene into the studied aerogels (dotted line - Langmuir; solid line - Freundlich; dashed line - BET). (b) - Representative plots of the fit of non-linearized form of pseudo-first order (dashed line) or pseudo-second order (solid line) equations to the data of experimental adsorption capacity as function of time, for the studied adsorbents towards xylene (C_0 = 100 ppm, 15 rpm, 20 °C).

As suggested for benzene and toluene, the interaction between the xylene and the adsorbents is probably occurring by hydrophobic interactions, as shown in Scheme 5.3, which is in agreement with the results of the kinetic models, especially for the CNTs-silica aerogels composites, as PFO model is used for the physical adsorption [409].
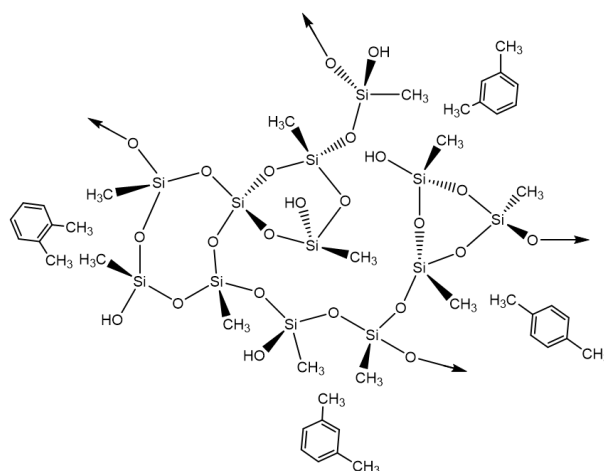
Scheme 5.3: Proposed adsorption mechanisms between silica aerogels and xylene.

The highest q_e experimental was obtained for the 100M_CNT-HNO$_3$_10 showing an improvement with the addition of the carbon nanotubes, but all materials showed good results in removing xylene from aqueous solutions. All these materials have removal rates of more than 90% for concentrations up to 300 mg.L^{-1}, with sample 100M_CNT-HNO$_3$_10 having removals superior than 80% until concentrations of 500 mg.L^{-1}.

As better results were achieved in the presence of CNTs, the materials containing 50 mg of CNTs in the MTMS-silica matrix were also tested for the removal of xylene. The results obtained for these pollutants are presented in Table 5.8.

Table 5.8: Removal efficiency of the carbon nanotubes-silica aerogel composites with two amounts of carbon nanostructure for different initial concentrations of xylene.

Sample	Removal Efficiency (%)			
	$C_0 = 50$ mg.L^{-1}	$C_0 = 100$ mg.L^{-1}	$C_0 = 200$ mg.L^{-1}	$C_0 = 400$ mg.L^{-1}
100M_CNT-TMOS_10	99.5 ± 0.1	99.7 ± 0.1	96.2 ± 0.4	73.7 ± 2.6
100M_CNT-TMOS_50	98.7 ± 0.3	99.0 ± 0.1	98.9 ± 0.1	76.4 ± 0.3
100M_CNT-HNO$_3$_10	96.7 ± 0.1	97.4 ± 0.6	97.7 ± 0.2	81.3 ± 1.7
100M_CNT-HNO$_3$_50	98.2 ± 0.3	99.1 ± 0.2	97.9 ± 0.1	73.0 ± 1.2

As observed in Table 5.8, for concentrations up to 200 mg.L^{-1}, all these materials have similar removal efficiencies, being able to remove more 95% of the pollutant from the aqueous solutions. Only for the highest tested concentration a difference was noticed, with the 100M_CNT-HNO$_3$_10 sample having the best performance. As observed in the toluene's case, the increase in the amount of CNTs does not have a significant impact in the removal of xylene, indicating that 10 mg of CNTs is an appropriate amount for the MTMS-based silica matrix.

The interaction between the hydrophobic surface of the MTMS aerogels and the adsorbate molecules is different for each organic compound. For the materials here developed, toluene and xylene are adsorbed to a greater extent than benzene, as both have higher maximum adsorption capacities for all adsorbent/adsorbate pairs. These differences can be correlated with the different properties of these organic compounds, which allows better interaction between the matrix and the benzene derivatives, than the silica materials with benzene itself.

Phenol

So far, benzene and its derivatives were better adsorbed by the materials without amine groups. However, the best phenol removal efficiency was observed with the 90M10A adsorbent when compared to 100M, for an initial concentration of 200 mg.L^{-1}, as seen in Table 5.1. This can be justified by the interaction of the amine group with the hydroxyl group of phenol molecules by hydrogen bonding, as represented in Scheme 5.4. It is clear that the addition of amine groups improves the q_e when compared with pure MTMS-based material.
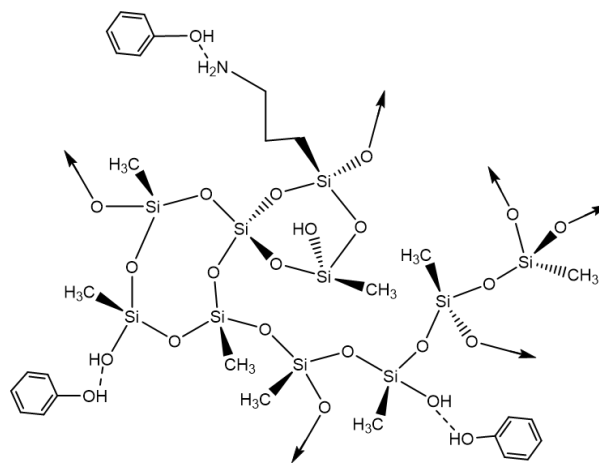
Scheme 5.4: Proposed adsorption mechanisms between silica aerogels and phenol.

As the presence of amine groups provided better removal efficiency for phenol, it was possible to also test the adsorption capacities for the composites materials made with graphene oxide. For the previous pollutants it was not possible to compare with graphene oxide-silica aerogel composites, as it was not possible to obtain these materials with only MTMS as silica precursor. The parameters of isotherm and kinetic models are presented for the composites with carbon nanotubes in Table 5.9 and for the materials developed with graphene oxide in Table 5.10. The experimental equilibrium and kinetic data, with the best isotherm/kinetic models for each material regarding the adsorption of phenol, are plotted in Figure 5.5.

For all the materials tested here for phenol removal, the BET model was not able to provide an adjustment to the data, with the calculated parameters values having no physical meaning, so these data will not be presented. For phenol adsorption, the Langmuir model explains better the interactions for all the materials, including the batch of GO-silica aerogel composites. The data for the 90M10A_CNT-HNO$_3$_10 was also confirmed by Akaike weights with Langmuir being 2.5 times more probable to be correct if compared with Freundlich (Table 5.9). This isotherm model indicates that a monolayer surface adsorption occurs at specific sites. According to the isotherms shapes, and the R$_L$ parameter (Tables 5.9 and 5.10), the adsorption of this pollutant by the silica-based adsorbents is favorable, which is in agreement with the findings of Matias *et al*. [414].

Comparing both systems here developed, when PEG was used as surfactant (GO-silica aerogel composites) much lower maximum q_e was obtained, around half than the results for the samples with CTAB. One possible explanation is that these PEG-samples have lower surface areas than the ones synthesized with CTAB, with this trend also being observed for higher amounts of both surfactants (Tables 4.1 and 4.2), which can have a significant impact in the amount of available sites for the adsorption of phenol.

Table 5.9: Parameters of non-linear isotherms and kinetic models for phenol adsorption on the silica-based aerogels with carbon nanotubes.

Isotherm Model	Parameters	90M10A	90M10A_CNT-TMOS_10	90M10A_CNT-HNO$_3$_10
Langmuir	q_m (mg.g^{-1})	48.0 ± 9.7	67.9 ± 7.0	53.1 ± 4.0
	K_L (L.mg^{-1})	0.006 ± 0.001	0.004 ± 0.001	0.006 ± 0.001
	R_L	0.26 - 0.95	0.32 - 0.96	0.26 - 0.95
	AIC	25.5	9.1	18.1
Freundlich	$1/n_F$	0.75 ± 0.07	0.74 ± 0.03	0.65 ± 0.02
	K_F ((mg.g^{-1}) (L.mg^{-1})$^{1/n_F}$)	0.52 ± 0.13	0.58 ± 0.07	0.80 ± 0.09
	AIC	38.4	16.5	19.9
	Maximum experimental q_e (mg.g^{-1})	32.4 ± 4.8	44.7 ± 5.5	37.9 ± 2.4
Kinetic Model	Parameters	90M10A	90M10A_CNT-TMOS_10	90M10A_CNT-HNO$_3$_10
Pseudo-First Order	k_1 (1.min^{-1})	0.1 ± 0.3	0.04 ± 0.01	0.25 ± 0.04
	q_e (mg.g^{-1})	14.6 ± 0.2	14.3 ± 0.1	16.2 ± 0.01
	AIC	50.5	52.9	21.0
Pseudo-Second Order	k_2 x 10^3 (g.(mg.min^{-1}))	20.5 ± 3.6	4.9 ± 0.5	47.1 ± 12.4
	q_e (mg.g^{-1})	15.2 ± 0.2	15.1 ± 0.1	16.4 ± 0.05
	AIC	36.0	42.9	19.2
	Experimental q_e at C_0 of 100 ppm (mg.g^{-1})	14.5 ± 1.9	15.7 ± 1.4	14.5 ± 1.6

In the case of CNTs-silica aerogel materials, the obtained q_e values are higher than those reported for granular activated carbon (1.48 mg.g^{-1}) [415], porous hydroxyapatite (8.2 mg.g^{-1}) [416], calcinated clay (2.9 mg.g^{-1}) [417], MTMS xerogels (4.9 mg.g^{-1}) [242] and MTMS aerogel (21.1 mg.g^{-1}) [242]. The removal efficiencies of these composite aerogels were also superior than those obtained by Matias *et al*. [414], using MTMS-based systems modified with Glymo and β-cyclodextrin for phenol adsorption. The GO composites showed higher q_e than most of the earlier cited materials. This difference can be, once again, correlated with the significant differences in the specific surface areas between these composites and the aerogels.

Table 5.10: Parameters of non-linear isotherms and kinetic models for phenol adsorption on silica-based aerogels with graphene oxide.

Isotherm Model	Parameters	90M10A	90M10A_GO_10
Langmuir	q_{m} (mg.g^{-1})	23.3 ± 1.4	19.6 ± 1.4
	K_{L} (L.mg^{-1})	0.011 ± 0.007	0.013 ± 0.001
	R_{L}	0.16 - 0.95	0.13 - 0.94
	AIC	15.9	27.8
Freundlich	$1/n_{\mathrm{F}}$	0.6 ± 0.1	0.6 ± 0.1
	K_{F} ((mg.g^{-1}) (L.mg^{-1})$^{1/n_{\mathrm{F}}}$)	0.5 ± 0.1	0.4 ± 0.1
	AIC	39.0	38.4
	Maximum experimental q_{e} (mg.g^{-1})	19.5 ± 1.6	17.9 ± 0.9

Kinetic Model	Parameters	90M10A	90M10A_GO_10
Pseudo-First Order	k_1 (1.min^{-1})	0.08 ± 0.008	0.06 ± 0.007
	q_{e} (mg.g^{-1})	14.2 ± 0.1	10.1 ± 0.1
	AIC	31.5	42.9
Pseudo-Second Order	k_2 x 10^3 (g.(mg.min^{-1}))	12.5 ± 1.6	10.3 ± 0.8
	q_{e} (mg.g^{-1})	14.6 ± 0.1	10.6 ± 0.07
	AIC	26.1	19.0
	Experimental q_{e} at C_0 of 100 ppm (mg.g^{-1})	11.5 ± 0.5	10.3 ± 0.4
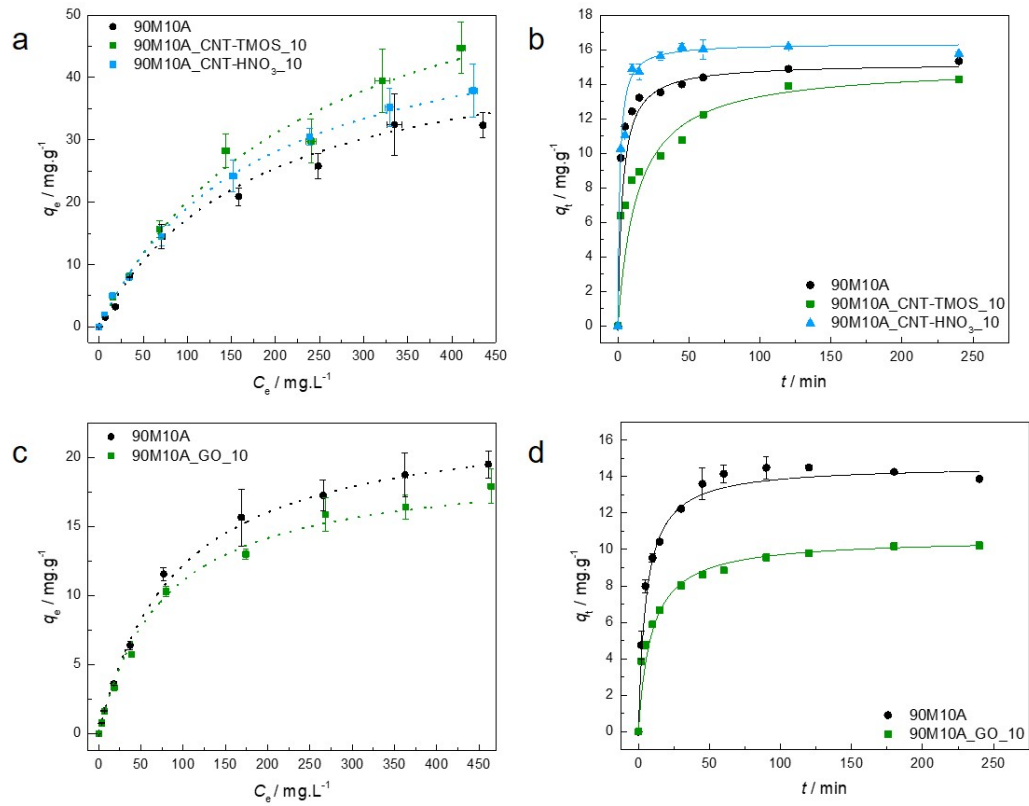
Figure 5.5: (a) - Experimental equilibrium data and the best fitted isotherm model for adsorption of phenol into the studied aerogels (dotted line - Langmuir; solid line - Freundlich). (b) - Representative plots of the fit of non-linearized form of pseudo-second order equation (solid line) to the data of experimental adsorption capacity as function of time, for the studied adsorbents towards phenol (C_0 = 100 ppm, 15 rpm, 20 °C).

For all the materials removing phenol, the pseudo-second order model provided the best fitting to the data (Figures 5.5b and 5.5d). Actually, for most of the composites here developed, when adsorbing organic compounds from the aqueous solutions, the pseudo-second order fits the data well. The kinetic data, together with the isotherm results, as Langmuir provides the best adjustment to the data, it is impelling to say that the chemisorption is the dominant mechanism taking place for these adsorptions systems, as obtained in the study of Matias *et al.* [414], that used MTMS-based systems modified with Glymo and β-cyclodextrin for phenol removal. However, taking into account the silica matrix here used, hydrogen bonds are the most likely interaction between the pollutant and the adsorbent, as indicated in Scheme 5.4. This divergence between the theory and experimental data is probably due to the fact that no sharp distinction between chemisorption and physisorption can be made, especially for cases such as adsorption involving strong hydrogen bonds, without further thermodynamic tests.

It is worth mentioning, that despite having better removal results with different matrices, the organic compounds were rapidly removed from the solutions, achieving the equilibrium in less than 30 min.

As the best results were obtained for the samples with carbon nanotubes, once again composites with 50 mg were tested to verify the influence of the quantities of these CNTs in the removal of the pollutant, in this case phenol, with these results being presented in Table 5.11.

Table 5.11: Removal efficiency of the carbon nanotubes-silica aerogel composites with two amounts of carbon nanostructure for different initial concentrations of phenol.

	Removal Efficiency (%)			
Sample	C_0 = 50 mg.L^{-1}	C_0 = 100 mg.L^{-1}	C_0 = 200 mg.L^{-1}	C_0 = 400 mg.L^{-1}
90M10A_CNT-TMOS_10	32.4 ± 0.9	31.3 ± 2.4	28.2 ± 2.3	17.2 ± 2.2
90M10A_CNT-TMOS_50	30.6 ± 1.0	26.4 ± 0.6	24.2 ± 1.1	21.0 ± 1.1
90M10A_CNT-HNO$_3$_10	31.9 ± 0.8	29.0 ± 2.7	24.2 ± 2.2	15.6 ± 1.3
90M10A_CNT-HNO$_3$_50	30.9 ± 0.4	28.3 ± 1.9	23.8 ± 1.2	21.3 ± 0.6

For concentrations up to 200 mg.L^{-1}, the presence of CNTs causes a decrease in the phenol removal, however, when the concentration is 400 mg.L^{-1}, the higher amount of the carbon nanostructure leads to an increase in the removal efficiency of this pollutant. In the phenol case, for lower concentrations better results were obtained with 10 mg of CNTs, as verified for the other organic compounds, while for values of C_0 superior to 400 mg.L^{-1}, the increase to 50 mg of CNTs in the silica matrix is beneficial for the removal of this pollutant from aqueous solutions, being the difference more expressive with CNT-HNO$_3$ (more exposed). This improvement can also be explained by a possible increase of the

available active sites for phenol removal, as the presence of CNTs leads to an alteration of the silica network, as already mentioned.

Amoxicillin

As already mentioned, drugs are relevant pollutants in wastewater, so their removal is important to assure the safety of water bodies. The first tests for drug removal from aqueous solutions were performed with amoxicillin, using the adsorbents with 90% of MTMS and 10% of APTMS. However, for this particular pollutant, when adding higher amounts of APTMS better results were obtained, so in this case, composites using 90M10A and 80M20A matrices were used as adsorbents.

The parameters of isotherm models are presented for the composites with carbon nanotubes in Tables 5.12 and 5.13, and the results for the materials developed with graphene oxide are shown in Table 5.14. The kinetic tests were performed only for the materials with better removal efficiency, and the parameter for the kinetic models are displayed in Table 5.15. For all the adsorbents, the BET model was not able to provide any adjustment to the data, providing values that have no physical meaning, so for AMX these data will not be presented. The experimental equilibrium and kinetic data, with the best isotherm models for each material, and the kinetics models for some of the adsorbents regarding the removal of AMX, are plotted in Figure 5.6.

For the carbon nanotubes-silica aerogel composites, the isotherms were better described by Freundlich, confirmed by the Akaike weights. As previously mentioned, the Freundlich model describes adsorption in heterogeneous surfaces, and the values obtained for the heterogeneity factor indicate a favorable adsorption [397]. The only exception was the sample 90M10A_CNT-HNO$_3$_10, for which Langmuir provided best results, suggesting a monolayer adsorption. For the GO-silica aerogel composites, the data for silica matrix with 10% of APTMS was better described by Langmuir model, while all the other samples show better fittings with the Freundlich isotherm model. As already mention, for these composites, a matrix with 20% of APTMS provided superior removal of AMX from the tested solution, but the presence of graphene oxide in the tested amount (10 mg) did not contributed to a better performance.

Table 5.12: Parameters of non-linear isotherms models for amoxicillin adsorption on the 90M10A silica-based aerogels with carbon nanotubes.

Isotherm Model	Parameters	90M10A	90M10A_CNT-TMOS_10	90M10A_CNT-HNO$_3$_10
Langmuir	q_m (mg.g^{-1})	3.5 ± 0.4	0.8 ± 0.1	6.7 ± 1.5
	K_L (L.mg^{-1})	0.08 ± 0.02	$3.4 \times 10^3 \pm 3.1 \times 10^7$	0.06 ± 0.02
	R_L	0.20-0.55	0	0.25-0.63
	AIC	27.1	34.0	33.1
Freundlich	$1/n_F$	0.38 ± 0.05	0.059 ± 0.01	0.51 ± 0.13
	K_F ((mg.g^{-1}) (L.mg^{-1})$^{1/n_F}$)	0.7 ± 0.1	0.7 ± 0.3	0.8 ± 0.3
	AIC	24.6	33.7	36.3
	Maximum experimental q_e (mg.g^{-1})	2.8 ± 0.2	1.0 ± 0.1	4.6 ± 0.3

Table 5.13: Parameters of non-linear isotherms models for amoxicillin adsorption on the 80M20A silica-based aerogels with carbon nanotubes.

Isotherm Model	Parameters	80M20A	80M20A_CNT-TMOS_10	80M20A_CNT-HNO$_3$_10
Langmuir	q_m (mg.g^{-1})	36.0 ± 4.3	45.4 ± 10.6	26.8 ± 2.3
	K_L (L.mg^{-1})	0.09 ± 0.02	0.07 ± 0.03	0.12 ± 0.02
	R_L	0.18-0.52	0.22-0.59	0.14-0.46
	AIC	20.8	22.9	32.5
Freundlich	$1/n_F$	0.63 ± 0.02	0.71 ± 0.07	0.56 ± 0.03
	K_F ((mg.g^{-1}) (L.mg^{-1})$^{1/n_F}$)	3.9 ± 0.2	3.6 ± 0.5	3.8 ± 0.2
	AIC	14.8	22.4	29.4
	Maximum experimental q_e (mg.g^{-1})	18.9 ± 0.1	19.5 ± 0.2	17.4 ± 0.3

Table 5.14: Parameters of non-linear isotherms models for amoxicillin adsorption on the silica-based aerogels with graphene oxide.

Isotherm Model	Parameters	90M10A	90M10A_GO_10	80M20A	80M20A_GO_10
Langmuir	q_m (mg.g^{-1})	14.7 ± 0.1	11.6 ± 1.9	24.7 ± 2.1	33.5 ± 4.3
	K_L (L.mg^{-1})	0.40 ± 0.02	0.11 ± 0.04	0.20 ± 0.06	0.09 ± 0.02
	R_L	0.048-0.20	0.22-0.59	0.091-0.33	0.18-0.53
	AIC	8.8	44.9	25.6	22.9
Freundlich	$1/n_F$	0.21 ± 0.03	0.37 ± 0.04	0.45 ± 0.03	0.61 ± 0.03
	K_F ((mg.g^{-1}) (L.mg^{-1})$^{1/n_F}$)	6.8 ± 0.6	2.5 ± 0.2	5.8 ± 0.5	3.8 ± 0.3
	AIC	28.5	38.3	20.5	17.5
	Maximum experimental q_e (mg.g^{-1})	13.4 ± 0.2	9.3 ± 0.2	18.3 ± 0.2	18.4 ± 0.4

Table 5.15: Parameters of non-linear kinetic models for amoxicillin adsorption on the silica-based aerogels with carbon nanotubes and graphene oxide.

Kinetic Model	Parameters	80M20A	80M20A_CNT-TMOS_10	80M20A	80M20A_GO_10
Pseudo-First Order	k_1 (1.min^{-1})	$-2\times10^{-7} \pm 6\times10^{-5}$	$3\times10^{-3} \pm 1\times10^{-4}$	$5\times10^{-3} \pm 7\times10^{-4}$	$6\times10^{-3} \pm 6\times10^{-4}$
	q_e (mg.g^{-1})	$-2\times10^{-4} \pm 8\times10^{6}$	9.5 ± 0.2	8.9 ± 0.7	10.5 ± 0.5
	AIC	103.5	34.3	55.2	37.7
Pseudo-Second Order	k_2 x 10^3 (g.(mg.min^{-1}))	0.24 ± 0.05	0.28 ± 0.01	$51\times10^3 \pm 2\times10^{10}$	0.32 ± 0.09
	q_e (mg.g^{-1})	9.7 ± 0.7	11.5 ± 0.3	2.8 ± 1.0	14.3 ± 1.4
	AIC	54.1	33.7	100.1	44.9
	Experimental q_e at C_0 of 25 ppm (mg.g^{-1})	9.7 ± 0.2	9.8 ± 0.1	10.5 ± 0.06	10.0 ± 0.04
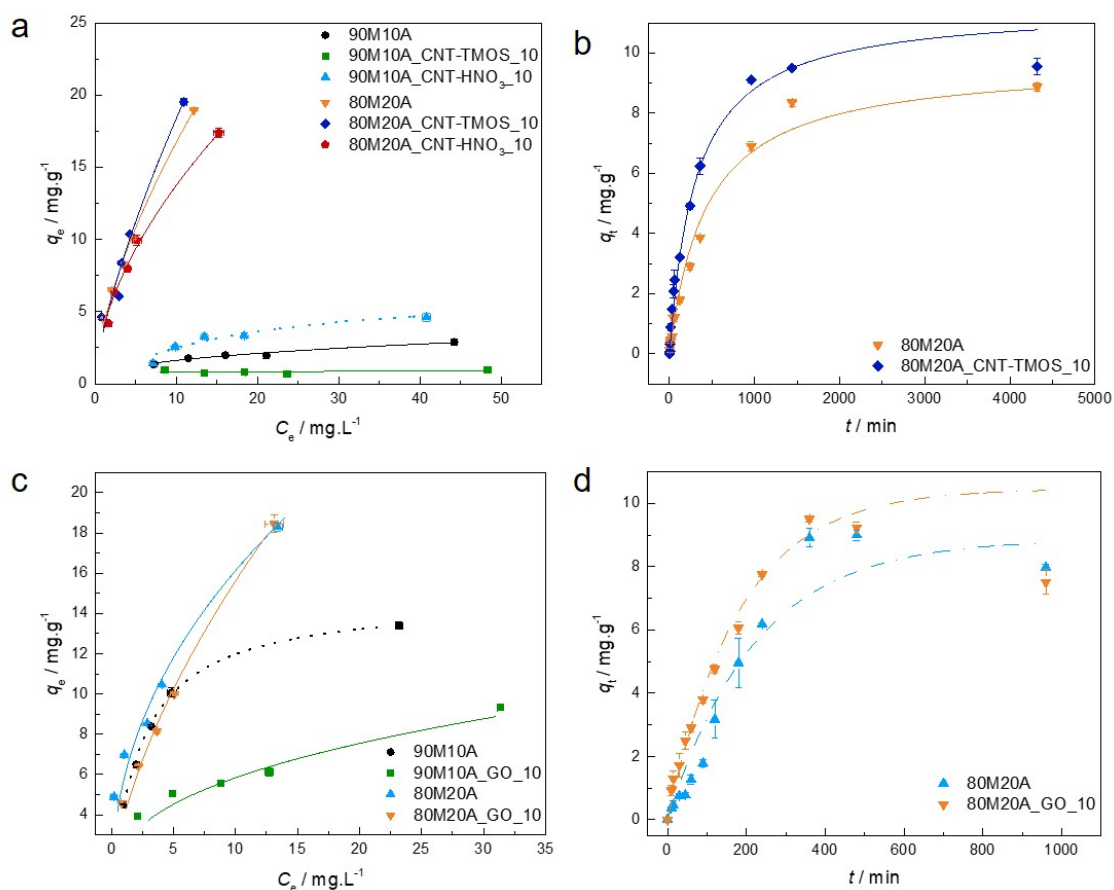
Figure 5.6: (a) and (c) - Experimental equilibrium data and the best fitted isotherm model for adsorption of amoxicillin into the studied aerogels (dotted line - Langmuir; solid line - Freundlich). (b) and (d) - Representative plots of the fit of non-linearized form of pseudo-first order (dashed line) or pseudo-second order (solid line) equations to the data of experimental adsorption capacity as function of time, for the studied adsorbents towards amoxicillin (C_0 =25 ppm, 15 rpm, 20 °C).

Regarding the kinetics, in the presence of CNTs, the PSO model provided the best adjust to the data, while for the GO composites, the best fit was achieved the PFO model. This divergence indicates that these materials can interact with the pollutant differently, as PSO is used to describe chemical adsorption as well as physical adsorptions [409, 410],

while PFO suggest that a physisorption mechanism takes place. If compared to the organic compounds previously tested, the AMX kinetic is much slower, only achieving equilibrium after 1000 min, in the case of CNTs-composites, and after 400 min for the samples with GO.

To confirm if any chemical interactions between the composite materials and the amoxicillin molecule occurred during the adsorption process, and provide a better indication if physisorption or chemisorption is happening in the adsorption process, SSNMR was performed, and the result obtained for the 80M20A_GO_10 after the adsorption process of AMX is represented in Figure 5.7.
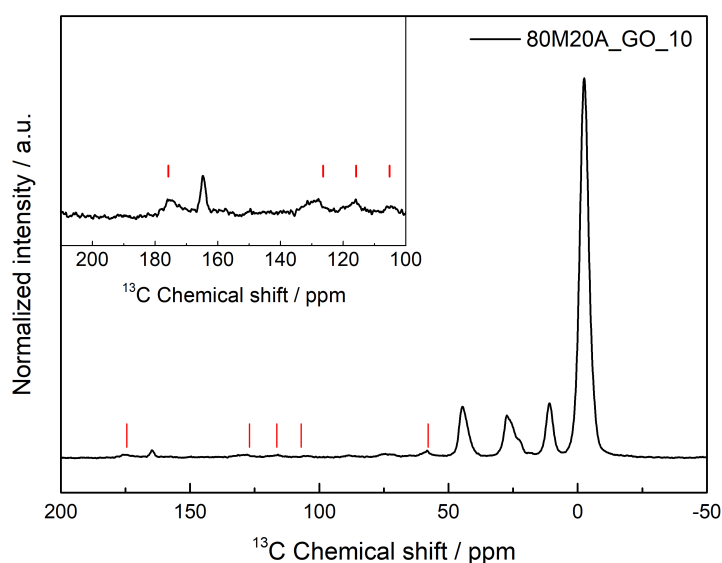
Figure 5.7: ^{1}H–^{13}C heteronuclear solid-state NMR spectra of 80M20A_GO_10 after the adsorption process of amoxicillin. The red lines indicate the detected AMX peaks.

As observed in Figure 5.7, some characteristics peaks of amoxicillin were detected in the spectra, around 57 ppm, 107 ppm, 116 ppm, 126-129 ppm and 174 ppm. No obvious sign of drug-GO interaction was verified, and the same pattern was observed for the AMX adsorption in composites with carbon nanotubes. This indicates that no chemical bond was formed with the silica aerogel during these processes, however, the detection of AMX peaks proves that the adsorption of the drug was effective in the composites by physisorption. So, it is possible to assume that hydrogen bonds, between the hydroxyl and amino groups of the silica aerogel and the three different groups of AMX (hydroxyl, carboxyl and amino groups), are the most likely interaction between them, as indicated in Scheme 5.5.
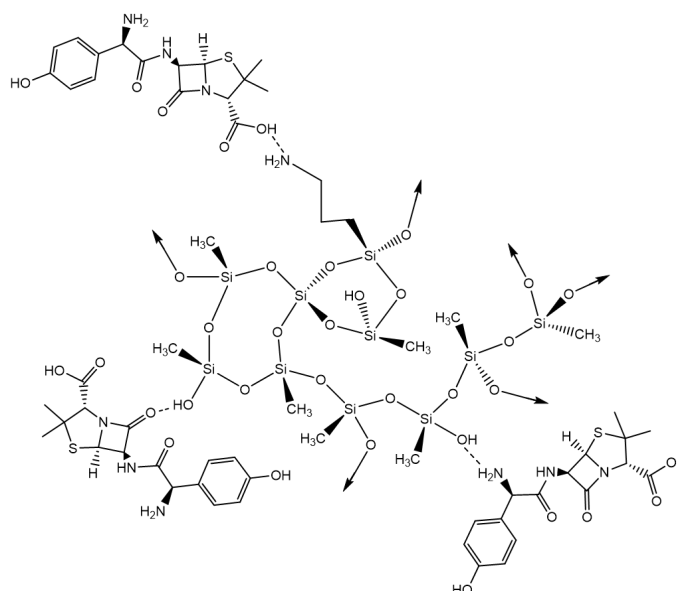
Scheme 5.5: Proposed adsorption mechanisms between silica aerogels and amoxicillin.

In the work developed by Pouretedal and Sadegh [418], the maximum sorption was achieved when 20 mg.L^{-1} of initial concentration was used, with the activated carbon nanoparticles prepared from vine wood being used as adsorbent, and having a removal efficiency of around 72% of AMX from the solution. For the same concentration, both carbon nanostructure-silica aerogel composites here developed (80M20A_CNT-TMOS_10 and 80M20A_GO_10) were able to have higher removal rates (around 82%). De Franco *et al.* [419] also used activated carbon to remove AMX from aqueous solutions and achieved a q_{max} of 4.4 mg.g^{-1}, a much lower result than the ones obtained for our materials (Tables 5.13 and 5.14). However, our results were lower than the ones presented by Moussavi *et al.* [420], which applied NH$_4$Cl-induced activated carbon for AMX removal, with this material being able to remove over 99% from an initial amoxicillin solution with a concentration of 50 mg.L^{-1}. The better performance of their material can be associated to the significantly larger surface area presented by their material (1029 m^2.g^{-1}), which can have an important influence in the material's adsorption capacities.

The next step was to verify if the amount of carbon nanostructure has any influence in the AMX removal. The quantities of CNT-TMOS and GO were increased in the samples 80M20A. The results are shown in Table 5.16.

Table 5.16: Removal efficiency of the carbon nanotubes and graphene oxide-silica aerogel composites with two amounts of carbon nanostructure for different initial concentrations of amoxicillin.

Sample	Removal Efficiency (%)			
	C_0 = 10 mg.L^{-1}	C_0 = 20 mg.L^{-1}	C_0 = 25 mg.L^{-1}	C_0 = 50 mg.L^{-1}
80M20A_CNT-TMOS_10	92.3 ± 2.3	83.9 ± 1.1	82.8 ± 1.1	78.2 ± 0.7
80M20A_CNT-TMOS_50	93.4 ± 0.6	93.8 ± 0.6	92.1 ± 0.5	77.3 ± 0.4
80M20A_GO_10	91.8 ± 1.2	81.6 ± 0.9	79.8 ± 0.3	73.8 ± 1.5
80M20A_GO_50	89.0 ± 4.3	83.6 ± 1.7	80.7 ± 0.3	71.5 ± 1.3

In the case of carbon nanotubes, the increase to 50 mg improved the removal efficiency of AMX until a concentration of 25 mg.L^{-1}. However, for the highest C_0, the removal efficiency remained practically the same. For the GO composites, the variation did not cause a meaningful alteration. As observed for the organic compounds, better removal efficiency of AMX were achieved when 10 mg of carbon nanostructure was added into the silica matrix.

Naproxen

The last pollutant tested with the carbon nanostructure-silica aerogel composites as adsorbents was naproxen. As already mentioned, both silica matrices were able to successfully remove NPX from aqueous solutions, so it is possible that distinct parts of the naproxen molecule are interacting with the different matrices, with hydrophobic interactions taking place between their methyl groups in the MTMS-silica aerogel (Scheme 5.6a), while for the matrix containing APTMS, in addition to these, the drugs' carboxyl groups can make hydrogen bonds with the silanol and amine groups of the aerogel (Scheme 5.6b).
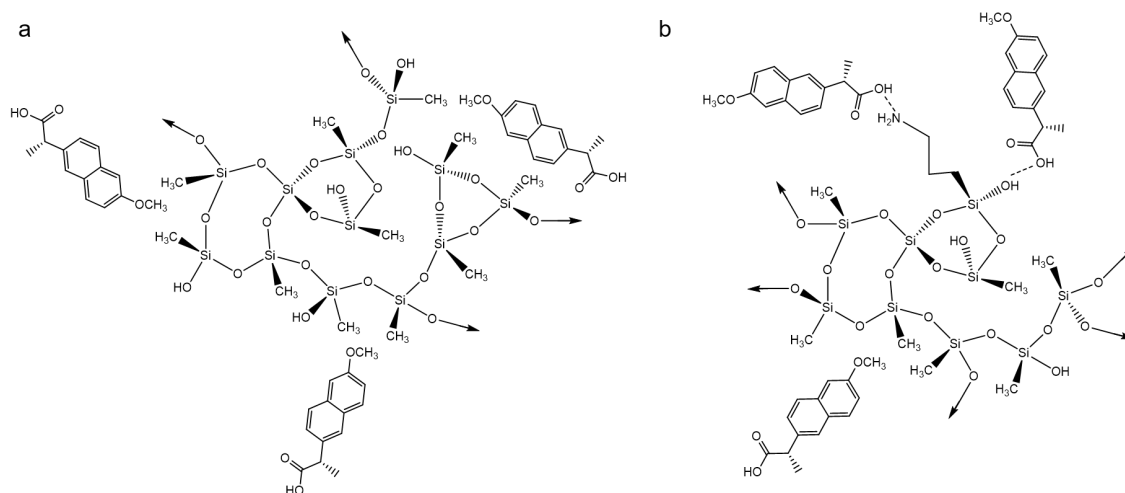
Scheme 5.6: Proposed adsorption mechanisms between naproxen and a) 100% MTMS silica aerogels and b) 90%MTMS and 10% APTMS silica aerogels.

The parameters of isotherm and kinetic models are presented for the 100M with carbon nanotubes in Table 5.17, for the 90M10A with CNTs in Table 5.18 and for the 90M10A with GO in Table 5.19. For the samples with 100M, and the 90M10A_GO_10, the Langmuir model presented fit parameters with no physical meaning, so they are not presented in the tables. For the samples 100M_CNT-HNO$_3$_10 and both samples with GO, the BET model was not able to adjust the data, so they are also not displayed in the tables. The experimental equilibrium and kinetic data, with the best isotherm models for each material, and the kinetics models for the adsorbents regarding the removal of NPX, are plotted in Figure 5.8.

For the 100M systems the Freundlich model provides the best fit to the data. The isotherms obtained from the adsorption process are unfavorable (Figure 5.8a), as shown by the values of $1/n_\mathrm{F}$ (Table 5.17). For these samples the addition of CNT leads to an increase in the maximum q_e. While the CNT-HNO$_3$ allowed the equilibrium to be reached in relatively shorter times, with the CNT-TMOS a decrease in the kinetic constant was observed. For the silica sample and the composite with CNT-TMOS, PFO provided a better adjustment to the data, while, for the 100M_CNT-HNO$_3$_10, PSO showed better results. According to Vareda *et al*. [398], when the heterogeneity factor is higher than one, as the ones here obtained, a cooperative (multilayer) adsorption occurs, which is in agreement with the kinetic results, as both models can represent the physisorption mechanism. So for the materials developed with only MTMS as precursor, no chemical interaction takes place during the adsorption process, which agrees with the proposed adsorption mechanisms presented in Scheme 5.6a.

Table 5.17: Parameters of non-linear isotherms and kinetic models for naproxen adsorption on the 100M silica aerogels with carbon nanotubes.

Isotherm Model	Parameters	100M	100M_CNT-TMOS_10	100M_CNT-HNO$_3$_10
	$1/n_\mathrm{F}$	1.2 ± 0.1	1.1 ± 0.1	1.8 ± 0.2
Freundlich	K_F			
	$((\mathrm{mg.g}^{-1})\,(\mathrm{L.mg}^{-1})^{1/n_\mathrm{F}})$	2.1 ± 0.2	4.9 ± 0.5	4.4 ± 0.5
	AIC	-2.7	-6.0	-
	q_S (mg.g^{-1})	10.7 ± 3.4	11.5 ± 5.4	-
BET	C_BET (L.mg^{-1})	3.2 ± 1.2	3.8 ± 2.3	-
	C_S (mg.L^{-1})	11.2 ± 1.6	6.7 ± 1.5	-
	AIC	21.1	21.4	-
Maximum experimental q_e (mg.g^{-1})		21.7 ± 0.1	23.0 ± 0.1	23.7 ± 0.02
Kinetic Model	Parameters	100M	100M_CNT-TMOS_10	100M_CNT-HNO$_3$_10
	k_1 (1.min^{-1})	0.024 ± 0.004	0.014 ± 0.004	0.056 ± 0.005
Pseudo-First Order	q_e (mg.g^{-1})	9.5 ± 0.5	10.5 ± 1.6	9.9 ± 0.2
	AIC	21.8	23.9	20.0
	k_2 x 10^3 (g.(mg.min^{-1}))	1.4 ± 0.5	0.6 ± 0.3	6.5 ± 0.9
Pseudo-Second Order	q_e (mg.g^{-1})	13.5 ± 1.4	16.3 ± 3.5	11.6 ± 0.3
	AIC	23.0	24.4	14.6
Experimental q_e at C_0 of 25 ppm (mg.g^{-1})		10.5 ± 0.1	11.4 ± 0.02	11.70 ± 0.02

For the 90M10A batch of samples with CNTs, the AIC showed that for 90M10A and 90M10A_CNT-HNO$_3$_10 Langmuir has the best adjustment to the data, with the shape of the isotherms (Figure 5.8) and the R_L values (Table 5.18) indicating a favorable adsorption. For the composite with CNT-TMOS, Freundlich has the best results, also having a favorable adsorption profile (Table 5.18 and Figure 5.8). The highest values of q_e were once again achieved by the composite with CNT-HNO$_3$. For the silica aerogel, pseudo-second order was the preferred kinetic model, while in the presence of CNTs, the best fit was obtained for the pseudo-first order, once again indicating that the adsorption is probably physical, and they all achieved the equilibrium in similar times.

Table 5.18: Parameters of non-linear isotherms and kinetic models for naproxen adsorption on the 90M10A silica aerogels with carbon nanotubes.

Isotherm Model	Parameters	90M10A	90M10A_CNT-TMOS_10	90M10A_CNT-HNO$_3$_10
Langmuir	q_m (mg.g^{-1})	12.5 ± 0.8	12.8 ± 4.4	14.3 ± 1.3
	K_L (L.mg^{-1})	0.8 ± 0.1	0.05 ± 0.03	0.4 ± 0.1
	R_L	0.024-0.11	0.286-0.667	0.048-0.20
	AIC	-4.9	32.4	12.6
Freundlich	$1/n_F$	0.16 ± 0.03	0.53 ± 0.08	0.23 ± 0.08
	K_F ((mg.g^{-1}) (L.mg^{-1})$^{1/n_F}$)	7.4 ± 0.4	1.3 ± 0.3	6.7 ± 1.0
	AIC	10.7	26.5	20.8
BET	q_S (mg.g^{-1})	11.6 ± 0.2	3.7 ± 0.3	-3.5×10^{-5} ± 41.1
	C_{BET} (L.mg^{-1})	373.8 ± 54.9	-6.5×10^7 ± 3.2×10^{12}	0.9 ± 4.2×10^3
	C_S (mg.L^{-1})	381.2 ± 75.1	48.9 ± 7.9	0.3 ± 1.3×10^4
	AIC	12.9	60.4	64.4
	Maximum experimental q_e (mg.g^{-1})	12.0 ± 0.9	9.3 ± 0.3	12.4 ± 1.3
Kinetic Model	Parameters	90M10A	90M10A_CNT-TMOS_10	90M10A_CNT-HNO$_3$_10
Pseudo-First Order	k_1 (1.min^{-1})	0.08 ± 0.01	0.1 ± 0.007	0.08 ± 0.003
	q_e (mg.g^{-1})	11.5 ± 0.05	11.3 ± 0.06	12.2 ± 0.02
	AIC	22.0	20.4	22.4
Pseudo-Second Order	k_2 x 10^3 (g.(mg.min^{-1}))	10.0 ± 0.3	19.5 ± 5.6	19.9 ± 4.2
	q_e (mg.g^{-1})	12.9 ± 0.3	12.0 ± 0.2	12.8 ± 0.1
	AIC	20.0	32.2	34.2
	Experimental q_e at C_0 of 25 ppm (mg.g^{-1})	9.9 ± 0.2	5.4 ± 0.05	10.1 ± 0.1

In the case of graphene oxide composites, the addition of GO leads to an improvement in the q_e and the data was adjusted by the Freundlich model, while the data of its silica counterpart was better fitted by the Langmuir model. The presence of GO changed the shape of the isotherm from favorable to unfavorable, with this being shown by the $1/n_F$ value (Table 5.19). The silica aerogel behavior is better described by the PFO model, while the PSO was more appropriate for the data of GO-silica aerogel composite.
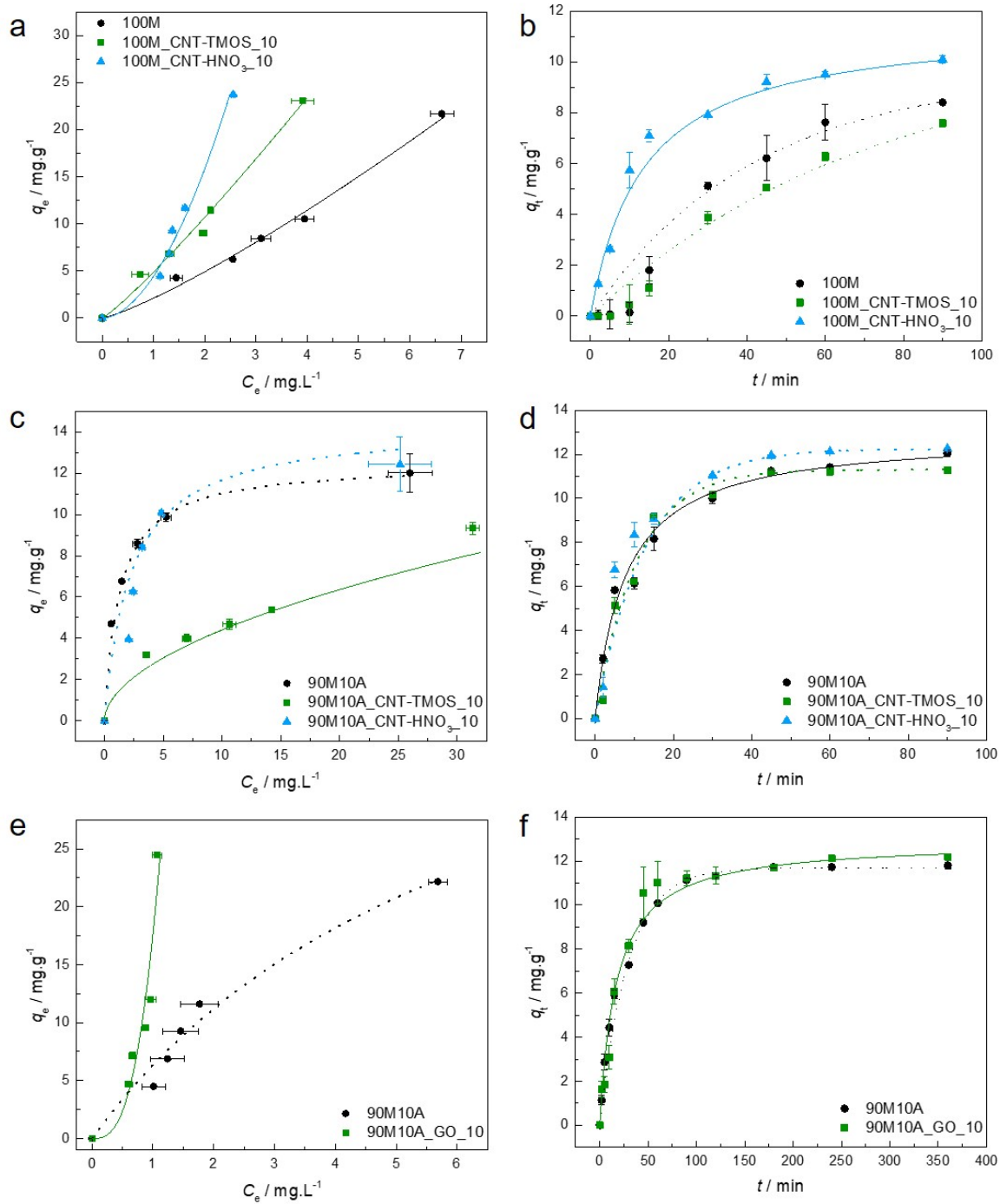
Figure 5.8: (a), (c) and (e) - Experimental equilibrium data and the best fitted isotherm model for adsorption of naproxen into the studied aerogels (dotted line - Langmuir; solid line - Freundlich). (b), (d) and (f) - Representative plots of the fit of non-linearized form of pseudo-first order (dashed line) or pseudo-second order (solid line) to the data of experimental adsorption capacity as function of time, for the studied adsorbents towards naproxen (C_0 = 25 ppm, 15 rpm, 20 °C).

Table 5.19: Parameters of non-linear isotherms and kinetic models for naproxen adsorption on the 90M10A silica aerogels with graphene oxide.

Isotherm Model	Parameters	90M10A	90M10A_GO_10
Langmuir	q_m (mg.g^{-1})	48.5 ± 8.8	-
	K_L (L.mg^{-1})	0.15 ± 0.05	-
	R_L	0.12-0.40	-
	AIC	16.4	-
Freundlich	$1/n_\mathrm{F}$	0.72 ± 0.08	2.9 ± 0.6
	K_F ((mg.g^{-1}) (L.mg^{-1})$^{1/n_\mathrm{F}}$)	6.3 ± 0.8	17.6 ± 2.3
	AIC	19.8	-
	Maximum experimental q_e (mg.g^{-1})	22.2 ± 0.4	24.5 ± 0.09
Kinetic Model	Parameters	90M10A	90M10A_GO_10
Pseudo-First Order	k_1 (1.min^{-1})	0.034 ± 0.001	0.04 ± 0.004
	q_e (mg.g^{-1})	11.7 ± 0.07	12.1 ± 0.05
	AIC	22.3	21.7
Pseudo-Second Order	k_2 x 10^3 (g.(mg.min^{-1}))	4.2 ± 0.4	4.5 ± 0.6
	q_e (mg.g^{-1})	12.9 ± 0.2	12.9 ± 0.1
	AIC	30.7	17.4
	Experimental q_e at C_0 of 25 ppm (mg.g^{-1})	10.1 ± 0.1	12.0 ± 0.1

Comparing the maximum experimental q_e, the 100M samples with CNTs and the 90M10A with GO have similar values and are higher than the ones for the 90M10A matrix with CNTs. So, for the study of the influence of carbon nanostructure amount, these three matrices were used. The removal efficiency for different concentration of NPX are reported in Table 5.20.

Table 5.20: Removal efficiency of the carbon nanotubes and graphene oxide-silica aerogel composites with two amounts of carbon nanostructure for different initial concentrations of naproxen.

	Removal Efficiency (%)			
Sample	C_0 = 10 mg.L^{-1}	C_0 = 20 mg.L^{-1}	C_0 = 25 mg.L^{-1}	C_0 = 50 mg.L^{-1}
100M_CNT-TMOS_10	92.4 ± 1.6	89.9 ± 0.3	91.3 ± 0.1	92.1 ± 0.4
100M_CNT-TMOS_50	84.7 ± 0.5	87.5 ± 0.4	89.1 ± 0.8	89.3 ± 0.7
100M_CNT-HNO$_3$_10	88.2 ± 0.4	93.1 ± 0.2	93.5 ± 0.2	94.8 ± 0.1
100M_CNT-HNO$_3$_50	88.5 ± 1.1	90.1 ± 0.6	89.6 ± 0.9	91.6 ± 0.6
90M10A_GO_10	94.0 ± 0.6	95.3 ± 0.3	96.2 ± 0.8	98.2 ± 0.4
90M10A_GO_50	97.2 ± 2.9	96.2 ± 0.6	96.4 ± 0.4	98.9 ± 0.1

The best results were achieved by the samples containing 50 mg of graphene oxide in the silica matrix, with removals superior to 96% up to an initial concentration of 50 mg.L^{-1}. The removal efficiency of naproxen obtained for 90M10A_GO_50 is higher

than those reported for magnetic activated carbon (87.8%) [421], Fe_3O_4 nanoparticles on multi-walled carbon nanotubes (67.2%) [421] and functionalized nano-clay composite (92.2%) [422], all having an initial concentration of 10 mg.L^{-1}. For C_0 of 20 mg.L^{-1}, the GO-silica aerogel composites (96.2%) still have better performance than other materials, such as olive waste cakes ($\sim$ 95%) [423] and amberlite XAD-7 ($\sim$ 60%) [424].

As the highest removal efficiency was achieved for the 90M10A_GO_50 composite, SSNMR was performed for this sample, after the adsorption of naproxen, to verify if any interaction between adsorbent-adsorbate occurred during this experiment. The NMR spectrum is represented in Figure 5.9.
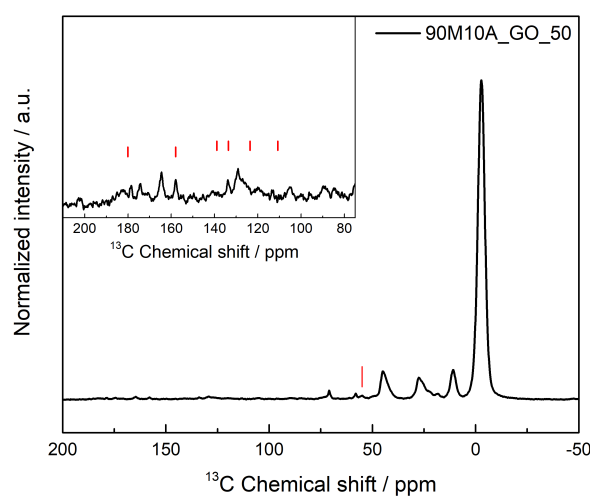
Figure 5.9: ^{1}H–^{13}C heteronuclear solid-state NMR spectra of 90M10A_GO_50 after the adsorption process of naproxen. The red lines indicate the detected NPX peaks.

By analyzing the spectrum, NPX is clearly detected, with its characteristics peaks around 55 ppm, 105 ppm, 119 ppm, 126-133 ppm, 134 ppm, 158 ppm and 180 ppm. The intensities qualitatively also fit with the concentration removed from the solution. It is possible that a specific interaction occurs during the adsorption process, as shown by the appearance three peaks instead of only one around 180 ppm. The arising of these peaks can indicate an interaction between the carboxyl group of naproxen, for which the carbon appears at 180 ppm, with the graphene oxide. This theory, and the possibility of π-π interaction between graphene oxide and benzene ring of naproxen, can explain the higher sorption efficiency of this material.

5.4   Conclusion

The possibility of changing the silica aerogels characteristics allows the tailoring of these adsorbents to better remove different pollutants from wastewaters. The presence of

amine groups has a significant impact in the materials properties, as well as the addition of carbon nanostructures such as carbon nanotubes and graphene oxide. In this chapter, we proved that amine modification played a major role in the removal of different types of pollutants. The presence of carbon nanostructures also led to an increase in the removal performance of the silica aerogels for most of the contaminants. However, without further investigation, it is not possible to affirm that was in fact the carbon nanostructures that removed the pollutants, or were the alterations that they cause in the silica structures that led to the formation of new active sites, which can also improve the removal of these contaminants.

The MTMS-based aerogels were able to effectively remove different organic compounds, benzene, toluene and xylene. In the case of phenol, the amine presence showed a significant impact in the removal efficiency. For both drugs, amoxicillin and naproxen, the addition of APTMS was also fundamental to obtain a better performance.

After this analysis, it is noteworthy that the presence of amine groups and carbon nanostructures is an important tool to the development of new adsorbents, by altering their properties in order to enhance the adsorption of relevant pollutants. Therefore, this work clearly demonstrates the high potential of these materials to be used as alternative industrial sorbents due to their higher and fast removal efficiency towards different types of pollutants.

Chapter 6

Final Remarks

6.1 Conclusions

Silica aerogels are amorphous materials, synthesized by the sol-gel process, with a porous three-dimensional network. Due to their combination of unique features, from high specific surface areas and porosity to low density and thermal conductivity, they have been widely used as, for example, adsorbents, drug carriers and catalysts. However, a few applications have been restricted due to the limitations of silica aerogel's mechanical strength, which causes the material to collapse during processing. One possibility to surpass these restrictions is the addition of different compounds into their network, as the presence of these new phases can lead to distinctive characteristics when compared to the native silica aerogels.

The incorporation of carbon-based nanomaterials such as carbon nanotubes (CNTs) and graphene oxide (GO) with high electrical conductivity and mechanical strength is one possibility to change the silica aerogel' properties. A few studies have been already performed in systems composed by these carbon nanostructures and TEOS or water glass-based silica aerogels. These works concluded that the addition of CNT or GO can improve different properties of the silica aerogels, such as photophysical, mechanical and thermal properties.

Motivated by the promising properties observed in the referred systems, and with the perspective of improving the interactions between carbon nanomaterials and silica matrix, in relation to pristine silica (TEOS-based materials), the main objective of this research was to develop composite materials of MTMS-based silica aerogels and carbon nanostructures, namely carbon nanotubes and graphene oxide, and study the effect of these nanomaterials on the composites' final properties. Thus, in order to assess the influence of the carbon materials addition in the silica matrix, this project extensively characterized the synthesized materials in terms of morphology and nano-, micro- and

macrostructure, chemical composition, thermal and electrical conductivities, and mechanical resistance.

The first step was to study the polysilsesquioxane-based aerogel composites with CNTs. The addition of a silica co-precursor (APTMS) and a surfactant (CTAB) improved the physical and mechanical properties of these materials. By using Raman spectroscopy it was possible to confirm that the addition of carbon nanotubes did not affect the formation of the silica network at the primary particles scale, as eight-membered rings were observed for samples with and without the carbon material. The use of 4 wt% of surfactant during the synthesis step allowed a better control of the pore structure, while the addition of APTMS led to a significant increase in the secondary particles size. In the presence of CNTs, a distinctive silica structure was observed by electron microscopy techniques, with the silica particles following the format of the CNT, changing from spherical to more a cylindrical shape. This alteration can indicate a chemical binding between the carbon nanostructure, especially for the silanized CNTs, and the silica precursors during the composites' synthesis.

We were able to obtain final materials with low thermal conductivities and improved mechanical properties, without compromising the high porosities, low densities and superhydrophobicity. Due to the simplicity of the sol-gel process, these composites can be tailored according to the desired application; if mechanical properties are needed, the samples can be synthesized by lowering the amount of surfactant and adding amine groups, while if the thermal properties are the priority, materials with high recovery rates and low thermal conductivities can be obtained by increasing the CTAB quantity without the use of APTMS as co-precursor.

After establishing the best parameters to obtain monolithic samples, the influence of different carbon nanostructures, carbon nanotubes (1D) and graphene (2D), as well as the amount of these nanomaterials in the properties of MTMS-based silica aerogels was studied. The presence of carbon nanomaterials did not prevent the formation of a silica three-dimensional network, and while the presence of CNTs did not interfered in the chemical structure of the silica aerogels, when GO was added into the system, some impact was detected through NMR spectroscopy. The physical properties were also affected by their addition, with variations being observed mainly in the specific surface area and average pore sizes, however, it seems that the presence of APTMS in the silica matrix has more effect in these characteristics than the carbon nanomaterials.

Regarding the microstructure, the presence of CNTs leads to a more significant impact than the addition of graphene oxide. As previously mentioned, by the results of SEM and TEM, it was possible to see that the silica matrix grows around the CNTs and is able

to follow their shape, especially for the ones modified with TMOS. The carbon nanotubes also caused a more substantial alteration in the thermal conductivity of the composites, with this effect being more significant in temperatures above 50 °C, while, once again, GO did not have a meaningful influence in the thermal properties. However, this is probably caused by the presence of macropores in the micrometers order, which have a dominant effect in this property when compared to the GO presence.

The effect of the carbon nanostructures was also assessed in the electrochemical properties of silica aerogels, and, as expected, the presence of CNTs or GO leads to an increase in the specific capacitance and a decrease in the electrons flow' resistance at the interface of the silica aerogels. The highest specific capacitances were obtained by the 90M10A systems with CNTs-TMOS and GO ($\sim$4 wt% of the aerogel), and, for most systems, as the amount of carbon increased, lower resistances were obtained. In summary, we were able to conclude that the CNTs have a more substantial impact in the overall properties of the silica aerogel, being possible to change the silica matrix and the amount of the carbon nanostructure to achieve the desired features.

The carbon nanomaterials-silica aerogel composites here obtained can be proposed for a wide range of applications, especially due to the possibility of changing the silica aerogels properties. These materials can be tailored to achieve better removal rates of pollutants, such as benzene and its derivatives and drugs, from wastewaters. In general, the amine modification played a major role in the removal of different types of pollutants. And, for most of the contaminants, the presence of carbon nanostructures led to an increase in the removal performance of the silica aerogels. For the removal of three of the organic compounds, benzene, toluene and xylene, the MTMS-based aerogels presented the better results, while for effectively remove phenol, it was necessary the addition of the APTMS as co-precursor. In the drugs case, amoxicillin and naproxen, the presence of amine groups also led to an increment in the adsorption performances of the silica aerogels. The presence of amine groups and carbon nanostructures was an important tool to the development of these new adsorbent materials, as both allowed the change of silica aerogels' properties, enhancing their capability of removing relevant pollutants from water bodies. After these tests, it is possible to state that these materials have a high potential to be used as alternative industrial adsorbents due to their higher and fast removal efficiency towards different types of pollutants.

In summary, we were able to extensively study the properties of new composite systems composed by carbon nanostructures and MTMS-based silica aerogel. A large number of different techniques were used to achieve this goal, which allowed a better understanding of the influence of the CNTs and GO in MTMS-based silica aerogels, and

provided a new insight on these composites structure and properties. Comparatively, the carbon nanotubes caused a larger influence in the methyltrimethoxysilane silica matrix, leading to more significant alterations in their properties than the graphene oxide. In addition, a new solvent mixture system was used during the sol-gel process to obtain these composites, which allowed the synthesis of materials with properties similar to aerogels while using ambient pressure drying. The development of this work contributed to a significant increase in the knowledge of the aerogels' community regarding the studied systems and allowed the synthesis of several composite materials with potential to be used in different applications, from adsorbents, as already tested here, to thermal insulators, due to their low thermal conductivity values, especially at high temperatures, and electric double-layer capacitors, since they have high surface areas, with the possibility of controlling the distribution of pores, and high specific capacitances.

6.2   Future work

Although, we consider that the goal of understanding the effect of incorporating carbon nanostructures into silica aerogels has been accomplished, there are improvements that could be made in order to achieve better results. In this section we suggest the following future extensions to our work:

- Recycling the silica aerogels used as adsorbents - determine if the materials are able to be reused and to maintain their adsorption capacities and hydrophobic character after being submitted to several cycles of adsorption/regeneration.

- Perform adsorption tests at different temperatures - allowing the determination of thermodynamic parameters which will provide additional information regarding the adsorption mechanism (chemisorption or physisorption).

- Further studies of electrochemical properties - cycles of charge/discharge will help to assess if the carbon nanostructures-silica aerogel composites have potential to be used as electrochemical capacitors.

- Incorporation of nanodiamonds - this would allow the study of the influence of carbon nanomaterials with zero dimensions in the silica structure and composite properties.

In addition to the specific characterizations and the development of new composite materials as mentioned above, further larger scale tests could also provide new insights about the systems, such as:

- Using the materials as adsorbents of pollutants in industrial effluents - determine the efficiency of the aerogels for real effluents.

- Develop a continuous fixed-bed sorption layout - assess the aerogels performance when using higher quantities of wastewater (higher pollution load).

- Assemble coin-type electric double-layer capacitors (EDLC) - evaluate the specific capacitance of the electrode material as EDLC electrodes, and also their energy and power densities.

Bibliography

[1] S. Dervin and S. C. Pillai. *An Introduction to Sol-Gel Processing for Aerogels*, pages 1–22. Springer, 2017.

[2] A. Du, B. Zhou, Z. Zhang, and J. Shen. A special material or a new state of matter: a review and reconsideration of the aerogel. *Materials*, 6(3):941–968, 2013.

[3] S. S. Kistler. Coherent expanded aerogels and jellies. *Nature*, 127(3211):741–741, 1931.

[4] IUPAC. Compendium of chemical terminology, 1997.

[5] T. F. Baumann, A. E. Gash, S. C. Chinn, A. M. Sawvel, R. S. Maxwell, and J. H. Satcher. Synthesis of high-surface-area alumina aerogels without the use of alkoxide precursors. *Chemistry of materials*, 17(2):395–401, 2005.

[6] J. Innerlohinger, H. K. Weber, and G. Kraft. Aerocellulose: aerogels and aerogel-like materials made from cellulose. In *Macromolecular Symposia*, volume 244, pages 126–135. Wiley Online Library, 2006.

[7] J. L. Gurav, I.-K. Jung, H.-H. Park, E. S. Kang, and D. Y. Nadargi. Silica aerogel: synthesis and applications. *Journal of Nanomaterials*, 2010:23, 2010.

[8] M. A. Aegerter, N. Leventis, and M. M. Koebel. *Aerogels Handbook*. Springer Science & Business Media, 2011.

[9] J. C. Williams, B. N. Nguyen, L. McCorkle, D. Scheiman, J. S. Griffin, S. A. Steiner III, and M. A. B. Meador. Highly porous, rigid-rod polyamide aerogels with superior mechanical properties and unusually high thermal conductivity. *ACS applied materials & interfaces*, 9(2):1801–1809, 2017.

[10] N. Leventis, A. Sadekar, N. Chandrasekaran, and C. Sotiriou-Leventis. Click synthesis of monolithic silicon carbide aerogels from polyacrylonitrile-coated 3D silica networks. *Chemistry of Materials*, 22(9):2790–2803, 2010.

[11] N. Hüsing and U. Schubert. *Aerogels*. Wiley-VCH Verlag GmbH & Co. KGaA, 2000.

[12] C. J. Brinker and G. W. Scherer, editors. *Sol-gel science: the physics and chemistry of sol-gel processing*. Academic press, 1990.

[13] C. Ziegler, A. Wolf, W. Liu, A.-K. Herrmann, N. Gaponik, and A. Eychmüller. Modern inorganic aerogels. *Angewandte Chemie International Edition*, 56(43):13200–13221, 2017.

[14] A. S. Dorcheh and M. H. Abbasi. Silica aerogel; synthesis, properties and characterization. *Journal of Materials Processing Technology*, 199(1-3):10–26, 2008.

[15] H. Maleki, L. Durães, and A. Portugal. An overview on silica aerogels synthesis and different mechanical reinforcing strategies. *Journal of Non-Crystalline Solids*, 385:55–74, 2014.

[16] C. Stöcker and A. Baiker. Zirconia aerogels: effect of acid-to-alkoxide ratio, alcoholic solvent and supercritical drying method on structural properties. *Journal of non-crystalline solids*, 223(3):165–178, 1998.

[17] Y. Tokudome, K. Nakanishi, K. Kanamori, K. Fujita, H. Akamatsu, and T. Hanada. Structural characterization of hierarchically porous alumina aerogel and xerogel monoliths. *Journal of colloid and interface science*, 338(2):506–513, 2009.

[18] D. C. M. Dutoit, M. Schneider, and A. Baiker. Titania aerogels prepared by low-temperature supercritical drying. influence of extraction conditions. *Journal of Porous Materials*, 1(2):165–174, 1995.

[19] J. H. Harreld, W. Dong, and B. Dunn. Ambient pressure synthesis of aerogel-like vanadium oxide and molybdenum oxide. *Materials research bulletin*, 33(4):561–567, 1998.

[20] W. Dong, D. R. Rolison, and B. Dunna. Electrochemical properties of high surface area vanadium oxide aerogels. *Electrochemical and Solid-State Letters*, 3(10):457–459, 2000.

[21] V. Augustyn and B. Dunn. Vanadium oxide aerogels: nanostructured materials for enhanced energy storage. *Comptes Rendus Chimie*, 13(1-2):130–141, 2010.

[22] J. W. Long, R. M. Stroud, and D. R. Rolison. Controlling the pore-solid architecture of mesoporous, high surface area manganese oxides with the birnessite structure. *Journal of non-crystalline solids*, 285(1-3):288–294, 2001.

[23] C. Laberty-Robert, J. W. Long, E. M. Lucas, K. A. Pettigrew, R. M. Stroud, M. S. Doescher, and D. R. Rolison. Sol- gel-derived ceria nanoarchitectures: synthesis, characterization, and electrical properties. *Chemistry of materials*, 18(1):50–58, 2006.

[24] J. L. Gasser-Ramirez, B. C. Dunn, D. W. Ramirez, E. P. Fillerup, G. C. Turpin, Y. Shi, R. D. Ernst, R. J. Pugmire, E. M. Eyring, K. A. Pettigrew, et al. A simple synthesis of catalytically active, high surface area ceria aerogels. *Journal of non-crystalline solids*, 354(52-54):5509–5514, 2008.

[25] M. A. Thundathil, W. Lai, . Noailles, B. S. Dunn, and S. M. Haile. High surface-area ceria aerogel. *Journal of the American Ceramic Society*, 87(8):1442–1445, 2004.

[26] Y. Tao, M. Endo, and K. Kaneko. A review of synthesis and nanopore structures of organic polymer aerogels and carbon aerogels. *Recent Patents on Chemical Engineering*, 1:192–200, 2008.

[27] H. Ren, J. Zhu, Y. Bi, Y. Xu, and L. Zhang. Facile fabrication of mechanical monolithic polyamide aerogels via a modified sol-gel method. *Journal of Sol-Gel Science and Technology*, 82(2):417–423, 2017.

[28] X. M. Zhang, J. G. Liu, and S. Y. Yang. Synthesis and characterization of flexible and high-temperature resistant polyimide aerogel with ultra-low dielectric constant. *Express Polymer Letters*, 10(10), 2016.

[29] L. Weigold, D. P. Mohite, S. Mahadik-Khanolkar, N. Leventis, and G. Reichenauer. Correlation of microstructure and thermal conductivity in nanoporous solids: the case of polyurea aerogels synthesized from an aliphatic tri-isocyanate and water. *Journal of non-crystalline solids*, 368:105–111, 2013.

[30] N. Leventis, C. Sotiriou-Leventis, N. Chandrasekaran, S. Mulik, Z. J. Larimore, H. Lu, G. Churu, and J. T. Mang. Multifunctional polyurea aerogels from isocyanates and water. a structure- property case study. *Chemistry of Materials*, 22(24):6692–6710, 2010.

[31] C. Chidambareswarapattar, P. M. McCarver, H. Luo, H. Lu, C. Sotiriou-Leventis, and N. Leventis. Fractal multiscale nanoporous polyurethanes: flexible to extremely rigid aerogels from multifunctional small molecules. *Chemistry of Materials*, 25(15):3205–3224, 2013.

[32] N. Diascorn, S. Calas, H. Sallee, P. Achard, and A. Rigacci. Polyurethane aerogels synthesis for thermal insulation–textural, thermal and mechanical properties. *The Journal of Supercritical Fluids*, 106:76–84, 2015.

[33] R. W. Pekala, S. T. Mayer, J. L. Kaschmitter, and F. M. Kong. Carbon aerogels: An update on structure, properties, and applications. In Y. A. Attia, editor, *Sol-Gel Processing and Applications*, chapter 32, pages 369–377. Springer, 1994.

[34] T. F. Baumann, M. A. Worsley, T. Y. Han, and J. H. Satcher Jr. High surface area carbon aerogel monoliths with hierarchical porosity. *Journal of Non-Crystalline Solids*, 354(29):3513–3515, 2008.

[35] J. Li, X. Wang, Y. Wang, Q. Huang, C. Dai, S. Gamboa, and P. J. Sebastian. Structure and electrochemical properties of carbon aerogels synthesized at ambient temperatures as supercapacitors. *Journal of Non-Crystalline Solids*, 354(1):19–24, 2008.

[36] J. P. Vareda, A. Lamy-Mendes, and L. Durães. A reconsideration on the definition of the term aerogel based on current drying trends. *Microporous and Mesoporous Materials*, 258:211–216, 2018.

[37] U. Schubert. Chemistry and fundamentals of the sol–gel process. *The Sol-Gel Handbook*, pages 1–28, 2015.

[38] Z. Li, X. Cheng, S. He, X. Shi, and H. Yang. Characteristics of ambient-pressure-dried aerogels synthesized via different surface modification methods. *Journal of Sol-Gel Science and Technology*, 76(1):138–149, 2015.

[39] S.-W. Hwang, T.-Y. Kim, and S.-H. Hyun. Optimization of instantaneous solvent exchange/surface modification process for ambient synthesis of monolithic silica aerogels. *Journal of colloid and interface science*, 322(1):224–230, 2008.

[40] P. R. Aravind, P. Shajesh, P. Mukundan, and K. G. K. Warrier. Silica–titania aerogel monoliths with large pore volume and surface area by ambient pressure drying. *Journal of sol-gel science and technology*, 52(3):328–334, 2009.

[41] S.-W. Hwang, T.-Y. Kim, and S.-H. Hyun. Effect of surface modification conditions on the synthesis of mesoporous crack-free silica aerogel monoliths from waterglass via ambient-drying. *Microporous and mesoporous materials*, 130(1-3):295–302, 2010.

[42] C. E. Kim, J. S. Yoon, and H. J. Hwang. Synthesis of nanoporous silica aerogel by ambient pressure drying. *Journal of sol-gel science and technology*, 49(1):47, 2009.

[43] K. S. Kim, Y. Zhao, H. Jang, S. Y. Lee, J. M. Kim, K. S. Kim, J.-H. Ahn, P. Kim, J.-Y. Choi, and B. H. Hong. Large-scale pattern growth of graphene films for stretchable transparent electrodes. *Nature*, 457(7230):706–710, 2009.

[44] P. B. Sarawade, J.-K. Kim, H.-K. Kim, and H.-T. Kim. High specific surface area TEOS-based aerogels with large pore volume prepared at an ambient pressure. *Applied Surface Science*, 254(2):574–579, 2007.

[45] M. Shi, C. Tang, X. Yang, J. Zhou, F. Jia, Y. Han, and Z. Li. Superhydrophobic silica aerogels reinforced with polyacrylonitrile fibers for adsorbing oil from water and oil mixtures. *RSC Advances*, 7:4039–4045, 2017.

[46] L. Cai and G. Shan. Elastic silica aerogel using methyltrimethoxysilane precusor via ambient pressure drying. *Journal of Porous Materials*, 22(6):1455–1463, 2015.

[47] M. Ochoa, A. Lamy-Mendes, A. Maia, A. Portugal, and L. Durães. Influence of structure-directing additives on the properties of poly(methylsilsesquioxane) aerogel-like materials. *Gels*, 5(1):6, 2019.

[48] Z. Li, X. Cheng, S. He, X. Shi, L. Gong, and H. Zhang. Aramid fibers reinforced silica aerogel composites with low thermal conductivity and improved mechanical performance. *Compos. Part A - Appl. S.*, 84:316–325, 2016.

[49] L. A. Capadona, M. A. B. Meador, A. Alunni, E. F. Fabrizio, P. Vassilaras, and N. Leventis. Flexible, low-density polymer crosslinked silica aerogels. *Polymer*, 47(16):5754–5761, 2006.

[50] N. Leventis. Three-dimensional core-shell superstructures: mechanically strong aerogels. *Accounts of chemical research*, 40(9):874–884, 2007.

[51] N. Leventis, A. Palczer, L. McCorkle, G. Zhang, and C. Sotiriou-Leventis. Nanoengineered silica-polymer composite aerogels with no need for supercritical fluid drying. *Journal of sol-gel science and technology*, 35(2):99–105, 2005.

[52] R. B. Torres, J. P. Vareda, A. Lamy-Mendes, and L. Durães. Effect of different silylation agents on the properties of ambient pressure dried and supercritically dried vinyl-modified silica aerogels. *The Journal of Supercritical Fluids*, 147:81–89, 2019.

[53] H. Maleki, L. Durães, and A. Portugal. Synthesis of lightweight polymer-reinforced silica aerogels with improved mechanical and thermal insulation properties for space applications. *Microporous and Mesoporous Materials*, 197:116–129, 2014.

[54] L. Durães, M. Ochoa, N. Rocha, R. Patrício, N. Duarte, V. Redondo, and A. Portugal. Effect of the drying conditions on the microstructure of silica based xerogels and aerogels. *J. Nanosci. Nanotechnol.*, 12(8):6828–6834, 2012.

[55] S. Yun, H. Luo, and Y. Gao. Low-density, hydrophobic, highly flexible ambient-pressure-dried monolithic bridged silsesquioxane aerogels. *Journal of Materials Chemistry A*, 3(7):3390–3398, 2015.

[56] P. R. Aravind and G. D. Soraru. Porous silicon oxycarbide glasses from hybrid ambigels. *Microporous and mesoporous materials*, 142(2-3):511–517, 2011.

[57] Z. Shao, X. He, Z. Niu, T. Huang, X. Cheng, and Y. Zhang. Ambient pressure dried shape-controllable sodium silicate based composite silica aerogel monoliths. *Materials Chemistry and Physics*, 162:346–353, 2015.

[58] T. Noisser, G. Reichenauer, and N. Hüsing. In situ modification of the silica backbone leading to highly porous monolithic hybrid organic–inorganic materials via ambient pressure drying. *ACS Appl. Mater. Interfaces*, 6(2):1025–1029, 2014.

[59] G. Markevicius, R. Ladj, P. Niemeyer, T. Budtova, and A. Rigacci. Ambient-dried thermal superinsulating monolithic silica-based aerogels with short cellulosic fibers. *Journal of materials science*, 52(4):2210–2221, 2017.

[60] Z. T. Mazraeh-Shahi, A. M. Shoushtari, A. R. Bahramian, and M. Abdouss. Synthesis, pore structure and properties of polyurethane/silica hybrid aerogels dried at ambient pressure. *Journal of Industrial and Engineering Chemistry*, 21:797–804, 2015.

[61] W. Zhu, H. Yang, Y. Xie, S. Sun, and X. Guo. Hierarchically porous titania xerogel monoliths: Synthesis, characterization and electrochemical properties. *Materials Research Bulletin*, 73:48–55, 2016.

[62] L. Wu, Y. Huang, Z. Wang, L. Liu, and H. Xu. Fabrication of hydrophobic alumina aerogel monoliths by surface modification and ambient pressure drying. *Applied Surface Science*, 256(20):5973–5977, 2010.

[63] J. Huang, H. Liu, S. Chen, and C. Ding. Hierarchical porous MWCNTs-silica aerogel synthesis for high-efficiency oily water treatment. *Journal of Environmental Chemical Engineering*, 4(3):3274–3282, 2016.

[64] C. Li, L. Qiu, B. Zhang, D. Li, and C.-Y. Liu. Robust vacuum-/air-dried graphene aerogels and fast recoverable shape-memory hybrid foams. *Advanced Materials*, 28(7):1510–1516, 2016.

[65] X. Jia, B. Dai, Z. Zhu, J. Wang, W. Qiao, D. Long, and L. Ling. Strong and machinable carbon aerogel monoliths with low thermal conductivity prepared via ambient pressure drying. *Carbon*, 108:551–560, 2016.

[66] S. Katiyar, N. Kalaiselvi, and A. Sharma. Facile synthesis of hierarchical porous carbon monolith: A free-standing anode for Li-ion battery with enhanced electrochemical performance. *Industrial & Engineering Chemistry Research*, 55(45):11818–11828, 2016.

[67] Z. Wang, Z. Dai, J. Wu, N. Zhao, and J. Xu. Vacuum-dried robust bridged silsesquioxane aerogels. *Advanced Materials*, 25(32):4494–4497, 2013.

[68] J. Yang, S. Li, L. Yan, J. Liu, and F. Wang. Compressive behaviors and morphological changes of resorcinol–formaldehyde aerogel at high strain rates. *Microporous and Mesoporous Materials*, 133(1-3):134–140, 2010.

[69] Z.-L. Yu, G.-C. Li, N. Fechler, N. Yang, Z.-Y. Ma, X. Wang, M. Antonietti, and S.-H. Yu. Polymerization under hypersaline conditions: a robust route to phenolic polymer-derived carbon aerogels. *Angewandte Chemie International Edition*, 55(47):14623–14627, 2016.

[70] O. A. Shlyakhtin and Y.-J. Oh. Inorganic cryogels for energy saving and conversion. *Journal of electroceramics*, 23(2-4):452, 2009.

[71] X. Pei, W. Zhai, and W. Zheng. Preparation of poly (aryl ether ketone ketone)–silica composite aerogel for thermal insulation application. *Journal of Sol-Gel Science and Technology*, 76(1):98–109, 2015.

[72] J. Kang, H. Gi, R. Choe, and S. I. Yun. Fabrication and characterization of poly (3-hydroxybutyrate) gels using non-solvent-induced phase separation. *Polymer*, 104:61–71, 2016.

[73] X. Pei, W. Zhai, and W. Zheng. Preparation and characterization of highly cross-linked polyimide aerogels based on polyimide containing trimethoxysilane side groups. *Langmuir*, 30(44):13375–13383, 2014.

[74] Z. Zhao, D. Chen, and X. Jiao. Zirconia aerogels with high surface area derived from sols prepared by electrolyzing zirconium oxychloride solution: Comparison of aerogels prepared by freeze-drying and supercritical CO_2(l) extraction. *The Journal of Physical Chemistry C*, 111(50):18738–18743, 2007.

[75] J. Meng, Y. Cao, Y. Suo, Y. Liu, J. Zhang, and X. Zheng. Facile fabrication of 3D SiO_2@graphene aerogel composites as anode material for lithium ion batteries. *Electrochimica Acta*, 176:1001–1009, 2015.

[76] X. Wang, M. Lu, H. Wang, Y. Pei, H. Rao, and X. Du. Three-dimensional graphene aerogels–mesoporous silica frameworks for superior adsorption capability of phenols. *Separation and Purification Technology*, 153:7–13, 2015.

[77] S. Yun, H. Kim, H. Lee, and H. S. Park. Three-dimensionally macroporous, Si and N-incorporated graphene aerogels for gas adsorbents. *Materials Express*, 5(5):463–469, 2015.

[78] G. Zu, K. Kanamori, T. Shimizu, Y. Zhu, A. Maeno, H. Kaji, K. Nakanishi, and J. Shen. Versatile double cross-linking approach to transparent, machinable, super-compressible, highly bendable aerogel thermal superinsulators. *Chem. Mater.*, 30(8):2759–2770, 2018.

[79] A. C. Pierre and A. Rigacci. SiO_2 aerogels. In *Aerogels Handbook*, pages 21–45. Springer, 2011.

[80] A. V. Rao, S. D. Bhagat, H. Hirashima, and G. M. Pajonk. Synthesis of flexible silica aerogels using methyltrimethoxysilane (MTMS) precursor. *J. Colloid Interface Sci.*, 300(1):279–285, 2006.

[81] S. Štandeker, Z. an Novak, and Ž. Knez. Adsorption of toxic organic compounds from water with hydrophobic silica aerogels. *J. Colloid Interface Sci.*, 310(2):362–368, 2007.

[82] G. Qin, Y. Yao, W. Wei, and T. Zhang. Preparation of hydrophobic granular silica aerogels and adsorption of phenol from water. *Appl. Surf. Sci.*, 280:806–811, 2013.

[83] I. Smirnova, J. Mamic, and W. Arlt. Adsorption of drugs on silica aerogels. *Langmuir*, 19(20):8521–8525, 2003.

[84] M. Mohammadian, T. S. J. Kashi, M. Erfan, and F. P. Soorbaghi. Synthesis and characterization of silica aerogel as a promising drug carrier system. *J. Drug Deliv. Sci. Technol.*, 44:205–212, 2017.

[85] S. M. Jones. Aerogel: space exploration applications. *Journal of Sol-Gel Science and Technology*, 40(2-3):351–357, 2006.

[86] J. E. Amonette and J. Matyáš. Functionalized silica aerogels for gas-phase purification, sensing, and catalysis: A review. *Microporous Mesoporous Mater.*, 250:100–119, 2017.

[87] Y. N. Kharzheev. Use of silica aerogels in Cherenkov counters. *Phys. Part. Nucl.*, 39(1):107–135, 2008.

[88] M. Sachithanadam and S. C. Joshi. *Silica Aerogel Composites: Novel Fabrication Methods*. Springer, 2016.

[89] A. Lamy-Mendes, R. F. Silva, and L. Duraes. Advances in carbon nanostructure-silica aerogel composites: A review. *J. Mater. Chem. A*, 6:1340–1369, 2018.

[90] J. S. Lee, S. K. Hong, N. J. Hur, W.-S. Seo, and H. J. Hwang. Fabrication of spherical silica aerogel/magnetite nanocomposite particles. *Materials Letters*, 112:153–157, 2013.

[91] K. D. Sattler. *Carbon Nanomaterials Sourcebook: Graphene, Fullerenes, Nanotubes, and Nanodiamonds*. CRC Press, 2016.

[92] J. G. Duque, C. E. Hamilton, G. Gupta, S. A. Crooker, J. J. Crochet, A. Mohite, H. Htoon, K. A. D. Obrey, A. M. Dattelbaum, and S. K. Doorn. Fluorescent single-walled carbon nanotube aerogels in surfactant-free environments. *ACS Nano*, 5(8):6686–6694, 2011.

[93] A. I. Chernov, A. Y. Predein, A. F. Danilyuk, V. L. Kuznetsov, T. V. Larina, and E. D. Obraztsova. Optical properties of silica aerogels with embedded multiwalled carbon nanotubes. *Phys. Status Solidi B*, 253(12):2440–2445, 2016.

[94] H. Bargozin, L. Amirkhani, J. S. Moghaddas, and M. M. Ahadian. Synthesis and application of silica aerogel-MWCNT nanocomposites for adsorption of organic pollutants. *Scientia Iranica*, 17(2):122–132, 2010.

[95] T. Sun, Q. Zhuo, X. Liu, Z. Sun, Z. Wu, and H. Fan. Hydrophobic silica aerogel reinforced with carbon nanotube for oils removal. *J. Porous Mater.*, 21(6):967–973, 2014.

[96] M. Sachithanadam and S. C. Joshi. Thermal conductivity variations with composition of gelatin-silica aerogel-sodium dodecyl sulfate with functionalized multi-walled carbon nanotube doping in their composites. *International Journal of Heat and Mass Transfer*, 87:606–615, 2015.

[97] M. Piñero, M. del Mar Mesa-Díaz, D. de los Santos, M. V. Reyes-Peces, J. A. Díaz-Fraile, N. de la Rosa-Fox, L. Esquivias, and V. Morales-Florez. Reinforced silica-carbon nanotube monolithic aerogels synthesised by rapid controlled gelation. *J. Sol-Gel Sci. Technol.*, 86(2):391–399, 2018.

[98] Y. Lei, Z. Hu, B. Cao, X. Chen, and H. Song. Enhancements of thermal insulation and mechanical property of silica aerogel monoliths by mixing graphene oxide. *Materials Chemistry and Physics*, 187:183–190, 2017.

[99] D. Loche, L. Malfatti, D. Carboni, V. Alzari, A. Mariani, and M. F. Casula. Incorporation of graphene into silica-based aerogels and application for water remediation. *RSC Advances*, 6:66516–66523, 2016.

[100] S. Kabiri, D. N. H. Tran, S. Azari, and D. Losic. Graphene-diatom silica aerogels for efficient removal of mercury ions from water. *ACS Applied Materials & Interfaces*, 7(22):11815–11823, 2015.

[101] H. Maleki. Recent advances in aerogels for environmental remediation applications: a review. *Chemical Engineering Journal*, 300:98–118, 2016.

[102] H. H. Tang, E. S. Orndoff, and L. A. Trevino. Thermal performance of space suit elements with aerogel insulation for moon and Mars exploration. Technical report, SAE Technical Paper, 2006.

[103] J. Wang, J. Kuhn, and X. Lu. Monolithic silica aerogel insulation doped with TiO_2 powder and ceramic fibers. *Journal of Non-Crystalline Solids*, 186:296–300, 1995.

[104] M. B. Fernández van Raap, F. H. Sanchez, A. G. Leyva, M. L. Japas, E. Cabanillas, and H. Troiani. Synthesis and magnetic properties of iron oxide–silica aerogel nanocomposites. *Physica B: Condensed Matter*, 398(2):229–234, 2007.

[105] D. Nadargi, J. Gurav, M. A. Marioni, S. Romer, S. Matam, and M. M. Koebel. Methyltrimethoxysilane (MTMS)-based silica–iron oxide superhydrophobic nanocomposites. *Journal of Colloid and Interface Science*, 459:123–126, 2015.

[106] Y. Yang, E. Shi, P. Li, D. Wu, S. Wu, Y. Shang, W. Xu, A. Cao, and Q. Yuan. A compressible mesoporous SiO_2 sponge supported by a carbon nanotube network. *Nanoscale*, 6(7):3585–3592, 2014.

[107] Z. Fan, D. Z. Y. Tng, C. X. T. Lim, P. Liu, S. T. Nguyen, P. Xiao, A. Marconnet, C. Y. H. Lim, and H. M. Duong. Thermal and electrical properties of graphene/carbon nanotube aerogels. *Colloids and Surfaces A: Physicochemical and Engineering Aspects*, 445:48–53, 2014.

[108] M. M. Shokrieh and R. Rafiee. A review of the mechanical properties of isolated carbon nanotubes and carbon nanotube composites. *Mechanics of Composite Materials*, 46(2):155–172, 2010.

[109] R. J. Young, I. A. Kinloch, L. Gong, and K. S. Novoselov. The mechanics of graphene nanocomposites: a review. *Composites Science and Technology*, 72(12):1459–1476, 2012.

[110] A. G. Pandolfo and A. F. Hollenkamp. Carbon properties and their role in supercapacitors. *Journal of Power Sources*, 157(1):11–27, 2006.

[111] L. L. Zhang and X. S. Zhao. Carbon-based materials as supercapacitor electrodes. *Chemical Society Reviews*, 38(9):2520–2531, 2009.

[112] P. B. Wagh, A. Venkateswara Rao, and D. Haranath. Influence of molar ratios of precursor, solvent and water on physical properties of citric acid catalyzed TEOS silica aerogels. *Materials Chemistry and Physics*, 53(1):41–47, 1998.

[113] A. V. Rao, G. M. Pajonk, S. D. Bhagat, and P. Barboux. Comparative studies on the surface chemical modification of silica aerogels based on various organosilane compounds of the type R_nSiX_{4-n}. *Journal of Non-Crystalline Solids*, 350:216–223, 2004.

[114] S. D. Bhagat and A. V. Rao. Surface chemical modification of TEOS based silica aerogels synthesized by two step (acid-base) sol-gel process. *Applied Surface Science*, 252(12):4289–4297, 2006.

[115] L. L. Hench and J. K. West. The sol-gel process. *Chemical Reviews*, 90(1):33–72, 1990.

[116] C.-L. Chiang, C.-C. M. Ma, D.-L. Wu, and H.-C. Kuan. Preparation, characterization, and properties of novolac-type phenolic/SiO_2 hybrid organic-inorganic nanocomposite materials by sol-gel method. *Journal of Polymer Science Part A: Polymer Chemistry*, 41(7):905–913, 2003.

[117] D. A. Loy and K. J. Shea. Bridged polysilsesquioxanes. Highly porous hybrid organic-inorganic materials. *Chemical Reviews*, 95(5):1431–1442, 1995.

[118] K. J. Shea and D. A. Loy. Bridged polysilsesquioxanes. Molecular-engineered hybrid organic-inorganic materials. *Chemistry of Materials*, 13(10):3306–3319, 2001.

[119] A. E. Danks, S. R. Hall, and Z. Schnepp. The evolution of 'sol-gel' chemistry as a technique for materials synthesis. *Materials Horizons*, 3(2):91–112, 2016.

[120] A. P. Rao, G. M. Pajonk, and A. V. Rao. Effect of preparation conditions on the physical and hydrophobic properties of two step processed ambient pressure dried silica aerogels. *Journal of Materials Science*, 40(13):3481–3489, 2005.

[121] N. Hüsing, U. Schubert, B. Riegel, and W. Kiefer. Chemical functionalization of silica aerogels. *MRS Online Proceedings Library Archive*, 435, 1996.

[122] L. M. Sanz-Moral, M. Rueda, A. Nieto, Z. Novak, Ž. Knez, and Á. Martín. Gradual hydrophobic surface functionalization of dry silica aerogels by reaction with silane precursors dissolved in supercritical carbon dioxide. *The Journal of Supercritical Fluids*, 84:74–79, 2013.

[123] R.-A. Strøm, Y. Masmoudi, A. Rigacci, G. Petermann, L. Gullberg, B. Chevalier, and M.-A. Einarsrud. Strengthening and aging of wet silica gels for up-scaling of aerogel preparation. *Journal of Sol-Gel Science and Technology*, 41(3):291–298, 2007.

[124] K. Kraiwattanawong, H. Tamon, and P. Praserthdam. Influence of solvent species used in solvent exchange for preparation of mesoporous carbon xerogels from resorcinol and formaldehyde via subcritical drying. *Microporous and Mesoporous Materials*, 138(1-3):8–16, 2011.

[125] A. Venkateswara Rao, G. M. Pajonk, U. K. H. Bangi, A. P. Rao, and M. M. Koebel. Sodium silicate based aerogels via ambient pressure drying. In Michel Andre Aegerter, Nicholas Leventis, and Matthias M Koebel, editors, *Aerogels Handbook*, chapter 5, pages 103–124. Springer Science & Business Media, 2011.

[126] L. Zubizarreta, A. Arenillas, A. Domínguez, J. A. Menéndez, and J. J. Pis. Development of microporous carbon xerogels by controlling synthesis conditions. *Journal of Non-Crystalline Solids*, 354(10-11):817–825, 2008.

[127] N. Job, F. Panariello, J. Marien, M. Crine, J.-P. Pirard, and A. Léonard. Synthesis optimization of organic xerogels produced from convective air-drying of resorcinol-formaldehyde gels. *Journal of Non-Crystalline Solids*, 352(1):24–34, 2006.

[128] C. Scherdel and G. Reichenauer. Microporous and mesoporous carbon xerogel having a characteristic mesopore size and precursors thereof and also a process for producing these and their use, 2012.

[129] T. Yamamoto, T. Nishimura, T. Suzuki, and H. Tamon. Effect of drying conditions on mesoporosity of carbon precursors prepared by sol-gel polycondensation and freeze drying. *Carbon*, 15(39):2374–2376, 2001.

[130] A. C. Pierre and G. M. Pajonk. Chemistry of aerogels and their applications. *Chemical Reviews*, 102(11):4243–4266, 2002.

[131] R. Kocklenberg, B. Mathieu, S. Blacher, R. Pirard, J.-P. Pirard, R. Sobry, and G. Van den Bossche. Texture control of freeze-dried resorcinol-formaldehyde gels. *Journal of Non-Crystalline Solids*, 225:8–13, 1998.

[132] M. Yoshimune, T. Yamamoto, M. Nakaiwa, and K. Haraya. Preparation of highly mesoporous carbon membranes via a sol–gel process using resorcinol and formaldehyde. *Carbon*, 46(7):1031–1036, 2008.

[133] N. Job, R. Pirard, J. Marien, and J.-P. Pirard. Porous carbon xerogels with texture tailored by pH control during sol-gel process. *Carbon*, 42(3):619–628, 2004.

[134] E. G. Calvo, J. A. Menéndez, and A. Arenillas. Designing nanostructured carbon xerogels. In Mohammed Muzibur Rahman, editor, *Nanomaterials*, chapter 9, pages 619–628. IntechOpen, Rijeka, 2011.

[135] P. J. M. Carrott, F. L. Conceição, and M. M. L. Ribeiro Carrott. Use of n-nonane pre-adsorption for the determination of micropore volume of activated carbon aerogels. *Carbon*, 45(6):1310–1313, 2007.

[136] T. Woignier and J. Phalippou. Mechanical strength of silica aerogels. *Journal of Non-Crystalline Solids*, 100(1-3):404–408, 1988.

[137] M. A. B. Meador, S. L. Vivod, L. McCorkle, D. Quade, R. M. Sullivan, L. J. Ghosn, N. Clark, and L. A. Capadona. Reinforcing polymer cross-linked aerogels with carbon nanofibers. *Journal of Materials Chemistry*, 18(16):1843–1852, 2008.

[138] S. Iijima. Helical microtubules of graphitic carbon. *Nature*, 354(6348):56–58, 1991.

[139] S. Iijima and T. Ichihashi. Single-shell carbon nanotubes of 1-nm diameter. *Nature*, 363(6430):603–605, 1993.

[140] T. W. Odom, J.-L. Huang, P. Kim, and C. M. Lieber. Atomic structure and electronic properties of single-walled carbon nanotubes. *Nature*, 391(6662):62–64, 1998.

[141] A. Misra. Carbon nanotubes for sensing applications. In Klaus D Sattler, editor, *Carbon Nanomaterials Sourcebook: Graphene, Fullerenes, Nanotubes, and Nanodiamonds*, volume 1, chapter 18, pages 443–454. CRC Press, 2016.

[142] A. Krishnan, E. Dujardin, T. W. Ebbesen, P. N. Yianilos, and M. M. J. Treacy. Young's modulus of single-walled nanotubes. *Physical Review B*, 58(20):14013–14019, 1998.

[143] D. Mata, M. H. Fernandes, M. A. Lopes, and R. F. Silva. Biomedical carbon nanotubes. In Klaus D Sattler, editor, *Carbon Nanomaterials Sourcebook: Graphene, Fullerenes, Nanotubes, and Nanodiamonds*, volume 1, chapter 19, pages 455–490. CRC Press, 2016.

[144] Z. Zhou, C. Lai, L. Zhang, Y. Qian, H. Hou, D. H. Reneker, and H. Fong. Development of carbon nanofibers from aligned electrospun polyacrylonitrile nanofiber bundles and characterization of their microstructural, electrical, and mechanical properties. *Polymer*, 50(13):2999–3006, 2009.

[145] M. M. Shokrieh and R. Rafiee. Prediction of Young's modulus of graphene sheets and carbon nanotubes using nanoscale continuum mechanics approach. *Materials & Design*, 31(2):790–795, 2010.

[146] H. O. Pierson. Pyrolytic graphite. In Hugh O. Pierson, editor, *Handbook of Carbon, Graphite, Diamonds and Fullerenes*, chapter 7, pages 141–165. William Andrew Publishing, Oxford, 1993.

[147] A. A. Balandin, S. Ghosh, W. Bao, I. Calizo, D. Teweldebrhan, F. Miao, and C. N. Lau. Superior thermal conductivity of single-layer graphene. *Nano Letters*, 8(3):902–907, 2008.

[148] T.-Y. Wei and S.-Y. Lu. Aerogels for energy saving and storage. In Ling Zang, editor, *Energy Efficiency and Renewable Energy Through Nanotechnology*, pages 873–911. Springer London, London, 2011.

[149] N. K. Mahanta, A. R. Abramson, M. L. Lake, D. J. Burton, J. C. Chang, H. K. Mayer, and J. L. Ravine. Thermal conductivity of carbon nanofiber mats. *Carbon*, 48(15):4457–4465, 2010.

[150] J. Zhang and X. S. Zhao. Graphene-based materials for electrochemical energy storage. In Z. Shen Y. Wu and T. Yu, editors, *Two-Dimensional Carbon: Fundamental Properties, Synthesis, Characterization, and Applications*, chapter 8, pages 183–246. CRC Press, 2014.

[151] A. Peigney, C. Laurent, E. Flahaut, R. R. Bacsa, and A. Rousset. Specific surface area of carbon nanotubes and bundles of carbon nanotubes. *Carbon*, 39(4):507–514, 2001.

[152] M. D. Stoller, S. Park, Y. Zhu, J. An, and R. S. Ruoff. Graphene-based ultracapacitors. *Nano Letters*, 8(10):3498–3502, 2008.

[153] C. Lu and C. Liu. Removal of nickel (II) from aqueous solution by carbon nanotubes. *Journal of Chemical Technology & Biotechnology: International Research in Process, Environmental & Clean Technology*, 81(12):1932–1940, 2006.

[154] B. Zhang, F. Kang, J.-M. Tarascon, and J.-K. Kim. Recent advances in electrospun carbon nanofibers and their application in electrochemical energy storage. *Progress in Materials Science*, 76:319–380, 2016.

[155] M. Sarno and A. Senatore. CVD-synthesized carbon nanotubes. In Klaus D Sattler, editor, *Carbon Nanomaterials Sourcebook: Graphene, Fullerenes, Nanotubes, and Nanodiamonds*, volume 1, chapter 13, pages 337–356. CRC Press, 2016.

[156] J. Robertson. Heterogeneous catalysis model of growth mechanisms of carbon nanotubes, graphene and silicon nanowires. *Journal of Materials Chemistry*, 22(37):19858–19862, 2012.

[157] A. C. Dillon, A. H. Mahan, P. A. Parilla, J. L. Alleman, M. J. Heben, K. M. Jones, and K. E. H. Gilbert. Continuous hot wire chemical vapor deposition of high-density carbon multiwall nanotubes. *Nano Letters*, 3(10):1425–1429, 2003.

[158] C. J. Lee, D. W. Kim, T. J. Lee, Y. C. Choi, Y. S. Park, Y. H. Lee, W. B. Choi, N. S. Lee, G.-S. Park, and J. M. Kim. Synthesis of aligned carbon nanotubes using thermal chemical vapor deposition. *Chemical Physics Letters*, 312(5-6):461–468, 1999.

[159] M. Chhowalla, K. Bt. K. Teo, C. Ducati, N. L. Rupesinghe, G. A. J. Amaratunga, A. C. Ferrari, D. Roy, J. Robertson, and W. I. Milne. Growth process conditions of vertically aligned carbon nanotubes using plasma enhanced chemical vapor deposition. *Journal of Applied Physics*, 90(10):5308–5317, 2001.

[160] B. Gan, J. Ahn, Q. Zhang, S. F. Yoon, Q.-F. Huang, H. Yang, M.-B. Yu, W.-Z. Li, et al. Branching carbon nanotubes deposited in HFCVD system. *Diamond and Related Materials*, 9(3-6):897–900, 2000.

[161] S. Hofmann, C. Ducati, B. Kleinsorge, and J. Robertson. Direct growth of aligned carbon nanotube field emitter arrays onto plastic substrates. *Applied Physics Letters*, 83(22):4661–4663, 2003.

[162] K. Inaba, K. Saida, P. Ghosh, K. Matsubara, M. Subramanian, A. Hayashi, Y. Hayashi, M. Tanemura, M. Kitazawa, and R. Ohta. Determination of Young's modulus of carbon nanofiber probes fabricated by the argon ion bombardment of carbon coated silicon cantilever. *Carbon*, 49(13):4191–4196, 2011.

[163] Y. A. Kim, T. Hayashi, M. Endo, and M. S. Dresselhaus. Carbon nanofibers. In R. Vajtai, editor, *Springer Handbook of Nanomaterials*, chapter 7, pages 233–262. Springer, 2013.

[164] J. Huang, Y. Liu, and T. You. Carbon nanofiber based electrochemical biosensors: A review. *Analytical Methods*, 2(3):202–211, 2010.

[165] P. Serp, M. Corrias, and P. Kalck. Carbon nanotubes and nanofibers in catalysis. *Applied Catalysis A: General*, 253(2):337–358, 2003.

[166] S.-U. Kim and K.-H. Lee. Carbon nanofiber composites for the electrodes of electrochemical capacitors. *Chemical Physics Letters*, 400(1-3):253–257, 2004.

[167] R. L. Poveda and N. Gupta. Carbon nanofibers: Structure and fabrication. In *Carbon Nanofiber Reinforced Polymer Composites*, pages 11–26. Springer, 2016.

[168] H. Song and W. Shen. Carbon nanofibers: synthesis and applications. *Journal of Nanoscience and Nanotechnology*, 14(2):1799–1810, 2014.

[169] N. M. Rodriguez. A review of catalytically grown carbon nanofibers. *Journal of Materials Research*, 8(12):3233–3250, 1993.

[170] L. Feng, N. Xie, and J. Zhong. Carbon nanofibers and their composites: a review of synthesizing, properties and applications. *Materials*, 7(5):3919–3945, 2014.

[171] L. Zhang, A. Aboagye, A. Kelkar, C. Lai, and H. Fong. A review: carbon nanofibers from electrospun polyacrylonitrile and their applications. *Journal of Materials Science*, 49(2):463–480, 2014.

[172] M. Inagaki, Y. Yang, and F. Kang. Carbon nanofibers prepared via electrospinning. *Advanced Materials*, 24(19):2547–2566, 2012.

[173] S. K. Nataraj, K. S. Yang, and T. M. Aminabhavi. Polyacrylonitrile-based nanofibers—a state-of-the-art review. *Progress in Polymer Science*, 37(3):487–513, 2012.

[174] C. N. Rao, A. K. Sood, K. S. Subrahmanyam, and A. Govindaraj. Graphene: the new two-dimensional nanomaterial. *Angewandte Chemie International Edition*, 48(42):7752–7777, 2009.

[175] K. S. Novoselov and A. K. Geim. The rise of graphene. *Nature Materials*, 6(3):183–191, 2007.

[176] K. S. Novoselov, A. K. Geim, S. V. Morozov, D. Jiang, Y. Zhang, S. V. Dubonos, I. V. Grigorieva, and A. A. Firsov. Electric field effect in atomically thin carbon films. *Science*, 306(5696):666–669, 2004.

[177] P. A. Denis and F. Iribarne. Comparative study of defect reactivity in graphene. *The Journal of Physical Chemistry C*, 117(37):19048–19055, 2013.

[178] C. Lee, X. Wei, J. W. Kysar, and J. Hone. Measurement of the elastic properties and intrinsic strength of monolayer graphene. *Science*, 321(5887):385–388, 2008.

[179] G. E. Dieter and D. J. Bacon. *Mechanical metallurgy*, volume 3. McGraw-Hill New York, 1986.

[180] M. Ahmad, I. Khalid, A. Ayaz, and M. Hussain. Graphene Network. In Klaus D Sattler, editor, *Carbon Nanomaterials Sourcebook: Graphene, Fullerenes, Nanotubes, and Nanodiamonds*, volume 1, chapter 3, pages 67–88. CRC Press, 2016.

[181] X.-M. Chen, G.-H. Wu, Y.-Q. Jiang, Y.-R. Wang, and X. Chen. Graphene and graphene-based nanomaterials: the promising materials for bright future of electroanalytical chemistry. *Analyst*, 136(22):4631–4640, 2011.

[182] X. Li, W. Cai, J. An, S. Kim, J. Nah, D. Yang, R. Piner, A. Velamakanni, I. Jung, E. Tutuc, et al. Large-area synthesis of high-quality and uniform graphene films on copper foils. *Science*, 324(5932):1312–1314, 2009.

[183] R. W. Pekala. Organic aerogels from the polycondensation of resorcinol with formaldehyde. *Journal of Materials Science*, 24(9):3221–3227, 1989.

[184] A. K. Meena, G. K. Mishra, P. K. Rai, C. Rajagopal, and P. N. Nagar. Removal of heavy metal ions from aqueous solutions using carbon aerogel as an adsorbent. *Journal of Hazardous Materials*, 122(1-2):161–170, 2005.

[185] R. W. Pekala, J. C. Farmer, C. T. Alviso, T. D. Tran, S. T. Mayer, J. M. Miller, and B. Dunn. Carbon aerogels for electrochemical applications. *Journal of Non-Crystalline Solids*, 225:74–80, 1998.

[186] R. Saliger, U. Fischer, C. Herta, and J. Fricke. High surface area carbon aerogels for supercapacitors. *Journal of Non-Crystalline Solids*, 225:81–85, 1998.

[187] C. Moreno-Castilla and F. J. Maldonado-Hódar. Carbon aerogels for catalysis applications: An overview. *Carbon*, 43(3):455–465, 2005.

[188] L. W. Hrubesh and R. W. Pekala. Thermal properties of organic and inorganic aerogels. *Journal of Materials Research*, 9(3):731–738, 1994.

[189] S. Mulik and C. Sotiriou-Leventis. Resorcinol–formaldehyde aerogels. In Michel Andre Aegerter, Nicholas Leventis, and Matthias M Koebel, editors, *Aerogels Handbook*, chapter 11, pages 215–234. Springer Science & Business Media, 2011.

[190] S. A. Al-Muhtaseb and J. A. Ritter. Preparation and properties of resorcinol–formaldehyde organic and carbon gels. *Advanced Materials*, 15(2):101–114, 2003.

[191] A. Šebenik, U. Osredkar, and I. Vizovišek. Study of the reaction between resorcinol and formaldehyde. *Polymer*, 22(6):804–806, 1981.

[192] R. W. Pekala, C. T. Alviso, F. M. Kong, and S. S. Hulsey. Aerogels derived from multifunctional organic monomers. *Journal of Non-Crystalline Solids*, 145:90–98, 1992.

[193] C. Lin and J. A. Ritter. Effect of synthesis pH on the structure of carbon xerogels. *Carbon*, 35(9):1271–1278, 1997.

[194] L. Zuo, Y. Zhang, L. Zhang, Y.-E. Miao, W. Fan, and T. Liu. Polymer/carbon-based hybrid aerogels: preparation, properties and applications. *Materials*, 8(10):6806–6848, 2015.

[195] N. Job, C. J. Gommes, R. Pirard, and J.-P. Pirard. Effect of the counter-ion of the basification agent on the pore texture of organic and carbon xerogels. *Journal of Non-Crystalline Solids*, 354(40-41):4698–4701, 2008.

[196] X. Lu, R. Caps, J. Fricke, C. T. Alviso, and R. W. Pekala. Correlation between structure and thermal conductivity of organic aerogels. *Journal of Non-Crystalline Solids*, 188(3):226–234, 1995.

[197] H. Tamon, H. Ishizaka, M. Mikami, and M. Okazaki. Porous structure of organic and carbon aerogels synthesized by sol-gel polycondensation of resorcinol with formaldehyde. *Carbon*, 35(6):791–796, 1997.

[198] Y. Zhu, H. Hu, W. Li, and X. Zhang. Resorcinol-formaldehyde based porous carbon as an electrode material for supercapacitors. *Carbon*, 45(1):160–165, 2007.

[199] L. Lei, Z. Fu, Y. Yi, X. Huang, H. Tu, and C. Wang. Preparation and characterization of RF aerogel on UV irradiation method. *Journal of Sol-Gel Science and Technology*, 72(3):553–558, 2014.

[200] S. Berthon, O. Barbieri, F. Ehrburger-Dolle, E. Geissler, P. Achard, F. Bley, A.-M. Hecht, F. Livet, G. M. Pajonk, N. Pinto, et al. DLS and SAXS investigations of organic gels and aerogels. *Journal of non-crystalline solids*, 285(1-3):154–161, 2001.

[201] O. Barbieri, F. Ehrburger-Dolle, T. P. Rieker, G. M. Pajonk, N. Pinto, and A. V. Rao. Small-angle x-ray scattering of a new series of organic aerogels. *Journal of Non-Crystalline Solids*, 285(1-3):109–115, 2001.

[202] K. Y. Kang, B. I. Lee, and J. S. Lee. Hydrogen adsorption on nitrogen-doped carbon xerogels. *Carbon*, 47(4):1171–1180, 2009.

[203] X.-Y. Song, W. Cao, M. R. Ayers, and A. J. Hunt. Carbon nanostructures in silica aerogel composites. *Journal of Materials Research*, 10(2):251–254, 1995.

[204] U. K. H. Bangi, M. S. Kavale, S. Baek, and H.-H. Park. Synthesis of MWCNTs doped sodium silicate based aerogels by ambient pressure drying. *J. Sol-Gel Sci. Technol.*, 62(2):201–207, 2012.

[205] B. Wang, K. Song, Y. Han, and T. Zhang. Synthesis and characterization of multi-walled carbon nanotube doped silica aerogels. *J. Wuhan Univ. Technol.*, 27(3):512–515, 2012.

[206] M. Sachithanadam and S. C. Joshi. High strain recovery with improved mechanical properties of gelatin–silica aerogel composites post-binding treatment. *Journal of Materials Science*, 49(1):163–179, Jan 2014.

[207] F. H. Gojny, J. Nastalczyk, Z. Roslaniec, and K. Schulte. Surface modified multi-walled carbon nanotubes in CNT/epoxy-composites. *Chemical Physics Letters*, 370(5-6):820–824, 2003.

[208] A. Ślosarczyk. Synthesis and characterization of silica aerogel-based nanocomposites with carbon fibers and carbon nanotubes in hybrid system. *Journal of Sol-Gel Science and Technology*, 84(1):16–22, 2017.

[209] W. Lu, E. S. Steigerwalt, J. T. Moore, L. M. Sullivan, E. W. Collins, and C. M. Lukehart. Carbothermal transformation of a graphitic carbon nanofiber/silica aerogel composite to a SiC/silica nanocomposite. *Journal of Nanoscience and Nanotechnology*, 4(7):803–808, 2004.

[210] P. E. Anderson and N. M. Rodriguez. Growth of graphite nanofibers from the decomposition of CO/H_2 over silica-supported iron–nickel particles. *Journal of Materials Research*, 14(7):2912–2921, 1999.

[211] T.-Y. Wei, S.-Y. Lu, and Y.-C. Chang. A new class of opacified monolithic aerogels of ultralow high-temperature thermal conductivities. *The Journal of Physical Chemistry C*, 113(17):7424–7428, 2009.

[212] S. Tajik, B. Nasernejad, and A. Rashidi. Preparation of silica-graphene nanohybrid as a stabilizer of emulsions. *Journal of Molecular Liquids*, 222:788–795, 2016.

[213] S. Dervin, Y. Lang, T. Perova, S. H. Hinder, and S. C. Pillai. Graphene oxide reinforced high surface area silica aerogels. *Journal of Non-Crystalline Solids*, 465:31–38, 2017.

[214] D. C. Marcano, D. V. Kosynkin, J. M. Berlin, A. Sinitskii, Z. Sun, A. Slesarev, L. B. Alemany, W. Lu, and J. M. Tour. Improved synthesis of graphene oxide. *ACS Nano*, 4(8):4806–4814, 2010.

[215] L. Hong-li, H. Xiang, L. Hong-yan, L. Jing, and L. Ya-jing. Novel GO/silica composite aerogels with enhanced mechanical and thermal insulation properties prepared at ambient pressure. *Ferroelectrics*, 528(1):15–21, 2018.

[216] J. Zhu, H. Ren, and Y. Bi. Opacified graphene-doped silica aerogels with controllable thermal conductivity. *Journal of Porous Materials*, 25(6):1697–1705, 2018.

[217] K. Oikawa, K. Toyota, S. Sakatani, Y. Hayashi, and H. Takizawa. Facile synthesis and thermal properties of waterglass-based silica xerogel nanocomposites containing reduced graphene oxide. *Ceramics International*, 45(4):4201–4207, 2019.

[218] S. V. Thakkar, A. Pinna, C. M. Carbonaro, L. Malfatti, P. Guardia, A. Cabot, and M. F. Casula. Performance of oil sorbents based on reduced graphene oxide–silica composite aerogels. *Journal of Environmental Chemical Engineering*, 8(1):103632, 2020.

[219] M. Zhang, Q. Xiao, C. Chen, L. Li, and W. Yuan. Developing a heat-insulating composite phase change material with light-to-thermal conversion performance from graphene oxide/silica hybrid aerogel. *Applied Thermal Engineering*, page 115303, 2020.

[220] W. S. Hummers and R. E. Offeman. Preparation of graphitic oxide. *Journal of the American Chemical Society*, 80(6):1339, 1958.

[221] H. Fei, L. Ya, L. Jin, F. Min-Han, and H. Xiao-Dong. Development of SiO_2/C and SiC/C composites featuring aerogel structures. *Journal of Inorganic Materials*, 32(5):449–458, 2017.

[222] L. Chen, R. Zhang, D.-H. Long, and L.-C. Ling. Synthesis and structure of carbon/silica hybrid aerogels. *Journal of Inorganic Materials*, 24(4):690–694, 2009.

[223] L. Ye, Z.-H. Ji, W.-J. Han, J.-D. Hu, and T. Zhao. Synthesis and characterization of silica/carbon composite aerogels. *Journal of the American Ceramic Society*, 93(4):1156–1163, 2010.

[224] K. Chen, Z. Bao, A. Du, X. Zhu, G. Wu, J. Shen, and B. Zhou. Synthesis of resorcinol–formaldehyde/silica composite aerogels and their low-temperature conversion to mesoporous silicon carbide. *Microporous and Mesoporous Materials*, 149(1):16–24, 2012.

[225] K. Chen, Z. Bao, A. Du, X. Zhu, J. Shen, G. Wu, Z. Zhang, and B. Zhou. One-pot synthesis, characterization and properties of acid-catalyzed resorcinol/formaldehyde cross-linked silica aerogels and their conversion to hierarchical porous carbon monoliths. *Journal of Sol-Gel Science and Technology*, 62(3):294–303, 2012.

[226] Y. Kong, Y. Zhong, X. Shen, S. Cui, M. Yang, K. Teng, and J. Zhang. Facile synthesis of resorcinol–formaldehyde/silica composite aerogels and their transformation to monolithic carbon/silica and carbon/silicon carbide composite aerogels. *Journal of Non-Crystalline Solids*, 358(23):3150–3155, 2012.

[227] B. Xu, H. Wu, C. X. Lin, B. Wang, Z. Zhang, and X. S. Zhao. Stabilization of silicon nanoparticles in graphene aerogel framework for lithium ion storage. *RSC Advances*, 5:30624–30630, 2015.

[228] X. Hu, Y. Jin, B. Zhu, Y. Tan, S. Zhang, L. Zong, Z. Lu, and J. Zhu. Free-standing graphene-encapsulated silicon nanoparticle aerogel as an anode for lithium ion batteries. *ChemNanoMat*, 2:671–674, 2016.

[229] H. C. Shim, I. Kim, C.-S. Woo, H.-J. Lee, and S. Hyun. Nanospherical solid electrolyte interface layer formation in binder-free carbon nanotube aerogel/Si nanohybrids to provide lithium-ion battery anodes with a long-cycle life and high capacity. *Nanoscale*, 9(14):4713–4720, 2017.

[230] A. Katti, N. Shimpi, S. Roy, H. Lu, E. F. Fabrizio, A. Dass, L. A. Capadona, and N. Leventis. Chemical, physical, and mechanical characterization of isocyanate cross-linked amine-modified silica aerogels. *Chemistry of Materials*, 18(2):285–296, 2006.

[231] Y. Pan, S. He, L. Gong, X. Cheng, C. Li, Z. Li, Z. Liu, and H. Zhang. Low thermal-conductivity and high thermal stable silica aerogel based on MTMS/water-glass co-precursor prepared by freeze drying. *Materials & Design*, 113:246 –253, 2017.

[232] J. He, X. Li, D. Su, H. Ji, and XiaoJing Wang. Ultra-low thermal conductivity and high strength of aerogels/fibrous ceramic composites. *Journal of the European Ceramic Society*, 36(6):1487–1493, 2016.

[233] J. Feng, D. Le, S. T. Nguyen, V. T. C. Nien, D. Jewell, and H. M. Duong. Silica-cellulose hybrid aerogels for thermal and acoustic insulation applications. *Colloids and Surfaces A: Physicochemical and Engineering Aspects*, 506:298–305, 2016.

[234] C. Yue, J. Feng, J. Feng, and Y. Jiang. Ultralow-density and high-strength graphene aerogels composites for thermal insulation. *Materials Letters*, 188:169–171, 2017.

[235] J. C. H. Wong, H. Kaymak, P. Tingaut, S. Brunner, and M. M. Koebel. Mechanical and thermal properties of nanofibrillated cellulose reinforced silica aerogel composites. *Microporous and Mesoporous Materials*, 217:150–158, 2015.

[236] J. Li, Y. Lei, D. Xu, F. Liu, J. Li, A. Sun, J. Guo, and G. Xu. Improved mechanical and thermal insulation properties of monolithic attapulgite nanofiber/silica aerogel composites dried at ambient pressure. *Journal of Sol-Gel Science and Technology*, 82(3):702–711, Jun 2017.

[237] C. Yue, J. Feng, J. Feng, and Y. Jiang. Efficient gaseous thermal insulation aerogels from 2-dimension nitrogen-doped graphene sheets. *International Journal of Heat and Mass Transfer*, 109:1026–1030, 2017.

[238] A. V. Rao, N. D. Hegde, and H. Hirashima. Absorption and desorption of organic liquids in elastic superhydrophobic silica aerogels. *Journal of Colloid and Interface Science*, 305(1):124–132, 2007.

[239] S. Štandeker, A. Veronovski, Z. Novak, and Ž. Knez. Silica aerogels modified with mercapto functional groups used for Cu(II) and Hg(II) removal from aqueous solutions. *Desalination*, 269(1):223–230, 2011.

[240] S. Motahari, M. Nodeh, and K. Maghsoudi. Absorption of heavy metals using resorcinol formaldehyde aerogel modified with amine groups. *Desalination and Water Treatment*, 57(36):16886–16897, 2016.

[241] P. S. Suchithra, L. Vazhayal, A. P. Mohamed, and S. Ananthakumar. Mesoporous organic–inorganic hybrid aerogels through ultrasonic assisted sol–gel intercalation of silica–PEG in bentonite for effective removal of dyes, volatile organic pollutants and petroleum products from aqueous solution. *Chemical Engineering Journal*, 200–202:589–600, 2012.

[242] M. L. N. Perdigoto, R. C. Martins, N. Rocha, M. J. Quina, L. Gando-Ferreira, R. Patrício, and L. Durães. Application of hydrophobic silica based aerogels and xerogels for removal of toxic organic compounds from aqueous solutions. *Journal of Colloid and Interface Science*, 380(1):134–140, 2012.

[243] M. Firoozmandan, J. Moghaddas, and N. Yasrebi. Performance of water glass-based silica aerogel for adsorption of phenol from aqueous solution. *Journal of Sol-Gel Science and Technology*, 79(1):67–75, 2016.

[244] D. Mata, R. M. Silva, A. J. S. Fernandes, F. J. Oliveira, P. M. F. J. Costa, and R. F. Silva. Upscaling potential of the CVD stacking growth method to produce dimensionally-controlled and catalyst-free multi-walled carbon nanotubes. *Carbon*, 50(10):3585–3606, 2012.

[245] M. T. Kim, K. Y. Rhee, S. J. Park, and D. Hui. Effects of silane-modified carbon nanotubes on flexural and fracture behaviors of carbon nanotube-modified epoxy/basalt composites. *Compos. Part B - Eng.*, 43(5):2298–2302, 2012.

[246] M. Ochoa, L. Durães, A. M. Beja, and A. Portugal. Study of the suitability of silica based xerogels synthesized using ethyltrimethoxysilane and/or methyltrimethoxysilane precursors for aerospace applications. *J Sol-Gel Sci Technol*, 61(1):151–160, 2012.

[247] M. D. Clark, S. Subramanian, and R. Krishnamoorti. Understanding surfactant aided aqueous dispersion of multi-walled carbon nanotubes. *J. Colloid Interface Sci.*, 354(1):144–151, 2011.

[248] C. J. Brinker, Y. Lu, A. Sellinger, and H. Fan. Evaporation-induced self-assembly: Nanostructures made easy. *Adv. Mater.*, 11(7):579–585, 1999.

[249] X. Cheng, C. Li, X. Shi, Z. Li, L. Gong, and H. Zhang. Rapid synthesis of ambient pressure dried monolithic silica aerogels using water as the only solvent. *Mater. Lett.*, 204:157–160, 2017.

[250] W. Li, M. Zhang, J. Zhang, and Y. Han. Self-assembly of cetyl trimethylammonium bromide in ethanol-water mixtures. *Front. Chem. China*, 1(4):438–442, 2006.

[251] J. P. Vareda, P. Maximiano, L. P. Cunha, A. F. Ferreira, P. N. Simões, and L. Durães. Effect of different types of surfactants on the microstructure of methyltrimethoxysilane-derived silica aerogels: A combined experimental and computational approach. *J. Colloid Interface Sci.*, 512:64–76, 2018.

[252] H. Maleki, L. Durães, and A. Portugal. Development of mechanically strong ambient pressure dried silica aerogels with optimized properties. *J. Phys. Chem. C*, 119(14):7689–7703, 2015.

[253] G. Hayase, K. Kugimiya, M. Ogawa, Y. Kodera, K. Kanamori, and K. Nakanishi. The thermal conductivity of polymethylsilsesquioxane aerogels and xerogels with varied pore sizes for practical application as thermal superinsulators. *J. Mater. Chem.A*, 2(18):6525–6531, 2014.

[254] G. Hayase, S. Nagayama, K. Nonomura, K. Kanamori, A. Maeno, H. Kaji, and K. Nakanishi. Fabrication of hydrophobic polymethylsilsesquioxane aerogels by a surfactant-free method using alkoxysilane with ionic group. *J. Asian Ceram. Soc.*, 5(2):104–108, 2017.

[255] H. Murphy, P. Papakonstantinou, and T. I. T. Okpalugo. Raman study of multiwalled carbon nanotubes functionalized with oxygen groups. *J. Vac. Sci. Technol. B*, 24(2):715–720, 2006.

[256] M. A. Pimenta, G. Dresselhaus, M. S. Dresselhaus, L. G. Cancado, A. Jorio, and R. Saito. Studying disorder in graphite-based systems by Raman spectroscopy. *Phys. Chem. Chem. Phys.*, 9(11):1276–1290, 2007.

[257] A. Merlen, J. G. Buijnsters, and C. Pardanaud. A guide to and review of the use of multiwavelength Raman spectroscopy for characterizing defective aromatic carbon solids: From graphene to amorphous carbons. *Coatings*, 7(10):153, 2017.

[258] S. W. Harun. *Handbook of Graphene, Volume 8: Technology and Innovations*. John Wiley & Sons, 2019.

[259] E. Flahaut, C. Laurent, and A. Peigney. Catalytic CVD synthesis of double and triple-walled carbon nanotubes by the control of the catalyst preparation. *Carbon*, 43(2):375–383, 2005.

[260] L. G. Bulusheva, A. V. Okotrub, I. A. Kinloch, I. P. Asanov, A. G. Kurenya, A. G. Kudashov, X. Chen, and H. Song. Effect of nitrogen doping on Raman spectra of multi-walled carbon nanotubes. *Physica Status Solidi (B)*, 245(10):1971–1974, 2008.

[261] L. Hoa and T. Mai. Characterization of multi-walled carbon nanotubes functionalized by a mixture of HNO_3/H_2SO_4. *Diamond and Related Materials*, 89:43–51, 2018.

[262] B. Scheibe, E. Borowiak-Palen, and R. J. Kalenczuk. Oxidation and reduction of multiwalled carbon nanotubes—preparation and characterization. *Materials characterization*, 61(2):185–191, 2010.

[263] Z. X. Guo, J. W. Ding, Y. Xiao, and D. Y. Xing. Raman frequency shift in oxygen-functionalized carbon nanotubes. *Nanotechnology*, 18(46):465706, 2007.

[264] A. K. Karumuri, L. He, and S. M. Mukhopadhyay. Tuning the surface wettability of carbon nanotube carpets in multiscale hierarchical solids. *Applied Surface Science*, 327:122–130, 2015.

[265] A. K. Karumuri, D. P. Oswal, H. A. Hostetler, and S. M. Mukhopadhyay. Silver nanoparticles supported on carbon nanotube carpets: Influence of surface functionalization. *Nanotechnology*, 27(14):145603, 2016.

[266] L. He, A. Karumuri, and S. M. Mukhopadhyay. Wettability tailoring of nanotube carpets: morphology-chemistry synergy for hydrophobic-hydrophilic cycling. *RSC advances*, 7(41):25265–25275, 2017.

[267] Y. Peng and H. Liu. Effects of oxidation by hydrogen peroxide on the structures of multiwalled carbon nanotubes. *Industrial & Engineering Chemistry Research*, 45(19):6483–6488, 2006.

[268] A. Misra, P. K. Tyagi, M. K. Singh, and D. S. Misra. FTIR studies of nitrogen doped carbon nanotubes. *Diamond and related materials*, 15(2-3):385–388, 2006.

[269] Z.-M. Dang, L. Wang, and L.-P. Zhang. Surface functionalization of multiwalled carbon nanotube with trifluorophenyl. *Journal of Nanomaterials*, 2006, 2006.

[270] N. B. A. Mansor, J.-P. Tessonnier, A. Rinaldi, S. Reiche, and M. G. Kutty. Chemically modified multi-walled carbon nanotubes (MWCNTs) with anchored acidic groups. *Sains Malays*, 41(5):603–609, 2012.

[271] V. Ţucureanu, A. Matei, and A. M. Avram. FTIR spectroscopy for carbon family study. *Critical reviews in analytical chemistry*, 46(6):502–520, 2016.

[272] R. Yudianti, H. Onggo, Y. Saito, T. Iwata, J.-i. Azuma, et al. Analysis of functional group sited on multi-wall carbon nanotube surface. *The Open Materials Science Journal*, 5(1), 2011.

[273] A. Baykal, M. Senel, B. Unal, E. Karaoğlu, H. Sözeri, and M. S. Toprak. Acid functionalized multiwall carbon nanotube/magnetite (MWCNT)-COOH/Fe_3O_4 hybrid: synthesis, characterization and conductivity evaluation. *Journal of Inorganic and Organometallic Polymers and Materials*, 23(3):726–735, 2013.

[274] L.-H. Teng and T.-D. Tang. IR study on surface chemical properties of catalytic grown carbon nanotubes and nanofibers. *Journal of Zhejiang University-SCIENCE A*, 9(5):720–726, 2008.

[275] R. Al-Oweini and H. El-Rassy. Synthesis and Characterization by FTIR Spectroscopy of Silica Aerogels Prepared Using Several $Si(OR)_4$ and R"$Si(OR')_3$ precursors. *J. Mol. Struct.*, 919(1-3):140–145, 2009.

[276] N. Hüsing, U. Schubert, R. Mezei, P. Fratzl, B. Riegel, W. Kiefer, D. Kohler, and W. Mader. Formation and structure of gel networks from $Si(OEt)_4/(MeO)_3Si(CH_2)_3NR'_2$ mixtures (NR'_2= NH_2 or $NHCH_2CH_2NH_2$). *Chem. Mater.*, 11(2):451–457, 1999.

[277] M. A. B. Meador, E. F. Fabrizio, F. Ilhan, A. Dass, G. Zhang, P. Vassilaras, J. C. Johnston, and N. Leventis. Cross-linking amine-modified silica aerogels with epoxies: Mechanically strong lightweight porous materials. *Chem. Mater.*, 17(5):1085–1098, 2005.

[278] G. E. Walrafen, M. S. Hokmabadi, N. C. Holmes, W. J. Nellis, and S. Henning. Raman spectrum and structure of silica aerogel. *J. Chem. Phys.*, 82(5):2472–2476, 1985.

[279] C. J. Brinker, D. R. Tallant, E. P. Roth, and C. S. Ashley. Sol-gel transition in simple silicates: III. Structural studies during densification. *J. Non-Cryst. Solids*, 82(1-3):117–126, 1986.

[280] B. Humbert, A. Burneau, J. P. Gallas, and J. C. Lavalley. Origin of the raman bands, D1 and D2, in high surface area and vitreous silicas. *J. Non-Cryst. Solids*, 143:75–83, 1992.

[281] B. Riegel, I. Hartmann, W. Kiefer, J. Groβ, and J. Fricke. Raman spectroscopy on silica aerogels. *J. Non-Cryst. Solids*, 211(3):294–298, 1997.

[282] C. Kinowski, S. Turrell, M. Bouazaoui, B. Capoen, J.-M. Nedelec, and L. L. Hench. Raman spectroscopic investigations of the effects of Ag^+ and Ce^{3+} doping on the densification of nanoporous silica xerogels. *J Sol-Gel Sci Technol*, 32(1-3):345–348, 2004.

[283] J. Amonkosolpan, D. Wolverson, B. Goller, S. Polisski, D. Kovalev, M. Rollings, M. D. W. Grogan, and T. A. Birks. Porous silicon nanocrystals in a silica aerogel matrix. *Nanoscale Res. Lett.*, 7(1):397, 2012.

[284] C. R. Ehgartner, S. Grandl, A. Feinle, and N. Hüsing. Flexible organofunctional aerogels. *Dalton Trans.*, 46(27):8809–8817, 2017.

[285] C.-Y. Kim and A. R. Jang. Control of flexibility and pore structure of tetraethylorthosilicate/methyltriethoxysilane aerogels by hybridization. *Asian J. Chem.*, 24(9):4217–4224, 2012.

[286] M. S. Dresselhaus, G. Dresselhaus, R. Saito, and A. Jorio. Raman spectroscopy of carbon nanotubes. *Phys. Rep.*, 409(2):47–99, 2005.

[287] L. Bokobza, J.-L. Bruneel, and M. Couzi. Raman spectroscopy as a tool for the analysis of carbon-based materials (highly oriented pyrolitic graphite, multilayer graphene and multiwall carbon nanotubes) and of some of their elastomeric composites. *Vib. Spectrosc.*, 74:57–63, 2014.

[288] S. L. B. Lana and A. B. Seddon. X-ray diffraction studies of sol-gel derived ORMOSILs based on combinations of tetramethoxysilane and trimethoxysilane. *J Sol-Gel Sci Technol*, 13(1-3):461–466, 1998.

[289] B. Orel, R. Ješe, A. Vilčnik, and U. L. Štangar. Hydrolysis and solvolysis of methyltriethoxysilane catalyzed with HCl or trifluoroacetic acid: IR spectroscopic and surface energy studies. *J. Sol-Gel Sci. Technol.*, 34(3):251–265, 2005.

[290] B. Bhushan and Y. C. Jung. Natural and biomimetic artificial surfaces for superhydrophobicity, self-cleaning, low adhesion, and drag reduction. *Prog. Mater Sci.*, 56(1):1–108, 2011.

[291] L. Mammen, X. Deng, M. Untch, D. Vijayshankar, P. Papadopoulos, R. Berger, E. Riccardi, F. Leroy, and D. Vollmer. Effect of nanoroughness on highly hydrophobic and superhydrophobic coatings. *Langmuir*, 28(42):15005–15014, 2012.

[292] A. Ayral, J. Phalippou, and T. Woignier. Skeletal density of silica aerogels determined by helium pycnometry. *J. Mater. Sci.*, 27(5):1166–1170, 1992.

[293] J. H. Lehman, M. Terrones, E. Mansfield, K. E. Hurst, and V. Meunier. Evaluating the characteristics of multiwall carbon nanotubes. *Carbon*, 49(8):2581–2602, 2011.

[294] A. V. Rao, N. D. Hegde, and P. M. Shewale. Imperviousness of the hydrophobic silica aerogels against various solvents and acids. *Appl. Surf. Sci.*, 253(9):4137–4141, 2007.

[295] N. D. Hegde and A. V. Rao. Physical properties of methyltrimethoxysilane based elastic silica aerogels prepared by the two-stage sol-gel process. *J. Mater. Sci.*, 42(16):6965–6971, 2007.

[296] I. R. Shaikh, N. M. N. Maldar, C. S. Lee, R. C. Pawar, H.-H. Park, and U. K.-H. Bangi. MWCNT incorporated silica aerogel prepared by ambient pressure drying: A recyclable catalyst for multicomponent synthesis of benzylpyrazolyl coumarin at room temperature. *Iranian Chemical Communication*, 6:19–29, 2018.

[297] C. Rudaz, R. Courson, L. Bonnet, S. Calas-Etienne, H. Sallée, and T. Budtova. Aeropectin: Fully biomass-based mechanically strong and thermal superinsulating aerogel. *Biomacromolecules*, 15(6):2188–2195, 2014.

[298] S. Groult and T. Budtova. Thermal conductivity/structure correlations in thermal super-insulating pectin aerogels. *Carbohydr. Polym.*, 196:73–81, 2018.

[299] W. J. Malfait, S. Zhao, R. Verel, S. Iswar, D. Rentsch, R. Fener, Y. Zhang, B. Milow, and M. M. Koebel. Surface chemistry of hydrophobic silica aerogels. *Chem. Mater.*, 27(19):6737–6745, 2015.

[300] G. Reichenauer and G. W. Scherer. Effects upon nitrogen sorption analysis in aerogels. *J. Colloid Interface Sci.*, 236(2):385–386, 2001.

[301] G. Reichenauer and G. W. Scherer. Nitrogen sorption in aerogels. *J. Non-Cryst. Solids*, 285(1-3):167–174, 2001.

[302] D. W. Schaefer. Polymers, fractals, and ceramic materials. *Science*, 243(4894):1023–1027, 1989.

[303] P. Wang, A. Emmerling, W. Tappert, O. Spormann, J. Fricke, and H.-G. Haubold. High-temperature and low-temperature supercritical drying of aerogels–structural investigations with SAXS. *J. Appl. Crystallogr.*, 24(5):777–780, 1991.

[304] B. P. Jelle, R. Baetens, and A. Gustavsen. Aerogel insulation for building applications. *The Sol-Gel Handbook*, pages 1385–1412, 2015.

[305] J. C. H. Wong, H. Kaymak, S. Brunner, and M. M. Koebel. Mechanical properties of monolithic silica aerogels made from polyethoxydisiloxanes. *Microporous Mesoporous Mater*, 183:23–29, 2014.

[306] T. Matias, C. Varino, H. C. de Sousa, M. E. M. Braga, A. Portugal, J. F. J. Coelho, and L. Durães. Novel flexible, hybrid aerogels with vinyl-and methyltrimethoxysilane in the underlying silica structure. *J Mater Sci*, 51(14):6781–6792, 2016.

[307] S. P. Patil, P. Shendye, and B. Markert. Mechanical properties and behavior of glass fiber-reinforced silica aerogel nanocomposites: Insights from all-atom simulations. *Scripta Materialia*, 177:65–68, 2020.

[308] A. Lamy-Mendes, A. V. Girão, R. F. Silva, and L. Duraes. Polysilsesquioxane-based silica aerogel monoliths with embedded cnts. *Microporous and Mesoporous Materials*, 288:109575, 2019.

[309] K. Kanamori, M. Aizawa, K. Nakanishi, and T. Hanada. New transparent methylsilsesquioxane aerogels and xerogels with improved mechanical properties. *Advanced materials*, 19(12):1589–1593, 2007.

[310] S. D. Bhagat, C.-S. Oh, Y.-H. Kim, Y.-S. Ahn, and J.-G. Yeo. Methyltrimethoxysilane based monolithic silica aerogels via ambient pressure drying. *Microporous and mesoporous Materials*, 100(1-3):350–355, 2007.

[311] K. Kanamori, Y. Kodera, G. Hayase, K. Nakanishi, and T. Hanada. Transition from transparent aerogels to hierarchically porous monoliths in polymethylsilsesquioxane sol–gel system. *Journal of colloid and interface science*, 357(2):336–344, 2011.

[312] G. Hayase, K. Kanamori, and K. Nakanishi. Structure and properties of polymethylsilsesquioxane aerogels synthesized with surfactant n-hexadecyltrimethylammonium chloride. *Microporous and mesoporous materials*, 158:247–252, 2012.

[313] W. J. Malfait, R. Verel, and M. M. Koebel. Hydrophobization of silica aerogels: insights from quantitative solid-state nmr spectroscopy. *The Journal of Physical Chemistry C*, 118(44):25545–25554, 2014.

[314] G. Zu, K. Kanamori, T. Shimizu, Y. Zhu, A. Maeno, H. Kaji, K. Nakanishi, and J. Shen. Versatile double-cross-linking approach to transparent, machinable, supercompressible, highly bendable aerogel thermal superinsulators. *Chemistry of Materials*, 30(8):2759–2770, 2018.

[315] P. R. Oliveira, A. C. Lamy-Mendes, E. I. P. Rezende, A. S. Mangrich, L. H. Marcolino Junior, and M. F. Bergamini. Electrochemical determination of copper ions in spirit drinks using carbon paste electrode modified with biochar. *Food chemistry*, 171:426–431, 2015.

[316] V. D. Nithya, B. Hanitha, S. Surendran, D. Kalpana, and R. K. Selvan. Effect of ph on the sonochemical synthesis of $BiPO_4$ nanostructures and its electrochemical properties for pseudocapacitors. *Ultrasonics sonochemistry*, 22:300–310, 2015.

[317] A. A. Ensafi, N. Ahmadi, and B. Rezaei. Electrochemical preparation of $CuBi_2O_4$ nanoparticles on nanoporous stainless steel as a binder-free supercapacitor electrode. *Journal of Alloys and Compounds*, 652:39–47, 2015.

[318] A. A. Ensafi, N. Ahmadi, and B. Rezaei. Electrochemical preparation and characterization of a polypyrrole/nickel-cobalt hexacyanoferrate nanocomposite for supercapacitor applications. *RSC advances*, 5(111):91448–91456, 2015.

[319] K. Krishnamoorthy, M. Veerapandian, K. Yun, and S.-J. Kim. The chemical and structural analysis of graphene oxide with different degrees of oxidation. *Carbon*, 53:38 – 49, 2013.

[320] N. M. S. Hidayah, W.-W. Liu, C.-W. Lai, N. Z. Noriman, C.-S. Khe, U. Hashim, and H. C. Lee. Comparison on graphite, graphene oxide and reduced graphene oxide: Synthesis and characterization. In *AIP Conference Proceedings*, volume 1892, page 150002. AIP Publishing LLC, 2017.

[321] N. R. Wilson, P. A. Pandey, R. Beanland, R. J. Young, I. A. Kinloch, L. Gong, Z. Liu, K. Suenaga, J. P. Rourke, S. J. York, et al. Graphene oxide: structural analysis and application as a highly transparent support for electron microscopy. *ACS nano*, 3(9):2547–2556, 2009.

[322] F. L. Galeener. Planar rings in glasses. *Solid State Communications*, 44(7):1037–1040, 1982.

[323] W. J. Malfait. Vibrational properties of glasses and melts. In *Magmas Under Pressure*, pages 211–236. Elsevier, 2018.

[324] Z. Li, S. Zhao, M. M. Koebel, and W. J. Malfait. Silica aerogels with tailored chemical functionality. *Materials & Design*, page 108833, 2020.

[325] G. Wang, X. Sun, C. Liu, and J. Lian. Tailoring oxidation degrees of graphene oxide by simple chemical reactions. *Applied Physics Letters*, 99(5):053114, 2011.

[326] S. Thangavel and G. Venugopal. Understanding the adsorption property of graphene-oxide with different degrees of oxidation levels. *Powder technology*, 257:141–148, 2014.

[327] L. Stobinski, B. Lesiak, A. Malolepszy, M. Mazurkiewicz, B. Mierzwa, J. Zemek, P. Jiricek, and I. Bieloshapka. Graphene oxide and reduced graphene oxide studied by the XRD, TEM and electron spectroscopy methods. *Journal of Electron Spectroscopy and Related Phenomena*, 195:145–154, 2014.

[328] F. Y. Ban, S. R. Majid, N. M. Huang, and H. N. Lim. Graphene oxide and its electrochemical performance. *Int. J. Electrochem. Sci*, 7(5):4345–4351, 2012.

[329] M.-C. Hsiao, S.-H. Liao, M.-Y. Yen, P.-I. Liu, N.-W. Pu, C.-A. Wang, and C.-C. M. Ma. Preparation of covalently functionalized graphene using residual oxygen-containing functional groups. *ACS applied materials & interfaces*, 2(11):3092–3099, 2010.

[330] K. Kanamori, M. Aizawa, K. Nakanishi, and T. Hanada. Elastic organic–inorganic hybrid aerogels and xerogels. *Journal of sol-gel science and technology*, 48(1-2):172–181, 2008.

[331] K. Kanamori, K. Nakanishi, and T. Hanada. Sol-gel synthesis, porous structure, and mechanical property of polymethylsilsesquioxane aerogels. *J. Ceram. Soc. Jpn.*, 117(1372):1333–1338, 2009.

[332] A. V. Rao, M. M. Kulkarni, D. P. Amalnerkar, and T. Seth. Superhydrophobic silica aerogels based on methyltrimethoxysilane precursor. *Journal of Non-Crystalline Solids*, 330(1-3):187–195, 2003.

[333] N. H. Borzęcka, B. Nowak, J. M. Gac, T. Głaz, and M. Bojarska. Kinetics of MTMS-based aerogel formation by the sol-gel method-experimental results and theoretical description. *Journal of Non-Crystalline Solids*, 547:120310, 2020.

[334] P. Cui, J. Lee, E. Hwang, and H. Lee. One-pot reduction of graphene oxide at subzero temperatures. *Chemical Communications*, 47(45):12370–12372, 2011.

[335] J. Luo, G. Panzarasa, A. Osypova, F. Sorin, F. Spano, R. M. Rossi, A. Sadeghpour, and L. F. Boesel. Polyphenols as morphogenetic agents for the controlled synthesis of mesoporous silica nanoparticles. *Chemistry of Materials*, 31(9):3192–3200, 2019.

[336] G Fritz, A Bergmann, and O Glatter. Evaluation of small-angle scattering data of charged particles using the generalized indirect fourier transformation technique. *The Journal of Chemical Physics*, 113(21):9733–9740, 2000.

[337] D. Parida, K. A. Salmeia, A. Sadeghpour, S. Zhao, A. K. Maurya, K. I. Assaf, E. Moreau, R. Pauer, S. Lehner, M. Jovic, H. Cordula, and S. Gaan. Template-free synthesis of hybrid silica nanoparticle with functionalized mesostructure for efficient methylene blue removal. *Materials & Design*, page 109494, 2021.

[338] N. Hüsing and U. Schubert. Aerogels—airy materials: chemistry, structure, and properties. *Angewandte Chemie International Edition*, 37(1-2):22–45, 1998.

[339] K.-L. Yang, T.-Y. Ying, S. Yiacoumi, C. Tsouris, and E. S. Vittoratos. Electrosorption of ions from aqueous solutions by carbon aerogel: an electrical double-layer model. *Langmuir*, 17(6):1961–1969, 2001.

[340] G. Rasines, P. Lavela, Ca. Macías, M. Haro, C. O. Ania, and J. L. Tirado. Electrochemical response of carbon aerogel electrodes in saline water. *Journal of Electroanalytical Chemistry*, 671:92–98, 2012.

[341] C. Gouveia-Caridade and C. M. A. Brett. The influence of Triton-X-100 surfactant on the electroanalysis of lead and cadmium at carbon film electrodes–an electrochemical impedance study. *Journal of Electroanalytical Chemistry*, 592(1):113–120, 2006.

[342] M. M. Barsan, R. C. Carvalho, Y. Zhong, X. Sun, and C. M. A. Brett. Carbon nanotube modified carbon cloth electrodes: Characterisation and application as biosensors. *Electrochimica acta*, 85:203–209, 2012.

[343] R. Atchudan, T. N. J. I. Edison, S. Perumal, and Y. R. Lee. Green synthesis of nitrogen-doped graphitic carbon sheets with use of prunus persica for supercapacitor applications. *Applied Surface Science*, 393:276–286, 2017.

[344] M. Mirzaeian, Q. Abbas, D. Gibson, and M. Mazur. Effect of nitrogen doping on the electrochemical performance of resorcinol-formaldehyde based carbon aerogels as electrode material for supercapacitor applications. *Energy*, 173:809–819, 2019.

[345] C. Chen, Fe. Li, Y. Zhang, B. Wang, Y. Fan, X. Wang, and R. Sun. Compressive, ultralight and fire-resistant lignin-modified graphene aerogels as recyclable absorbents for oil and organic solvents. *Chemical Engineering Journal*, 350:173–180, 2018.

[346] H. Nourmoradi, M. Khiadani, and M. Nikaeen. Multi-component adsorption of benzene, toluene, ethylbenzene, and xylene from aqueous solutions by montmorillonite modified with tetradecyl trimethyl ammonium bromide. *Journal of Chemistry*, 2013, 2013.

[347] L. F. Lima, J. R. de Andrade, M. G. C. da Silva, and M. G. A. Vieira. Fixed bed adsorption of benzene, toluene, and xylene (BTX) contaminants from monocomponent and multicomponent solutions using a commercial organoclay. *Industrial & Engineering Chemistry Research*, 56(21):6326–6336, 2017.

[348] J. Marques, T. Matias, A. J. M. Valente, A. Portugal, M. J. Quina, L. Gando-Ferreira, and L. Durães. Adsorption of phenol on silica aerogels using a stirred tank and a fixed bed column. *Ciência & Tecnologia dos materiais*, 29(1):e229–e233, 2017.

[349] M. C. Cesar Filho, T. Matias, L. Duraes, and A. J. M. Valente. Efficient simultaneous removal of petroleum hydrocarbon pollutants by a hydrophobic silica aerogel-like material. *Colloids and Surfaces A: Physicochemical and Engineering Aspects*, 520:550–560, 2017.

[350] D. Loomis, K. Z. Guyton, Y. Grosse, F. El Ghissassi, V. Bouvard, L. Benbrahim-Tallaa, N. Guha, N. Vilahur, H. Mattock, and K. Straif. Carcinogenicity of benzene. *The Lancet Oncology*, 18(12):1574–1575, 2017.

[351] W. Raza, J. Lee, N. Raza, Y. Luo, K.-H. Kim, and J. Yang. Removal of phenolic compounds from industrial waste water based on membrane-based technologies. *Journal of industrial and engineering chemistry*, 71:1–18, 2019.

[352] L. Damjanović, V. Rakić, V. Rac, D. Stošić, and A. Auroux. The investigation of phenol removal from aqueous solutions by zeolites as solid adsorbents. *Journal of hazardous materials*, 184(1-3):477–484, 2010.

[353] O. M. Fayemiwo, M. O. Daramola, and K. Moothi. BTEX compounds in water–future trends and directions for water treatment. *Water Sa*, 43(4):602–613, 2017.

[354] N. S. Chary and A. R. Fernandez-Alba. Determination of volatile organic compounds in drinking and environmental waters. *TrAC Trends in Analytical Chemistry*, 32:60–75, 2012.

[355] G. Jaria, M. A. O. Lourenço, C. P. Silva, P. Ferreira, M. Otero, V. Calisto, and V. I. Esteves. Effect of the surface functionalization of a waste-derived activated carbon on pharmaceuticals' adsorption from water. *Journal of Molecular Liquids*, 299:112098, 2020.

[356] A. Modi and J. Bellare. Amoxicillin removal using polyethersulfone hollow fiber membranes blended with ZIF-L nanoflakes and cgo nanosheets: Improved flux and fouling-resistance. *Journal of Environmental Chemical Engineering*, 8(4):103973, 2020.

[357] M. J. Luján-Facundo, M. I. Iborra-Clar, J. A. Mendoza-Roca, and M. I. Alcaina-Miranda. Pharmaceutical compounds removal by adsorption with commercial and reused carbon coming from a drinking water treatment plant. *Journal of Cleaner Production*, 238:117866, 2019.

[358] J. W. Hounfodji, W. G. Kanhounnon, G. Kpotin, G. S. Atohoun, J. Lainé, Y. Foucaud, and M. Badawi. Molecular insights on the adsorption of some pharmaceutical residues from wastewater on kaolinite surfaces. *Chemical Engineering Journal*, page 127176, 2020.

[359] Q. Sui, X. Cao, S. Lu, W. Zhao, Z. Qiu, and G. Yu. Occurrence, sources and fate of pharmaceuticals and personal care products in the groundwater: A review. *Emerging Contaminants*, 1(1):14 – 24, 2015.

[360] M. Huerta-Fontela, M. T. Galceran, and F. Ventura. Occurrence and removal of pharmaceuticals and hormones through drinking water treatment. *Water Research*, 45(3):1432 – 1442, 2011.

[361] L. Liu, W. Cui, C. Lu, A. Zain, W. Zhang, G. Shen, S. Hu, and X. Qian. Analyzing the adsorptive behavior of amoxicillin on four Zr-MOFs nanoparticles: Functional groups dependence of adsorption performance and mechanisms. *Journal of Environmental Management*, 268:110630, 2020.

[362] K. Changanaqui, H. Alarcón, E. Brillas, and I. Sirés. Blue LED light-driven photoelectrocatalytic removal of naproxen from water: Kinetics and primary by-products. *Journal of Electroanalytical Chemistry*, 867:114192, 2020.

[363] E. Aydin and I. Talinli. Analysis, occurrence and fate of commonly used pharmaceuticals and hormones in the Buyukcekmece watershed, turkey. *Chemosphere*, 90(6):2004 – 2012, 2013.

[364] P. B. Deroco, R. C. Rocha-Filho, and O. Fatibello-Filho. A new and simple method for the simultaneous determination of amoxicillin and nimesulide using carbon black within a dihexadecylphosphate film as electrochemical sensor. *Talanta*, 179:115–123, 2018.

[365] M. G. P. Valenga, M. L. Felsner, C. F. de Matos, E. G. de Castro, and A. Galli. Development and validation of voltammetric method for determination of amoxicillin in river water. *Analytica Chimica Acta*, 1138:79 – 88, 2020.

[366] F. A. Caliman and M. Gavrilescu. Pharmaceuticals, personal care products and endocrine disrupting agents in the environment–a review. *CLEAN–Soil, Air, Water*, 37(4-5):277–303, 2009.

[367] B. Sáenz-Roblero, J. E. Durán, M. Masís-Mora, D. Ramírez-Morales, and C. E. Rodríguez-Rodríguez. Removal of cimetidine, ketoprofen and naproxen by heterogeneous catalytic ozonation over volcanic sand at low pH. *Journal of Water Process Engineering*, 37:101461, 2020.

[368] P. K. Mutiyar and A. K. Mittal. Occurrences and fate of an antibiotic amoxicillin in extended aeration-based sewage treatment plant in Delhi, India: a case study of emerging pollutant. *Desalination and Water Treatment*, 51(31-33):6158–6164, 2013.

[369] N. H. Tran, M. Reinhard, and K. Y.-H. Gin. Occurrence and fate of emerging contaminants in municipal wastewater treatment plants from different geographical regions-a review. *Water Research*, 133:182 – 207, 2018.

[370] M. Verma and A. K. Haritash. Photocatalytic degradation of amoxicillin in pharmaceutical wastewater: A potential tool to manage residual antibiotics. *Environmental Technology & Innovation*, 20:101072, 2020.

[371] E. Kurtulbaş, M. Bilgin, S. Şahin, and Ş. S. Bayazit. Comparison of different polymeric resins for naproxen removal from wastewater. *Journal of Molecular Liquids*, 241:633 – 637, 2017.

[372] J. C. Lancheros, C. A. Madera-Parra, A. Caselles-Osorio, W. A. Torres-López, and X. M. Vargas-Ramírez. Ibuprofen and naproxen removal from domestic wastewater using a horizontal subsurface flow constructed wetland coupled to ozonation. *Ecological Engineering*, 135:89 – 97, 2019.

[373] Y. Wang, J. Lu, S. Zhang, . Li, L. Mao, Z. Yuan, P. L. Bond, and J. Guo. Non-antibiotic pharmaceuticals can enhance the spread of antibiotic resistance via conjugation. *bioRxiv*, page 724500, 2019.

[374] Z. Aksu and Ö. Tunç. Application of biosorption for penicillin G removal: comparison with activated carbon. *Process Biochemistry*, 40(2):831 – 847, 2005.

[375] P. Sehonova, Z. Svobodova, P. Dolezelova, P. Vosmerova, and C. Faggio. Effects of waterborne antidepressants on non-target animals living in the aquatic environment: A review. *Science of The Total Environment*, 631-632:789 – 794, 2018.

[376] P. V. Messina and P. C. Schulz. Adsorption of reactive dyes on titania–silica mesoporous materials. *Journal of Colloid and Interface Science*, 299(1):305–320, 2006.

[377] M. A. Hashim, S. Mukhopadhyay, J. N. Sahu, and B. Sengupta. Remediation technologies for heavy metal contaminated groundwater. *Journal of environmental management*, 92(10):2355–2388, 2011.

[378] F. Fu and Q. Wang. Removal of heavy metal ions from wastewaters: a review. *Journal of environmental management*, 92(3):407–418, 2011.

[379] C. Liu, H. Liu, A. Xu, K. Tang, Y. Huang, and C. Lu. In situ reduced and assembled three-dimensional graphene aerogel for efficient dye removal. *Journal of Alloys and Compounds*, 714:522–529, 2017.

[380] J. P. Vareda, A. J. M. Valente, and L. Durães. Assessment of heavy metal pollution from anthropogenic activities and remediation strategies: A review. *Journal of environmental management*, 246:101–118, 2019.

[381] M. Sa. H. Hashemi, F. Eslami, and R. Karimzadeh. Organic contaminants removal from industrial wastewater by CTAB treated synthetic zeolite y. *Journal of environmental management*, 233:785–792, 2019.

[382] V. B. Cashin, D. S. Eldridge, A. Yu, and D. Zhao. Surface functionalization and manipulation of mesoporous silica adsorbents for improved removal of pollutants: a review. *Environmental Science: Water Research & Technology*, 4(2):110–128, 2018.

[383] M. Ge and H. Liu. A silsesquioxane-based thiophene-bridged hybrid nanoporous network as a highly efficient adsorbent for wastewater treatment. *Journal of Materials Chemistry A*, 4(42):16714–16722, 2016.

[384] L. Durães, H. Maleki, J. P. Vareda, A. Lamy-Mendes, and A. Portugal. Exploring the versatile surface chemistry of silica aerogels for multipurpose application. *MRS Advances*, 2(57):3511–3519, 2017.

[385] W. Zhao, J. Zhu, W. Wei, L. Ma, J. Zhu, and J. Xie. Comparative study of modified/non-modified aluminum and silica aerogels for anionic dye adsorption performance. *RSC advances*, 8(51):29129–29140, 2018.

[386] J. Aguado, J. M. Arsuaga, A. Arencibia, M. Lindo, and V. Gascón. Aqueous heavy metals removal by adsorption on amine-functionalized mesoporous silica. *Journal of hazardous materials*, 163(1):213–221, 2009.

[387] X. Guo, J. Shan, Z. Lai, W. Lei, R. Ding, Y. Zhang, and H. Yang. Facile synthesis of flexible methylsilsesquioxane aerogels with surface modifications for sound-absorbance, fast dye adsorption and oil/water separation. *Molecules*, 23(4):945, 2018.

[388] K. Y. Ho, G. McKay, and K. L. Yeung. Selective adsorbents from ordered mesoporous silica. *Langmuir*, 19(7):3019–3024, 2003.

[389] K. Wörmeyer and I. Smirnova. Adsorption of CO_2, moisture and ethanol at low partial pressure using aminofunctionalised silica aerogels. *Chemical engineering journal*, 225:350–357, 2013.

[390] W. Wei, H. Hu, X. Ji, Z. Yan, W. Sun, and J. Xie. Selective adsorption of organic dyes by porous hydrophilic silica aerogels from aqueous system. *Water Science and Technology*, 78(2):402–414, 2018.

[391] D. Wang, E. McLaughlin, R. Pfeffer, and Y. S. Lin. Adsorption of organic compounds in vapor, liquid, and aqueous solution phases on hydrophobic aerogels. *Industrial & engineering chemistry research*, 50(21):12177–12185, 2011.

[392] K. K. Chenab, B. Sohrabi, A. Jafari, and S. Ramakrishna. Water treatment: functional nanomaterials and applications from adsorption to photodegradation. *Materials Today Chemistry*, 16:100262, 2020.

[393] S. C. Smith and D. F. Rodrigues. Carbon-based nanomaterials for removal of chemical and biological contaminants from water: a review of mechanisms and applications. *Carbon*, 91:122–143, 2015.

[394] F. Su, C. Lu, and S. Hu. Adsorption of benzene, toluene, ethylbenzene and p-xylene by NaOCl-oxidized carbon nanotubes. *Colloids and Surfaces A: Physicochemical and Engineering Aspects*, 353(1):83–91, 2010.

[395] E. F. Eydi, A. Shariati, and M. R. Khosravi-Nikou. Separation of BTEX compounds (benzene, toluene, ethylbenzene and xylenes) from aqueous solutions using adsorption process. *Journal of Dispersion Science and Technology*, 40(3):453–463, 2019.

[396] S Handayani, R Safitri, W Surono, H Astika, R Damayanti, M Agung, et al. Biodegradation of BTEX by indigenous microorganisms isolated from UCG project area, south sumatra. In *IOP Conference Series: Earth and Environmental Science*, volume 308, page 012017. IOP Publishing, 2019.

[397] M. A. Al-Ghouti and D. A. Da'ana. Guidelines for the use and interpretation of adsorption isotherm models: A review. *Journal of Hazardous Materials*, page 122383, 2020.

[398] J. P. Vareda, A. J. M. Valente, and L. Durães. Heavy metals in iberian soils: Removal by current adsorbents/amendments and prospective for aerogels. *Advances in Colloid and Interface Science*, 237:28–42, 2016.

[399] L. Zhang, Y. Zeng, and Z. Cheng. Removal of heavy metal ions using chitosan and modified chitosan: A review. *Journal of Molecular Liquids*, 214:175–191, 2016.

[400] K. Y. Foo and B. H. Hameed. Insights into the modeling of adsorption isotherm systems. *Chemical engineering journal*, 156(1):2–10, 2010.

[401] Y. Shen and N. Zhang. Facile synthesis of porous carbons from silica-rich rice husk char for volatile organic compounds (VOCs) sorption. *Bioresource technology*, 282:294–300, 2019.

[402] M. C. Cesar Filho, P. V. A. Bueno, A. F. Y . Matsushita, A. F. Rubira, E. C. Muniz, L. Durães, D. M. B. Murtinho, and A. J. M. Valente. Synthesis, characterization and sorption studies of aromatic compounds by hydrogels of chitosan blended with β-cyclodextrin-and PVA-functionalized pectin. *RSC advances*, 8(26):14609–14622, 2018.

[403] K. P. Burnham and D. R. Anderson. Multimodel inference: understanding aic and bic in model selection. *Sociological methods & research*, 33(2):261–304, 2004.

[404] M. Mazerolle. Improving data analysis in herpetology: using akaike's information criterion (aic) to assess the strength of biological hypotheses. *Amphibia-Reptilia*, 27(2):169–180, 2006.

[405] J. P. Vareda and L. Durães. Functionalized silica xerogels for adsorption of heavy metals from groundwater and soils. *Journal of Sol-Gel Science and Technology*, 84(3):400–408, 2017.

[406] Frank J Fabozzi, Sergio M Focardi, Svetlozar T Rachev, and Bala G Arshanapalli. *The basics of financial econometrics: Tools, concepts, and asset management applications*. John Wiley & Sons, 2014.

[407] L. Moreira da Costa, S. R. Stoyanov, S. Gusarov, P. R. Seidl, J. Walkimar de M. Carneiro, and A. Kovalenko. Computational study of the effect of dispersion interactions on the thermochemistry of aggregation of fused polycyclic aromatic hydrocarbons as model asphaltene compounds in solution. *The Journal of Physical Chemistry A*, 118(5):896–908, 2014.

[408] H. Pourzamani, Y. Hajizadeh, S. Fadaei, et al. Efficiency enhancement of multi-walled carbon nanotubes by ozone for benzene removal from aqueous solution. *International Journal of Environmental Health Engineering*, 4(1):29, 2015.

[409] Ming-Jun Tian, Fang Liao, Qin-Fei Ke, Ya-Jun Guo, and Ya-Ping Guo. Synergetic effect of titanium dioxide ultralong nanofibers and activated carbon fibers on adsorption and photodegradation of toluene. *Chemical Engineering Journal*, 328:962–976, 2017.

[410] F. Yu, Y. Wu, X. Li, and J. Ma. Kinetic and thermodynamic studies of toluene, ethylbenzene, and m-xylene adsorption from aqueous solutions onto KOH-activated multiwalled carbon nanotubes. *Journal of agricultural and food chemistry*, 60(50):12245–12253, 2012.

[411] R. Kh. Khamizov, D. A. Sveshnikova, A. E. Kucherova, and L. A. Sinyaeva. Kinetic models of batch sorption in a limited volume. *Russian Journal of Physical Chemistry A*, 92(9):1782–1789, 2018.

[412] D. Wang, E. McLaughlin, R. Pfeffer, and Y. S. Lin. Aqueous phase adsorption of toluene in a packed and fluidized bed of hydrophobic aerogels. *Chemical engineering journal*, 168(3):1201–1208, 2011.

[413] W. Zou, B. Gao, Y. S. Ok, and L. Dong. Integrated adsorption and photocatalytic degradation of volatile organic compounds (VOCs) using carbon-based nanocomposites: A critical review. *Chemosphere*, 218:845–859, 2019.

[414] T. Matias, J. Marques, F. Conceição, H. Maleki, M. J. Quina, L. Gando-Ferreira, A. J. M. Valente, A. Portugal, and L. Durães. Towards improved adsorption of phenolic compounds by surface chemistry tailoring of silica aerogels. *Journal of Sol-Gel Science and Technology*, 84(3):409–421, 2017.

[415] I. Vázquez, J. Rodríguez-Iglesias, E. Maranon, L. Castrillon, and M. Alvarez. Removal of residual phenols from coke wastewater by adsorption. *Journal of Hazardous Materials*, 147(1-2):395–400, 2007.

[416] A. Bahdod, S. El Asri, A. Saoiabi, T. Coradin, and A. Laghzizil. Adsorption of phenol from an aqueous solution by selected apatite adsorbents: Kinetic process and impact of the surface properties. *Water research*, 43(2):313–318, 2009.

[417] H. Ouallal, Y. Dehmani, H. Moussout, L. Messaoudi, and M. Azrour. Kinetic, isotherm and mechanism investigations of the removal of phenols from water by raw and calcined clays. *Heliyon*, 5(5):e01616, 2019.

[418] H. R. Pouretedal and N. Sadegh. Effective removal of amoxicillin, cephalexin, tetracycline and penicillin G from aqueous solutions using activated carbon nanoparticles prepared from vine wood. *Journal of Water Process Engineering*, 1:64–73, 2014.

[419] M. A. E. de Franco, C. B. de Carvalho, M. M. Bonetto, R. de Pelegrini Soares, and L. A. Féris. Removal of amoxicillin from water by adsorption onto activated carbon in batch process and fixed bed column: kinetics, isotherms, experimental design and breakthrough curves modelling. *Journal of Cleaner Production*, 161:947–956, 2017.

[420] G. Moussavi, A. Alahabadi, K. Yaghmaeian, and M. Eskandari. Preparation, characterization and adsorption potential of the NH$_4$Cl-induced activated carbon for the removal of amoxicillin antibiotic from water. *Chemical engineering journal*, 217:119–128, 2013.

[421] Z. Ilbay, S. Şahin, Ö. Kerkez, and Ş. S. Bayazit. Isolation of naproxen from wastewater using carbon-based magnetic adsorbents. *International journal of environmental science and technology*, 12(11):3541–3550, 2015.

[422] L. Rafati, M. H. Ehrampoush, A. A. Rafati, M. Mokhtari, and A. H. Mahvi. Modeling of adsorption kinetic and equilibrium isotherms of naproxen onto functionalized nano-clay composite adsorbent. *Journal of Molecular Liquids*, 224:832–841, 2016.

[423] R. Baccar, M. Sarrà, J. Bouzid, M. Feki, and P. Blánquez. Removal of pharmaceutical compounds by activated carbon prepared from agricultural by-product. *Chemical engineering journal*, 211:310–317, 2012.

[424] J. R. Domínguez-Vargas, T. Gonzalez, P. Palo, and E. M. Cuerda-Correa. Removal of carbamazepine, naproxen, and trimethoprim from water by amberlite XAD-7: A kinetic study. *CLEAN–Soil, Air, Water*, 41(11):1052–1061, 2013.

[425] H. G. O. Becker, W. Berger, E. G. Domschke, E. Fanghanel, J. Faust, M. Fischer, F. Gentz, K. Gewald, R. Gluch, R. Mayer, et al. *Organikum: Química Orgânica Experimental*. Fundação Calouste Gulbenkian, 1997.

Appendix A

The tables shown in this appendix are complementary information to the results presented in Chapter 3.

Table A1: Vibrational frequencies (cm^{-1}) observed in the FTIR spectra of silica aerogels and CNTs-silica aerogel composites with 0.83 wt% of CTAB

100M_S	100M_CNT_S	90M10A_S	90M10A_CNT_S	80M20A_S	80M20A_CNT_S	Types of vibration [275, 425]	Structure unit [275, 425]
-	-	-	-	3378.6	3384.4	v_s N-H	$-NH_2$
2976.5	2975.6	2971.7	2970.8	2971.7	2971.7	v_s C-H	$-CH_3$
-	2923.5	2932.2	2928.3	2929.3	2926.4	v_{as} C-H	$-CH_2$
-	-	2865.7	2856	2857.9	2868.5	v_s C-H	$-CH_2$
-	-	1580.3	1570.7	1584.5	1565.9	δ_s N-H	$-NH_2$
-	1414.5	1416.4	1425.1	1415.7	-	δ_{as} C-H	Si-R
1274.7	1274.7	1272.7	1272.7	1273.7	1272.7	δ_s C-H	Si-R
1132.0	1133.9	1131.1	1131.0	1132.9	1132.0	v_{as} Si-O-Si (LO mode)	$\equiv$Si-O-Si$\equiv$
1029.8	1030.7	1032.6	1034.6	1031.7	1034.6	v_{as} Si-O-Si (TO mode)	$\equiv$Si-O-Si$\equiv$
916.9	917.0	938.2	938.2	934.3	938.2	v_β Si-O	Free Si-O-
852.4	852.4	847.6	847.6	-	852.4	v Si-C	Si-R
779.1	780.1	779.1	778.1	777.2	777.2	v_s Si-O	$\equiv$Si-O-Si$\equiv$
681.7	680.7	671.1	675.0	671.1	678.8	v_s Si-O-Si	$\equiv$Si-O-Si$\equiv$
554.4	554.5	552.5	570.8	550.6	564.1	v Si-O	SiO_2 defects
439.7	443.5	425.2	444.5	442.6	432.0	δ O-Si-O	-O-Si-O-

v – stretching vibration; v_s – symmetric stretching vibration; v_{as} – asymmetric stretching vibration; v_β – in-plane stretching vibration; δ – deformation vibration; δ_s – symmetric deformation vibration (bending); δ_{as} – asymmetric deformation vibration (bending).

Table A2: Vibrational frequencies (cm^{-1}) observed in the FTIR spectra of silica aerogels and CNTs-silica aerogel composites with 4.0 wt% of CTAB

100M_S1	100M_CNT_S1	90M10A_S1	90M10A_CNT_S1	80M20A_S1	80M20A_CNT_S1	Types of vibration [275, 425]	Structure unit [275, 425]
-	-	-	-	3439.4	3400.8	v_s N-H	$-NH_2$
2971.7	2972.7	2970.8	2970.8	2972.7	2970.8	v_s C-H	$-CH_3$
2921.6	2920.6	2929.3	2929.3	2925.4	2930.3	v_{as} C-H	$-CH_2$
-	-	2865.7	2861.8	2868.5	2866.7	v_s C-H	$-CH_2$
-	-	1550.4	1564.9	1590.9	1550.5	δ_s N-H	$-NH_2$
1422.2	1416.4	1420.3	1420.3	1418.3	1410.7	δ_{as} C-H	Si-R
1272.7	1272.7	1271.8	1272.7	1275.6	1271.8	δ_s C-H	Si-R
1133.9	1135.8	1132.9	1131.0	1126.2	1131.0	v_{as} Si-O-Si (LO mode)	$\equiv$Si-O-Si$\equiv$
1037.5	1037.5	1035.5	1034.6	1033.6	1034.6	v_{as} Si-O-Si (TO mode)	$\equiv$Si-O-Si$\equiv$
912.2	914.1	936.3	941.1	927.6	943.9	v_β Si-O	Free Si-O-
849.5	847.6	850.5	847.6	841.8	849.5	v Si-C	Si-R
779.1	780.1	778.1	777.2	777.1	778.1	v_s Si-O	$\equiv$Si-O-Si$\equiv$
676.9	676.9	676.9	677.8	670.1	676.9	v_s Si-O-Si	$\equiv$Si-O-Si$\equiv$
559.2	563.1	554.4	567.9	578.6	566.9	v Si-O	SiO_2 defects
435.8	441.6	440.6	432.9	447.4	443.5	δ O-Si-O	-O-Si-O-

v – stretching vibration; v_s – symmetric stretching vibration; v_{as} – asymmetric stretching vibration; v_β – in-plane stretching vibration; δ – deformation vibration; δ_s – symmetric deformation vibration (bending); δ_{as} – asymmetric deformation vibration (bending).

Table A3: Onset temperatures and mass losses observed in the thermograms of Figures 3.8c and 3.8f, and corresponding thermal events.

Samples	T_{onset} (°C)	Mass loss (%)	Samples	T_{onset} (°C)	Mass loss (%)	Phenomena [306]
100M_S	469.4	5.7	100M_CNT_S	340.6	2.3	First stage of thermal decomposition of methyl groups
	601.0	14.0		744.2	11.6	Second stage of thermal decomposition of methyl groups
90M10A_S	444.2	6.8	90M10A_CNT_S	434.8	7.7	First stage of thermal decomposition of methyl groups and amine decomposition
	723.1	7.1		719.6	8.0	Second stage of thermal decomposition of methyl groups
80M20A_S	28.0	2.6	80M20A_CNT_S	29.1	2.3	Removal of residual solvents/ adsorbed water
	438.8	15.6		451.3	10.2	First stage of thermal decomposition of methyl groups and amine decomposition
	716.2	7.3		722.5	6.8	Second stage of thermal decomposition of methyl groups
100M_S1	405.3	7.3	100M_CNT_S1	476.0	10.1	First stage of thermal decomposition of methyl groups
	518.5	37.7		686.0	19.4	Second stage of thermal decomposition of methyl groups
90M10A_S1	423.9	11.6	90M10A_CNT_S1	467.2	10.0	First stage of thermal decomposition of methyl groups and amine decomposition
	733.3	9.2		729.7	6.9	Second stage of thermal decomposition of methyl groups
80M20A_S1	26.3	1.8	80M20A_CNT_S1	28.4	1.0	Removal of residual solvents/ adsorbed water
	-	-		204.9	0.9	Removal of residual CTAB
	440.0	11.5		467.7	10.8	First stage of thermal decomposition of methyl groups and amine decomposition
	708.5	8.8		724.1	7.3	Second stage of thermal decomposition of methyl groups

Appendix B

The figures and table shown in this appendix are complementary information to the results presented in Chapter 4.

Figure B1: Photograph of phase separation when CTAB was added into the solution containing ethanol-water as solvent and graphene oxide.
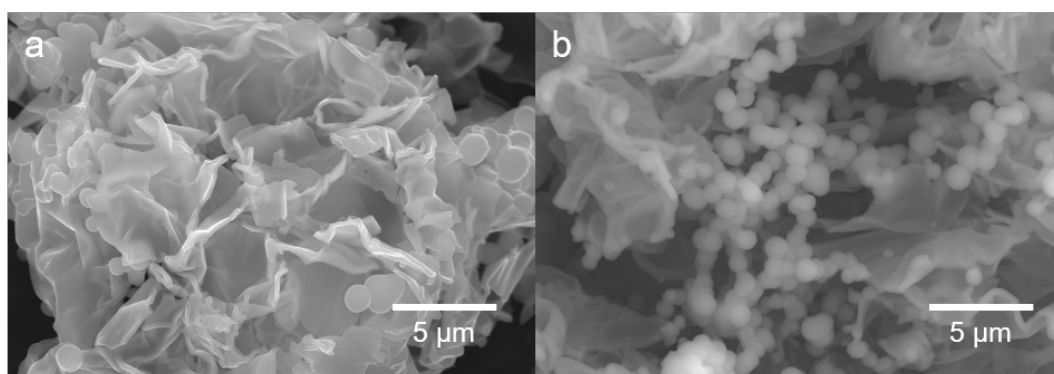
Figure B2: SEM images of a) 90M10A_GO_10 and b) 80M20A_GO_10 without surfactant.

Table B1: Chemical systems nomenclature, silica precursors proportion, quantities of solvent, catalysts surfactant and carbon nanomaterial used for each sample.

Samples	EtOH (mL)	H$_2$O (mL)	CTAB (g)	CNT (mg (wt% of the sol))	MTMS (mL)	APTMS (mL)	Acid catalyst (mL)	Basic catalyst (mL)
100M	12.0	12.0	1.25	-	5.0	-	2.5	2.7
100M_CNT_10	12.0	12.0	1.25	10 (0.03)	5.0	-	2.5	2.7
100M_CNT_50	12.0	12.0	1.25	50 (0.15)	5.0	-	2.5	2.7
100M_CNT_100	12.0	12.0	1.25	100 (0.3)	5.0	-	2.5	2.7
100M_CNT_200	12.0	12.0	1.25	200 (0.6)	5.0	-	2.5	2.7
90M10A	12.0	12.0	1.25	-	4.5	0.6	2.5	2.7
90M10A_CNT_10	12.0	12.0	1.25	10 (0.03)	4.5	0.6	2.5	2.7
90M10A_CNT_50	12.0	12.0	1.25	50 (0.15)	4.5	0.6	2.5	2.7
90M10A_CNT_100	12.0	12.0	1.25	100 (0.3)	4.5	0.6	2.5	2.7
90M10A_CNT_200	12.0	12.0	1.25	200 (0.6)	4.5	0.6	2.5	2.7
80M20A	12.0	12.0	1.25	-	4.0	1.2	2.5	2.7
80M20A_CNT_10	12.0	12.0	1.25	10 (0.03)	4.0	1.2	2.5	2.7
80M20A_CNT_50	12.0	12.0	1.25	50 (0.15)	4.0	1.2	2.5	2.7
80M20A_CNT_100	12.0	12.0	1.25	100 (0.3)	4.0	1.2	2.5	2.7
80M20A_CNT_200	12.0	12.0	1.25	200 (0.6)	4.0	1.2	2.5	2.7
Samples	EtOH (mL)	H$_2$O (mL)	PEG (mL)	GO[a] (mL (wt% of the sol))	MTMS (mL)	APTMS (mL)	Acid catalyst (mL)	Basic catalyst (mL)
90M10A	12.0	12.0	1.1	-	4.5	0.6	2.5	2.7
90M10A_GO_10	12.0	10.8	1.1	1.2 (0.03)	4.5	0.6	2.5	2.7
90M10A_GO_50	12.0	5.8	1.1	6.2 (0.15)	4.5	0.6	2.5	2.7
90M10A_GO_100	12.0	-	1.1	12.0 [b] (0.3)	4.5	0.6	2.5	2.7
80M20A	12.0	12.0	1.1	-	4.0	1.2	2.5	2.7
80M20A_GO_10	12.0	10.8	1.1	1.2 (0.03)	4.0	1.2	2.5	2.7
80M20A_GO_50	12.0	5.8	1.1	6.2 (0.15)	4.0	1.2	2.5	2.7
80M20A_GO_100	12.0	-	1.1	12.0 [b] (0.3)	4.0	1.2	2.5	2.7

(a) GO aqueous solution has a concentration of 8 mg.mL^{-1}. (b) For these samples the solution was concentrated to avoid further addition of water.
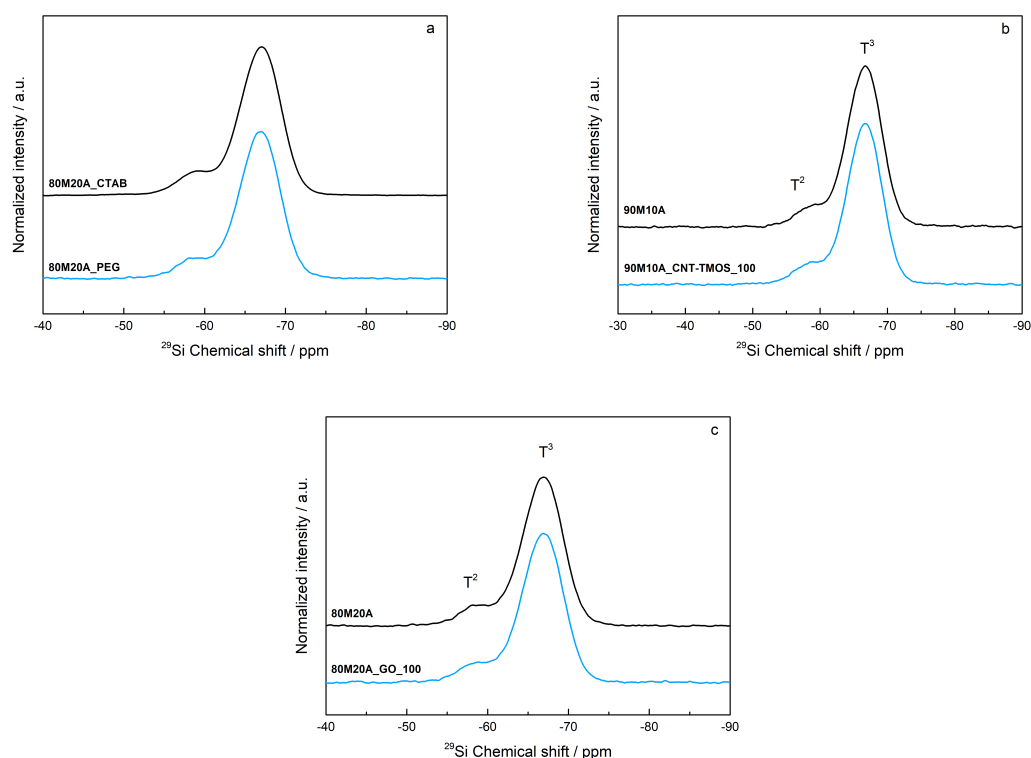
Figure B3: ^{1}H–^{29}Si solid-state MAS-NMR spectra of a) 80%MTMS/20%APTMS silica aerogels synthesized with CTAB and PEG; b) 90%MTMS/10%APTMS silica aerogels synthesized with and without CNTs; c) 80%MTMS/20%APTMS silica aerogels synthesized with and without GO.
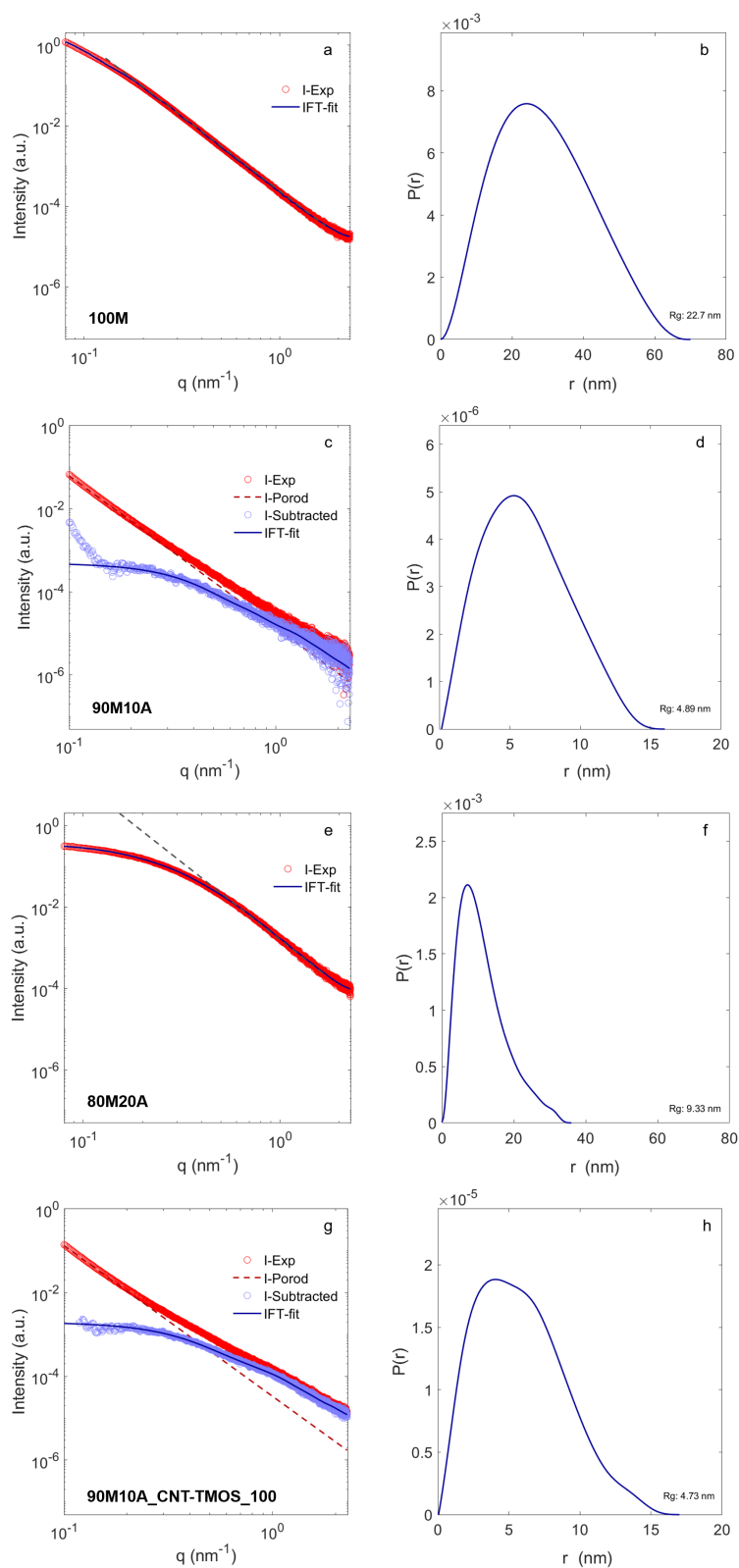
Figure B4: (a,c,e,g) Experimental scattering patterns and their relevant residual scattering obtained from subtraction of Porod line are shown together with the indirect Fourier transformation (IFT) evaluation of residual scattering. (b,d,f,h) Pair-distance distribution function, $P(r)$, obtained from IFT analysis of residual scattering from pores.

**Table B2:** Young's modulus of silica aerogels without carbon nanostructures and with different amounts of CNTs-HNO₃, CNTs-TMOS and GO.

| Samples	Young's modulus (kPa)		
	100M_CNTs-HNO₃	90M10A_CNTs-HNO₃	80M20A_CNTs-HNO₃
0 mg [308]	40.1 ± 0.2	68.7 ± 0.2	-
10 mg	34.2 ± 0.3	11.5 ± 0.2	-
50 mg	44.6 ± 0.5	51.6 ± 0.5	9414.7 ± 6.0
100 mg	96.0 ± 1.0	21.4 ± 0.2	12947.8 ± 17.5
200 mg	154.5 ± 0.3	15.9 ± 0.2	14111.7 ± 17.1
	100M_CNTs-TMOS	90M10A_CNTs-TMOS	80M20A_CNTs-TMOS
0 mg [308]	40.1 ± 0.2	68.7 ± 0.2	-
10 mg [308]	50.2 ± 0.3	191.3 ± 0.1	-
50 mg	26.9 ± 0.3	50.3 ± 0.5	6748.8 ± 8.6
100 mg	23.2 ± 0.4	32.2 ± 0.3	10356.9 ± 12.7
200 mg	50.5 ± 0.4	20.1 ± 0.2	839.6 ± 1.5
		90M10A_GO	80M20A_GO
0 mg	-	44.3 ± 0.3	43.8 ± 0.4
10 mg	-	24.9 ± 0.2	15.5 ± 0.2
50 mg	-	50.7 ± 0.4	24.3 ± 0.8
100 mg	-	32.6 ± 0.2	150.1 ± 0.8
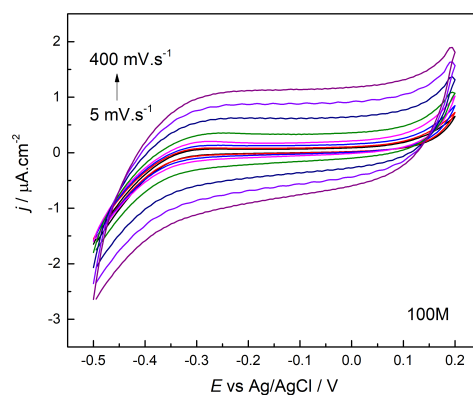
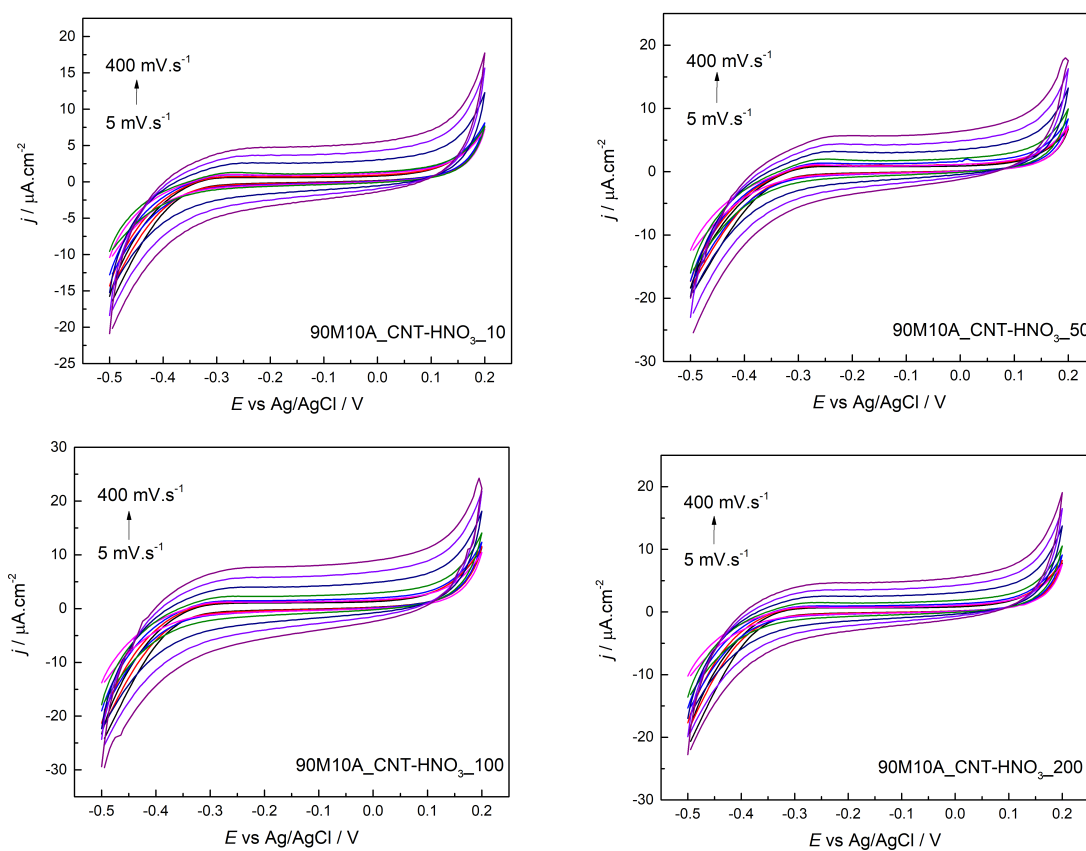**Figure B5:** Cyclic voltammograms obtained for the sample 100M in 6 M KOH.
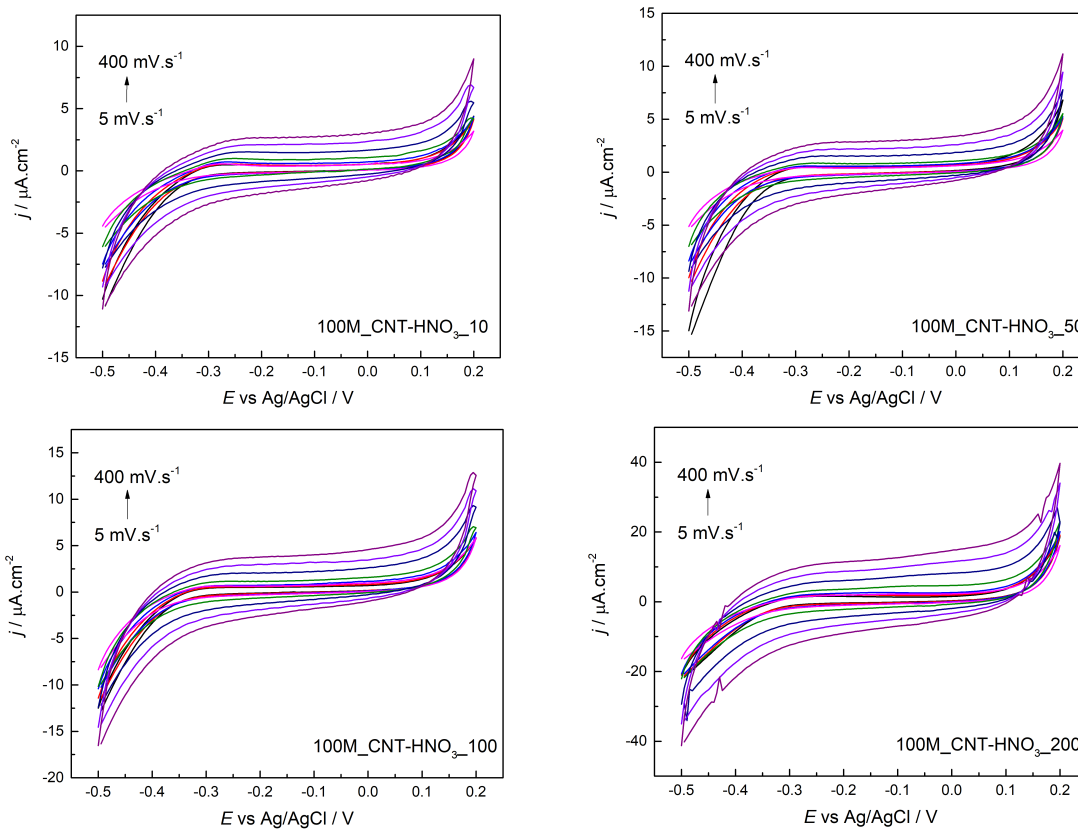
Figure B6: Cyclic voltammograms obtained for the samples 100M with different amount of CNT-HNO₃ in 6 M KOH.
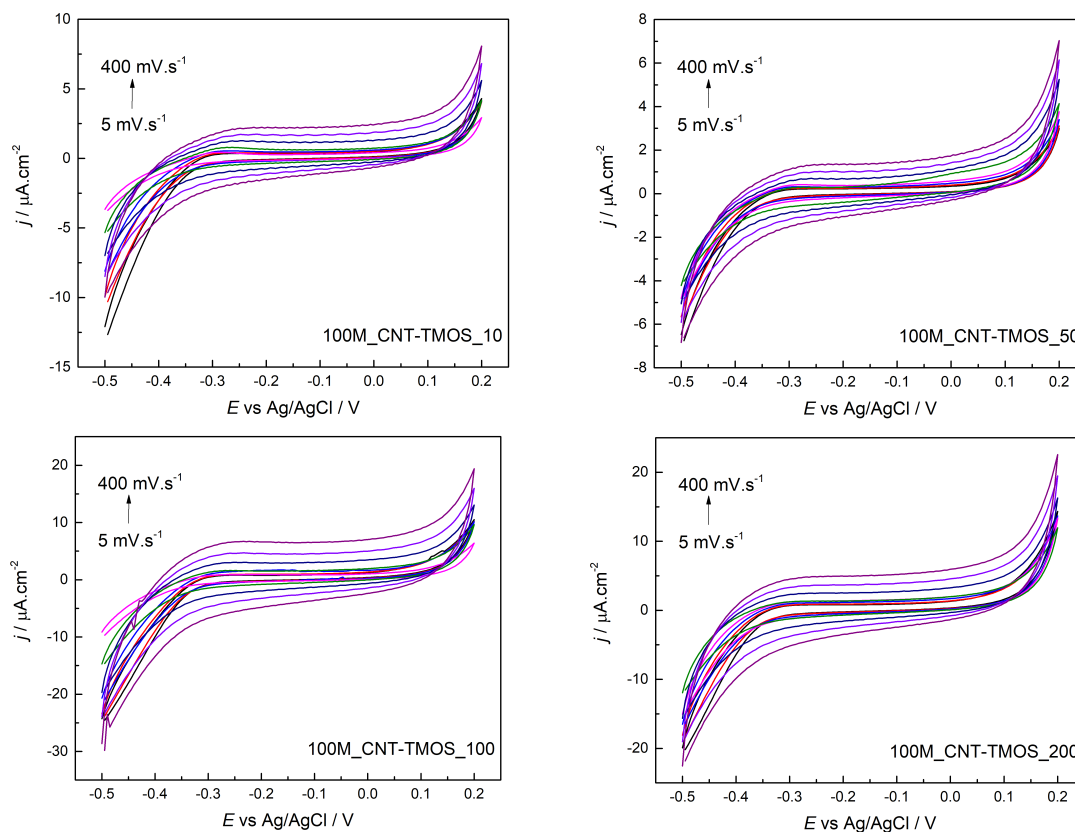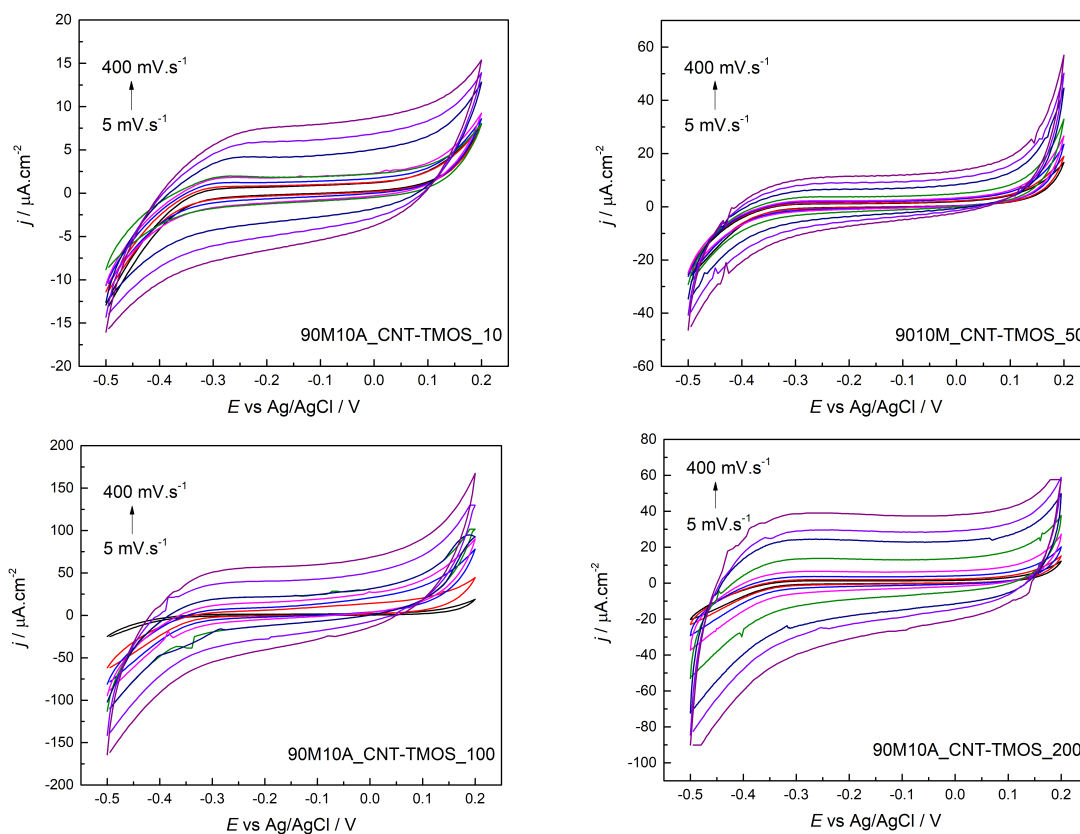

Figure B7: Cyclic voltammograms obtained for the samples 100M with different amount of CNT-TMOS in 6 M KOH.
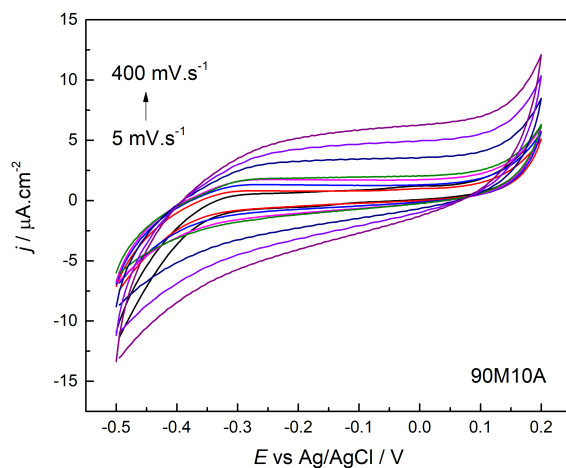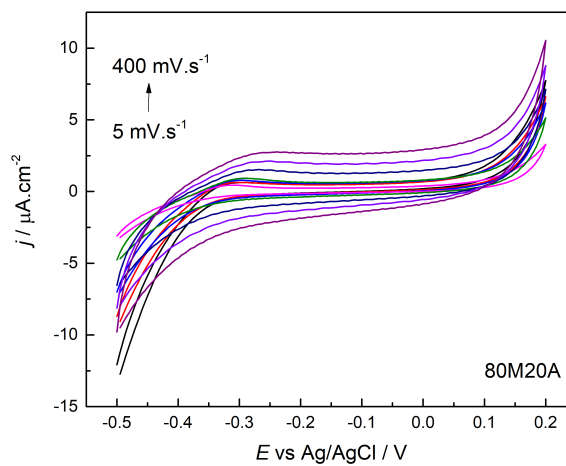
Figure B8: Cyclic voltammograms obtained for the sample 90M10A in 6 M KOH.
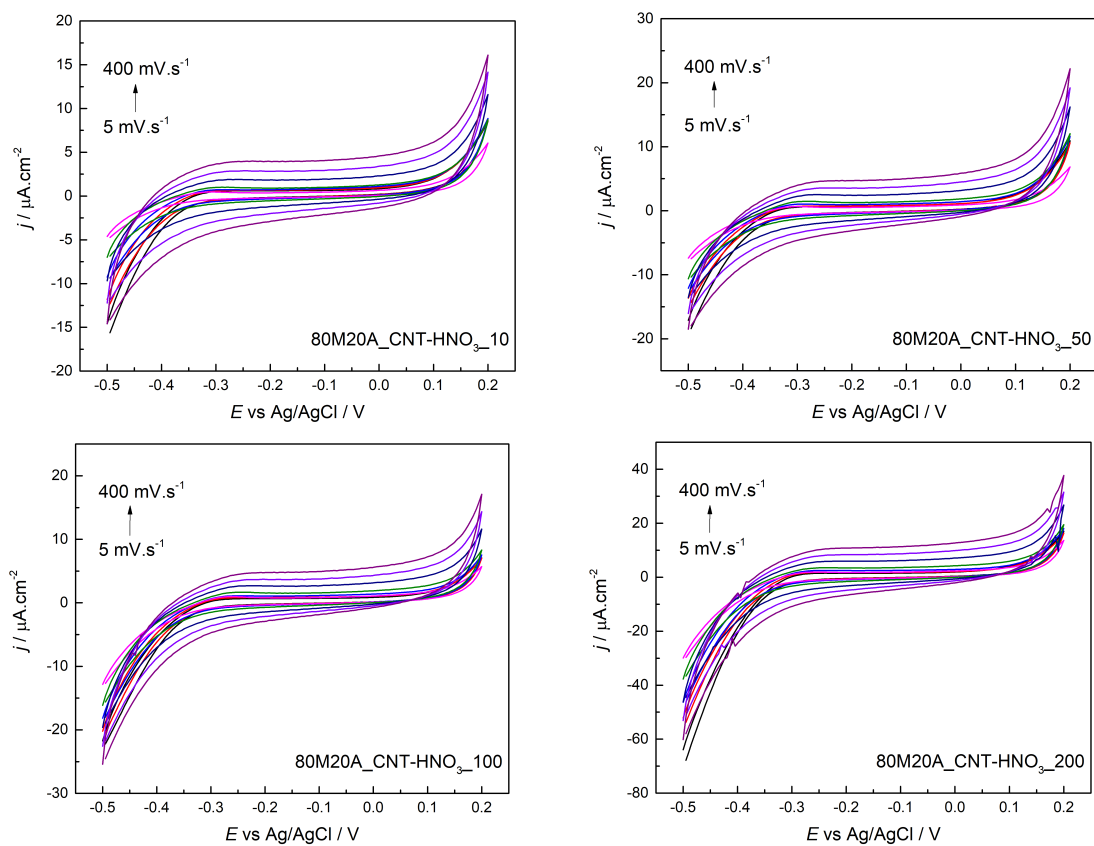

Figure B9: Cyclic voltammograms obtained for the samples 90M10A with different amount of CNT-HNO$_3$ in 6 M KOH.
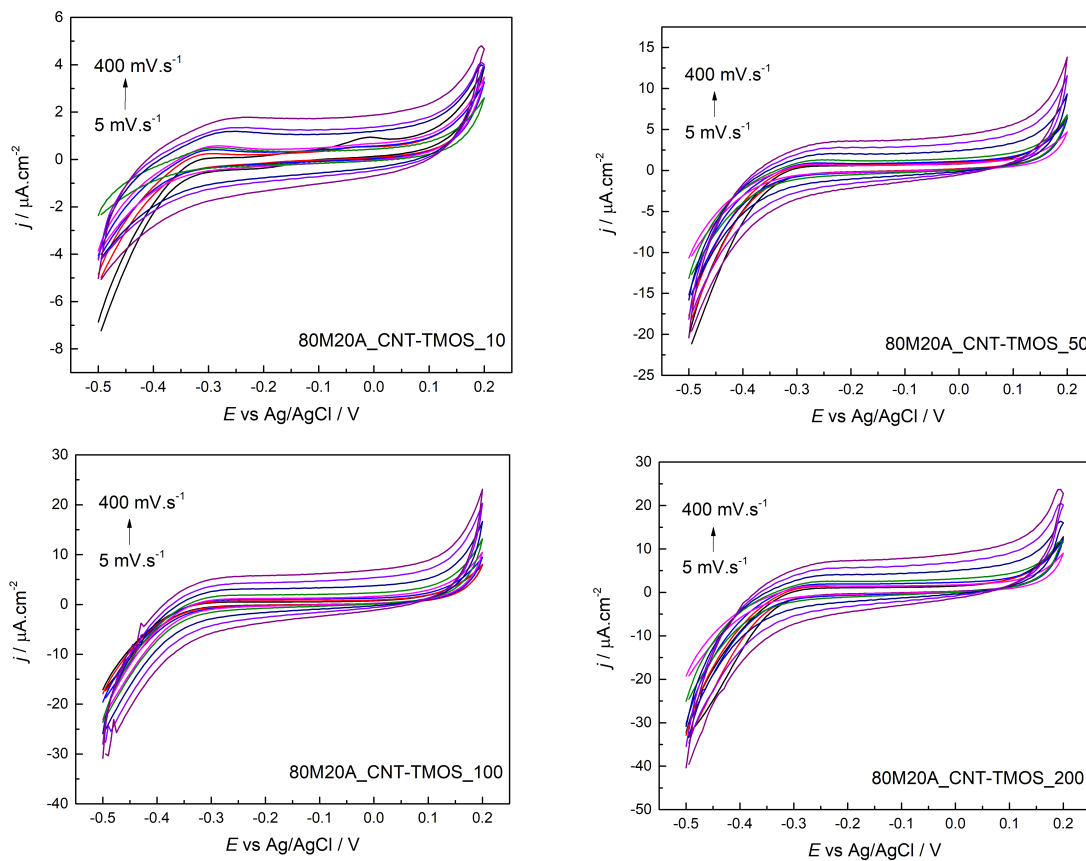
Figure B10: Cyclic voltammograms obtained for the samples 90M10A with different amount of CNT-TMOS in 6 M KOH.
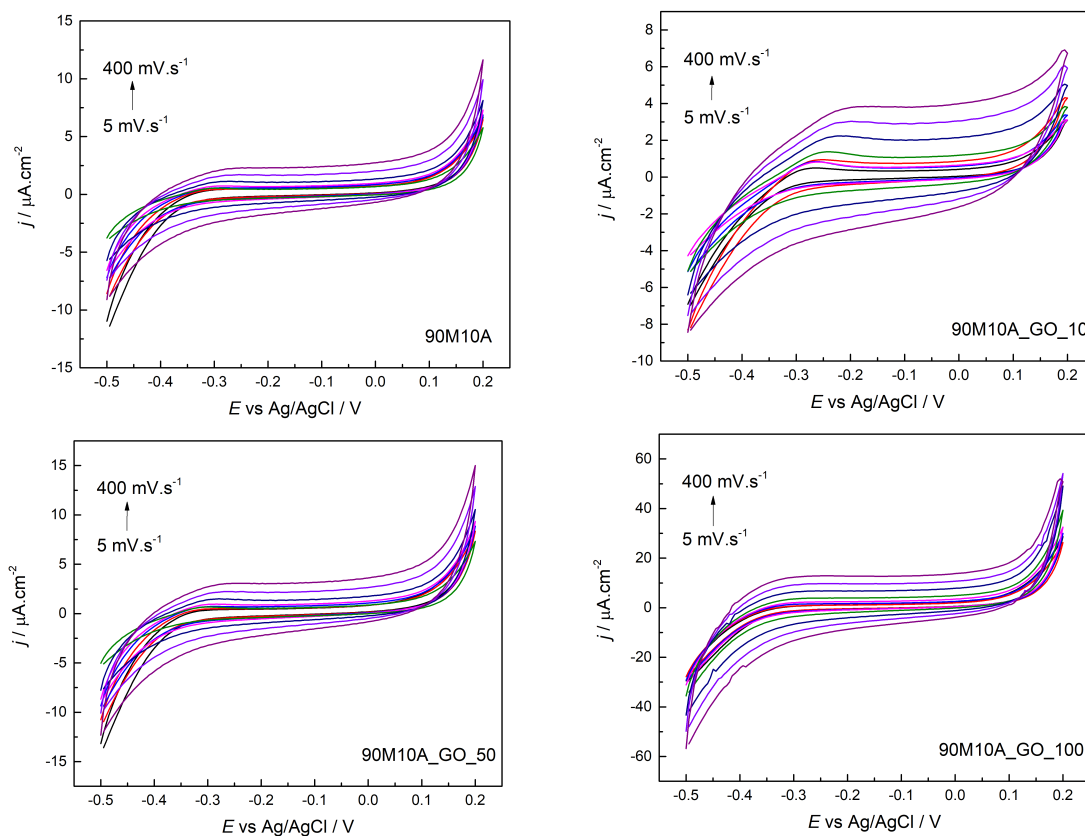

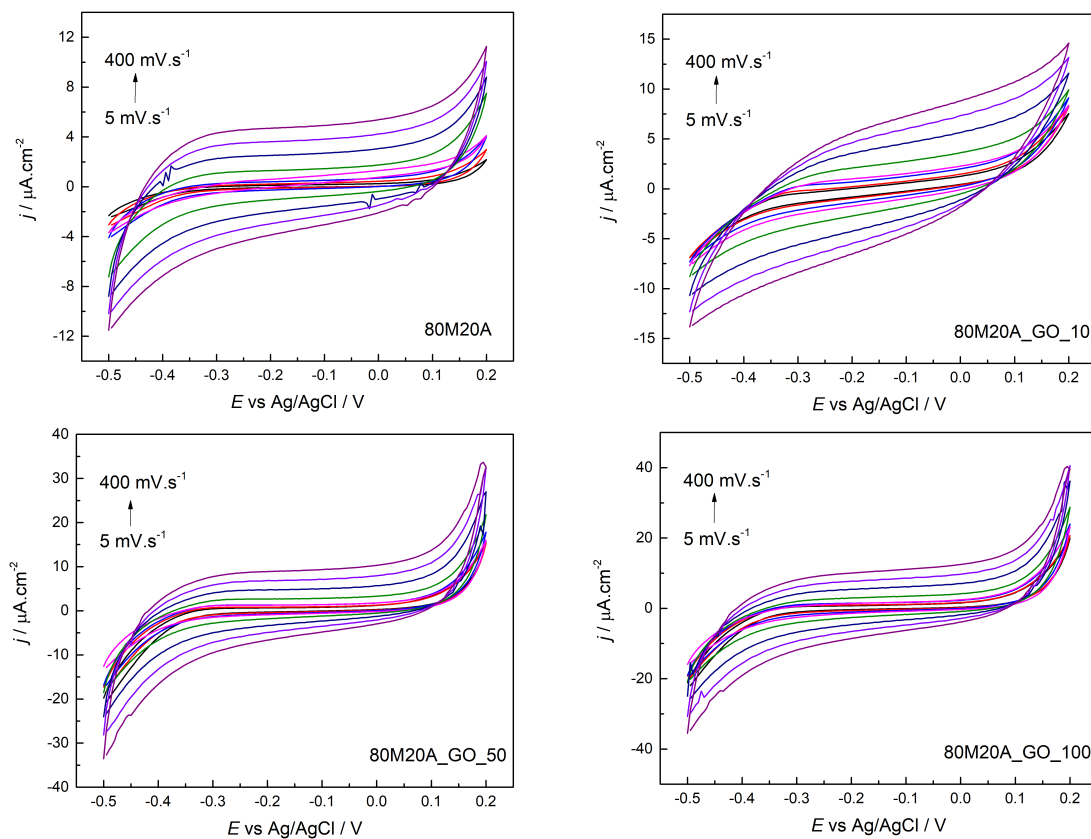**Figure B11:** Cyclic voltammograms obtained for the sample 80M20A in 6 M KOH.

Figure B12: Cyclic voltammograms obtained for the samples 80M20A with different amount of CNT-HNO$_3$ in 6 M KOH.

Figure B13: Cyclic voltammograms obtained for the samples 80M20A with different amount of CNT-TMOS in 6 M KOH.

Figure B14: Cyclic voltammograms obtained for the samples 90M10A with different amount of GO in 6 M KOH.

Figure B15: Cyclic voltammograms obtained for the samples 80M20A with different amount of GO in 6 M KOH.